DEVELOPMENT OF SPINEL-BASED ELECTRODE SUPPORTS FOR SOLID OXIDE FUEL CELLS

Elena Stefan

A Thesis Submitted for the Degree of PhD
at the
University of St Andrews

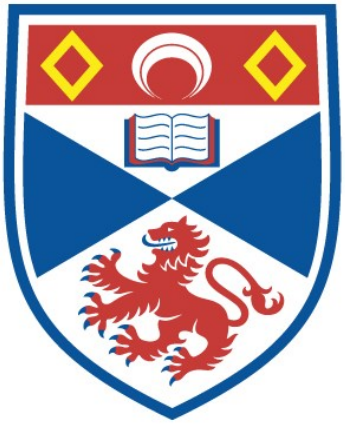

2013

Development of Spinel-based Electrode Supports for Solid Oxide Fuel Cells

Elena Stefan

Supervised by Professor John T.S. Irvine

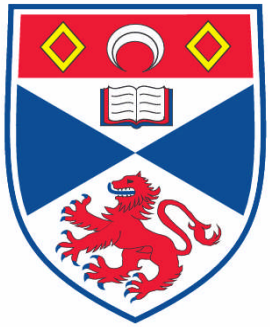

A Thesis Submitted for the Degree of PhD

at the

University of St Andrews

December 2012

Declaration

I, Elena Stefan, hereby certify that this thesis, which is approximately 38000 words in length, has been written by me, that it is the record of work carried out by me and that it has not been submitted in any previous application for a higher degree.

I was admitted as a research student in November, 2008 and as a candidate for the degree of Doctor of Philosophy in September 2009; the higher study for which this is a record was carried out in the University of St Andrews between 2008 and 2012.

Date ……..... signature of candidate …….....

I hereby certify that the candidate has fulfilled the conditions of the Resolution and Regulations appropriate for the degree of Doctor of Philosophy in the University of St Andrews and that the candidate is qualified to submit this thesis in application for that degree.

Date ……..... signature of supervisor …….....

In submitting this thesis to the University of St Andrews I understand that I am giving permission for it to be made available for use in accordance with the regulations of the University Library for the time being in force, subject to any copyright vested in the work not being affected thereby. I also understand that the title and the abstract will be published, and that a copy of the work may be made and supplied to any bona fide library or research worker, that my thesis will be electronically accessible for personal or research use unless exempt by award of an embargo as requested below, and that the library has the right to migrate my thesis into new electronic forms as required to ensure continued access to the thesis. I have obtained any third-party copyright permissions that may be required in order to allow such access and migration, or have requested the appropriate embargo below.

The following is an agreed request by candidate and supervisor regarding the electronic publication of this thesis:

Access to printed copy but embargo of electronic publication of thesis for a period of one year on the following ground(s):

publication would preclude future publication;

Date ……..... signature of candidate ……..... signature of supervisor... ……..

Acknowledgements

I would like to express my gratitude to my supervisor, Professor John T.S. Irvine for offering me the opportunity to study in his group and complete this work. Thank you for the unconditioned support, valuable suggestions, discussions and for helping me improve my knowledge in solid state chemistry.

I would like to thank my colleagues from the JTSI group, to Dr Paul Connor for advice in experimental work, setups, useful discussions and software. His knowledge, skills and experience were always shared with good will and a true benefit for my work during these years. Also Dr Abul Kalam Azad, Dr George Tsekouras and Dr Maarten Verbraeken who taught me a lot about analyzing my experimental results.

Also, my sincere thanks goes to Dr Mark Cassidy for both theoretical and experimental advice on screen printing and cell fabrication. Dr Martin Smith and Dr David Miller for useful suggestions and discussions, and Dr Cristian Savaniu for guidance in material synthesis. Chengsheng Ni and Xiangling Yue thank you for useful discussions about cell fabrication.

I could not forget the valuable help of Mrs. Julie Nairn with various matters including introduction to tape casting process and various other equipment, and continuous assistance for the good functioning of the laboratory equipment. I am also deeply grateful to Mrs. Sylvia Williamson and Mr. Ross Blackley for the time and experience they shared with me in matters of thermogravimetric analysis, dilatometry and X-ray diffraction or Scanning Electron Microscopy. Also, Mr George Anthony, Robert Cathcart and Brian Walker, thank you for assistance with fixing various pieces of equipment.

I wish to thank to Office of Naval Research for the Postgraduate Scholarship and EPSRC for funding support.

Abstract

The high temperature oxidation of ferritic stainless steel interconnects results in chromium poisoning of the solid oxide fuel cell (SOFC) electrodes, which is a limiting factor for their utilisation as SOFC interconnects. Chromium-rich spinel materials were studied as electrode supports that would be situated at the interface between interconnect and electrode, in order to reduce the effect of chromium poisoning of the electrodes. The main goal of this thesis was to find chromium-rich spinel materials with good electrical conductivity ($\sigma \geq 0.1$ S·cm^{-1}) in air and reducing atmosphere, chemically and mechanically stable in SOFC testing conditions.

The structure and properties of newly formulated chromium-rich spinels, such as $Mn_{1+x}Cr_{2-x}O_4$ (x = 0, 0.5), $MnFe_xCr_{2-x}O_4$ (x = 0.1, 1), $MgMnCrO_4$, $MnLi_xCr_{2-x}O_4$ (x = 0.1) and $MgM_xCr_{2-x}O_4$, (M = Li, Mg, Ti, Fe, Cu, Ga) were studied aiming at their application as electrode support material for solid oxide fuel cells. Cation distributions were determined by Rietveld refinement from X-ray diffraction (XRD), within the limits of XRD precision and correlated with electrical properties determined experimentally. The chemical stability in reducing conditions was studied and the reduction effects upon materials were evaluated by XRD phase analysis and microstructure analysis. It was found that $MnM_xCr_{2-x}O_4$ materials have a limited stability to reduction, only $MnCr_2O_4$ proved to have good stability when reduced, with negative influence for its p-type semiconductor conductivity. Even though $MnFeCrO_4$ had limited stability to reduction, in reducing conditions the conductivity changed from p-type to n-type semiconductor. A similar behaviour to reduction was observed for $MgFeCrO_4$. Also the mechanical and chemical compatibility of some spinels with YSZ was studied in terms of thermal expansion coefficient (TEC/K^{-1}), sintering step and possible chemical reactions.

Lithium titanate spinels, starting with $LiCrTiO_4$, were investigated in terms of structure, properties and spinel - ramsdellite phase transition temperature also with the purpose of new material development. For these materials positive results were obtained in conductivity and chemical stability in reducing conditions.

The performance of $MnFeCrO_4$ and $MgFeCrO_4$ as electrode support materials was investigated when used alone or impregnated with $(La_{0.75}Sr_{0.25})_{0.97}Cr_{0.5}Mn_{0.5}O_3$, $La_{0.8}Sr_{0.2}FeO_3$, $Ce_{0.9}Gd_{0.1}O_2$, CeO_2 or Pd. Composite anodes for SOFC were prepared by aqueous infiltration of nitrate salts into porous $MnFeCrO_4$ and $MgFeCrO_4$ scaffolds and studied by electrochemical impedance spectroscopy (EIS) in symmetrical cell configuration. The performance of the composite anodes was evaluated in humidified $5\%H_2/Ar$ in order to understand their stability and performance at 850 °C or lower temperature with respect to the porous substrates. It was found that all the impregnated phases adhere very well to the spinel and considerably enhance performance and stability to a level required for SOFC applications.

An interesting next step in this work would be to apply such spinel materials on steel interconnects, integrate them into testing SOFC devices and evaluate their effect upon chromium poisoning of the electrodes.

List of Figures

Figure 1-1 World energy consumption since 1990 to 2035 in quadrillion British thermal units (Btu); (OECD – Organization for Economic Cooperation and Development with the members OECD Americas – United States, Canada, Mexico/Chile, OECD Asia – Japan, South Korea, Australia/New Zealand and OECD Europe – Austria, Belgium, Czech Republic, Denmark, Finland, France, Germany, Greece, Hungary, Iceland, Ireland, Italy, Luxembourg, the Netherlands, Norway, Poland, Portugal, Slovakia, Slovenia, Spain, Sweden, Switzerland, Turkey, and the United Kingdom;).[1] 20
Figure 1-2 World net electricity generation by fuel type, 2008-2035(trillion KWh).[1] 21
Figure 1-3 Electrochemical processes in a fuel cell with O_2 oxidant and H_2 fuel. a = anode, c = cathode, e = electrolyte (after [12]) 23
Figure 1-4 Planar solid oxide fuel cell design with metallic interconnects (after [6]) 26
Figure 1-5 Representation of chromium poisoning process in SOFC caused by diffusion of Cr volatile species from Cr - interconnect into the LSM cathode and at the interface cathode/electrolyte.[12] 27
Figure 1-6 Spinel structure for $MgCr_2O_4$ represented with atoms; the representation has origin choice 2. ●- O^{2-}; • - Cr^{3+}; • - Mg^{2+}. 29
Figure 1-7 Spinel structure for $MgCr_2O_4$ represented with polyhedral model..... 29
Figure 1-8 Ionic radius [32] for Mn^{2+}, Fe^{2+}, Li^{+}, Cu^{2+}, Mg^{2+}, Mn^{3+}, Fe^{3+} and Ga^{3+} and coordination numbers (CN). Dashed lines illustrate the absence of ionic radii of Cr^{3+} and Mn^{3+} for CN = 4. 30
Figure 1-9 Kröger-Vink diagram for ZrO_2 in which oxygen anti-Frenkel defects dominate the intrinsic defect structure (after [46,48]). 36
Figure 1-10 Schematic representation of an electron hole hopping at B site..... 39
Figure 1-11 Example of Arrhenius plots log(σ) vs. 1000/T for $MgCr_2O_4$ and $MgFeCrO_4$ with slope change at 400 °C and 500 °C, respectively. Slope change corresponds to change in activation energy. 40
Figure 1-12 Representation of composite electrodes: a) cermet; b) by infiltration of electrode materials into porous YSZ scaffolds. 42
Figure 1-13 Quaternary system Mn_2O_3-MgO-Cr_2O_3-Fe_2O_3. Spinel compositions investigated in the quaternary oxide system are also represented in the diagram..... 43
Figure 1-14 Schematic diagram of spinel solid solutions investigated in the systems $MgCr_2O_4$ – $LiCrTiO_4$, Mg_2TiO_4 – $LiCrTiO_4$ and Mg_2TiO_4 – $LiCrTiO_4$ – $MgFeCrO_4$. 44
Figure 2-1 Generation of X-rays resulted from electron transitions to K-shell from higher energy shells: Kα1 line corresponds to an electron transition from 2p to 1s, while Kα2 line corresponds to a transition from 2s to 1s. 52
Figure 2-2 Diffraction of X-rays by electrons resulting in constructive interference (reflected beams are in phase); d_{hkl} is the interplanar distance with h k l - the Miller

indices , the black thickened lines represent the path difference between beams reflected by consecutive layers. 53
Figure 2-3 Scattering of X-rays by s electrons with introduction a path difference, δ, in the scattered wave front (after [3,5]) 54
Figure 2-4 Basic construction of Scanning Electron Microscope (after [12]) 57
Figure 2-5 Electron species resulting from the interaction of the electron beam with the sample (after [12]) 57
Figure 2-6 Functional diagram of a pushrod dilatometer.[13] 59
Figure 2-7 Schematic representation of 4-terminal conductivity experimental setup (after [14]). 60
Figure 2-8 Contact geometry used for 4-terminal conductivity measurements. 60
Figure 2-9 Schematic representation of the basic principle of tape casting process.[16]61
Figure 2-10 YSZ-screen printed green tapes with 1 and 2 layers printed area (5x5 cm^2) before co-lamination. 63
Figure 2-11 Schematic representation of: a) Nyquist and b) Bode plots for a set of data collected experimentally for this work (R_e- electrolyte resistance, R_p-polarisation resistance); c) the considered equivalent circuit ($R_s = R_e$, the electrolyte contribution, $R_{p1}+R_{p2} = R_p$, the total polarisation resistance with contribution of two electrode processes and CPE_1, CPE_2 - constant phase elements accounting for the capacitive component). 65
Figure 2-12 Equivalent circuit specific for fitting bulk and grain boundary for a ceramic material (after [18,26,21]). 67
Figure 2-13 Representation of: a) Nyquist and b) Bode plots of electrochemical impedance obtained on the $MnFeCrO_4$/LSCM|YSZ|$MnFeCrO_4$/LSCM symmetrical cell at 835 °C, in stagnant air; c) the considered equivalent circuit (L=inductive component, $R_s = R_e$, the electrolyte contribution, $R_{p1}+R_{p2} = R_p$, the total polarisation resistance with contribution of two electrode processes and CPE_1, CPE_2 - constant phase elements accounting for the capacitive component). 69
Figure 2-14 Schematic representation of the EIS measurements experimental setup. 70
Figure 3-1 X-ray diffraction pattern for $MgCr_2O_4$ after sintering at 1400 °C 74
Figure 3-2 X-ray diffraction patterns for $Mg_{0.9}Cr_{2.1}O_4$ sintered in air and in 5%H_2/Ar at 1400 °C for 12 hours. 75
Figure 3-3 Rietveld refinement profiles for $MnCr_2O_4$ with Si as internal standard; Observed data are represented with red dots, calculated profile with black line and difference profile with blue line. 77
Figure 3-4 Rietveld refinement profiles of: a) $MnFe_{0.1}Cr_{1.9}O_4$ and b) $MnFeCrO_4$ with Si as internal standard. Observed data are represented with red dots, calculated profile with black line and difference profile with blue line. 78
Figure 3-5 Rietveld refinement profiles of $MgCr_2O_4$ XRD pattern. Observed data are represented with red dots, calculated profile with black line and difference profile with blue line. 79

Figure 3-6 Rietveld refinement profiles of $MgFeCrO_4$ (random distribution). Observed data are represented with red dots, calculated profile with black line and difference profile with blue line. 80
Figure 3-7 The evolution of the cell parameter with the average ionic radii for B sites; (empty squares) – r_B for $MnM_xCr_{2-x}O_4$; (empty circles) – r_B for $MgM_xCr_{2-x}O_4$; (grey line – guiding lines for linear trend)..... 83
Figure 3-8 Variation of refined u parameter with $(r_A-r_B)/a$ based on Equation 3-1,[17] where r_A and r_B are average ionic radii resulted from the considered cation distribution; (empty squares) – refined u for $MnM_xCr_{2-x}O_4$; (empty circles) – refined u parameters for $MgM_xCr_{2-x}O_4$. 83
Figure 3-9 Micrographs of a) $Mn_{1.5}Cr_{1.5}O_4$; b) $MnFeCrO_4$; c) $MgMnCrO_4$ d) $MnCr_2O_4$ sintered at 1400 °C for 12 hours in air. 85
Figure 3-10 Micrographs of: a) $MgCr_2O_4$; b) $MgFe_{0.1}Cr_{1.9}O_4$ c) $MgGa_{0.1}Cr_{1.9}O_4$; d) $MgCu_{0.1}Cr_{1.9}O_4$; e) $MgLi_{0.1}Cr_{1.9}O_4$; f) $Mg_{1.5}Ti_{0.5}CrO_4$ sintered at 1400 °C for 12 hours in air. 86
Figure 3-11 X-ray diffraction pattern of $MnFeCrO_4$ scaffold reduced in dry $5\%H_2/Ar$ or humidified $5\%H_2/Ar$ at 1000 °C for 20 hours..... 87
Figure 3-12 Micrographs and picture of $Mn_{1.5}Cr_{1.5}O_4$: a) as synthesized; b), c) - reduced for 20 hours at 950 °C; d) picture of $Mn_{1.5}Cr_{1.5}O_4$ after reduction. 89
Figure 3-13 Micrographs of $MnFeCrO_4$: a) - as synthesized; b) - reduced for 20 hours at 950 °C; the magnification scale was chosen to be representative for different microstructures. 90
Figure 3-14 X-ray Diffraction Pattern of $MgFeCrO_4$ reduced at 1000 °C for 20 hours: (a) in humidified (3% H_2O) $5\%H_2/Ar$ and (b) dry $5\%H_2/Ar$; Lines Cu $K\alpha_1$ and $K\alpha_2$ are specified in comparison with the: As synthesised scan that only contains Cu $K\alpha_1$ line. 91
Figure 3-15 Log(σ) vs. a) cell parameter of $MnM_xCr_{2-x}O_4$; b) cell parameter of $MgM_{0.1}Cr_{1.9}O_4$; c) the Fe content of $MgFe_xCr_{2-x}O_4$; d) the Ga content of $MgGa_xCr_{2-x}O_4$ in air and reducing conditions at 850 °C. 94
Figure 3-16 Evolution of electrical conductivity of $Mg_{1.5}Ti_{0.5}CrO_4$ and $MgFeCrO_4$ and $MnCr_2O_4$ in reducing conditions at 850 °C, with p-type conductivity of $MnCr_2O_4$ and n-type conductivity of $Mg_{1.5}Ti_{0.5}CrO_4$ and $MgFeCrO_4$. 95
Figure 3-17 Activation energy dependence upon unit cell parameter and temperature in air of listed materials; the two marked positions correspond to $MgFe_{0.5}Cr_{1.5}O_4$ (full squares), $MgFeCrO_4$ (full square red) and $MnFe_{0.1}Cr_{1.9}O_4$ (empty squares). 96
Figure 3-18 Sintering step determined for $MgCr_2O_4$, $MgCr_2O_4$/YSZ (40 : 60 mol.%) and YSZ at 1350 °C with dwell 15 minutes. 98
Figure 3-19 Sintering step for $MnFeCrO_4$, $MgFeCrO_4$ and YSZ at 1400 °C with 1 hour dwell. 99
Figure 3-20 X-ray diffraction pattern of $MnFeCrO_4$ as synthesized and $MnFeCrO_4$/YSZ (1:1 wt.%) sintered at 1400 °C for 10 hours. 100
Figure 3-21 X-ray diffraction pattern of $MgCr_2O_4$ as synthesized and $MgCr_2O_4$/YSZ (1:1 wt.%) sintered at 1400 °C for 10 hours..... 100

Figure 3-22 Micrographs of: a) $MgMnCrO_4$/YSZ; b) $MgCr_2O_4$/YSZ; c), d) $MnFeCrO_4$/YSZ mixtures after sintering at 1400 °C for 10 hours. 101
Figure 4-1 Schematic representation of studied oxides spinels with determined temperatures of phase transition spinel − ramsdellite. i = 0.42 represents the inversion degree determined of $MgFeCrO_4$ (chapter 3) 106
Figure 4-2 Rietveld refinement profiles of $LiTiCrO_4$ quenched from 950 °C to room temperature; Observed data are represented with red dots, calculated profile with black line and difference profile with blue line. 107
Figure 4-3 Rietveld refinement profiles of $Li_{0.8}Mg_{0.3}Cr_{0.9}Ti_{0.9}Fe_{0.1}O_4$ quenched from 1200 °C to room temperature. Observed data are represented with red dots, calculated profile with black line and difference profile with blue line. 108
Figure 4-4 Rietveld refinement profiles of $Li_{0.7}Mg_{0.4}Cr_{0.9}Ti_{0.8}Fe_{0.2}O_4$ quenched from 1300 °C to room temperature. Observed data are represented with red dots, calculated profile with black line and difference profile with blue line. 109
Figure 4-5 Ramsdellite structure of $LiTiCrO_4$ represented with polyhedral model; with yellow are represented the Cr/Ti octahedra and with blue, the Li cations located in the channels. 110
Figure 4-6 Rietveld refinement profiles of $Li_{0.9}Mg_{0.2}Cr_{0.9}TiO_4$ quenched from 1100 °C to room temperature. The pattern contains reflections corresponding to spinel (Bragg positions marked with blue) and ramsdellite (Bragg positions marked with red) forms of the material. The third phase is internal standard Si (green Bragg positions). Observed data are represented with red dots, calculated profile with black line and difference profile with blue line. 111
Figure 4-7 Micrographs of : a) $Li_{0.9}Mg_{0.1}Cr_{1.1}Ti_{0.9}O_4$ quenched from 1100 °C; b) $Li_{0.85}Mg_{0.3}Cr_{0.85}TiO_4$ quenched from 1200 °C; c) $Li_{0.9}Mg_{0.2}Cr_{0.9}TiO_4$ quenched from 1100 °C to room temperature. 113
Figure 4-8 Cell parameter vs. sintering temperature for 5 °C/min heating-cooling rate (represented as open circle) and quenched samples (represented as open square). 114
Figure 4-9 The evolution of the cell parameter with the average ionic radii for B sites; (grey line – guiding lines for linear trend) 116
Figure 4-10 Variation of refined u parameter with $(r_A-r_B)/a$ based on Equation 3-1,[8] where r_A and r_B are average ionic radii resulted from the considered cation distribution. 116
Figure 4-11 Micrographs of a) $Li_{0.9}Mg_{0.2}Cr_{0.9}TiO_4$; b) $Li_{0.9}Mg_{0.1}Cr_{1.1}Ti_{0.9}O_4$; c) $Li_{0.85}Mg_{0.3}Cr_{0.85}TiO_4$ sintered at 1000 °C for 12 hours and d) $Li_{0.85}Mg_{0.3}Cr_{0.85}TiO_4$ sintered at 1100 °C for 12 hours in air. 117
Figure 4-12 Micrographs of: a) $Li_{0.7}Mg_{0.4}Cr_{0.9}Ti_{0.8}Fe_{0.2}O_4$ sintered at 1000 °C; b) $Li_{0.7}Mg_{0.4}Cr_{0.9}Ti_{0.8}Fe_{0.2}O_4$ sintered at 1100 °C; c) $Li_{0.7}Mg_{0.4}Cr_{0.9}Ti_{0.8}Fe_{0.2}O_4$ sintered at 1200 °C; d) $Li_{0.8}Mg_{0.3}Cr_{0.9}Ti_{0.9}Fe_{0.1}O_4$ sintered at 1100 °C for 12 hours in air. 118
Figure 4-13 X-ray diffraction pattern of $Li_{0.7}Mg_{0.4}Cr_{0.9}Ti_{0.8}Fe_{0.2}O_4$ sintered at: a) 1100 °C and b) 1200 °C and reduced in dry 5%H_2/Ar at 1000 °C for 20 hours. 119

Figure 4-14 Arrhenius plots measured in air of $Li_{0.9}Mg_{0.2}Cr_{0.9}TiO_4$/1000 °C, $Li_{0.85}Mg_{0.3}Cr_{0.85}TiO_4$/1100 °C, $Li_{0.85}Mg_{0.3}Cr_{0.85}TiO_4$/1200 °C and $Li_{0.7}Mg_{0.4}Cr_{0.9}Ti_{0.8}Fe_{0.2}O_4$/1100 °C in temperature range 150 – 800 °C..... 120
Figure 4-15 Arrhenius plots measured in 5%H_2/Ar of $Li_{0.85}Mg_{0.3}Cr_{0.85}TiO_4$/1100 °C, $Li_{0.85}Mg_{0.3}Cr_{0.85}TiO_4$/1200 °C and $Li_{0.7}Mg_{0.4}Cr_{0.9}Ti_{0.8}Fe_{0.2}O_4$/1100 °C in temperature range 180 – 800 °C..... 121
Figure 4-16 Evolution of electrical conductivity for LiCrTiO4, $Li_{0.9}Mg_{0.2}Cr_{0.9}TiO_4$ and $Li_{0.7}Mg_{0.4}Cr_{0.9}Ti_{0.8}Fe_{0.2}O_4$ in reducing conditions at 800 °C, with p-type conductivity for LiCrTiO4 and $Li_{0.9}Mg_{0.2}Cr_{0.9}TiO_4$ initially, and n-type conductivity for longer reducing time and lower p_{O_2}. 122
Figure 5-1 DC electrical conductivity of a dense $MnFeCrO_4$ pellet as a function of time after switching from static air to humidified 5%H_2/Ar. The inset shows the same data as a function of p_{O_2}. 127
Figure 5-2 SEM images of $MnFeCrO_4$ scaffold: a) – three layer wafer consisting of dense YSZ electrolyte with porous $MnFeCrO_4$ on either side; b) – microstructure of spinel layer after testing in air; c) – microstructure of spinel layer after testing in humidified 5%H_2/Ar at 850 °C for 11 hours; d) – detail of the sample tested. 128
Figure 5-3 X-ray diffraction pattern of $MnFeCrO_4$ – LSCM(27%) and $MnFeCrO_4$ – LSCM(22%) – CGO(12%) with LSCM sintered at 1200 °C for 4 hours and CGO sintered at 1000 °C for 4 hours. 129
Figure 5-4 X-ray diffraction pattern of $MnFeCrO_4$ – LSF(20%) sintered at 900 °C for 4 hours; Fe_2O_3 (hematite) marked peaks are observed on this pattern. 129
Figure 5-5 SEM images of: a) $MnFeCrO_4$ - LSCM(27%) tested in air and humidified 5%H_2/Ar; b) $MnFeCrO_4$ - LSF(20%) tested in air. 130
Figure 5-6 SEM images of: a) $MnFeCrO_4$ – LSCM(22%) – CGO(12%) after tests in air and humidified 5%H_2/Ar; b) $MnFeCrO_4$ – LSCM(22%) – CeO_2(6%) tested in humidified – 5%H_2/Ar..... 131
Figure 5-7 SEM images of: a) $MnFeCrO_4$ –LSCM(22%) – CGO(12%) –Pd(1%) tested in humidified 5%H_2/Ar; b) $MnFeCrO_4$ – LSCM(22%) – CeO_2(6%) – Pd(1%) tested in humidified 5%H_2/Ar. 131
Figure 5-8 Symmetrical cells measured in stagnant air at 870 °C: a) – Nyquist plot containing data for the whole cell (2 equal electrodes); b) – Bode plot of phase angle vs frequency; c), d) – Arrhenius plots for R_s and R_p obtained from equivalent circuits fitting of experimental data; plotted R_s and R_p values are for one electrode..... 134
Figure 5-9 Equivalent circuit used to fit experimental data, where L = inductor; R_s = series resistance; R_p = polarisation resistance and CPE = constant phase element..... 134
Figure 5-10 Symmetrical cells measured in humidified 5%H_2/Ar at 850 °C: a) – Nyquist plot containing data for the whole cell (2 equal electrodes); b) – Bode plot of phase angle vs frequency; c), d) – Arrhenius plots for R_s and R_p obtained from equivalent circuits fitting of experimental data; plotted R_s and R_p values are for one electrode..... 139

Figure 5-11 Nyquist plots of $MnFeCrO_4$ scaffold and $MnFeCrO_4$/LSCM reduced at 850 °C for 1 hour/ 11 hours and corresponding equivalent circuits fit; spectra contain data for two identical electrodes. 143
Figure 5-12 Nyquist plots of $MnFeCrO_4$/LSCM/CeO_2 and $MnFeCrO_4$/LSCM/CeO_2/Pd reduced at 850 °C for 1 hour/ 11 hours and corresponding equivalent circuits fit; spectra contain data for two identical electrodes. 144
Figure 5-13 Nyquist plots of $MnFeCrO_4$/LSCM/CGO and $MnFeCrO_4$/LSCM/CGO/Pd reduced at 850 °C for 1 hour/ 11 hours and corresponding equivalent circuits fit; spectra contain data for two identical electrodes. 145
Figure 5-14 Electrical conductivity plotted as a function of time in reducing conditions at 850 °C; the inner plot shows the same data as a function of the partial pressure of the oxygen;..... 147
Figure 5-15 SEM images of $MgFeCrO_4$|YSZ|$MgFeCrO_4$ three layer wafer with details presented for the spinel - YSZ interface and the microstructure of the spinel porous layer. 148
Figure 5-16 XRD pattern of $MgFeCrO_4$/LSCM and $MgFeCrO_4$/LSCM/CGO with LSCM sintered at 1200 °C (4 hours) and CGO at 1000 °C (4 hours); Oxide phases: spinel, perovskite and CGO. 149
Figure 5-17 XRD pattern of MgFeCrO4/LSCM/CeO_2 with LSCM sintered at 1200 °C for 4 hours and CeO_2 at 450 °C (4 hours); Oxide phases: spinel, perovskite and CeO_2. 149
Figure 5-18 SEM images in cross section of: a) MgFeCrO4/LSCM; b) MgFeCrO4/LSCM/CeO_2; c) $MgFeCrO_4$/LSCM/CGO; d) $MgFeCrO_4$/LSCM/CeO_2/Pd; e) $MgFeCrO_4$/LSCM/CGO/Pd and f) surface micrograph for $MgFeCrO_4$/LSCM/CGO/Pd – Pd particles are present; the micrographs were made after the samples were tested in humidified – 5%H_2/Ar.. 151
Figure 5-19 Symmetrical cells measured in humidified 5%H_2/Ar at 850 °C: a) Nyquist plot containing data for the whole cell (2 equal electrodes); b) – Bode plot of phase angle vs frequency; c), d) – Arrhenius plots for R_s and R_p obtained from equivalent circuits fitting of experimental data; plotted R_s and R_p values are for one electrode..... 154
Figure 5-20 Equivalent circuit used to fit experimental data, where L = inductor; R_s = series resistance; R_p = polarisation resistance and CPE = constant phase element..... 155
Figure 5-21 Nyquist plots of $MgFeCrO_4$ and $MgFeCrO_4$/LSCM reduced at 850 °C for 1 hour/ 11 hours and corresponding equivalent circuits fit; spectra contain data for two identical electrodes. 158
Figure 5-22 Nyquist plots of $MgFeCrO_4$/LSCM/CeO_2 and $MgFeCrO_4$/LSCM/CGO reduced at 850 °C for 1 hour/ 11 hours and corresponding equivalent circuits fit; spectra contain data for two identical electrodes..... 159

Figure 5-23 Nyquist plots of $MgFeCrO_4$/LSCM/CeO_2/Pd and $MgFeCrO_4$/LSCM/CGO/Pd reduced at 850 °C for 1 hour/ 11 hours and corresponding equivalent circuits fit; spectra contain data for two identical electrodes. 160
Figure 7-1 Rietveld refinement profiles of MgFeCrO4 after initial stages of refinement and before refining the degree of inversion in the spinel and the atomic isotropic displacement factors, which corresponds to stages 1-6 described in the refinement strategy. 170
Figure 7-2 Rietveld refinement profiles of $MgFeCrO_4$ after refining the degree of inversion in the spinel. 172
Figure 7-3 Rietveld refinement profiles of $MgFeCrO_4$ after refining the degree of inversion in the spinel and scale factor, cell parameter, oxygen parameter and peak profile parameters 173
Figure 7-4 Rietveld refinement profiles of $MgFeCrO_4$ after refining the degree of inversion in the spinel and scale factor, cell parameter, oxygen parameter and peak profile parameters repeated several times. 174
Figure 7-5 Rietveld refinement profiles of $MgFeCrO_4$ after refining the atomic isotropic displacement factors, scale factor, cell parameter, oxygen parameter and peak profile parameters. 175
Figure 7-6 Final stage of the Rietveld refinement of $MgFeCrO_4$, after refining the atomic isotropic displacement factors, and cation inversion alternatively, along with the other refinable parameters: scale factor, cell parameter, oxygen parameter and peak profile parameters. 177
Figure 8-1 Rietveld refinement profiles for $MnLi_{0.1}Cr_{1.9}O_4$ with Si as internal standard; Observed data is represented with red dots, calculated profile with black line and difference profile with blue line. 180
Figure 8-2 Rietveld refinement profiles for $Mn_{1.5}Cr_{1.5}O_4$. Experimental data is represented with red dots, calculated profile with black line and difference profile with blue line. 181
Figure 8-3 Rietveld refinement profiles for $MgMnCrO_4$ with Si as internal standard. 182
Figure 8-4 Rietveld refinement profiles for: a) $MgFe_{0.1}Cr_{1.9}O_4$ and b) $MgFe_{0.5}Cr_{1.5}O_4$. Experimental data is represented with red dots, calculated profile with black line and difference profile with blue line. 183
Figure 8-5 Rietveld refinement profiles for $Mg_{1.5}Ti_{0.5}CrO_4$. Experimental data is represented with red dots, calculated profile with black line and difference profile with blue line. 185
Figure 8-6 Rietveld refinement profiles for: a) $Li_{0.9}Mg_{0.1}Cr_{1.1}Ti_{0.9}O_4$ sintered at 900 °C, b) $Li_{0.9}Mg_{0.2}Cr_{0.9}TiO_4$ sintered at 1000 °C, c) $Li_{0.85}Mg_{0.3}Cr_{0.85}TiO_4$ sintered at 1000 °C and d) $Li_{0.8}Mg_{0.3}Cr_{0.9}Ti_{0.9}Fe_{0.1}O_4$ sintered at 1100 °C. Observed data is represented with red dots, calculated profile with black line and difference profile with blue line. 187

Figure 9-1 Equivalent circuit model for characterising the impedance spectra for $MnFeCrO_4$/LSCM symmetrical cell. 190
Figure 9-2 Electrochemical impedance spectroscopy of $MnFeCrO_4$/LSCM symmetrical cell measured in 5%H_2/Ar at several temperatures between 675 °C and 850 °C: a), b) and c) Nyquist plots containing data for the whole cell (2 equal electrodes); d) Bode plots. 192
Figure 9-3 Fitting of the experimental data using the equivalent circuit presented above: a) Nyquist plot; b) Bode plot; c) Arrhenius plots for R_s, R_p, R_{p1} and R_{p2} resulted from the data fitting. 194

List of Tables

Table 2-1 Equivalent circuit components with corresponding symbols in ZView software and impedance formula.[23] 66
Table 3-1 Parameters resulted from refinement of $MnCr_2O_4$, $MnFe_{0.1}Cr_{1.9}O_4$ and $MnFeCrO_4$ XRD patterns and refinement reliability factors. 78
Table 3-2 Parameters resulted from refinement of $MgCr_2O_4$ and $MgFeCrO_4$ XRD patterns and refinement reliability factors. 80
Table 3-3 Cation distribution, a and u determined from the Rietveld refinement; (@) – u calculated with Equation 3-1.[17] 81
Table 3-4 Summary of reduction experiments in terms of experimental conditions and formed secondary phases. 88
Table 3-5.Thermal expansion coefficients between 100 and 900 °C. 97
Table 4-1 Parameters resulted from refinement of $LiTiCrO_4$, $Li_{0.8}Mg_{0.3}Cr_{0.9}Ti_{0.9}Fe_{0.1}O_4$ and $Li_{0.7}Mg_{0.4}Cr_{0.9}Ti_{0.8}Fe_{0.2}O_4$ XRD patterns and refinement reliability factors. 109
Table 4-2 Parameters resulted from refinement of XRD data for $Li_{0.9}Mg_{0.2}Cr_{0.9}TiO_4$ quenched from 1100°C, $Li_{0.9}Mg_{0.1}Cr_{1.1}Ti_{0.9}O_4$ quenched from 1100°C and $Li_{0.85}Mg_{0.3}Cr_{0.85}TiO_4$ quenched from 1200 °C and refinement reliability factors; (*) - dataset collected on Philips diffractometer. 111
Table 4-3 Cation distribution determined from the Rietveld refinement for quenched oxides, as described above. Only the samples found to be pure spinels are listed... 112
Table 4-4 Cation distribution, a and u determined from the Rietveld refinement for stable spinel oxides cooled slowly to room temperature. 115
Table 5-1 Materials impregnated into $MnFeCrO_4$ porous substrates in wt.% and labels used throughout this chapter. 126
Table 5-2 Relaxation frequencies and polarisation resistances for symmetrical cells tested in air at ~ 870 °C; R_{p1} and R_{p2} are determined from equivalent circuits fitting and listed values are for one electrode, where $R_{p1} + R_{p2} = R_p$. 134

Table 5-3 Relaxation frequencies and polarisation resistances for symmetrical cells tested in humidified – 5%H_2/Ar at ~850 °C; R_s and R_p (R_{p1}, R_{p2})are determined from equivalent circuits fitting and listed values are for one electrode..... 140
Table 5-4 Materials impregnated into $MgFeCrO_4$ porous substrates in wt.% and labels used throughout this section. 146
Table 5-5 Relaxation frequencies and polarisation resistances for symmetrical cells tested in humidified 5%H_2/Ar at ~ 850 °C; R_s and R_p (R_{p1}, R_{p2}) determined from equivalent circuits fitting and listed values are for one electrode..... 155
Table 7-1 Parameters resulted from refinement of $MgFeCrO_4$ XRD pattern and refinement reliability factors at corresponding the stage of the refinement illustrated in Figure 7-1. 170
Table 7-2 Parameters resulted from refinement of $MgFeCrO_4$ diffraction pattern and the reliability factors at corresponding the stage of the refinement illustrated in Figure 7-2. 172
Table 7-3 Parameters resulted from refinement of $MgFeCrO_4$ diffraction pattern and the reliability factors at corresponding the stage of the refinement illustrated in Figure 7-3. 173
Table 7-4 Parameters resulted from refinement of $MgFeCrO_4$ diffraction pattern and the reliability factors at corresponding the stage of the refinement illustrated in Figure 7-4. 174
Table 7-5 Parameters resulted from refinement of $MgFeCrO_4$ diffraction pattern and the reliability factors at corresponding the stage of the refinement illustrated in Figure 7-5. 176
Table 7-6 Final parameters resulted from refinement of $MgFeCrO_4$ diffraction pattern and the reliability factors of the refinement illustrated in Figure 7-5..... 177
Table 8-1 Parameters resulted from refinement of $MnLi_{0.1}Cr_{1.9}O_4$, $Mn_{1.5}Cr_{1.5}O_4$ and $MgMnCrO_4$ XRD patterns and refinement reliability factors; B_iso_A, B_iso_B and B_iso_O are isotropic thermal factors for cations at A and B sites and oxygen anions. 181
Table 8-2 Parameters resulted from refinement of $MgFe_{0.1}Cr_{1.9}O_4$, $MgFe_{0.5}Cr_{1.5}O_4$ and $MgLi_{0.1}Cr_{1.9}O_4$ XRD patterns and refinement reliability factors, with B_iso_A, B_iso_B and B_iso_O isotropic thermal factors..... 184
Table 8-3 Parameters resulted from refinement of $MgGa_{0.1}Cr_{1.9}O_4$, $MgGa_{0.2}Cr_{1.8}O_4$ and $MgCu_{0.1}Cr_{1.9}O_4$ XRD patterns and refinement reliability factors, with B_iso_A, B_iso_B and B_iso_O isotropic thermal factors..... 184
Table 8-4 Parameters resulted from refinement of $Li_{0.9}Mg_{0.2}Cr_{0.9}TiO_4$ sintered at 900 °C, $Li_{0.9}Mg_{0.2}Cr_{0.9}TiO_4$ sintered at 1000 °C, $Li_{0.9}Mg_{0.1}Cr_{1.1}Ti_{0.9}O_4$ sintered at 900 °C, $Li_{0.9}Mg_{0.1}Cr_{1.1}Ti_{0.9}O_4$ sintered at 1000 °C XRD patterns and refinement reliability factors, with B_iso_A, B_iso_B and B_iso_O isotropic thermal factors. 188
Table 8-5 Parameters resulted from refinement of $Li_{0.85}Mg_{0.3}Cr_{0.85}TiO_4$ sintered at 1000 °C, $Li_{0.85}Mg_{0.3}Cr_{0.85}TiO_4$ sintered at 1100 °C and $Li_{0.8}Mg_{0.3}Cr_{0.9}Ti_{0.9}Fe_{0.1}O_4$ sintered at 1100 °C XRD patterns and refinement reliability factors, with B_iso_A, B_iso_B and B_iso_O isotropic thermal factors..... 188

Table 8-6 Parameters resulted from refinement of $Li_{0.7}Mg_{0.4}Cr_{0.9}Ti_{0.8}Fe_{0.2}O_4$ sintered at 1000 °C, $Li_{0.7}Mg_{0.4}Cr_{0.9}Ti_{0.8}Fe_{0.2}O_4$ sintered at 1100 °C and $Li_{0.7}Mg_{0.4}Cr_{0.9}Ti_{0.8}Fe_{0.2}O_4$ sintered at 1200 °C XRD patterns and refinement reliability factors, with B_iso_A, B_iso_B and B_iso_O isotropic thermal factors..... 189
Table 9-1 Fitting results of $MnFeCrO_4$/LSCM symmetrical cell measured in 5%H_2/Ar at temperatures between 675-850 °C..... 193

Contents

Acknowledgements 3
Abstract 4
Contents 19
1 Introduction 20
1.1 Solid oxide fuel cells 22
1.2 Component requirements for solid oxide fuel cells 24
1.3 The effects of chromium poisoning on SOFC electrodes 27
1.4 The spinel structure 28
1.4.1 Overview of the spinel structure 28
1.4.2 Cation site preference in the spinel structure 30
1.5 Aliovalent substitution and defect chemistry exemplified on spinels 31
1.5.1 Defect chemistry 31
1.5.2 Defects in spinels 36
1.5.3 Conduction mechanism for chromium–rich spinels 39
1.6 Composite electrodes and electrode support materials 41
1.7 Aims and objectives of the thesis 42
1.8 References 44
2 Experimental procedures 49
2.1 Synthesis and processing 49
2.1.1 Combustion synthesis 49
2.1.2 Solid state synthesis 50
2.2 X-ray Diffraction 51
2.2.1 Background 51
2.2.2 Diffraction of X-rays 52
2.2.3 Rietveld Refinement of Crystal Structures 55
2.3 Scanning Electron Microscopy 56
2.4 Dilatometry 58
2.5 Chemical stability in reducing conditions 59
2.6 Electrical conductivity measurement 59
2.6.1 Conductivity Measurements by 4-point method 59
2.7 Fabrication of symmetrical cells 61
2.7.1 Fabrication of scaffolds by tape casting process 61

2.7.2 Screen printing of YSZ electrolyte 62
2.7.3 Insertion of electrode materials into scaffolds by impregnation 63
2.8 Electrochemical tests on symmetrical cells 64
2.8.1 Electrochemical Impedance Spectroscopy 64
2.8.2 The analysis of impedance spectroscopy by equivalent circuit method 67
2.8.3 Symmetrical cells testing parameters 69
2.9 References 70
3 Studies on $MnM_xCr_{2-x}O_4$ and $MgM_xCr_{2-x}O_4$ spinels as electrode support materials 73
3.1 Introduction 73
3.2 Structural characterization of materials 73
3.3 Chemical stability in reducing conditions 87
3.4 Electrical properties 91
3.5 Compatibility with yttrium stabilized zirconia 96
3.6 Conclusions 101
3.7 References 103
4 Studies on $LiTiCrO_4$ and related oxide spinels 105
4.1 Introduction 105
4.2 Spinel - ramsdellite phase transition temperature 105
4.2.1 Characterization of quenched materials 106
4.3 Structural characterization of non-quenched materials 114
4.4 Chemical stability in reducing conditions 119
4.5 Electrical properties 120
4.6 Conclusions 122
4.7 References 123
5 Development and performance of $MnFeCrO_4$ and $MgFeCrO_4$ - based electrodes for SOFC 125
5.1 Introduction 125
5.2 $MnFeCrO_4$ based electrodes tests 125
5.2.1 Phase analysis, conductivity and microstructure of the scaffold 126
5.2.2 Phase analysis and microstructure of impregnated scaffolds 128
5.2.3 Performance of impregnated scaffolds 132

5.2.4 Influence of reduction upon electro-chemical performance 141
5.3 $MgFeCrO_4$ based electrodes tests 146
5.3.1 Electrical conductivity and microstructure of the scaffold 147
5.3.2 Phase analysis and microstructure of impregnated scaffolds 148
5.4 Performance of impregnated scaffolds 151
5.5 Influence of reduction upon electro-chemical performance 156
5.6 Conclusions 161
5.7 References 163
6 Conclusions 164
7 Appendix 1 – Rietveld refinement – general procedure and detailed steps exemplified on a selected composition 167
7.1 Structural models reported in literature 167
7.2 The intermediary stages of the refinement 168
7.2.1 Initial premises of the structural model 168
7.2.2 Rietveld refinement steps 169
7.2.3 The refinement of the inversion degree: 171
7.3 References 179
8 Appendix 2 - Rietveld refinement result for spinel oxides 180
9 Appendix 3 – Impedance spectra analysis by equivalent circuit method 190
9.1 References 195

Chapter 1

Contents

1 Introduction 20
1.1 Solid oxide fuel cells 22
1.2 Component requirements for solid oxide fuel cells 24
1.3 The effects of chromium poisoning on SOFC electrodes 27
1.4 The spinel structure 28
1.4.1 Overview of the spinel structure 28
1.4.2 Cation site preference in the spinel structure 30
1.5 Aliovalent substitution and defect chemistry exemplified on spinels 31
1.5.1 Defect chemistry 31
1.5.2 Defects in spinels 36
1.5.3 Conduction mechanism for chromium–rich spinels 39
1.6 Composite electrodes and electrode support materials 41
1.7 Aims and objectives of the thesis 42
1.8 References 44

1 Introduction

International commissions such as the U.S. Energy Information Administration have analysed the projections of world energy consumption from 2008 to 2035 and it was evaluated that the world energy demand will increase by 53% of current energy demand (Figure 1-1). The increase in energy consumption will be determined by strong long term economic growth of developing countries. In the long term, the study projects an increase in world consumption of energy from all fuel sources and, even though the oil remains the largest source of energy, it is expected a decrease in petroleum based marketed energy from 34% in 2008 to 29% in 2035. Renewable energy is the fastest growing form and an increase in its use is expected in the total of energy use from 10% in 2008 to 14% in 2035.[1]

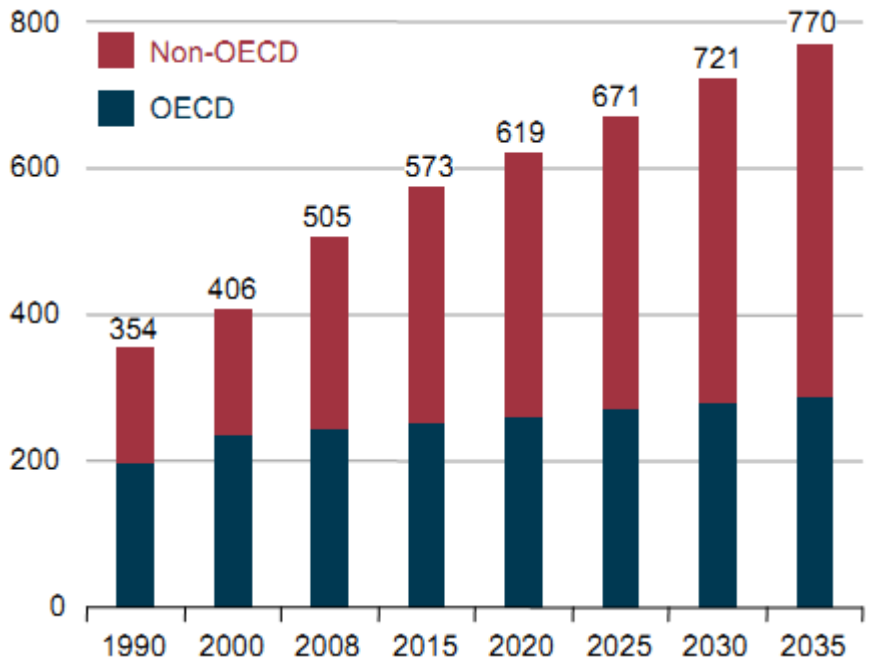

Figure 1-1 World energy consumption since 1990 to 2035 in quadrillion British thermal units (Btu); (OECD – Organization for Economic Cooperation and Development with the members OECD Americas – United States, Canada, Mexico/Chile, OECD Asia – Japan, South Korea, Australia/New Zealand and OECD Europe – Austria, Belgium, Czech Republic, Denmark, Finland, France, Germany, Greece, Hungary, Iceland, Ireland, Italy, Luxembourg, the Netherlands, Norway, Poland, Portugal, Slovakia, Slovenia, Spain, Sweden, Switzerland, Turkey, and the United Kingdom;).[1]

The expectations in electrical energy production are a 84% increase in world net electricity generation from 2008 to 2035 and, although coal remains the largest

source of world electricity until 2035, the contribution from renewable energy sources is the fastest growing source (3.1% per year), as presented in Figure 1-2.

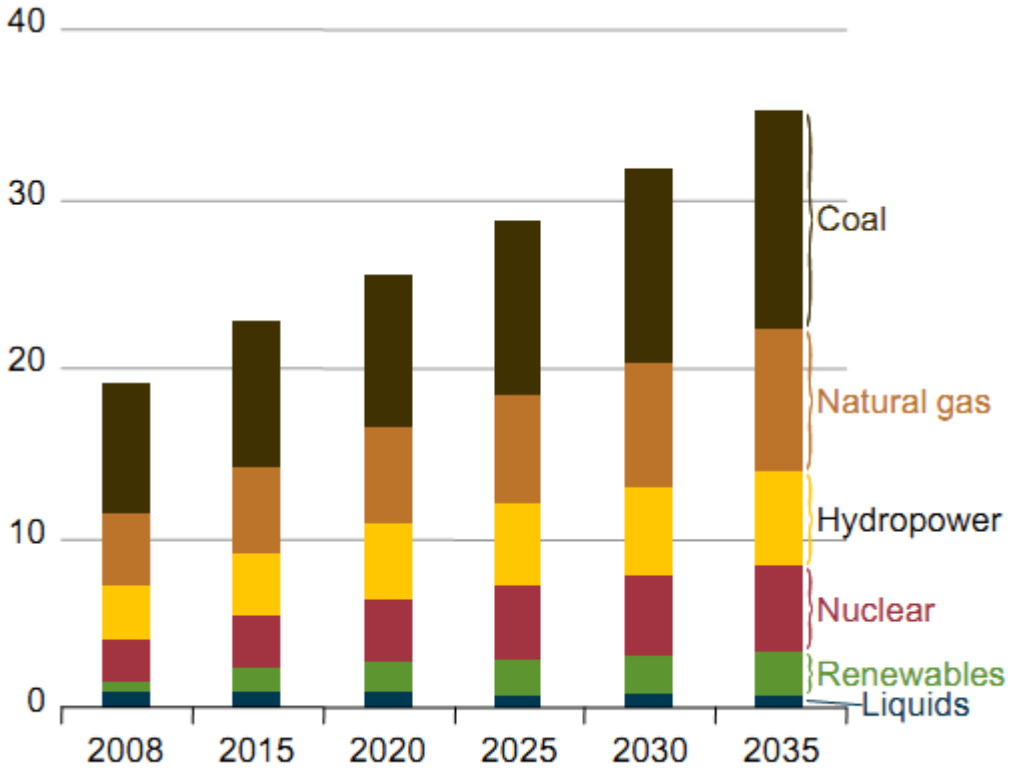

Figure 1-2 World net electricity generation by fuel type, 2008-2035(trillion KWh).[1]

The limited character of fossil energy sources results in the necessity to shift the energy technology towards renewable sources. A consequence of the worldwide economic growth led to an increase of total greenhouse emissions in the last century that could have important negative effects for the global climate. The growing awareness of climate change and the predicted decline in worlds oil production has reinforced the concept of renewable energy usage and the development of appropriate technologies.[2] The development of fuel cell technology is encouraged by clean production of electricity from a variety of fuels and its high efficiency of transforming chemical energy directly to electrical energy with low emissions of pollutants, such as CO and NO_x.[3–6]

The conversion of a fuel to electricity is made without the combustion step, while intermediate steps of producing heat and mechanical work are avoided resulting in

higher conversion efficiency. Emissions of pollutants from fuel cells are several orders of magnitude lower than those produced by conventional power generators. Also, cells can be made in different sizes, so they can be placed at different locations with minimum spacing restrictions. Another notable feature is the quiet operation due to no moving parts of the cell.[7] Fuel cell applications are various considering all their advantages. For long term applications, fuel cells are projected as devices for clean energy, using as fuel, hydrogen. In the short-term, for high temperature fuel cells, due to high temperature operation, they offer the possibility of using different fuels with higher conversion efficiencies and lower carbon dioxide and NO_x emissions.

The most suitable applications for fuel cell technology are for use in stationary power generation plants of industrial power systems, auxiliary power units for vehicles and home power generation, as well as back-up power for hospitals, companies or airports. Stationary power generation is suitable for urban areas, where localised pollution is a major issue, but also for primary power sources for distributed residences which have no access to power grid.[3,5,8]

There are six fuel cell types which are primarily being investigated and they are considered suitable in different applications, depending on their functional properties. For example, experts believe that proton exchange membrane fuel cell (PEM) will be the most efficient for powering cars and buses and may also be used for residential power applications. Solid oxide fuel cells (SOFCs) are promising technologies for electric power plants and combined with gas turbines their efficiency is expected to be over 70%. Direct methanol fuel cells are promising as battery replacement for portable applications, as cellular phones and laptop computers.[5]

1.1 Solid oxide fuel cells

Solid oxide fuel cells (SOFC) have certain advantages over other fuel cell types and a significant one consists in the possibility of using different fuels such as hydrogen, methane or natural gases due to high operating temperatures in range of 600 to 1000 °C.[5,9,10]

The main components of a solid oxide fuel cell are the cathode (air electrode), the anode (fuel electrode), a dense oxide electrolyte with high ionic conductivity and interconnect.[11] The functioning principle is based on electrochemical reactions that take place at the electrodes as illustrated in Figure 1-3.

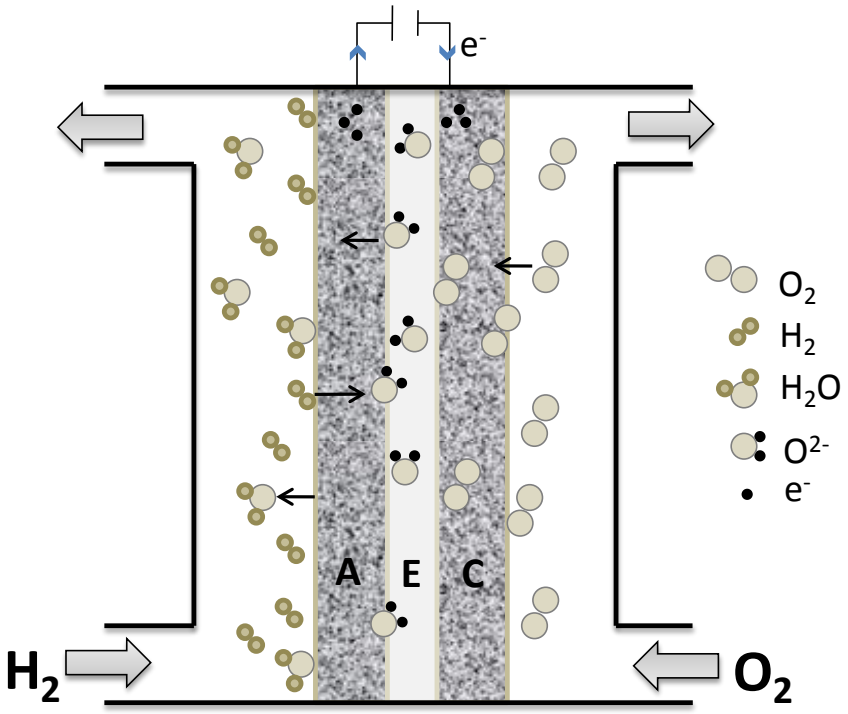

Figure 1-3 Electrochemical processes in a fuel cell with O_2 oxidant and H_2 fuel. a = anode, c = cathode, e = electrolyte (after [12])

In operation, oxygen supplied at the cathode is reduced to form an oxygen ion which migrates through the electrolyte/anode interface. Fuels such as H_2, CH_4, or natural gas, are oxidized at the anode side releasing electrons to the external circuit.[4, 8] The reactions that take place at electrodes considering hydrogen as fuel are written below:

Cathode:

$$O_2 + 4e^- \rightarrow 2O^{2-}$$

Anode:

$$2H_2 + 2O^{2-} \rightarrow 2H_2O + 4e^-$$

Overall:

$$2H_2 + O_2 \rightarrow 2H_2O$$

The electrons transferred in the reaction are released to the external circuit. The driving force for the oxygen ions is the chemical potential difference between anode (low oxygen chemical potential) and cathode (high oxygen chemical potential).

Depending on the fuel, the reactions taking place may be different, as SOFCs offer the possibility of using available fuels with a lower rate of pollution and a higher efficiency.[9,10]

1.2 Component requirements for solid oxide fuel cells

A SOFC device contains all ceramic components and they should meet several conditions for good performance and durability. The cathode and the anode consist of porous oxide ceramics and the electrolyte is a dense layer of oxygen ion conducting material. The materials for the cell components must have chemical and structural stability during the preparation and operation, similar thermal expansion coefficients, adequate porosity and catalytic activity to achieve the highest performances.[12–14]

Based on these requirements, there are few materials that can be used and the most used electrolytes materials are zirconia and ceria fluorites, and $LaGaO_3$ – based perovskites. For cathodes, doped lanthanum manganite ($LaMnO_3$) is most commonly used, but also lanthanum cobaltite ($LaCoO_3$) and for anodes Ni-YSZ cermet. The idea of a metal – ceramic (cermet) anode is also used in the development of new SOFC systems based on alternative electrolyte materials such as doped ceria, $La_{1-x}Sr_xGa_{1-y}Mg_yO_3$ (LSGM), and proton conducting electrolytes (doped $BaCeO_3$-$BaZrO_3$).[15]

In operation, the cathode is the catalyst for the reduction of the oxygen with electrons from the external circuit and conducts the O^{2-} ions to the electrolyte. Considering its functions, the requirements for the materials utilised are good ionic and electronic conductivity, good catalytic activity for the oxygen reduction, chemical and mechanical stability and thermal compatibility with the electrolyte and interconnect materials.

The anode is the catalyst for the oxidation of the fuel (hydrogen or hydrocarbons), the fuel is adsorbed at surface and the oxygen ions must be in contact with the

adsorbed fuel for the reaction to take place. The electrons resulted in the reaction must be delivered to the external circuit. The requirements for the anode materials are directly connected with its functioning and they must have also good electronic and ionic conductivity for a wide range of oxygen partial pressures, good catalytic activity, chemical and mechanical stability, and thermal compatibility with electrolyte and interconnect materials.[16] Both electrodes should be able to tolerate the gas from the other electrode through possible cracks and pinholes[17], although such pinholes lead to failure under operation.

Interconnects provide the electrical connection between the individual cells, separate the anode and the cathode compartments in solid oxide fuel cells and multiply the voltage output by connecting individual cells in series. The interconnect materials must possess a combination of physical and electrical properties for a proper functioning of the fuel cell such as, high temperature oxidation resistance in both anode and cathode atmospheres, high electrical conductivity and negligible ionic conductivity, thermal expansion compatibility with the other parts of the SOFC, zero open porosity and sufficient mechanical strength, chemical compatibility with the materials it contacts, thermodynamic stability over the applied temperature range. Also the microstructure of the interconnect should be stable with respect to the chemical potential gradient determined by the difference in oxygen partial pressure (p_{O_2}) between the oxidant and fuel sides. A microstructure change would determine the variation of electrical conductivity during its functioning. The gas impermeability can be achieved via full densification of the interconnect material during fabrication and the high density of the material should be preserved during functioning.

The interconnect should be easy to fabricate, while materials and fabrication process should be cost effective so that they will not represent major obstacles to large-scale manufacture and commercialisation. Currently, lanthanum chromite is the most commonly used ceramic interconnect material as it shows reasonably good conducting properties at operating temperatures above 800 °C. However, there are several obstacles for mass production of ceramic interconnects with $LaCrO_3$ or doped $LaCrO_3$ such as low sintering aptitude in air, the strong influence of p_{O_2} over the electrical conductivity and the most important would be the general tendency of decreasing the functioning temperatures for SOFCs.[18]

For intermediate temperature, at 800 °C, high temperature corrosion resistant metallic alloys such as ferritic stainless steels or chromium based alloys are considered to be suitable for interconnects. Chromium based alloys have some advantages to consider for interconnects as compatible coefficient of thermal expansion with the other cell components, low costs and good machinability.[5,19] In Figure 1-4 is presented the configuration of a planar SOFC as it is placed in a cell stack, between two interconnect pieces.

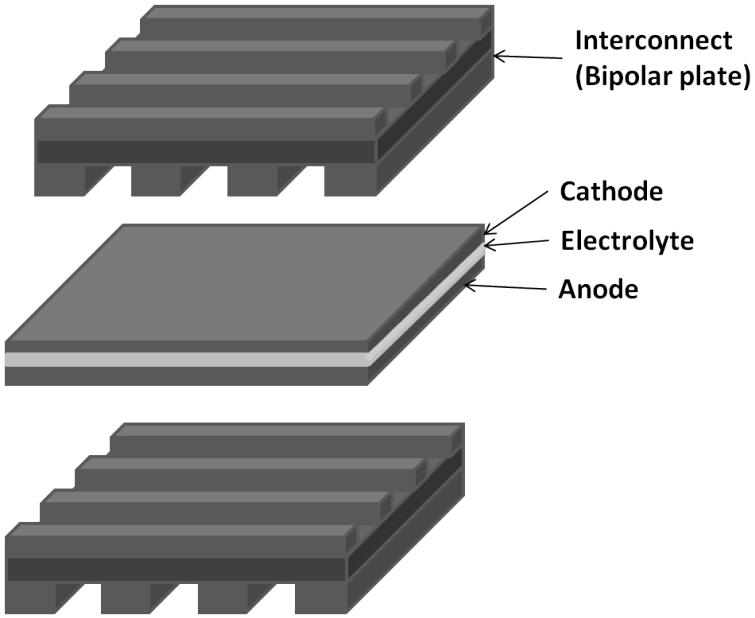

Figure 1-4 Planar solid oxide fuel cell design with metallic interconnects (after [6])

A major drawback in using chromium alloys in SOFCs is high temperature oxidation. Oxidation leads to dimensional changes and to the formation of oxide scales on component surfaces which have low electronic conductivities. Recent studies have shown that the main oxides forming on ferritic stainless steels are chromia (Cr_2O_3) and $(Mn,Cr)_3O_4$ spinel.[20,21] Other spinels, containing Cr, Mn, Fe, Co and Ni, can form depending on the composition of the steels and any other materials (cathode material) in contact with interconnect.

1.3 The effects of chromium poisoning on SOFC electrodes

One of the distinctive problems encountered with chromium based alloys and ferritic stainless steels has been identified as the formation of volatile gaseous Cr(VI) species in SOFC working conditions. Depending on temperature and partial pressure of H_2O and O_2, volatile Cr species, such as CrO_3 (g) and $Cr(OH)_2O_2$ (g) develop from the chromia scale. These species cause poisoning of the cathode and the cathode/electrolyte interface as they are reduced to Cr_2O_3 at triple phase boundary by electrochemical reactions, thus they determine the rapid degradation of the electrical properties of the fuel cell. The performance degradation of the fuel cell determined by the deposition of Cr_2O_3, is caused by the obstruction and decrease of the three phase area (electrode/electrolyte/gas) reducing the active sites for oxygen reduction.[19,22] For a Sr doped lanthanum manganite (LSM) cathode, the phases resulting from this process contain $(Mn,Cr)_3O_4$ spinels (Figure 1-5).[12,18,21]

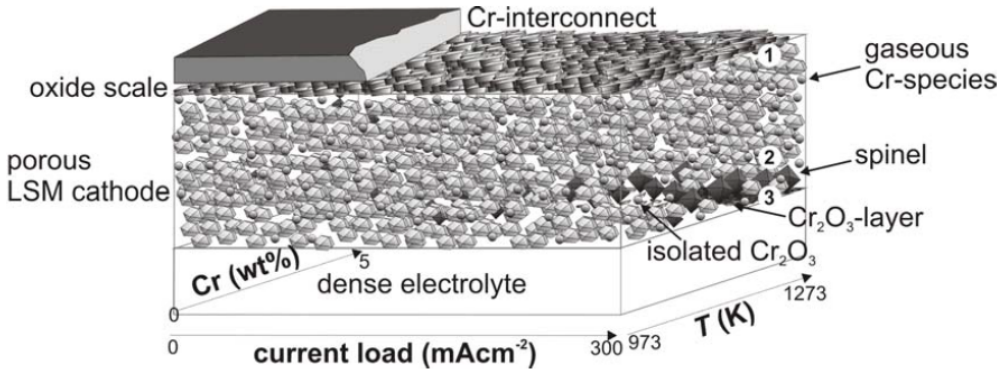

Figure 1-5 Representation of chromium poisoning process in SOFC caused by diffusion of Cr volatile species from Cr - interconnect into the LSM cathode and at the interface cathode/electrolyte.[12]

For metallic alloys that contain Cr, Mn, Fe, Co, Ni, spinels are also formed over interconnects surface. As a consequence of these observations, spinel systems were studied for protective coating on the interconnects surface, looking mostly at Mn cobaltites, as Mn-Co densified spinel coating was observed to significantly reduce Cr_2O_3 sub-scale formation, while Cr migration was blocked.[19,23,24] Chromium-rich spinels are anticipated to diminish the negative effects of chromium poisoning when employed at interconnect/electrode interface, as a lower chromium concentration gradient could lead to lower diffusion. For this application, the materials are required

to exhibit good chemical and structural stability in reducing and oxidising conditions, at high temperatures (500 to 900 °C), and sufficient electrical conductivity (> 0.1 $S \cdot cm^{-1}$). $(Mn,Cr)_3O_4$ spinels form on metallic interconnects surface resulting from high temperature oxidation process as described in section 1.3, thus their chemical composition which is compatible with the interconnects metallic alloys appoints these spinels as the right choice to be studied for electrode support materials. Several substitutions on the B site were investigated for $MnM_xCr_{2-x}O_4$ with M = Fe, Mn, Mg or Li.

1.4 The spinel structure

1.4.1 Overview of the spinel structure

The incidence of natural minerals with spinel structure determined a high interest for the study of these materials and their structure over time because of their important geological implications, but also their importance in many possible applications in solid state science.[25,26] Oxide spinels generally crystallize with a symmetry described by the space group Fd-3m (no. 227)[27] and they can be described by the general formula AB_2O_4 with A typically being a divalent cation and B, a trivalent cation. Oxygen anions form a cubic closed packed lattice with 64 tetrahedral and 32 octahedral sites partially occupied by cations. One unit cell contains 56 atoms with 8 A cations, 16 B cations and 32 oxygen anions. The occupancy for the octahedral sites is 1/2 and for the tetrahedral sites is only 1/8. Because of the similar size of the A and B cations, they can interchange sites, thus leading to the so called inverse spinels. Inversion can be synthetically expressed as $(A_{1-x}B_x)_{Td}(A_xB_{2-x})_{Oh}O_4$, where subscripts *Td* and *Oh* refer to the tetrahedral and octahedral sites, respectively. Normal spinels are formed for x = 0, perfectly inverse spinels for x = 1, while intermediate values of x ($0 < x < 1$) are called randomly inverse spinels.[25,28] The conventional unit cell of a spinel has 8 formula units per unit cell. Description of the atomic positions is influenced by the choice of the origin in the Fd-3m space group as $\bar{4}3m$ (origin on A site cation or tetrahedral vacancy) or $\bar{3}m$ (origin on B site cation or octahedral vacancy). Tetrahedral and octahedral sites have fixed coordinates and oxygen has coordinates (u,u,u) with the coordinate values depending on the origin choice with the vector (-1/8a, -1/8a, -1/8a).[28,27] Figure 1-6 represents the spinel cubic unit cell

from view (100) and the origin choice 2: origin on octahedral vacancy. Cation coordinates are (1/8, 1/8, 1/8) for A site cations, (1/2, 1/2, 1/2) for B site cations and the oxygen parameter, u=1/4 (0.250) for a perfect cubic close packed anion arrangement. Anions usually deviate away from their ideal positions with important implications in bond lengths, bond angles, interstice volumes and symmetries of coordination polyhedral.[28,29]

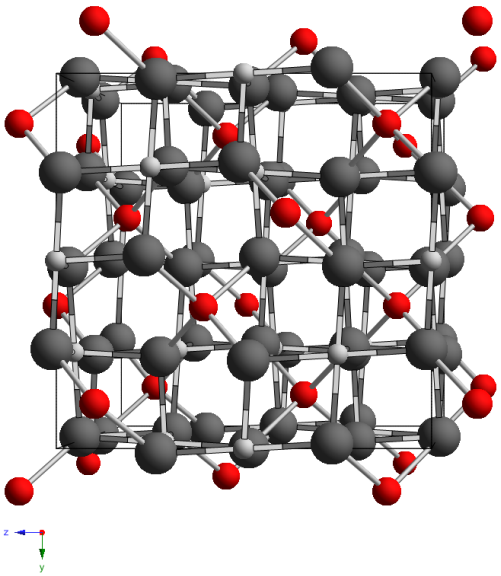

Figure 1-6 Spinel structure for $MgCr_2O_4$ represented with atoms; the representation has origin choice 2. ● **- O^{2-};** ● **- Cr^{3+};** ● **- Mg^{2+}.**

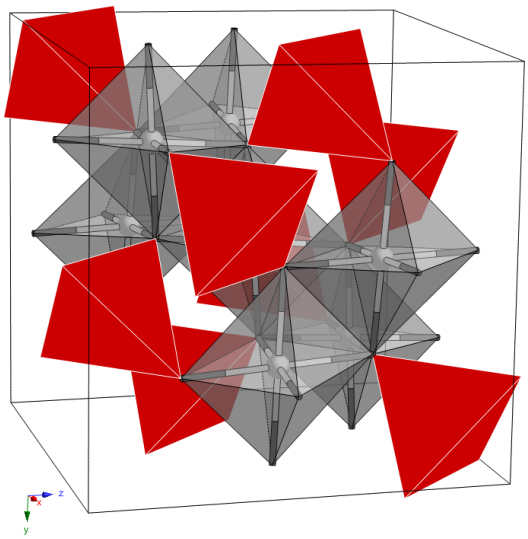

Figure 1-7 Spinel structure for $MgCr_2O_4$ represented with polyhedral model.

1.4.2 Cation site preference in the spinel structure

The equilibrium cation distribution corresponds to the minimisation of the total energy with respect to the stabilisation energy of cations in tetrahedral or octahedral field, as a result of their electronic configuration, the charge and the size of the cations and the electrostatic energies in the lattice.[30] Cation radii and charge effects have opposite tendencies concerning the preference for site occupancies, thus the cation disordering observed in spinels is, partly a consequence of these effects. The opposite influences originate in the necessity of efficient neutralisation for cations with high valences resulting in large coordination numbers (stated by Verwey-Heilman principle[28,31]), while it is known that high valence cations possess small ionic radii that prefer small interstices and small coordination numbers (according to Pauling's first rule).[28] Figure 1-8 illustrates the ionic radii of cations for coordination numbers (NC) 4 and 6.

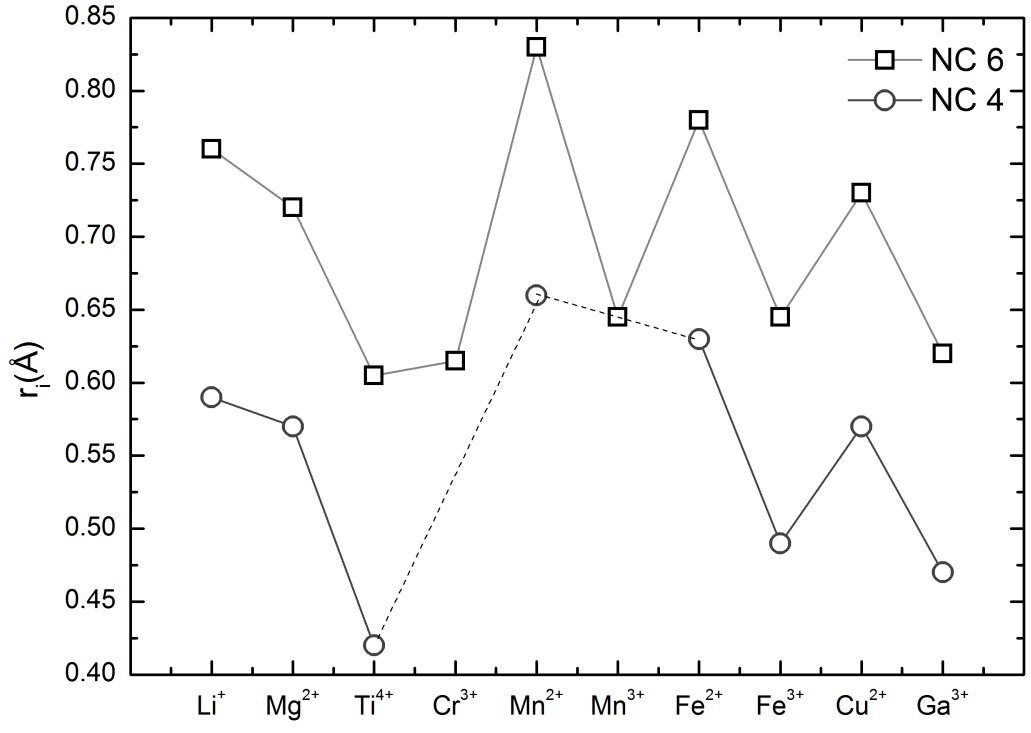

Figure 1-8 Ionic radius [32] for Mn^{2+}, Fe^{2+}, Li^{+}, Cu^{2+}, Mg^{2+}, Mn^{3+}, Fe^{3+} and Ga^{3+} and coordination numbers (CN). Dashed lines illustrate the absence of ionic radii of Cr^{3+} and Mn^{3+} for CN = 4.

Some general criteria stated by Gorter[30] concerning the preference of the cations for A or B sites are based on electronic configuration and energy field stabilisation, as

follows: (a) cations with noble gas configuration do not have individual preference for either coordination and their distribution is determined by the energy of the lattice (mostly dependant of charge, unit cell parameter and oxygen parameter), ions of this type are Li^{+}, Mg^{2+}, Al^{3+}, Ti^{4+}; (b) ions with half-filled 3d shells have spherical symmetry, in consequence they have no expected preference for either positions, *e.g.* Mn^{2+}, Fe^{3+}; (c) preference of other transition metals is influenced by the crystalline electric field from the neighbouring ions, as those with $3d^3$ and $3d^8$ which have strong preference for sixfold coordination: Cr^{3+}, Ni^{2+}, Mn^{4+}; (d) other cations with d^1, d^2, d^4, d^6, d^7 and d^9 have their preference for octahedral coordination evaluated from calculated energy of stabilization in octahedral field.[33]

1.5 Aliovalent substitution and defect chemistry exemplified on spinels

1.5.1 Defect chemistry

The previous section discussed cation site preference in spinels. This section will give a brief overview of possible aliovalent substitutions (i.e. cations having different charge) and charge compensation mechanisms, in general and in particular for spinels.

Cation substitution represents a well-known approach for tailoring material properties by taking advantage of the defect chemistry that may be induced in the material. This has often been used to develop new materials with desired properties or to eliminate/reduce undesirable effects.[34–36]

When cations are substituted in a concentration between 0.1 to 1%, the material usually referred to as being doped. If the concentration of the substituting cation exceeds 1% the material is referred to as a solid solution, rather than doped.[37]

In order to preserve the electroneutrality of the crystal, introduced aliovalent substitutions are compensated for by ionic and/or electronic defects.

Ionic compensation may be realized through several mechanisms, generally by creation of: a) cation vacancies; b) interstitial anions; c) anion vacancies; d) interstitial cations and e) double substitution.[37,38] Selected examples from each possible mechanism are presented and briefly discussed below.

a) A common example for ionic charge compensation by <u>cation vacancies</u> is the case of La doped $SrTiO_3$, $Sr_{1-3x/2}La_xTiO_3$. In this case, La^{3+} cations substitute Sr^{2+} cations and the extra positive charge is compensated for by the formation of A site vacancies in the perovskite:[38–40]

$$La_2O_3 + 3Sr_{Sr}^{X} \rightarrow 2La_{Sr}^{\cdot} + V_{Sr}^{''} + 3SrO \qquad \text{Equation 1-1}$$

b) For the substitution of cations with higher valence, the extra positive charge could be compensated by accommodating <u>interstitial anions</u> in the lattice. However, this charge compensation mechanism is not common because most of close packed structures do not have interstitial sites large enough to accommodate extra anions. This mechanism could occur in the fluorite structure, *e.g.* small amount of YF_3 could dissolve into CaF_2, with formation of interstitial fluoride anions.[37,41,42]

c) When doping with lower valence cations, the electroneutrality of the lattice may be maintained by forming <u>anion vacancies</u>. This was exemplified and demonstrated for the substitution of Zr^{4+} with Y^{3+} or Ca^{2+}in ZrO_2. The same mechanism occurs in CeO_2, when Ce^{4+} is substituted with Gd^{3+}.[35,43–45]

d) Charge compensation by <u>interstitial cations</u> occurs for substitutions where the host lattice has suitable interstitial sites to accommodate cations. Higher valence cations are replaced by lower valence cations and the charge balance is satisfied by accommodating alkali metal cations interstitially, *e.g.* in $Li_x(Si_{1-x}Al_x)O_2$ solid solutions, when Si^{4+} is substituted by Al^{3+} and Li^+ are at interstitial sites.[37]

e) <u>Double substitution</u> with iso or aliovalent cations, which prevails the overall electronetrality (*e.g.* $Mg_{2-x}Fe_x)(Si_{1-y}Ge_y)O_4$

Electronic charge compensation may take place by: a) formation of cation vacancies generated by deintercalation (*e.g.* delithiation); b) creating mixed valence cations; c) oxygen loss that results in formation of anion vacancies (reduction at high temperature- when e^- are liberated into the structure); d) interstitial cations of one element and mixed valence cations (*e.g.* lithiation). Several examples are presented below.

a) The processes described as a) deintercalation (*e.g.* delithiation) and d) interstitial cations of one element and mixed valence cations (*e.g.* lithiation) are describing the functioning principle of lithium batteries.[37,38]

b) Creating mixed valence cations may be associated with insertion of interstitial anions into a structure, *e.g.* in the case of YBCO for which the excess oxygen induces a mixed valence state for Cu cations of 2+ and 3+ that transforms the material form a semiconductor to superconductor;[37] For Nd_2CuO_4, the substitution of Nd^{3+} with Ce^{4+} is compensated by generating mixed valence state for the Cu cations 2+ and 1+ leading to n-type superconductor behaviour of the material.[40]

c) Oxidation and reduction reactions of metal ions at different oxygen partial pressures (p_{O_2}) generate electronic defects, for example the reduction of an oxide represents the removal of oxygen to the gas phase and formation of anion vacancies with generation of electrons that may contribute to n-type conductivity.

$$O_O^X \rightleftharpoons \frac{1}{2}O_2\,(g) + V_O^{\cdot\cdot} + 2e' \qquad \text{Equation 1-2}$$

The oxidation process occurs at high p_{O_2} when oxygen anions fill vacant oxygen sites, generating holes that typically contribute to p-type conductivity.[37,40,46]

$$V_O^{\cdot\cdot} + \frac{1}{2}O_2 \rightleftharpoons O_O^X + 2h^{\cdot} \qquad \text{Equation 1-3}$$

The most relevant intrinsic defects for a metal oxide, MO, include Schottky, anti-Schottky, Frenkel, anti-Frenkel and electronic defects. The corresponding formation equilibria and equilibrium constants are given below:

Schottky $\quad null \rightleftarrows V_M'' + V_O^{\cdot\cdot}$ Equation 1-4

$$K_S = [V_M''][V_O^{\cdot\cdot}] \qquad \text{Equation 1-5}$$

Anti-Schottky $\quad null \rightleftarrows M_i^{\cdot\cdot} + O_i''$ Equation 1-6

$$K_{\bar{S}} = [M_i^{\cdot\cdot}][O_i''] \qquad \text{Equation 1-7}$$

Frenkel $\quad null \rightleftarrows M_i^{\cdot\cdot} + V_M''$ Equation 1-8

$$K_F = [M_i^{\cdot\cdot}][V_M^{''}]$$ Equation 1-9

Anti-Frenkel $$null \rightleftarrows O_i^{''} + V_O^{\cdot\cdot}$$ Equation 1-10

$$K_{\bar{F}} = [O_i^{''}][V_O^{\cdot\cdot}]$$ Equation 1-11

Electronic $$null \rightleftarrows e' + h^{\cdot}$$ Equation 1-12

$$K_B = [e'][h^{\cdot}]$$ Equation 1-13

Defect concentrations vary with temperature, solute concentration and ambient gas (p_{O_2}). Typically, defect concentrations are studied with respect to p_{O_2}, and such dependences will be briefly reviewed next with the help of a Brouwer diagram (Figure 1-9). In the Brouwer diagram (also known as Kröger-Vink diagram) the concentration of defects is expressed as a function of log p_{O_2} at constant temperature.[40,46] The Brouwer diagram is constructed considering the possible intrinsic defects described by the Equations (1-4)-(1-13) and additionally some simplifying premises are used. For example, all the defects described above may occur in the material but some possess higher likelihood of occurrence compared to others, hence certain defects may be ignored in calculations (i.e. concentrations tends to zero).[46,47]

Reduction occurs according to Equation 1-2 and the corresponding equilibrium constant is given below in Equation 1-14 (n being the concentration of electrons released in the materials upon reduction):

$$K_R = n^2 \cdot [V_O^{\cdot\cdot}] \cdot {p_{O_2}}^{1/2}$$ Equation 1-14

In order to determine the defect concentrations, another equation is necessary to be considered, the condition of electroneutrality:

$$[V_O^{\cdot\cdot}] + [M_i^{\cdot\cdot}] + [h^{\cdot}] = [V_M^{''}] + [O_i^{''}] + [e']$$ Equation 1-15

The dominant type of defect chemistry determines the electronic defects with the p_{O_2}. For a Schottky defect dominated system, from the equilibrium constant for reduction (Equation 1-14), the electron concentration may be expressed as a function of p_{O_2}:[46,47]

$$K_S = [V_M^{''}][V_O^{\cdot\cdot}] \Rightarrow [V_O^{\cdot\cdot}] = K_S^{1/2}$$ Equation 1-16

By replacing $[V_O^{\cdot\cdot}]$ in the Equation 1-14, the p_{O_2} dependence of the electron concentration has a slope of -1/4.

$$n = K_R^{1/2} \cdot K_S^{-\frac{1}{2}} \cdot p_{O_2}^{-\frac{1}{4}} \Rightarrow log(n) \sim -\frac{1}{4} log(p_{O_2})$$ Equation 1-17

The hole concentration has a p_{O_2} dependence opposite to that of the electron concentration:

$$p = \frac{K_B}{n} = K_B \cdot K_R^{-\frac{1}{2}} \cdot K_S^{1/2} \cdot p_{O_2}^{1/4} \Rightarrow log(p) \sim \frac{1}{4} log(p_{O_2})$$ Equation 1-18

For low p_{O_2}, after the equilibration of the material, the electron concentration becomes: $\mathrm{n} = 2[\mathrm{V_O^{\cdot\cdot}}] \Rightarrow [\mathrm{V_O^{\cdot\cdot}}] = \frac{\mathrm{n}}{2}$, according to the Equation 1-2. When replacing in the Equation 1-14, results in dependence of the electron concentration and oxygen vacancies of -1/6 slope with log p_{O_2}, displaced by a factor by a factor of log 2:

$$n = (2 \cdot K_R)^{1/3} \cdot p_{O_2}^{-\frac{1}{6}} \Rightarrow log(n) \sim -\frac{1}{6} log(p_{O_2})$$ Equation 1-19

During oxidation, the hole concentration increases up to the level $\mathrm{p} = 2[\mathrm{V_M''}] \Rightarrow [\mathrm{V_M''}] = \frac{\mathrm{p}}{2}$. The hole concentration and the concentration of metal vacancies have a dependence of 1/6 slope with log p_{O_2}:

$$p = \frac{K_B}{n} = K_B \cdot (2 \cdot K_R)^{-\frac{1}{3}} \cdot p_{O_2}^{1/6} \Rightarrow log(p) \sim \frac{1}{6} log(p_{O_2})$$ Equation 1-20

When the material is dominated by anti-Frenkel defects, such as in the case of $Zr_{0.92}Y_{0.08}O_{1.96}$ (YSZ), the reaction with the ambient gas can be formulated as Equation 1-29 or Equation 1-22:

$$\frac{1}{2} O_2\,(g) + V_O^{\cdot\cdot} + 2e' = O_O^X$$ Equation 1-21

$$\frac{1}{2} O_2\,(g) + V_i = O_i'' + 2h^{\cdot}$$ Equation 1-22

At intermediate p_{O_2} values, $[\mathrm{O_i''}] \cong [\mathrm{V_O^{\cdot\cdot}}]$ the conduction is ionic. When the p_{O_2}decreases, the electron concentration increases (n-type conductivity) and it varies with p_{O_2} at slope of -1/4. In a similar manner, the hole concentration increases (p-type conductivity) at higher p_{O_2} with slope 1/4:

$$[e'] \sim p_{O_2}^{-\frac{1}{4}}$$ Equation 1-23

$$[h^{\cdot}] \sim p_{O_2}^{\frac{1}{4}}$$ Equation 1-24

At very low p_{O_2}, the electron concentration increases and the approximation $n = 2[V_O^{\cdot\cdot}]$ is more relevant to the system.

The conductivity of the YSZ changes from ionic to n-type conductivity and its variation with p_{O_2} is described by Equation 1-19. At high p_{O_2}, the concentration of interstitial oxygen, $[O_i'']$ and hole concentration, $[h^{\cdot}]$ increase and the influence of p_{O_2} change is described by Equation 1-20, while the conductivity of YSZ changes from ionic to p-type conductivity.

Figure 1-9 illustrates a Kröger-Vink diagram for the case of YSZ discussed above that indicates the electrolytic domain and the domains of p-type semiconductor and n-type semiconductor, respectively.[37,46,48]

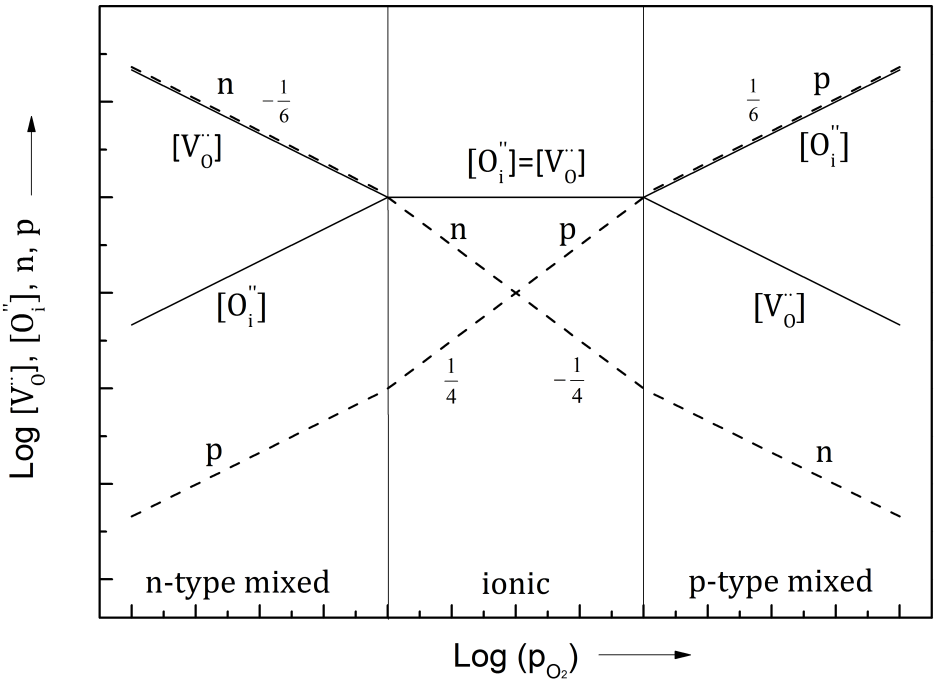

Figure 1-9 Kröger-Vink diagram for ZrO_2 in which oxygen anti-Frenkel defects dominate the intrinsic defect structure (after [46,48]).

1.5.2 Defects in spinels

Spinels are typically described by stoichiometry AB_2O_4. For this general formula, the formal charges on the A and B cations are given by the electroneutrality condition:

$$Q_A + 2Q_B + 4Q_O = 0 \qquad \text{Equation 1-25}$$

Where Q_A and Q_B are the charges of the A and B cations and Q_O is the charge of the anion, -2 for oxygen. This model is widely accepted in literature and mostly discussed is the cation distribution amongst the A and B sites, for various ferrites, cobaltites and other spinels based on transitional metals for which the cation distribution is a has been shown to strongly influence material properties .[19,23,25,26,28,30,49–62]

Poulsen[38] proposed an average valence defect model for $(Co_xFe_{1-x})_3O_4$ spinel and considered charge compensation was descried as averaged charge to all cations of: +8/3=+2.6(6) per cation and assumed a full occupation on the oxygen site at any p_{O_2}. Electrons and holes formation were stated as explaining electrical conduction upon reduction and oxidation, respectively.

In literature the formation of defects in spinels are discussed for several cases, as follows. Ionic charge compensation by cation vacancies is the case of $MgAl_2O_4$ spinel, for which Al^{3+} cation could replace Mg^{2+} cations with formation of tetrahedral site vacancies, in the case of solid solution formation or if the material is irradiated.[63,64]

$$Al_2\,O_3 + 3 \cdot Mg_{Mg}^{X} \rightarrow 2 \cdot Al_{Mg}^{\cdot} + V_{Mg}^{''} + 3MgO \qquad \text{Equation 1-26}$$

Moriwake *et al.*[65–67] described $MgCr_2O_4$ as nonstoichiometric, with formation of Cr vacancies at B site, and performed first principle molecular orbital calculations of $MgCr_2O_4$ and $MgAl_2O_4$ using model clusters, and first principle pseudo-potential calculations using plane-wave basis function. They concluded that Cr vacancies are abundant in $MgCr_2O_4$ when annealed in air, while Al vacancies are not present alone in $MgAl_2O_4$.

Flot and Irvine[68] reported on M (M=Mn, Fe, and Co) substituted Mg_2TiO_4 as: $Mg_{2-x}M_xTiO_4$, $Mg_2Ti_{1-x}M_xO_4$ and $Mg_{2-x/2}Ti_{1-x/2}M_xO_4$ and discussed the defect chemistry arising on oxidation/reduction reaction and the possible conductivity mechanisms resulted the conductivity measurements and TGA results. The studied spinels showed n-type semiconducting behaviour at low p_{O_2} with a slope of -1/4 which could be attributed to the reduction of Ti^{4+} to Ti^{3+}:

$$2Ti_{Ti}^{X} + O_O^X = 2 \cdot Ti_{Ti}^{\prime} + V_O^{\cdot\cdot} + \frac{1}{2} \cdot O_2\,(g) \qquad \text{Equation 1-27}$$

A dependence of $p_{O_2}^{-1/4}$ assumes a high concentration of oxygen vacancy, compared to the number of oxygen vacancies resulted from reduction. Also, oxygen vacancies

would not be expected to dominate spinel defect chemistry, but it would be possible that spinels incorporate more or less oxygen per formula unit through cation vacancies or interstitials *e.g.* $M_{3\pm\delta}O_4$. Thus, they have suggested a defect chemistry dominated by cation vacancies with surface oxygen loss, defect chemistry that could explain the $p_{O_2}^{-1/4}$ dependence:

$$V_M'' + Ti_{Ti}^X + MO_{(s)} = M_M^X + 2 \cdot Ti_{Ti}' + \frac{1}{2} \cdot O_2\ (g) \qquad \text{Equation 1-28}$$

Oxygen deficiency is discussed for $LiMn_2O_{4-\delta}$[69] and substituted $LiMn_{2-x}M_xO_{4-\delta}$ (x = 0.5, M = Ni),[36] (x = 0.1 M = Mg, Mo, Ti, Fe, Co, Ni, Al, Li)[70] spinels. Oxygen deficiency in $LiMn_2O_{4-\delta}$ was correlated with a phase transition of the spinel from cubic (Fd-3m) to tetragonal ($I4_1/amd$) with lowering the temperature slightly below room temperature (~280 K). It was reported for this spinel that oxygen deficiency acts as a favouring factor to the cubic-tetragonal phase transition.[69,36,70] Takahashi *et al.*[70] reported a smaller oxygen deficiency reached for $LiMn_{2-x}M_xO_{4-\delta}$, when the M substituted cation was Mg or Al and best results in decreasing oxygen deficiency was obtained for using both Mg and Ti doping.

Pasero *et al.*[36] reported several phase transformations of $LiMn_{1.5}Ni_{05}O_{4-\delta}$, which were also attributed to the oxygen loss in the spinel upon heating in air: the first change transformation of $LiMn_{1.5}Ni_{0.5}O_{4-\delta}$ was determined to occur between 650-680 °C from ordered spinel ($P4_332$) to Fd-3m spinel, associated with a variation in composition. Further oxygen loss determined the formation of cubic rock salt structure at secondary phase between 750-800 °C, and the rock salt structure became single main phase at 1100 °C. All these phase transformations were reported as reversible and for the $LiMn_{1.5}Ni_{0.5}O_{4-\delta}$ cooled slowly, the stoichiometric phase was obtained. However, it was demonstrated that some dopants (*e.g.* Mg, Ti, Al) have positive effects towards obtaining less oxygen deficient $LiMn_{2-x}M_xO_{4-\delta}$.

In comparison with the findings of Pasero *et al.*[36], for chromite, ferrite and titanate spinels no phase transformations were reported on sintering or processing the spinels in air. During material processing it would be expected that a small amount of cation vacancies form at high oxygen pressure (see also Moriwake *et al.*[65–67]), and it is rather expected that a certain degree of oxygen loss in combination with cation vacancies would occur during reduction as reported by Flot and Irvine.[68]

1.5.3 Conduction mechanism for chromium–rich spinels

Electrical conductivity in spinels typically occurs by thermally activated hopping of electron holes at the B site because of short B-B distances (~0.35·a) and no intervening anions to obstruct neighbouring cations (Figure 1-10).[28] Chromium rich spinels have the electrical conduction mechanism described by hopping of an electron hole h^+ between chromium ions with different valences:[71]

$$Cr_{Cr}^{X} + h^{\cdot} \leftrightarrow Cr_{Cr}^{\cdot} \qquad \text{Equation 1-29}$$

In reducing conditions, the conductivity decreases due to the formation of vacancies in the oxygen sublattice $V_O^{\cdot\cdot}$ of the spinel due to the reduction according to the equilibrium:

$$O_O'' + 2Cr_{Cr}^{\cdot} \leftrightarrow 2Cr_{Cr}^{X} + V_O^{\cdot\cdot} + {}^1/_2\, O_2 \qquad \text{Equation 1-30}$$

This leads to a decrease in the number of charge carrier sources (Cr^{4+} ions), equivalent with a decrease in the hole concentration. In Figure 1-10 there is schematically represented the hopping of a hole in the B site lattice. To simplify the representation, the A site lattice was omitted.

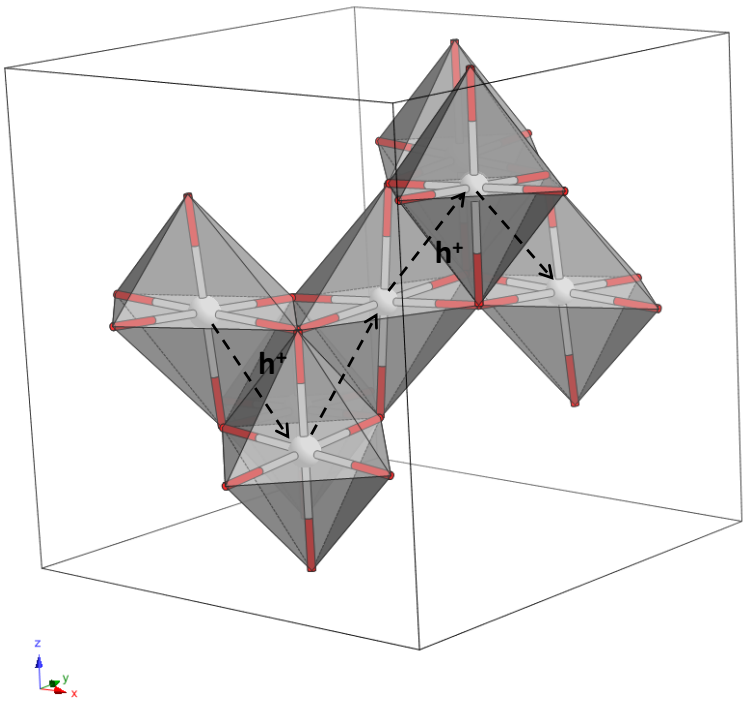

Figure 1-10 Schematic representation of an electron hole hopping at B site.

Conductivity is directly influenced by the numbers of charge carriers, their charge and the mobility of the charge carriers. In intrinsic semiconductors the number of

charge carriers is small, thus is can be multiplied by increasing the temperature to activate more electrons from the valence band to conduction band. Another possibility to increase the number of charge carriers consists of doping with impurities that form electrons or holes. When the temperature is increased, the increase in charge carrier numbers is described by Arrhenius equation that gives the activation energy (Ea) of the process for a certain material.[37]

$$\sigma = A \cdot e^{-\frac{E_a}{kT}} \qquad \text{Equation 1-31}$$

where σ represents the conductivity, A a constant (pre-exponential factor), E_a is the activation energy in eV, k is the Boltzmann constant and T[K], the temperature. The activation energy for p-type semiconductors is determined from the plot of the conductivity (σ) vs. 1/T, usually linear trendline. The slope of the plot gives the activation energy of the process. Figure 1-11 illustrates examples of Arrhenius plots for $MgCr_2O_4$ and $MgFeCrO_4$ from the present work.

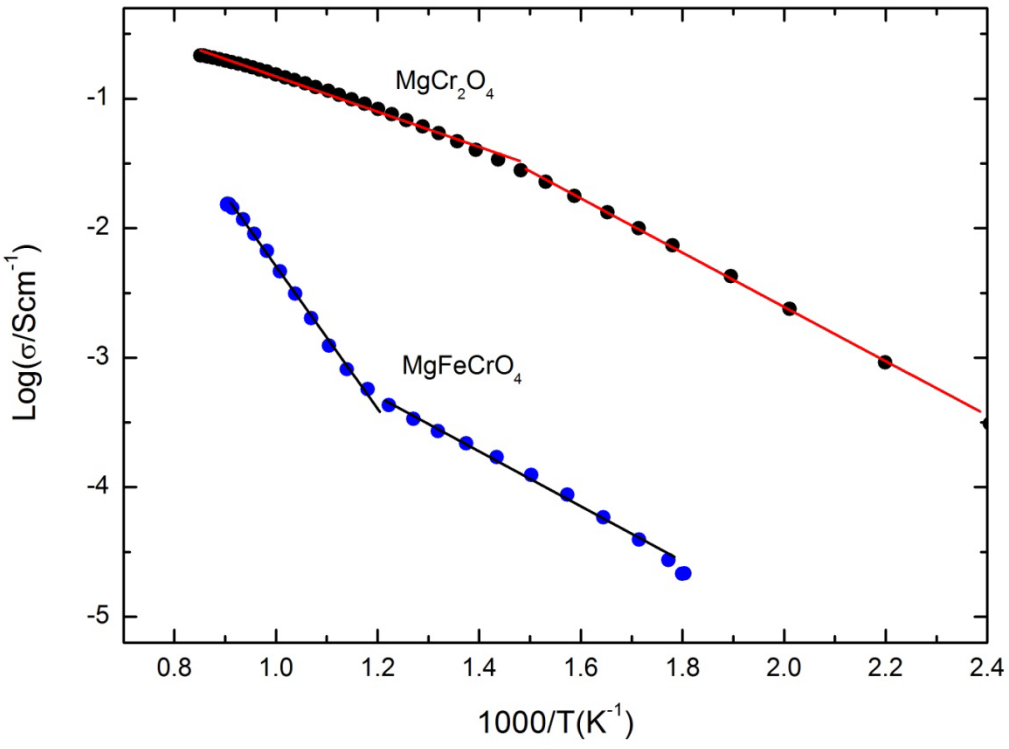

Figure 1-11 Example of Arrhenius plots log(σ) vs. 1000/T for $MgCr_2O_4$ and $MgFeCrO_4$ with slope change at 400 °C and 500 °C, respectively. Slope change corresponds to change in activation energy.

The material's conductivity could be changed by the partial substitution of Cr cations with other valence/size compatible cations. When other cations with variable

valences occupy octahedral sites along with chromium ions, the conduction mechanism is influenced by the cations present. Sakai *et al.*[49] determined the electrical conductivity for $MnCr_2O_4$ and $MnFeCrO_4$ and described the conduction mechanisms. The conductivity of $MnFeCrO_4$ was much improved in comparison with $MnCr_2O_4$, improvement that could be explained by the existence of the conducting couple Fe^{2+}/Fe^{3+} at B site with higher mobility than Cr^{3+}/Cr^{4+}. When chromium was substituted with other cations with variable valence states at the B site, *e.g.* Mn,[50] the materials conductivity was again improved.

1.6 Composite electrodes and electrode support materials

The requirements for SOFC electrodes, summarised in subsection 1.2, are very comprehensive and they cannot be fulfilled by only one material, thus usually SOFC electrodes are composite materials.

The tendency of decreasing the functioning temperature for SOFC from 900-1000 °C to temperatures of 600-800 °C allows use of a wider range of materials. However, at lower functioning temperatures electrolyte conductivity and electrode kinetics decrease, thus encouraging the development of new materials with better performance at lower temperatures.[6,18,72] Compared to the state-of-the-art composite anode Ni - yttria stabilised zirconia (YSZ), consisting of a mechanical mixture of the two materials[73] and strontium doped lanthanum manganite (LSM) or LSM-YSZ cathode, new anodes[3,74,75] and cathodes[72,76–79] were investigated and reported in literature. There are four different methods of developing new electrodes for SOFCs described in literature, such as: the modification of Ni-YSZ cermet by altering the nickel or YSZ or the synthesis of new single phase electrode materials, as perovskites.[80–83] A third option consists of adding catalyst materials as catalyst - oxide and catalyst – metal – oxide systems,[84–86] while the last mentioned method for new electrodes consists in the impregnation of oxide and metal precursors into pre-sintered YSZ porous substrates.[77,79,87–90]

The advantages of this method consist in the high reactivity of the electrode materials, provided by the low synthesis temperatures and the bi-functionality of the electrode, with the infiltrated materials being generally good electronic conductor and the YSZ scaffold as ionic conductor. In Figure 1-12 are presented two configurations of composite YSZ – based electrodes, cermet (mixture of YSZ and metals (Ni)) or

composite of two ceramic materials, *e.g.* LSM – YSZ and composite electrodes obtained by impregnation of electrode precursor solutions and catalysts into YSZ porous substrates followed by thermal treatment.

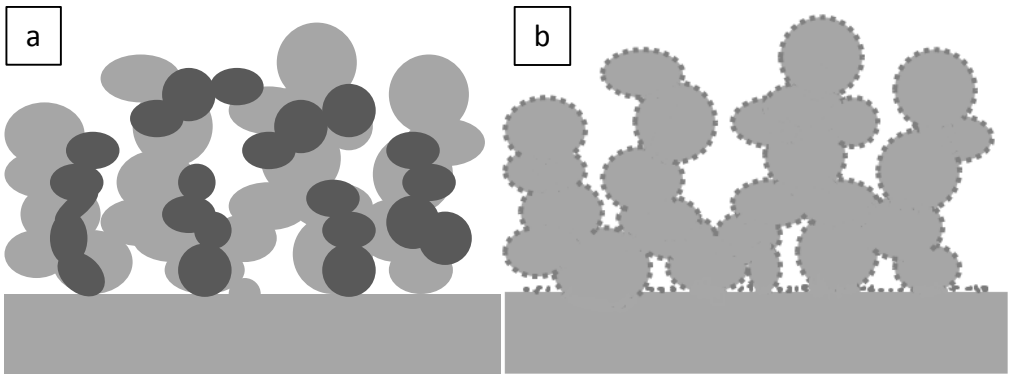

Figure 1-12 Representation of composite electrodes: a) cermet; b) by infiltration of electrode materials into porous YSZ scaffolds.

Composite electrodes developed by impregnation of electrode precursor solutions into porous scaffolds resulted in excellent performance at temperatures of 600-800 °C, in consequence this technique of developing new electrodes was applied in the present work. An electrode support consists of a material which has the role of support for other functional materials.

1.7 Aims and objectives of the thesis

Derived from the formation of Cr-rich spinels as products of high temperature oxidation of ferritic stainless steels used for interconnects, the aim of this work is to find Cr-rich suitable materials with spinel structure for electrode support material. For this application, the materials are required to exhibit good chemical and structural stability in reducing and oxidising conditions, at high temperatures (500-900 °C), and sufficient electrical conductivity (> 0.1 $S \cdot cm^{-1}$). Thus, the search for Cr-rich materials with spinel structure involves material characterisation, in order to appoint suitable material for electrode support material, the development of the electrode supports and their testing:

1. Synthesis and characterization of $MnM_xCr_{2-x}O_4$ (Mn, Mg, Fe) spinel in order to apply them as electrode support materials for intermediate temperature SOFC.

2. Synthesis and characterisation of newly formulated Cr-rich spinels, such as $Mg_{1-x-}M_xCr_2O_4$ (M = Cr), $MgM_xCr_{2-x}O_4$ (M = Cr, Li, Mg, Ti, Fe, Cu, Ga), in order to apply them as electrode support materials. The compositions with highest impact for this study are included in the quaternary diagram presented in Figure 1-13.

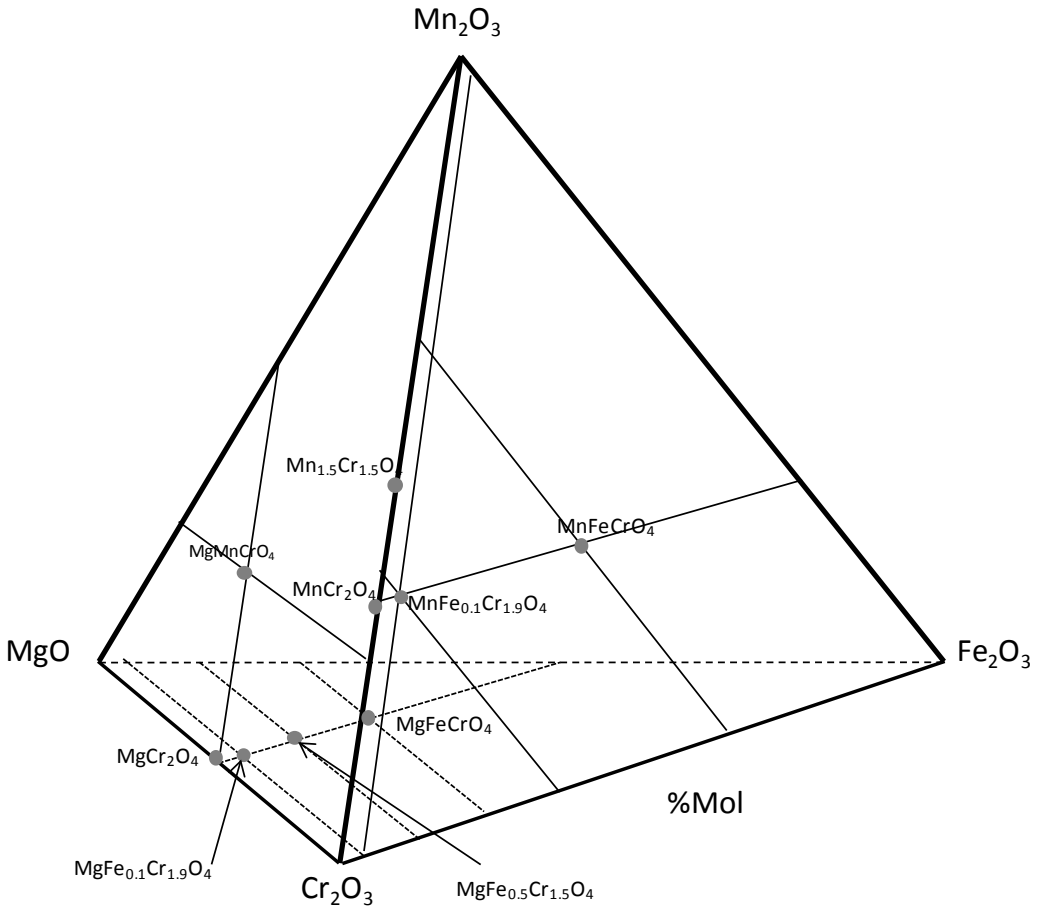

Figure 1-13 Quaternary system Mn_2O_3-MgO-Cr_2O_3-Fe_2O_3. Spinel compositions investigated in the quaternary oxide system are also represented in the diagram.

In order to develop new chromium rich materials with spinel structure and desired properties, other oxides starting with $LiCrTiO_4$ were investigated. $LiTiCrO_4$ is stable as spinel up to 900 °C and new compositions were formulated, as solid solutions in the systems $MgCr_2O_4$ – $LiCrTiO_4$, Mg_2TiO_4 – $LiCrTiO_4$ and Mg_2TiO_4 – $LiCrTiO_4$ – $MgFeCrO_4$ with the purpose of increasing the stability of spinel phase at higher temperatures. The compositions characterized are illustrated in the diagram presented in Figure 1-14.

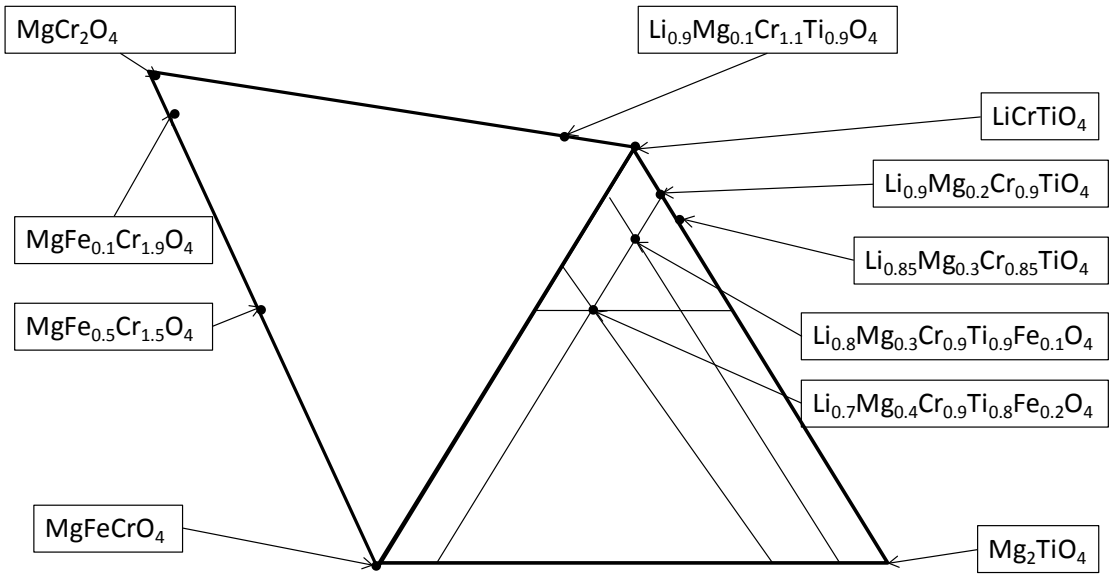

Figure 1-14 Schematic diagram of spinel solid solutions investigated in the systems $MgCr_2O_4$ – $LiCrTiO_4$, Mg_2TiO_4 – $LiCrTiO_4$ and Mg_2TiO_4 – $LiCrTiO_4$ – $MgFeCrO_4$.

3. Investigation of mechanical and chemical compatibility of some selected spinels with YSZ.

4. The fabrication of $MnFeCrO_4$ and $MgFeCrO_4$ porous scaffolds, assess thermo – mechanical stability to a multi-step impregnation process and chemical stability to impregnated electrode materials, and to evaluate the electrochemical performance of symmetrical cells based on such scaffolds impregnated with the electrode materials $(La_{0.75}Sr_{0.25})_{0.97}Cr_{0.5}Mn_{0.5}O_3$ (LSCM), $La_{0.8}Sr_{0.2}FeO_3$ (LSF), $Ce_{0.9}Gd_{0.1}O_2$ (CGO), CeO_2 and Pd.

1.8 References

1. *International Energy Outlook 2011*, U.S. Energy Information Administration, 2011.
2. A. Galich and L. Marz, *Energy Sustain. Soc.*, 2012, **2**, 2.
3. Atkinson, S. Barnett, R. J. Gorte, J. T. S. Irvine, A. J. McEvoy, M. Mogensen, S. C. Singhal, and J. Vohs, *Nat. Mater.*, 2004, **3**, 17–27.
4. W. Z. Zhu and S. C. Deevi, *Mater. Sci. Eng.*, 2003, **348**, 227–243.
5. N. Minh, *Solid State Ionics*, 2004, **174**, 271–277.
6. S. C. Singhal, *Solid State Ionics*, 2002, **152–153**, 405 – 410.
7. N. Q. Minh and T. Takahashi, *Science And Technology Of Ceramic Fuel Cells*, Elsevier, 1995.
8. R. M. Ormerod, *Chem Soc Rev*, 2003, **32**, 17–28.
9. J. W. Fergus, *Int. J. Hydrog. Energy*, 2007, **32**, 3664 – 3671.

10. M. Gödickemeier, *Mixed ionic electronic conductors for solid oxide fuel cells*, [Mikrofiche-Ausg.]., 1996.
11. K. Sasaki, *Phase equilibria, electrical conductivity, and electrochemical properties of ZrO2-In2O3*, [Mikrofiche-Ausg.]., 1993.
12. E. Povoden-Karadeniz, *Thermodynamic database of the La-Sr-Mn-Cr-O oxide system and applications to solid oxide fuel cells*, [s.n.], [S.l.], 2008.
13. J. C. Ruiz-Morales, J. Canales-Vázquez, B. Ballesteros-Pérez, J. Peña-Martínez, D. Marrero-López, J. T. S. Irvine, and P. Núñez, *J. Eur. Ceram. Soc.*, 2007, **27**, 4223 – 4227.
14. S. M. Plint, P. A. Connor, S. Tao, and J. T. S. Irvine, *Solid State Ionics*, **177**, 2005–2008.
15. J. Fergus, R. Hui, X. Li, D. P. Wilkinson, and J. Zhang, *Solid oxide fuel cells materials properties and performance*, CRC Press, Boca Raton, 2009.
16. J. Goodenough and Y. H. Huang, *J. Power Sources*, 2007, **173**, 1–10.
17. M. Mogensen, Sø. Primdahl, M. J. JØrgensen, and C. Bagger, *J. Electroceramics*, 2000, **5**, 141–152.
18. W. Zhu and M. Yan, *J. Zhejiang Univ. - Sci.*, 2004, **5**, 1471–1503.
19. X. Chen, P. Y. Hou, C. P. Jacobson, S. J. Visco, D. Jonghe, and L. C, 2004.
20. L. Cooper, S. Benhaddad, A. Wood, and D. G. Ivey, *J. Power Sources*, 2008, **184**, 220–228.
21. Qu, L. Jian, J. Hill, and D. Ivey, *J. Power Sources*, 2006, **153**, 114–124.
22. Konysheva, J. Laatsch, E. Wessel, F. Tietz, N. Christiansen, L. Singheiser, and K. Hilpert, *Solid State Ionics*, 2006, **177**, 923–930.
23. A. Petric and H. Ling, *J. Am. Ceram. Soc.*, 2007, **90**, 1515–1520.
24. Z. Yang, G.-G. Xia, C.-M. Wang, Z. Nie, J. Templeton, J. W. Stevenson, and P. Singh, *J. Power Sources*, 2008, **183**, 660–667.
25. H. S. C. O'Neill and A. Navrotsky, *Am. Miner.*, 1983, **68**, 181–194.
26. S. Wang, X. Liu, Y. Fei, Q. He, and H. Wang, *Phys. Chem. Miner.*, 2012, **39**, 189–198.
27. T. Hahn, *International Tables for Crystallography.*, Kluwer, Dordrecht, 2002.
28. K. E. Sickafus, J. M. Wills, and N. W. Grimes, *J. Am. Ceram. Soc.*, 2004, **82**, 3279–3292.
29. P. Ballirano, *J. Appl. Crystallogr.*, **36**, 1056–1061.
30. E. W. Gorter, *Saturation Magnetisation and Crystal Chemistry of Ferrimagnetic Oxides*, Phillips, 1954.
31. E. J. W. Verwey and E. L. Heilmann, *J. Chem. Phys.*, 1947, **15**, 174–180.
32. R. D. Shannon, *Acta Crystallogr. A*, 1976, **A32**, 751–767.
33. P. Kovtunenko, *Glass Ceram.*, 1997, **54**, 143–148.
34. D. M. Smyth, *Solid State Ionics*, 2000, **129**, 5–12.
35. B. C. H. Steele, *Solid State Ionics*, 2000, **129**, 95–110.
36. D. Pasero, N. Reeves, V. Pralong, and A. R. West, *J. Electrochem. Soc.*, 2008, **155**, A282–A291.
37. A. R. West, *Basic Solid State Chemistry*, Wiley-Blackwell, 2nd Edition., 1999.
38. F. W. Poulsen, Technical University of Denmark, 2007.
39. P. R. Slater, D. P. Fagg, and J. T. S. Irvine, *J. Mater. Chem.*, 1997, **7**, 2495–2498.
40. J. Irvine, I. Metcalfe, A. Thursfield, and A. Kruth, in *Metal Oxides*, ed. J. Fierro, CRC Press, 2005, vol. 108, pp. 55–86.
41. D. Shriver and P. Atkins, *Inorganic Chemistry*, W.H. Freeman & Company, 5 Sol Rep., 2010.
42. P. Kofstad and T. Norby, *Defects and Transport in Crystalline Solids*, University of Oslo, 2007.

43. M. Mogensen, N. M. Sammes, and G. A. Tompsett, *Solid State Ionics*, 2000, **129**, 63 – 94.
44. S. H. Jo, P. Muralidharan, and D. K. Kim, *Solid State Ionics*, 2008, **178**, 1990–1997.
45. P. P. Dholabhai, J. B. Adams, P. Crozier, and R. Sharma, *Phys. Chem. Chem. Phys.*, 2010, **12**, 7904–7910.
46. Y.-M. Chiang, D. Birnie III, and W. D. Kingery, *Physical Ceramics: Principles for Ceramic Science and Engineering*, Wiley, 1997, vol. 1.
47. J. Maier, *Physical Chemistry of Ionic Materials: Ions and Electrons in Solids*, John Wiley & Sons, 2004.
48. W. Gao, W. G. (Ph D.), and N. M. Sammes, *An Introduction to Electronic and Ionic Materials*, World Scientific, 1999.
49. Sakai, T. Horita, Y. P. Xiong, K. Yamaji, H. Kishimoto, M. E. Brito, H. Yokokawa, and T. Maruyama, *Solid State Ionics*, 2005, **176**, 681–686.
50. Z. Lu, J. Zhu, E. Andrew Payzant, and M. P. Paranthaman, *J. Am. Ceram. Soc.*, 2005, **88**, 1050–1053.
51. F. F. Fava, I. Baraille, A. Lichanot, C. Larrieu, and R. Dovesi, *J. Phys. Condens. Matter*, 1997, **9**, 10715.
52. T. Suzuki, K. Adachi, and T. Katsufuji, *J. Magn. Magn. Mater.*, 2007, **310**, 780–781.
53. J. M. R. González and C. O. Areán, *J Chem Soc Dalton Trans*, 1985, 2155–2159.
54. T. Yokoyamab, T. Meguroa, M. Nakamuraa, J. Tatamia, T. Wakiharaa, and K. Komeyaa, *J. Ceram. Process. Res.*, 2009, **10**, 683–688.
55. H. Furuhashi, M. Inagaki, and S. Naka, *J. Inorg. Nucl. Chem.*, 1973, **35**, 3009–3014.
56. S. M. Patange, S. E. Shirsath, G. S. Jangam, K. S. Lohar, S. S. Jadhav, and K. M. Jadhav, *J. Appl. Phys.*, Mar, **109**, 053909–053909–9.
57. I. S. Ahmed Farag, M. A. Ahmed, S. M. Hammad, and A. M. Moustafa, *Cryst. Res. Technol.*, 2001, **36**, 85–92.
58. S. H. Lee, S. J. Yoon, G. J. Lee, H. S. Kim, C. H. Yo, K. Ahn, D. H. Lee, and K. H. Kim, *Mater. Chem. Phys.*, 1999, **61**, 147–152.
59. D. H. Lee, H. S. Kim, C. H. Yo, K. Ahn, and K. H. Kim, *Mater. Chem. Phys.*, 1998, **57**, 169–172.
60. J. Nell, B. J. Wood, and T. O. Mason, *Am. Miner.*, 1989, **74**, 339–351.
61. A. Nakatsuka, Y. Ikeda, Y. Yamasaki, N. Nakayama, and T. Mizota, *Solid State Commun.*, 2003, **128**, 85–90.
62. S. J. Yoon, S. H. Lee, K. H. Kim, and K. S. Ahn, *Mater. Chem. Phys.*, 2002, **73**, 330–334.
63. S. T. Murphy, Ph.D., Imperial College London, 2009.
64. K. E. Sickafus, J. M. Wills, S.-P. Chen, J. H. Terry, T. Hartmann, and R. I. Sheldon, *Development of a Fundamental Understanding of Chemical Bonding and Electronic Structure in Spinel Compounds*, Los Alamos National Lab., NM (US), 1999.
65. H. Moriwake, I. Tanaka, F. Oba, and H. Adachi, *Jpn. J. Appl. Phys.*, 2000, **39**, 513–516.
66. H. Moriwake, I. Tanaka, F. Oba, Y. Koyama, and H. Adachi, *Int. J. Quantum Chem.*, 2003, **91**, 208–210.
67. H. Moriwake, S. Watanabe, and K. Ogasawara, *Jpn. J. Appl. Phys.*, 2007, **46**, 4175–4178.
68. D. M. Flot and J. T. S. Irvine, *Solid State Ionics*, 2000, **135**, 513–518(6).
69. J. Sugiyama, T. Atsumi, A. Koiwai, T. Sasaki, T. Hioki, S. Noda, and N. Kamegashira, *J. Phys. Condens. Matter*, 1997, **9**, 1729.

70. M. Takahashi, T. Yoshida, A. Ichikawa, K. Kitoh, H. Katsukawa, Q. Zhang, and M. Yoshio, *Electrochimica Acta*, 2006, **51**, 5508–5514.
71. L. Morozova and V. Popov, *Glass Phys. Chem.*, 2010, **36**, 86–91.
72. Bebelis, N. Kotsionopoulos, A. Mai, D. Rutenbeck, and F. Tietz, *Solid State Ionics*, 2006, **177**, 1843–1848.
73. C. Jiang, J. Ma, A. D. Bonaccorso, and J. T. S. Irvine, *Energy Env. Sci*, 2012, **5**, 6973–6980.
74. W. Z. Zhu and S. C. Deevi, *Mater. Sci. Eng.*, 2003, **362**, 228 – 239.
75. S. Tao and J. T. S. Irvine, *Chem. Rec.*, 2004, **4**, 83–95.
76. J. C. Ruiz-Morales, J. Canales-Vázquez, J. Peña-Martínez, D. Marrero-López, and P. Núñez, *Electrochim. Acta*, **52**, 278–284.
77. Y. Huang, J. M. Vohs, and R. J. Gorte, *J. Electrochem. Soc.*, 2004, **151**, A646.
78. F. Bidrawn, S. Lee, J. M. Vohs, and R. J. Gorte, *J. Electrochem. Soc.*, 2008, **155**, B660–B665.
79. W. Wang, M. Gross, J. Vohs, and R. Gorte, *J. Electrochem. Soc.*, 2007, **154**, 8439–8445.
80. S. Tao and J. T. S. Irvine, *Nat. Mater.*, 2003, **2**, 320–323.
81. G. Tsekouras and J. T. S. Irvine, *J Mater Chem*, 2011, **21**, 9367–9376.
82. D. Neagu and J. T. S. Irvine, *Chem. Mater. Acs Publ.*, 2011, **23**, 1607–1617.
83. D. Neagu and J. T. S. Irvine, *Chem. Mater. Acs Publ.*, 2010, **22**, 5042–5053.
84. J. Rossmeisl and W. G. Bessler, *Solid State Ionics*, 2008, **178**, 1694 – 1700.
85. J.-S. Kim, V. V. Nair, J. M. Vohs, and R. J. Gorte, *Scr. Mater.*, 2011, **65**, 90–95.
86. X. Yang and J. T. S. Irvine, *J Mater Chem*, 2008, **18**, 2349–2354.
87. Corre, G. Kim, M. Cassidy, J. M. Vohs, R. J. Gorte, and J. T. S. Irvine, *Chem. Mater.*, 2009, **21**, 1077–1084.
88. G. Kim, G. Corre, J. T. S. Irvine, J. M. Vohs, and R. J. Gorte, *Electrochem. Solid-State Lett.*, **11**.
89. J. H. Kim, D. Miller, H. Schlegl, D. McGrouther, and J. T. S. Irvine, *Chem. Mater.*, 2011, **23**, 3841–3847.
90. Bidrawn, G. Kim, G. Corre, J. T. S. Irvine, J. M. Vohs, and R. J. Gorte, *Electrochem. Solid-State Lett.*, 2008, **11**, B167.

Chapter 2

Contents

2 Experimental procedures 49

2.1 Synthesis and processing 49

2.1.1 Combustion synthesis 49

2.1.2 Solid state synthesis 50

2.2 X-ray Diffraction 51

2.2.1 Background 51

2.2.2 Diffraction of X-rays 52

2.2.3 Rietveld Refinement of Crystal Structures 55

2.3 Scanning Electron Microscopy 56

2.4 Dilatometry 58

2.5 Chemical stability in reducing conditions 59

2.6 Electrical conductivity measurement 59

2.6.1 Conductivity Measurements by 4-point method 59

2.7 Fabrication of symmetrical cells 61

2.7.1 Fabrication of scaffolds by tape casting process 61

2.7.2 Screen printing of YSZ electrolyte 62

2.7.3 Insertion of electrode materials into scaffolds by impregnation 63

2.8 Electrochemical tests on symmetrical cells 64

2.8.1 Electrochemical Impedance Spectroscopy 64

2.8.2 The analysis of impedance spectroscopy by equivalent circuit method 67

2.8.3 Symmetrical cells testing parameters 69

2.9 References 70

2 Experimental procedures

2.1 Synthesis and processing

Spinel oxides were synthesised by two different routes, solution combustion synthesis and solid state reaction. $MnM_xCr_{2-x}O_4$, with (M = Fe, Mn, Mg or Li), $MgM_xCr_{2-x}O_4$ (M = Cr, Li, Mg , Fe, Cu) and $Mg_{1-x}M_xCr_2O_4$ (M = Cr) were synthesized by combustion method, while $MgM_xCr_{2-x}O_4$ (M = Ti, Ga) and $Li_{1-x}Mg_xCr_{1+x}Ti_{1-x}O_4$ (x = 0.1), $Li_{1-x}Mg_{2x}Cr_{1-x}TiO_4$ (x = 0, 0.1, 0.15), $(LiTiCr)_{1-x-y}(MgFeCr)_x(Mg_2Ti)_yO_4$ (x = 0.1, 0.2; y = 0.1) were synthesised by solid state reaction. Since the available reagents for Ti (TiO_2) and for Ga (Ga_2O_3), were insoluble in water based solutions, the recommended synthesis route was solid state reaction.

2.1.1 Combustion synthesis

Solution combustion synthesis represents a fast and efficient method for obtaining oxide materials with very good homogeneity, small particle size and high specific surface area. It consists of dissolving metal salts into water and adding an organic complexing agent which also has the role of fuel in the combustion reaction. The solution has to be heated on a hot plate at 200 to 300 °C, until the complete water evaporation with formation of a dry residue. The ignition takes place with the formation of a powder. The synthesis is a self-sustained process due to the exothermicity of the redox reactions during combustion. The method is a relatively low cost technique, because the external thermal energy is necessary only for dehydration of the precursor mixture and the exothermic process provides the energy necessary for the formation of oxide material.[1,2] Citric acid – nitrate combustion synthesis implies the utilisation of nitrates as metal salts and citric acid as complexing agent. An excess of citric acid is necessary for the certainty of a complete reaction. An example of combustion reaction for obtaining $MnCr_2O_4$ from the corresponding nitrates is illustrated in Equation 2-1:

$$Mn(NO_3)_2 \cdot 4H_2O + 2(Cr(NO_3)_3 \cdot 9H_2O) + 2C_6H_8O_7 \rightarrow MnCr_2O_4 + 4N_2 \uparrow + 12CO_2 \uparrow + 21H_2O \uparrow + O_2 \uparrow \quad \text{Equation 2-1}$$

In the present work various spinels have been synthesised by combustion method and the molar ratio used for fuel and spinel is 2 : 1. For $MnM_xCr_{2-x}O_4$ spinel oxides, where M = Fe, Mn, Mg or Li, the appropriate amounts of $Mn(NO_3)_2 \cdot 4H_2O$ Alfa Aesar (99.98%), $Cr(NO_3)_3 \cdot 9H_2O$ Acros Organics (99%), $Fe(NO_3)_3 \cdot 9H_2O$ Sigma Aldrich (> 98%), $Mg(NO_3)_2 \cdot 6H_2O$ Sigma Aldrich (99%), Li_2CO_3 Sigma Aldrich (> 99%) and citric acid ($C_6H_8O_7 \cdot H_2O$) Fisher Chemical (> 99.5%) were dissolved into water. A hot plate with magnetic stirrer was used for stirring to dissolve the reactants and heating at 150 °C for water evaporation. After the complete evaporation of the water, the resulting gel was heated at 300 °C on the hot plate for the combustion reaction to take place.

$MgM_xCr_{2-x}O_4$ (M = Li, Mg, Fe, Cu) spinel oxides were synthesised also by citric acid – nitrate combustion synthesis. $Cr(NO_3)_3 \cdot 9H_2O$ Sigma Aldrich (99.5%), $Fe(NO_3)_3 \cdot 9H_2O$ Sigma Aldrich(> 98%), $Mg(NO_3)_2 \cdot 6H_2O$ Sigma Aldrich(99%), $Cu(NO_3)_2 \cdot 3H_2O$ BDH Laboratory Supplies(99.5%), Li_2CO_3 Sigma Aldrich(99%) and citric acid ($C_6H_8O_7$) Fisher Scientific (99.5%) were the initial reagents. All used nitrates were analysed by thermo-gravimetrical analysis, using a NETCH TG 209, in order to determine the real amount of crystallisation water. The final products of the nitrates decomposition were identified by X-ray diffraction as oxides of the corresponding metals (*e.g.* Fe_2O_3, Cr_2O_3, MgO).

After the synthesis reaction was complete, the obtained powders were calcined at 1000 °C for 10 hours, pressed into pellets (13 mm diameter and 2±0.3 mm thickness) at a pressure of ~200 MPa and sintered at 1400 °C for 12 hours in air.

2.1.2 Solid state synthesis

The classic method of synthesis is solid state reaction and consists of mixing the reagent powders, press them into pellets followed by prolonged periods of sintering at elevated temperatures.[3]

For solid state reaction synthesis Cr_2O_3 Alfa Aesar (99%), $(MgCO_3)_4Mg(OH)_2 \cdot 5H_2O$ Aldrich(99%), TiO_2 Alfa Aesar (99.5%), Ga_2O_3 Aldrich(99.99%), Fe_2O_3 Alfa Aesar (99.8%) and Li_2CO_3 Sigma Aldrich(99%), were the initial reagents.

The intimate homogenisation of the reactants in stoichiometric amounts was achieved by mixing the materials in a solvent (acetone) employing an ultrasonic

probe and a small amount of dispersant (polyester/polyamide copolymer KD-I) until a uniform dispersion was obtained. The dispersion was stirred on a magnetic stirrer for 2 hours, the mixture was dried and the resulting powder calcined. After calcination, the powders were ball milled in a planetary ball mill for 2 hours using acetone as milling solvent, dried and pressed into pellets (13 mm diameter and 2±0.3 mm thickness) at a pressure of ~200 MPa and sintered. The calcining and sintering process were adjusted based on involved materials. $MgM_xCr_{2-x}O_4$ (M = Ga, Ti) were calcined at 1000 °C for 10 hours and sintered at 1400 °C for 12 hours, while the lithium titanates were calcined at 700 °C for 12 hours and sintered at temperatures between 900 – 1300 °C for 12 hours in air, with a heating and cooling rate of 5 °C/min. Lithium titanates were also quenched (rapid cooling) from elevated temperatures to room temperature and their properties characterised.

2.2 X-ray Diffraction

2.2.1 Background

X-ray Diffraction is a non-destructive structural analysis method based on the interaction between short wavelength electromagnetic radiations with crystalline solids. In order to analyse atoms in crystalline solids, a source of rays and a suitable detector are required, since atoms are too small to be discerned using visible light source. Their dimensions are smaller than 1/1000 of the wavelengths present in visible light (4000-7000 Å), thus a suitable wavelength to observe individual atoms is that of X-ray. Generation of X-ray from a source occurs when the electrons from K-shell of the target atoms are bombarded with high energy electrons and they are displaced. Displaced electrons are then replaced by electrons from the outer shells, which emit their excess energy as X-rays (Figure 2-1). The emitted electromagnetic radiations have short wavelength with the order of 1 Å (10^{-10} m). Their wavelength is the same magnitude as with both atomic sizes and interatomic distances. In diffraction experiments, a monochromatic beam of X-ray represents a great convenience, thus the spectrum of X-ray emitted by Cu (or any other metal) is filtered keeping only Kα line(s).[3,4]

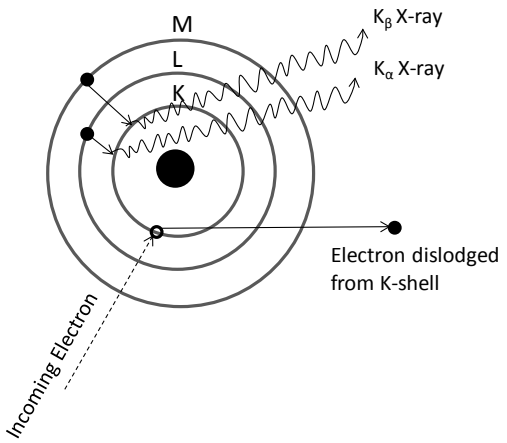

Figure 2-1 Generation of X-rays resulted from electron transitions to K-shell from higher energy shells: Kα1 line corresponds to an electron transition from 2p to 1s, while Kα2 line corresponds to a transition from 2s to 1s.

2.2.2 Diffraction of X-rays

When an electromagnetic wave goes through a crystal, it will be scattered in the crystal lattice by the electron clouds of atoms in the crystal. The atoms or ions act as secondary point sources and scatter the X-rays in all directions. If the scattering occurs without energy losses, the resultant wave has the same frequency as the incident wave (elastically scattered wave). When two or more points are involved, they produce spherical waves with the same wavelength which interfere with each other by adding their amplitudes. If the two scattered waves are completely in-phase, the resulting wave has the amplitude doubled (constructive interference), while if the scattered waves are completely out of phase, results in the cancelation of the two waves (destructive interference).[3–5]

The interaction of X-rays with a crystal is complex and the interpretation of diffraction effects in crystals are based on considering the layers of atoms in a crystal lattice as semi-transparent parallel planes that partially reflect the X-ray. When a X-ray beam interacts with a layer of atoms at an angle θ, the incident beam is partially absorbed into the crystal and partially scattered by the atoms. The scattered radiation interferes destructively or constructively resulting in diffracted X-ray beam. The constructive interference occurs when the distance between reflected waves from successive layers is equal to a whole number of wavelengths. The principle of

describing diffraction effects was developed by Bragg and the condition of diffraction is resumed by Bragg law:

$$2d_{hkl}sin\theta = n\lambda \qquad \text{Equation 2-2}$$

where d_{hkl} is the interplanar spacing and h k l are the Miller indices corresponding to a plane, λ is the wavelength of X-ray, θ is the angle between the beam and the plane and n is an integer. The same principle was described separately by Laue in a more general approach that describes rigorously and mathematically correct diffraction by crystals, but the drawback is that is more difficult to use. Figure 2-2 illustrates the diffraction of X-rays that occurs between such two layers when the diffraction conditions are fulfilled, resulting in constructive interference. If reflected beams are only partially in-phase, partial destructive interference occurs.

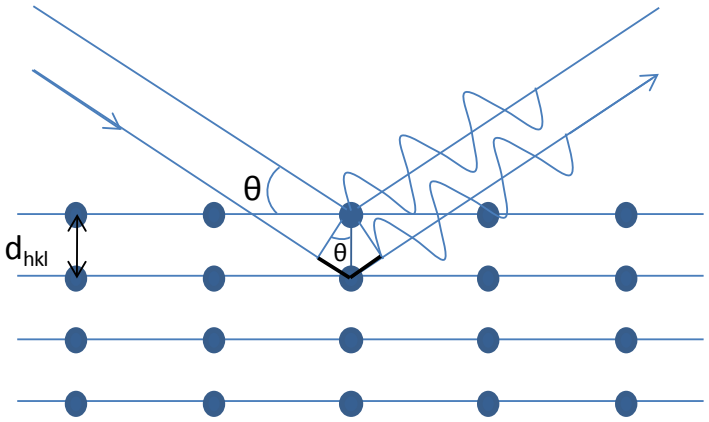

Figure 2-2 Diffraction of X-rays by electrons resulting in constructive interference (reflected beams are in phase); d_{hkl} is the interplanar distance with h k l - the Miller indices , the black thickened lines represent the path difference between beams reflected by consecutive layers.

The diffraction results are influenced by the number of electrons of each atom (or atomic number Z), as the electron clouds cause the scattering of X-rays. The scattering of X-rays by an atom is illustrated in Figure 2-3. For scattering in the direction of the incident beam, all electrons in the atom scatter in phase and the scattered intensity is the sum of the individual intensities. For scattering at an angle 2θ with respect to the incident beam a phase difference exists (partial destructive interference) and the effect of interference between the beam scattered by all electrons in the atoms causes a gradual decrease in scattered intensity with increasing

2θ angle, as interference becomes more destructive between Z waves (Z-atomic number). This effect causes the decrease in intensity of X-ray diffraction patterns at high angles (> 60-70°).[3–5]

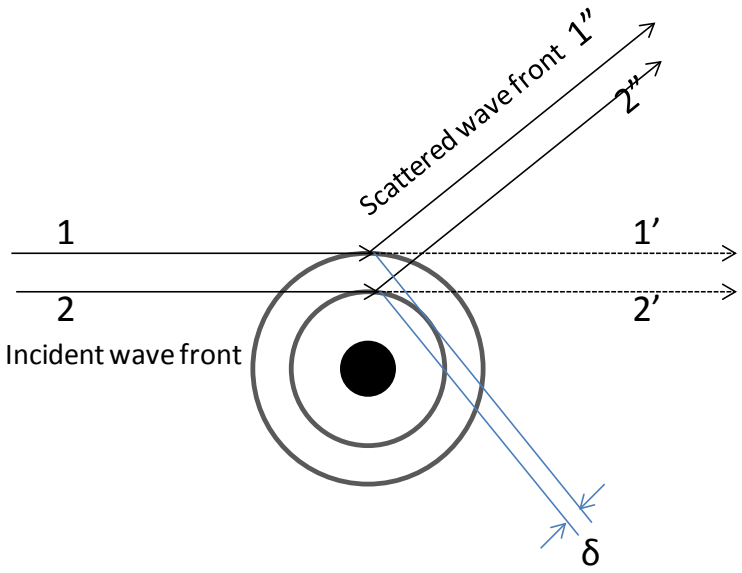

Figure 2-3 Scattering of X-rays by s electrons with introduction a path difference, δ, in the scattered wave front (after [3,5]).

The scattering factor for an atom is proportional to the atomic number Z, thus the scattering resulted from a unit cell represents the summation of the scattering factors for all atoms in the unit cell and its known as structure factor. The structure factor, F_{hkl} is determined by the distribution of atoms in the unit cell and the general expression for any crystal is:

$$F_{hkl} = \sum_{j=1,n} f_j exp2\pi i\left(hx_j + ky_j + lz_j\right) \qquad \text{Equation 2-3}$$

where n is the total number of atoms in the unit cell, f_j is the scattering factor of the atom j, which has the atomic positions (x_j, y_j, z_j). The intensity of a diffracted beam I_{hkl} is proportional to $|F_{hkl}|^2$ and atomic scattering factors are usually included (tabulated) in structure refinement software, thus the intensity of any hkl reflection can be calculated for known atomic coordinates. This facilitates the structure refinement from the intensities of diffracted X-rays by comparison with the calculated intensities, as described in sub-section 2.2.3.

In this work, X-ray powder diffraction was a convenient and key method for material characterisation for structure studies, phase purity, chemical compatibility between different materials or chemical stability in certain conditions (*e.g.* reducing atmosphere).

Two experimental setups were used: a Philips PW 1710 X-ray Diffractometer (CuKα radiation with graphite monochromator) and PANalytical Empyrean Diffractometer (CuKα1 radiation with curved germanium monochromator) in reflection mode. Data were processed by Rietveld method using Fullprof software.[6,7]

2.2.3 Rietveld Refinement of Crystal Structures

The Rietveld method was first developed by Hugo Rietveld to extract more information content from powder patterns and the work was placed in the public domain by publication of two papers [8,9] in 1967 and 1969.

The Rietveld refinement consists of fitting atomic parameters, structure parameters, specimen and instrument effects parameters to the diffraction pattern by the least square method. The quantity minimised in the least square method is the residual, S_y, which represent the summation of differences between experimental and calculated intensities (Y_i^{exp}-Y_i^{calc}):

$$S_y = \sum_i w_i (Y_i^{exp} - Y_i^{calc})^2 \qquad \text{Equation 2-4}$$

where Y_i^{exp} is the observed intensity at the i^{th} step and Y_i^{calc} is the calculated intensity at the i^{th} step, $w_i = 1/(\sigma_i^2)$ with σ_i^2 the variance of the observed Y_i^{exp} and the sum is the overall data points. The calculated intensities are determined from the structural model applied, thus it is important to have a reasonably good starting model. After calculating the diffraction data and comparing with observed data, the difference profile gives a good insight of which additional parameters must be further refined such as atomic positions, profile peak parameters, asymmetry etc. The quality of the Rietveld refinement is evaluated by reliability factors calculated as follows:[10,11]

Profile Factor:

$$R_p = 100 \cdot \frac{\sum_{i=1,n} |Y_i^{exp} - Y_i^{calc}|}{\sum_{i=1,n} Y_i^{exp}} \qquad \text{Equation 2-5}$$

Weighted Profile Factor:

$$R_{wp} = 100 \cdot \left[\frac{\sum_{i=1,n} \left| Y_i^{exp} - Y_i^{calc} \right|^2}{\sum_{i=1,n} w_i Y_i^{exp}} \right]^{\frac{1}{2}}$$ Equation 2-6

Expected Weighted Profile Factor:

$$R_{exp} = 100 \cdot \left[\frac{n-p}{\sum_{i=1,n} w_i (Y_i^{exp})^2} \right]^{\frac{1}{2}}$$ Equation 2-7

Reduced chi-square:

$$\chi^2 = \left[\frac{R_{wp}}{R_{exp}} \right]^2$$ Equation 2-8

where n-p is the number of degrees of freedom, p is the number of refined parameters, n represents the total number of points.

2.3 Scanning Electron Microscopy

Scanning Electron Microscopy represents a widely used technique for surface analysis of specimens and in solid state chemistry solid samples are analysed in terms of topography, morphology, orientation of grains, crystallography or chemistry. The Scanning Electron Microscope uses a beam of high energy electrons to analyse a sample. Electrons are emitted from a tungsten filament called an electron gun and are accelerated through a high voltage in a vacuum chamber. In order to use electrons instead of light, in a microscope, it is necessary the focusing of the electron beam. Electrons can be focused by the application of an electric or magnetic field and inside the scanning electron microscope there are several electromagnetic lenses. The electron beam is focused to a small spot on the sample surface. From the sample are emitted secondary electrons, backscattered electrons and even X-rays. Energy analysis of the emitted X-rays represents a technique to identify the chemical elements present on the sample surface.

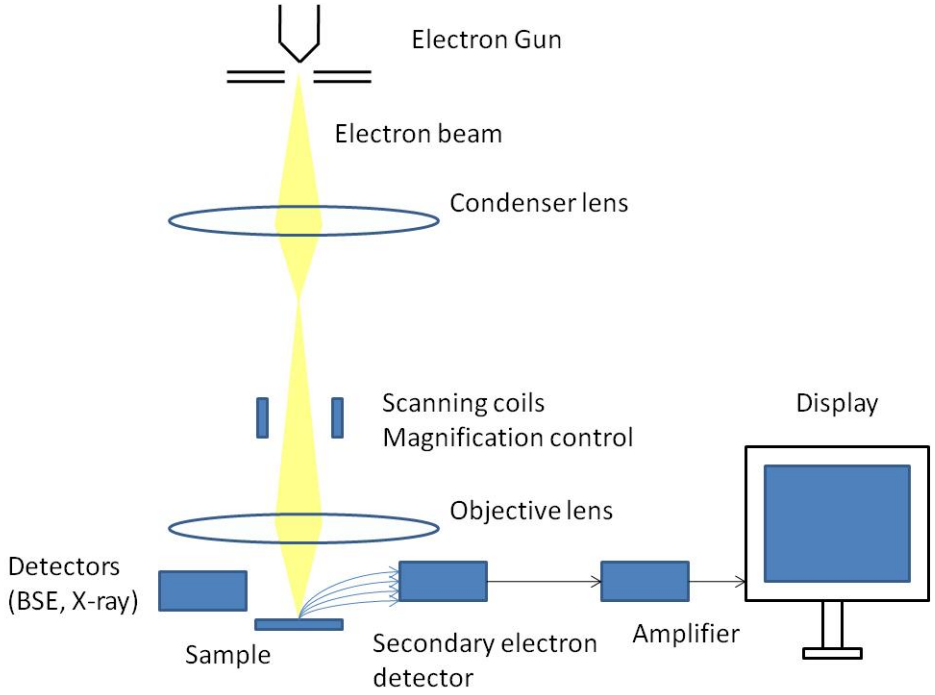

Figure 2-4 Basic construction of Scanning Electron Microscope (after [12])

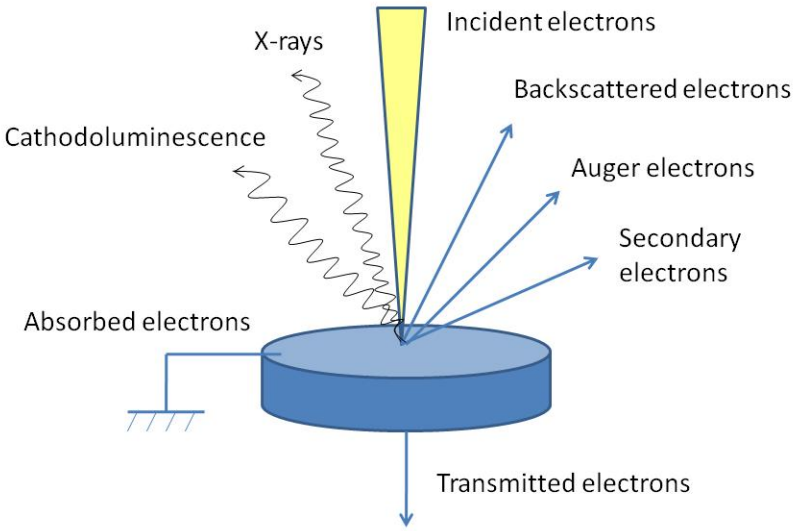

Figure 2-5 Electron species resulting from the interaction of the electron beam with the sample (after [12])

The interaction of the electron beam with the sample is described in Figure 2-5 and the types of electrons formed have different characteristics. Secondary electrons are generated from the collision of incident electrons with the valence electrons of the constituent atoms in the sample. Their energy is very small, the ones generated

deeper in the specimen are absorbed by the material and only the ones generated at the top of the surface are emitted. Backscattered electrons are electrons that interact with the nucleus but aren't captured inside the sample. They can be used for chemical analysis of the specimen as the nuclei are bigger the number of backscattered electrons will increase. Auger emissions occur when electrons (and not X-rays) are ejected from the sample as an energy release mechanism. When X-rays are emitted, they have characteristic emission spectra of chemical elements present and the technique is called Energy Dispersive X-ray spectroscopy.[3,12]

Microstructure of spinel materials or devices, such as symmetrical cells was observed on a JEOL JSM-5600 scanning electron microscope (SEM) or on a JEOL JSM-6700F SEM. JEOL JSM-5600 scanning electron microscope had very good performance in acquiring SEM images with magnification of maximum x5000, while with JEOL JSM-6700F SEM clear images can be obtained even for x100 000. High magnification images were collected when required (e.g. on cross-section images of the symmetrical cells to observe the microstructure of impregnated phases with respect to the scaffold).

2.4 Dilatometry

Thermal expansion coefficient (TEC) and the sintering step were determined in air or reducing atmosphere on sintered pellets with 11-13 mm diameter and 2±0.3 mm thickness, using a NETZSCH Dilatometer 402C. Dilatometry is a thermo-mechanical technique based on measuring the expansion or shrinkage in one direction (ΔL) of a material measured in a wide temperature range. It was accounted for the ΔL corresponding to dilatometer materials by using a blank run was for data correction.

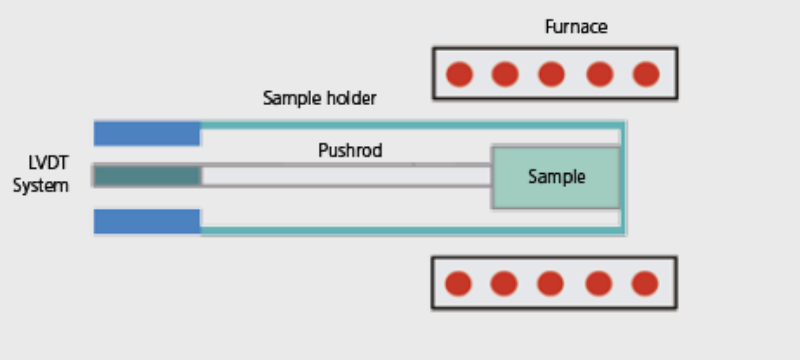

Figure 2-6 Functional diagram of a pushrod dilatometer.[13]

2.5 Chemical stability in reducing conditions

Chemical stability of materials in reducing conditions represents the ability of the material to remain pure phase with no segregation of secondary phases when exposed to reducing conditions. Materials stability was determined by heating ceramic bodies in a tube furnace with controlled atmosphere at high temperature (950 °C or 1000 °C) for various periods of time. The chemical stability of the samples was established afterwards using complementary techniques: the phase purity of the samples was determined post reduction by X-ray diffraction analysis and the change in morphology by scanning electron microscopy.

2.6 Electrical conductivity measurement

2.6.1 Conductivity Measurements by 4-point method

D.C. electrical conductivity measurements were performed in static air or in reducing atmosphere assured by a continuous gas flow of 50 cm^3/min 5%H_2/Ar. Four Pt foils of ~1 mm thickness were applied parallel onto a pellet surface with platinum paste and sintered at 900 °C for a good contact between the platinum contacts and the pellet. The experimental setup is comprised of a Carbolite furnace, an alumina jig with 4 electrical terminals, a thermocouple placed close to the sample and a zirconia p_{O_2} sensor. A current of known intensity was applied onto the sample, using a Keithley 220 Current Source, and the voltage of the sample was measured continuously as a function of temperature. Sample voltage was measured with a Keithley Voltmeter 182, the temperature was read continuously by a Solartron Digital

Multimeter model 7150, while the p_{O_2} was monitored by a Solartron Voltmeter model 7065. Figure 2-7 illustrates a schematic representation of the 4-terminal conductivity jig.

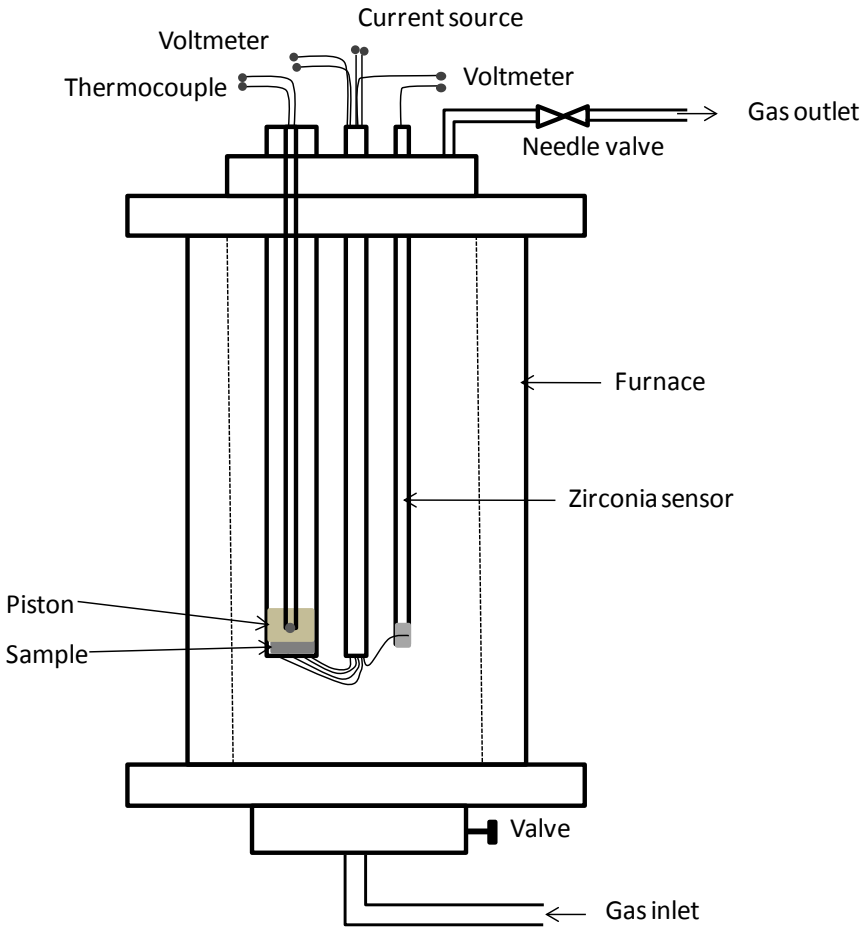

Figure 2-7 Schematic representation of 4-terminal conductivity experimental setup (after [14]).

The contact geometry applied in present work and sample shape are illustrated in Figure 2-8 with a geometric factor calculable considering the pin spacing and the thickness of the sample.

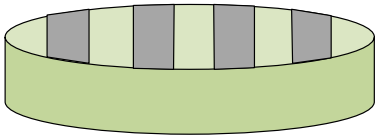

Figure 2-8 Contact geometry used for 4-terminal conductivity measurements.

2.7 Fabrication of symmetrical cells

The concept of symmetrical cell is based on developing symmetrical devices, using the same electrode material at the anode side and cathode side. The advantages to be considered in this design are the production of robust and reliable cells in a simpler manner, by reducing the number of components. Also, it would simplify the production process by decreasing the number of thermal treatments. Sulphur poisoning could be removed by a re-oxidation of the anode side and the device could still be used, because both electrodes could fulfil both functions (cathode, anode).[15] The electrochemical performance of such device can be tested when exposed to one atmosphere (e.g. air, pure H_2 etc), or exposed to different atmospheres (air, fuel). When exposed to different atmospheres, the device is tested as a whole cell and results in the evaluation of both anode and cathode performance. When tests are performed in one atmosphere, the materials performance as anode or cathode can be extracted.

2.7.1 Fabrication of scaffolds by tape casting process

Tape casting

A tape casting process is described by coating a wide surface with a viscous slurry in order to obtain large area thin, flat films of ceramic or metallic materials. Ceramic powders are processed as a slurry containing organic compounds such as plasticisers, binders and dispersant materials in order to obtain the optimum viscosity of the slurry to be cast.

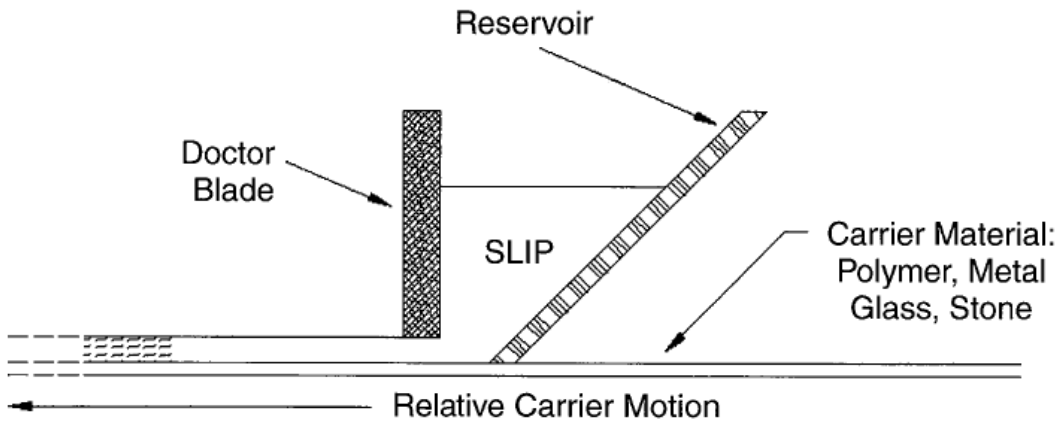

Figure 2-9 Schematic representation of the basic principle of tape casting process.[16]

Green ceramic tapes of $MnFeCrO_4$ and $MgFeCrO_4$ were obtained by tape casting a slurry containing spinel powder, organic binder (poly(vynil butyrate) - Butvar), dispersant (dibutyl(phthalate) - DBP), plasticiser (poly(ethylene glicol) - PEG) and graphite pore former (6 wt.% of total solids). The slurry was obtained by mixing in a plastic bottle 15 g of spinel powder with 1 g graphite and 8 g of solvent (3MEK : 1ETH). the mixture was then ball milled for 18 hours at 160 rpm. Next, 1.17 g PEG, 1.05 g DBP and 1.16 g of Butvar were added, the slurry was mixed for 20 minutes using an automatic device and the milling was then continued for 4 more hours at 100 rpm. The slurry was cast to a plastic tape at a speed of 50 rpm and with the height of the blade set to 0.24 mm to produce the tape of ~200 μm thickness.

2.7.2 Screen printing of YSZ electrolyte

The YSZ electrolyte was applied as an ink on 180-200 μm thick spinel green tapes resulting in very thin layer of 25-30 μm.

Ink preparation

The preparation of an uniform, viscous YSZ (8 mol.%) ink was made by mixing 12.5 g of powder with 0.25 g (1.5 wt.%) of KD-I dispersant, for a complete breaking of particle agglomerates, and was ultrasonicated for 15 minutes in acetone. An organic vehicle containing terpineol (95 wt.%) and poly(vynil butyrate) (PVB) (5 wt.%) was added ~25 wt.% and the mixture was stirred on a electromagnetic plate for ~3 days until the acetone evaporated completely and the ink formed.

Screen printing

Screen printing process is described by applying a thin layer of a ceramic material processed as an organic ink on a support (sintered pellet or green tape). A semi-automatic DEK 248 screen printer was used with most important component parts: the screen, which is a mask of the pattern to be printed, the blades, carried by a carousel, and the ink. The ink was printed on the green tapes by applying an accurate alignment between the screen, the substrate and the blades. Next, the ink was placed onto the screen on the edges of the porous fabric and the blades, running forward and backward with respect to the screen, conducted the ink through the porous mesh onto the substrate. The pressure applied on the blades was 9 kg/cm^2.

The green tape supports for screen printing were cut 6x6 cm^2 and the screen printed area was 5x5 cm^2 with one layer printed on a tape and two layers printed on a second identical tape. Two such green tapes were co-laminated and symmetrical cells (of 1.2 cm^2) with disc shape were cut and sintered at 1400 °C for 12 hours (Figure 2-10). On each side of the 25 µm thick electrolyte, the spinel layers were 180 µm ($MnFeCrO_4$) or 200 µm thick ($MgFeCrO_4$) and the porosity was ~55% and 45%, respectively.

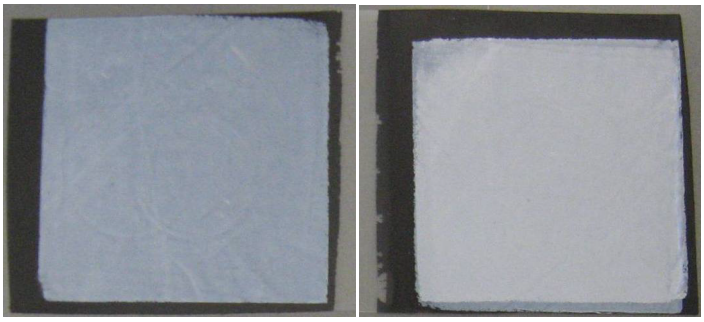

Figure 2-10 YSZ-screen printed green tapes with 1 and 2 layers printed area (5x5 cm^2) before co-lamination.

2.7.3 Insertion of electrode materials into scaffolds by impregnation

After sintering all organic binders, plasticisers and graphite formerly present in the green tapes were burnt out and resulted in porous symmetrical cell substrates. The porous layers were used as scaffold for LSCM, LSF and CGO, CeO_2 or Pd, which were impregnated into the supports as water based nitrate solutions prepared from $La(NO_3)_3 \cdot 6H_2O$ (Alfa Aesar, > 99.99%), $Sr(NO_3)_2$ (Sigma Aldrich, > 99%), $Cr(NO_3)_3 \cdot 9H_2O$ (Sigma Aldrich, 99.5%), $Mn(NO_3)_2 \cdot 4H_2O$ (Alfa Aesar, 99.98%), $Fe(NO_3)_3 \cdot 9H_2O$ (Sigma Aldrich, >98%), $Ce(NO_3)_3 \cdot 6H_2O$ (Aldrich, 99%) and $Gd(NO_3)_3 \cdot 6H_2O$ (Aldrich, 99.9%). In order to obtain the desired loadings of electrode and catalyst materials, the impregnation consisted in a multistep process with intermediary calcinations steps at 500 °C and final sintering steps at 1200 °C (4 hours) for LSCM, 900 °C (4 hours) for LSF, 1000 °C (4 hours) for CGO and 450 °C (1 hour) for CeO_2 and Pd.

2.8 Electrochemical tests on symmetrical cells

2.8.1 Electrochemical Impedance Spectroscopy

Electrochemical impedance spectroscopy (EIS) is a material characterisation technique for the evaluation of electrical and electrochemical properties of electroceramic materials and devices, such as fuel cells. This method is widely used for the performance evaluation and the degradation diagnosis of fuel cells, but also for corrosion diagnosis or mechanism diagnosis.[17,18] The concept of impedance represents the extension of resistance to alternative current (AC) circuits. It consists of applying a small AC potential to an electrochemical cell and measuring the current through the cell over a wide range of frequencies. The applied excitation signal is small for the cell response to be linear: the current response to a sinusoidal potential is a sinusoidal with the same frequency but shifted in phase. The sinusoidal voltage applied and the AC current response can be written as:

$$u(t) = U \cdot cos(\omega t)$$ Equation 2-9

where u(t) is the potential at time t, U is the amplitude, ω is the angular frequency (= 2πf).

$$i(t) = I \cdot cos(\omega t + \varphi)$$ Equation 2-10

where i(t) is the response signal, shifted in phase, I is the amplitude and φ is the phase shift of i(t). The impedance, Z, is defined as:

$$Z = \frac{u(t)}{i(t)} = \frac{U \cdot cos(\omega t)}{I \cdot cos(\omega t + \varphi)} = Z_0 \frac{cos(\omega t)}{cos(\omega t + \varphi)}$$ Equation 2-11

The expressions can be converted from time domain to a complex domain by using the Euler equation:

$$cos(\varphi) + jsin(\varphi) = exp(j\varphi)$$ Equation 2-12

$$Z = \frac{u(t)}{i(t)} = Z_0\, exp(j\varphi) = Z_0(cos\varphi + jsin\varphi)$$ Equation 2-13

The expression for impedance has a real part and an imaginary part and it can be represented as Nyquist plot, where the negative imaginary part of the impedance (Z'') is plotted vs. the real part of the impedance (Z'). The second type of representation is the Bode plot, where the real and imaginary components (Z', Z''), phase shift (-Θ) or the imaginary component of the complex modulus, (M'') are plotted as a function of

frequency. In impedance data characterisation, each representation may facilitate different specific details to be depicted. For example, the Bode plot of Z" vs. frequency may facilitate a better identification of relaxation frequencies of partially overlapped processes,[19,20] or the representation of M" against frequency may enable the identification of more than one component when characterising electroceramic materials.[21,22] Figure 2-11 illustrates the representation of Nyquist and Bode plot for a symmetrical cell measured for the present work.

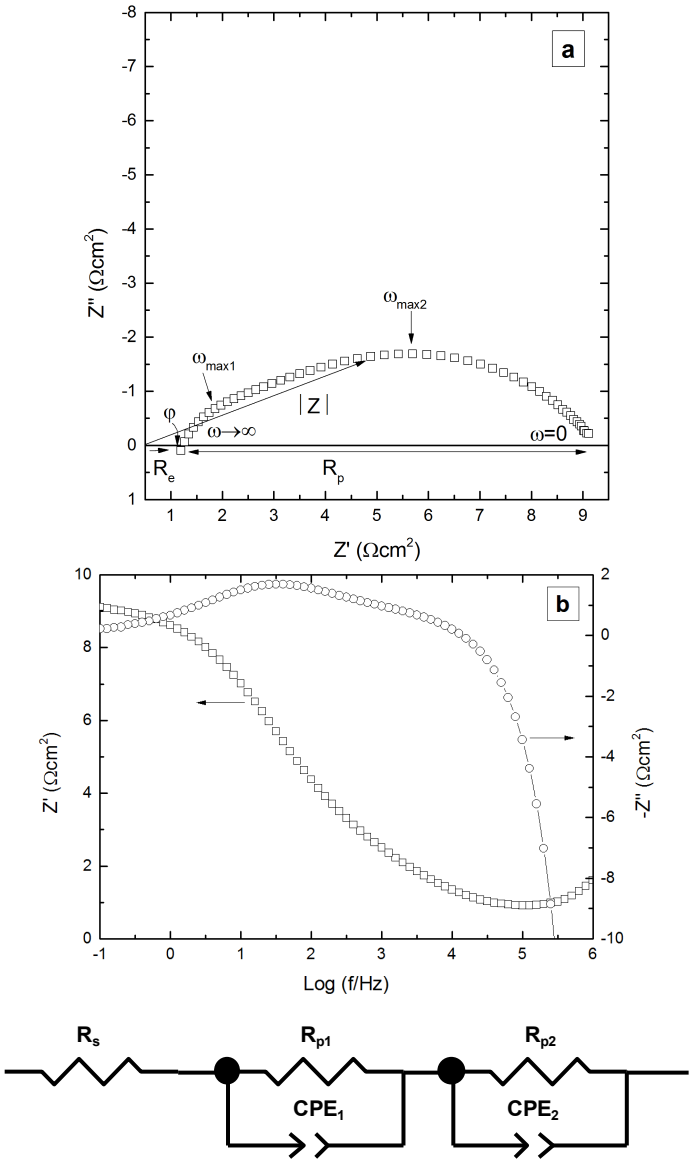

Figure 2-11 Schematic representation of: a) Nyquist and b) Bode plots for a set of data collected experimentally for this work (R_e- electrolyte resistance, R_p-polarisation resistance); c) the considered equivalent circuit ($R_s = R_e$, the electrolyte contribution, $R_{p1}+R_{p2} = R_p$, the total polarisation resistance with contribution of two electrode processes and CPE_1, CPE_2 - constant phase elements accounting for the capacitive component).

Equivalent circuit modelling has been used extensively in SOFC performance diagnosis as it is a method easily accepted and understood. Equivalent circuits are constructed to simulate the physical and chemical processes taking place in SOFC systems and each circuit element is supposed to have corresponding physical and chemical meanings. Electrochemical impedance spectra are analysed by fitting them to an equivalent circuit. The circuit elements in the model are resistors, capacitors and inductors with corresponding representation and impedance listed in Table 2-1.[17,18,23]

Component	Symbol in equivalent circuits	Impedance
Resistor		$Z = R$
Inductor	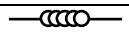	$Z = j\omega L$
Capacitor	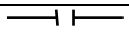	$Z = 1/j\omega C$
Constant phase element(CPE)	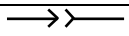	$Z = A(j\omega)^{-\alpha}$

Table 2-1 Equivalent circuit components with corresponding symbols in ZView software and impedance formula.[23]

Capacitors in EIS experiments may not behave ideally, thus the constant phase element is introduced and the difference is described by the impedance formula in Table 2-1, as when the equation describes an ideal capacitor, the constant $A = 1/C$ and the exponent is 1. For a CPE, the exponent α is less than 1. The necessity of replacing a capacitor with CPE in equivalent circuit models arises from the existence of distributed elements or surface roughness for the measured sample. For example, the interface between electrode and electrolyte in SOFCs is not smooth, uniform surface. It could be described by surface defects, local charge inhomogeneities, two and three phase regions, adsorbed species etc. In the impedance spectra only the average effect can be observed which leads to the replacement of an ideal RC with an R-CPE element in the equivalent circuit model.[24,25]

2.8.2 The analysis of impedance spectroscopy by equivalent circuit method

As explained previously, the analysis of impedance spectroscopy data is commonly performed by using equivalent circuits. The characterisation of a sample response in AC impedance facilitates the separation of the overall electrical properties into their component parts, which can be further studied and modified.[17,18,26] From the impedance spectrum is possible to identify different processes occurring in the material that can be characterised by resistance-capacitance (RC) elements usually placed in parallel. The various processes may be differentiated by the frequency dependence and by the specific capacitance resulted from fitting the impedance spectra to an equivalent circuit.[18,22,20,27,28] A classic example of fitting impedance spectra to processes is the characterisation of electroceramic materials, for which the bulk and grain boundary components may be differentiated by impedance spectroscopy. For example the ionic conductors or electronic hopping semiconductors are characterised by a resistance of the material to the hopping process. Also the process has an associated capacitance which measures the lattice polarisation for the applied voltage. The combination of these effects may be represented by parallel RC components.[22] The equivalent circuit applied is illustrated in Figure 2-12.

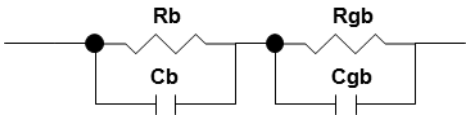

Figure 2-12 Equivalent circuit specific for fitting bulk and grain boundary for a ceramic material (after [18,26,21]).

Each parallel RC element should determine one semicircle, for which the R and C values may be extracted, using Equation 2-14 and Equation 2-15.

$$\omega_{max} RC = 1 \qquad \text{Equation 2-14}$$

where ω_{max} is the relaxation frequency.

$$C = \varepsilon' e_0 \frac{A}{l} \qquad \text{Equation 2-15}$$

Where ε_0 is the permittivity of free space, $8.854 \cdot 10^{-14} F \cdot cm^{-1}$ and $l/A = 1 cm^{-1}$. The sample regions specific to bulk and grain boundaries are assigned based on the capacitance values determined, i.e. specific for bulk the capacitance should be $\sim 1 \cdot 10^{-12}$ F, while for grain boundary $\sim 4 \cdot 10^{-9}$ F.(ref [18])

Impedance data collected for SOFCs may also be characterised by resistance of the material to ionic or electronic charge transport and material polarisation phenomena (*e.g.* anode, cathode polarisation), thus by combinations of parallel RC elements. When fitting impedance data collected for SOFC, the impedance spectra characterise different phenomenology than in the case of simple materials characterisation. The measured impedances may describe processes such as electrolyte contribution, electrode contributions (mass transfer, reaction kinetics, reaction activation, diffusion, adsorption/desorption). The contribution of each process may vary with electrode composition, fabrication procedure and testing conditions.[17,20] The fitting and interpretation of data is related to the number of distinguishable time constants in an impedance spectrum, the configuration of the studied device (*e.g.* symmetrical, half or full cells), relaxation frequencies and/or capacitance values.[27–29] Figure 2-13 illustrates the impedance spectrum for a $MnFeCrO_4$/LSCM|YSZ|$MnFeCrO_4$/LSCM[1] symmetrical cell tested in stagnant air, at 835 °C and the equivalent circuit for fitting the experimental data. The elements in the equivalent circuit consider the inductive contribution (L) of the testing jig, R_s represents the ohmic resistance, which is mainly the electrolyte contribution and two RC parallel elements that describe the processes which contribute to the electrode impedance spectrum. Generally, RC parallel elements are implemented in equivalent circuits in order to describe electrode processes.[20,27–29] In literature, similar equivalent circuit was considered when half-cells[30] or symmetrical cells[31] were tested and two time constants were observable in the impedance spectra. The electrode processes are generally attributed considering the relaxation frequencies and sometimes, equivalent capacitances resulted from equivalent circuit fitting. The processes that occur with higher speed are specific for high frequency domain *e.g.* transport of oxide ions, charge transfer reactions. Slow processes are situated in the low frequency domain in the impedance spectra *e.g.* dissociative adsorption of O_2, O-reduction and O-species transport at triple phase boundaries (TPB), or gas diffusion. [20,27–29,31–33] In Appendix 3 are presented the equivalent circuit fitting parameters and the electrode processes attribution for a chosen composition at several temperatures.

[1] / symbolises infiltrated component into a porous substrate; | symbolises electrode-electrolyte interface.

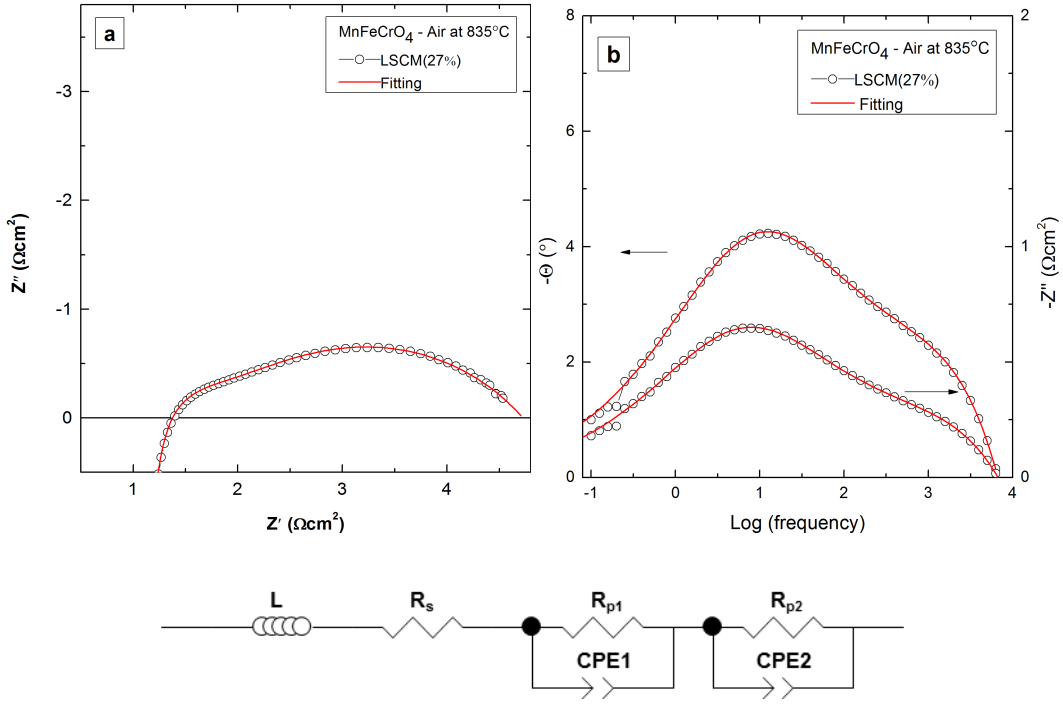

Figure 2-13 Representation of: a) Nyquist and b) Bode plots of electrochemical impedance obtained on the $MnFeCrO_4$/LSCM|YSZ|$MnFeCrO_4$/LSCM symmetrical cell at 835 °C, in stagnant air; c) the considered equivalent circuit (L=inductive component, $R_s = R_e$, the electrolyte contribution, $R_{p1}+R_{p2} = R_p$, the total polarisation resistance with contribution of two electrode processes and CPE_1, CPE_2 - constant phase elements accounting for the capacitive component).

2.8.3 Symmetrical cells testing parameters

Electrochemical performance was determined by EIS in the frequency range of 1 MHz-0.1 Hz with 20 mV AC perturbation amplitude using a Solartron 1260 frequency response analyser and SMaRT v2.8.0 (Solartron Analytical) and ZView v3.1c software (Scribner Associates). The geometric area of symmetrical cell electrodes was 1.2 cm^2 on either side of the dense electrolyte layer. $MnFeCrO_4$ symmetrical cells were evaluated in air or humidified (3%H_2O) 5%H_2/Ar. Measurements were made in a single chamber, two electrodes testing setup consisting of a quartz tube with one open end in which an alumina testing jig was inserted and closed gas tight. The alumina jig had inlet and outlet for gas flow and platinum wires for electrical contact to the sample. The schematic representation of the experimental setup is presented in Figure 2-14.

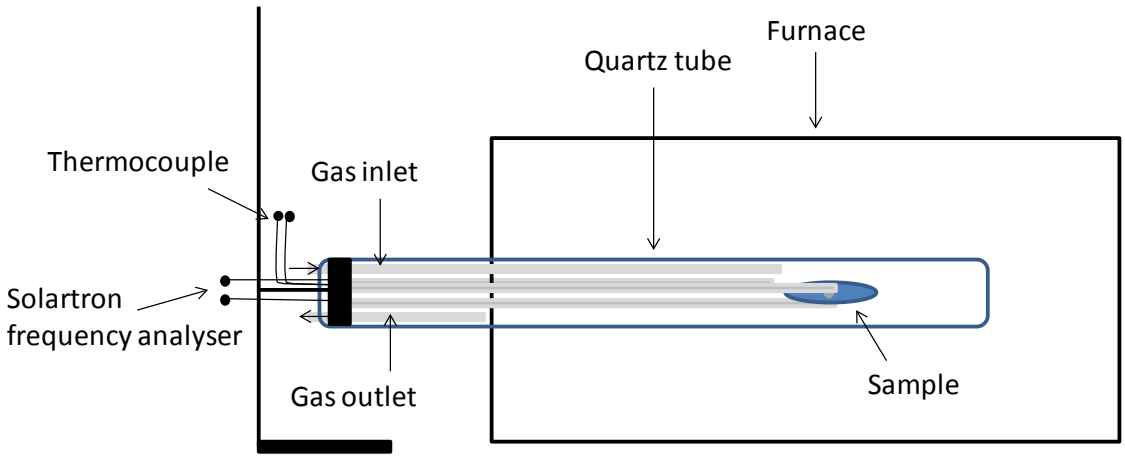

Figure 2-14 Schematic representation of the EIS measurements experimental setup.

Measurements included temperature dependence and assessment of the reduction process at a constant temperature of 850 °C. The ohmic resistance of the testing jig and its constituent Pt wires was measured and subtracted from the results obtained for symmetrical cells. The three layer wafer architecture of cells implies that the series resistance (R_s) is composed of the resistance of the thin YSZ electrolyte layer and the contributions from the two identical electrodes. In order to evaluate the contribution of the electrolyte to R_s, a pellet of YSZ was measured by AC impedance and the resistance of the electrolyte layer calculated and subtracted from cell R_s values.

2.9 References

1. M. De Andrade, M. D. Lima, R. Bonadiman, and C. P. Bergmann, *Mater. Res. Bull.*, 2006, **41**, 2070–2079.
2. W. Morales, M. Cason, O. Aina, N. de Tacconi, and K. Rajeshwar, *J. Am. Chem. Soc.*, 2008, **130**, 6318.
3. A. R. West, *Basic Solid State Chemistry*, Wiley-Blackwell, 2nd Edition., 1999.
4. L. S. D. Glasser, *Crystallography and its applications*, Van Nostrand Reinhold, New York, 1977.
5. V. Pecharsky and P. Zavalij, *Fundamentals of Powder Diffraction and Structural Characterization of Materials*, 2nd Edition., 2009.
6. J. Rodríguez-Carvajal, *Phys. B Condens. Matter*, 1993, **192**, 55 – 69.
7. Roisnel and J. Rodriguez-Carvajal, *Mater. Sci. Forum*, 2000, **378-381**, 118–123.
8. H. M. Rietveld, *J. Appl. Crystallogr.*, 1969, **2**, 65–71.
9. H. M. Rietveld, *Acta Crystallogr.*, 1967, **22**, 151–152.
10. R. A. Young, *The Rietveld method*, Oxford : Oxford University Press, 1993., 1993.

11. J. Rodriguez-Carvajal, *An Introduction to the program Fullprof 2000 (Version July 2001)*, Laboratoire Léon Brillouin (CEA-CNRS), CEA/Saclay, 91191 Gif sur Yvette Cedex, FRANCE, 2001.
12. Scanning Electron Microscope A to Z, JEOL, .
13. Netzch Analyzing & Testing, Technical Support, .
14. D. J. D. Corcoran, PhD Thesis, University of St Andrews, 2001.
15. J. C. Ruiz-Morales, J. Canales-Vázquez, J. Peña-Martínez, D. Marrero-López, and P. Núñez, *Electrochim. Acta*, **52**, 278–284.
16. R. E. Mistler and E. R. Twiname, *Tape Casting: Theory and Practice*, Wiley-American Ceramic Society, 1st Edition., 2000.
17. Q.-A. Huang, R. Hui, B. Wang, and J. Zhang, *Electrochim. Acta*, 2007, **52**, 8144 – 8164.
18. J. T. S. Irvine, D. C. Sinclair, and A. R. West, *Adv. Mater.*, 1990, **2**, 132–138.
19. A. Bieberle, Thesis/dissertation, 2000.
20. M. J. Jørgensen and M. Mogensen, *J. Electrochem. Soc.*, **148**, A433–A442.
21. J. T. S. Irvine, A. Huanosta, R. Valenzuela, and A. R. West, *J. Am. Ceram. Soc.*, 1990, **73**, 729–732.
22. A. R. West, T. B. Adams, F. D. Morrison, and D. C. Sinclair, *J. Eur. Ceram. Soc.*, 2004, **24**, 1439–1448.
23. X.-Z. Yuan, C. Song, H. Wang, and J. Zhang, *Electrochemical Impedance Spectroscopy in PEM Fuel Cells: Fundamentals and Applications*, Springer, 1st Edition., 2009.
24. E. Barsoukov and J. R. Macdonald, *Impedance Spectroscopy: Theory, Experiment, and Applications*, John Wiley & Sons, 2005.
25. J. R. Macdonald, *J. Electrochem. Soc.*, 1988, **135**, 2274–2279.
26. W. Gao, W. G. (Ph D.), and N. M. Sammes, *An Introduction to Electronic and Ionic Materials*, World Scientific, 1999.
27. T. Ramos, J. Hjelm, and M. Mogensen, *J. Electrochem. Soc.*, **158**.
28. I. M. Torres da Silva, J. Nielsen, J. Hjelm, and M. Mogensen, *Ecs Trans.*, 2009, **25**, 489–498.
29. J. Nielsen and M. Mogensen, *Solid State Ionics*, 2011, **189**, 74–81.
30. X. Yue and J. T. S. Irvine, *Ecs Trans.*, 2012, **41**, 87–95.
31. S. R. Gamble and J. T. S. Irvine, *Solid State Ionics*, 2011, **192**, 394–397.
32. G. Tsekouras and J. T. S. Irvine, *J Mater Chem*, 2011, **21**, 9367–9376.
33. Q. X. Fu, F. Tietz, and D. Stöver, *J. Electrochem. Soc.*, 2006, **153**, D74–D83.

Chapter 3

Contents

3 Studies on $MnM_xCr_{2-x}O_4$ and $MgM_xCr_{2-x}O_4$ spinels as electrode support materials 73

3.1 Introduction 73

3.2 Structural characterization of materials 73

3.3 Chemical stability in reducing conditions 87

3.4 Electrical properties 91

3.5 Compatibility with yttrium stabilized zirconia 96

3.6 Conclusions 101

3.7 References 103

3 Studies on $MnM_xCr_{2-x}O_4$ and $MgM_xCr_{2-x}O_4$ spinels as electrode support materials

3.1 Introduction

Studies concerning the synthesis, stability and electrical properties of $MnCr_2O_4$,[1–6] $MnM_xCr_{2-x}O_4$ (M = Mn, Fe),[1,2,7] $MgCr_2O_4$,[6,8–13] and $Mg_{1-x}M_xCr_2O_4$ (M = Fe)[14] spinel type oxides are numerously available in literature, while not many studies are available concerning the stability and electrical properties of such spinels in reducing conditions. Lu *et al.*[1] described in their study the electrical properties for $Mn_{1+x}Cr_{2-x}O_4$ series in air and reducing atmosphere (4%H_2/Ar saturated with H_2O) as a function of temperature, but their study is not conclusive about the stability of these materials in reducing conditions. Sakai *et al.*[2] determined electrical conductivities at constant temperatures for $MnCr_2O_4$ and $MnCr_{1.8}Fe_{0.2}O_4$ in reducing conditions assured by flowing gas mixtures (N_2 - O_2, CO_2 - H_2).

Spinel oxides $MnM_xCr_{2-x}O_4$ with (M = Fe, Mn, Mg or Li), $MgM_xCr_{2-x}O_4$ (M = Cr, Li, Mg, Ti, Fe, Cu, Ga) and $Mg_{1-x}M_xCr_2O_4$ (M = Cr) were synthesised by solution combustion synthesis or solid state reaction as described in chapter 2 - section 2.1, and were investigated with respect to phase analysis, density, chemical stability in reducing conditions and electrical conductivity.

3.2 Structural characterization of materials

The characterization of materials is essential for determining the structure of materials, for property studies, materials reproducibility and applications. The phase purity of synthesized materials was determined from X-ray diffraction patterns and the structural analysis, described by cell parameter values, a (Å), oxygen parameter, u (Å), and distribution of the cations amongst tetrahedral and octahedral sites were determined accurately based on the Rietveld refinement of calibrated datasets to Si peaks. Silicon powder was used as internal standard or scanned separately as solid silicon standard for an accurate determination of the angle shift (2θ zero). The peaks specific to spinel structure are indexed on the XRD diffraction pattern for $MgCr_2O_4$ presented in Figure 3-1.

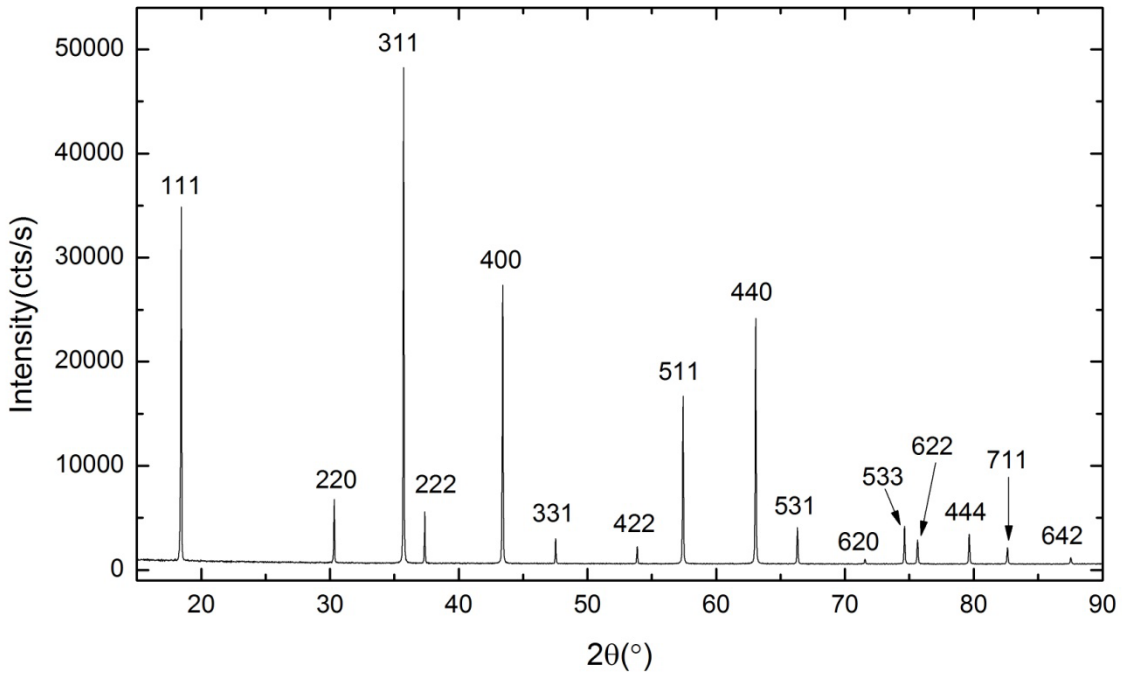

Figure 3-1 X-ray diffraction pattern for $MgCr_2O_4$ after sintering at 1400 °C

Compositions such as $MnMn_xCr_{2-x}O_4$ (x = 0, 0.5), $MnFe_xCr_{2-x}O_4$ (x = 0.1, 1) and $MnLi_xCr_{2-x}O_4$ (x = 0.1) formed single phase spinels when sintered in air with no special synthesis particularities.

Also $MgFe_xCr_{2-x}O_4$ (x = 0.1, 0.5, 1), $MgGa_xCr_{2-x}O_4$ (x = 0.1, 0.2), $MgLi_xCr_{2-x}O_4$ (x = 0.1), $MgCu_xCr_{2-x}O_4$ (x = 0.1) and $Mg_{1.5}Ti_{0.5}CrO_4$, were found to form single phase spinels in air, whereas $MgTi_xCr_{2-x}O_4$ (x = 0.1) and $Mg_{1-x}Cr_xCr_2O_4$ (x = 0.1) only formed single phase spinels when sintered in reducing conditions (dry 5%H_2/Ar).

When sintered in air, $Mg_{1-x}Cr_{2+x}O_4$ (x = 0.1) could not be obtained as pure spinel, instead forming $MgCr_2O_4$ and Cr_2O_3 (Eskolaite) (Figure 3-2). The pure phase $Mg_{0.9}Cr_{2.1}O_4$ formed when the material was sintered in 5%H_2/Ar. In air Cr cation kept its Cr^{3+} stable state, whereas in reducing atmosphere the excess Cr cations formed Cr^{2+} which occupied A site in spinel structure, as suggested by Greskovich *et al.*[15] who reported the formation of pure spinel containing Cr excess in reducing conditions, assuming that Cr^{2+} formed and occupied vacant A sites.

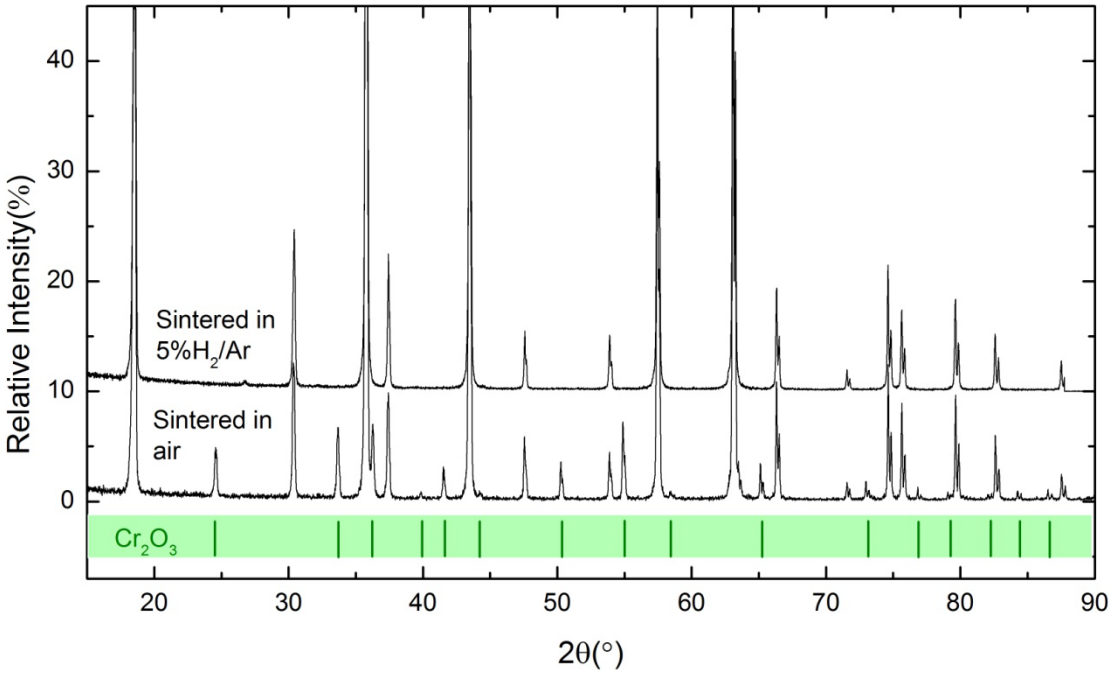

Figure 3-2 X-ray diffraction patterns for $Mg_{0.9}Cr_{2.1}O_4$ sintered in air and in 5%H_2/Ar at 1400 °C for 12 hours.

$Mg_{1+x}Cr_{2-x}O_4$ (x = 0.1) was obtained as pure phase spinel only by combustion synthesis, while when synthesised by solid state reaction MgO was detected as secondary phase. This observation suggested that combustion synthesis facilitated the formation of a quasi-stable spinel phase, with a higher Mg content than stoichiometric amount in $MgCr_2O_4$. Alper *et al.*[16] reported that for very high temperatures (~ 2300-2350 °C) the limit of solubility of MgO in $MgCr_2O_4$ is 5% wt., corresponding to $Mg_{1.1}Cr_{1.9}O_4$. The material was apparently metastable, as it was calcined at 1000 °C and fired at 1400 °C, after synthesis reaction, without the depletion of MgO detectable by XRD.

Rietveld refinements of $MnM_xCr_{2-x}O_4$ and $MgM_xCr_{2-x}O_4$ spinel oxides were performed on datasets collected on a PANalytical Empyrean Diffractometer in reflection mode (Cu Kα1), with high resolution of the collected diffraction data, thus refined cell parameters, a (Å), oxygen parameters, u (Å) and inversion rate (cation distributions) were determined with good precision. The full pattern fitting of spinel oxides was refined using the Fullprof software. The space group considered was Fd-3m (Z = 8) with origin at -3m and positions 8a (¼, ¼, ¼), 16d (½, ½, ½) and 32e

(u, u, u) for the cations on A, B sites and for oxygen anions, respectively. The diffraction peaks profiles were approximated with pseudo-Voigt profile, the thermal factors were refined first as general for the whole pattern and in further advanced stages of the refinement, atomic isotropic displacement factors were refined. The refined parameters are scale factor, background polynomial parameters, peak profile parameters u, v, w and η (Lorentzian/Gaussian distribution), unit cell parameters, atomic positions, site occupancies and isotropic displacement factors. Zero shift was corrected with respect to the Si standard and fixed in the refinement. In the final stage of the refinement, the profile and structural parameters were refined simultaneously to obtain correct estimated standard deviations. A detailed description of the intermediary stages for the full pattern fitting procedure is included in Appendix 1.

Refinement plots are illustrated below with observed intensities plotted with red dots, calculated intensities with black line and the difference between calculated and observed intensities is given as blue line. In the refined pattern for $MnCr_2O_4$, Si was present in the sample as internal standard and it was included in the refinement (peak positions for spinel and Si are indicated on the plot). $MnCr_2O_4$ had lattice parameter a = 8.43757(1) Å, oxygen parameter u = 0.2646(2) Å and unit cell volume V = 600,693(2) $Å^3$. Values of other refined parameters are listed in Table 3-1.

X-ray diffraction patterns of $MnFe_{0.1}Cr_{1.9}O_4$ and $MnFeCrO_4$ were refined considering the substituted Fe at B site, thus considered normal spinels. $MnFe_{0.1}Cr_{1.9}O_4$ had lattice parameter a = 8.44210(2) Å, oxygen parameter u = 0.2636(2) Å and unit cell volume V = 601.661(2) $Å^3$. $MnFeCrO_4$ had lattice parameter a = 8.46714(3) Å, oxygen parameter u = 0.2640(3) Å and unit cell volume V = 607.031(4) $Å^3$. The values of refined parameters are shown in Table 3-1. The reliability factors listed demonstrate the good quality of the XRD datasets and estimated standard deviation values are given in parenthesis for refined parameters.

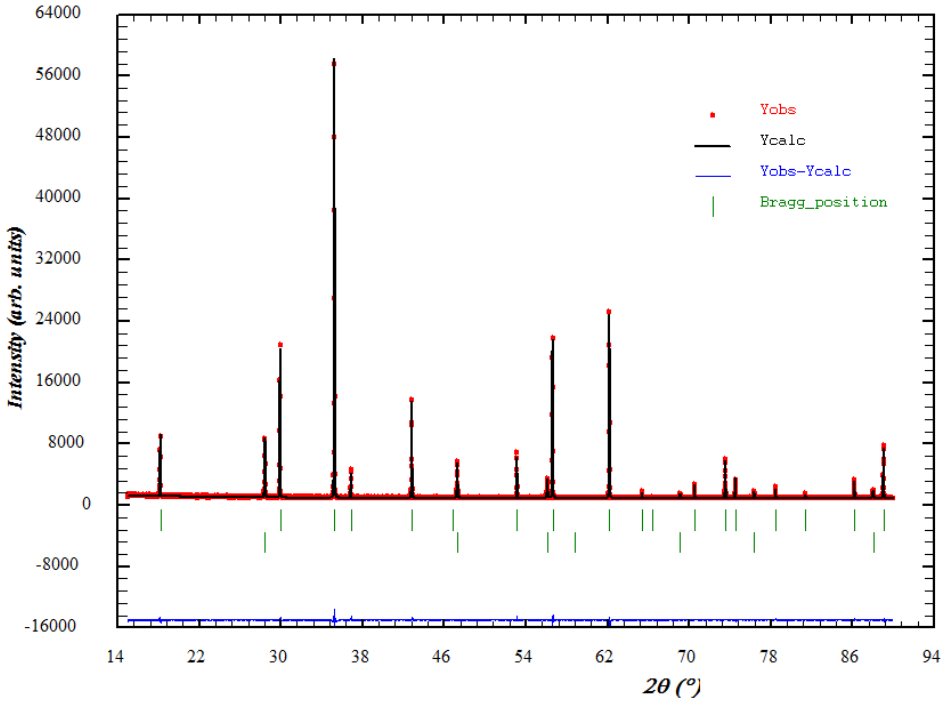

Figure 3-3 Rietveld refinement profiles for $MnCr_2O_4$ with Si as internal standard; Observed data are represented with red dots, calculated profile with black line and difference profile with blue line.

a

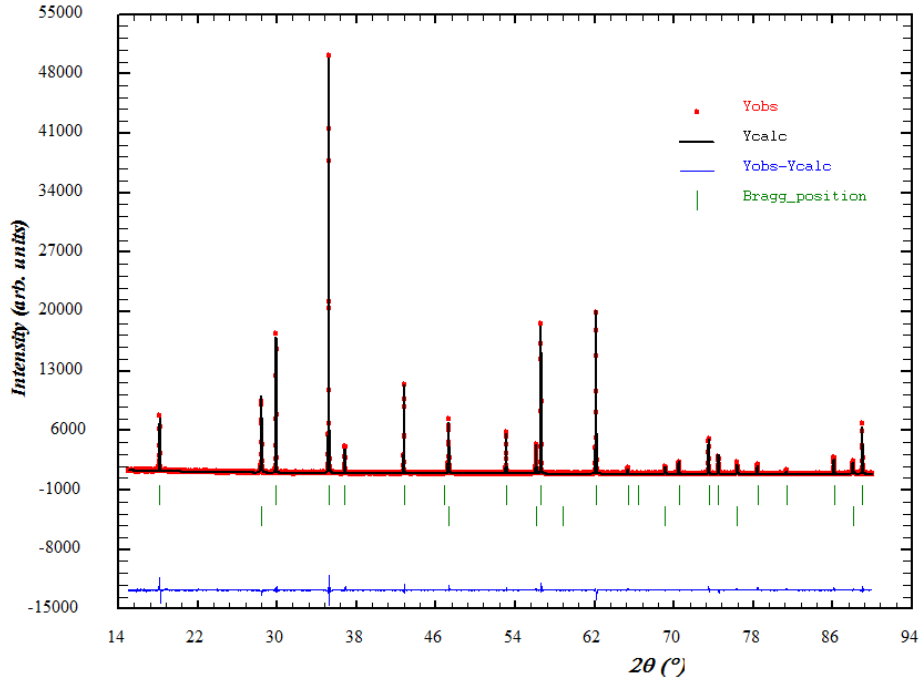

b

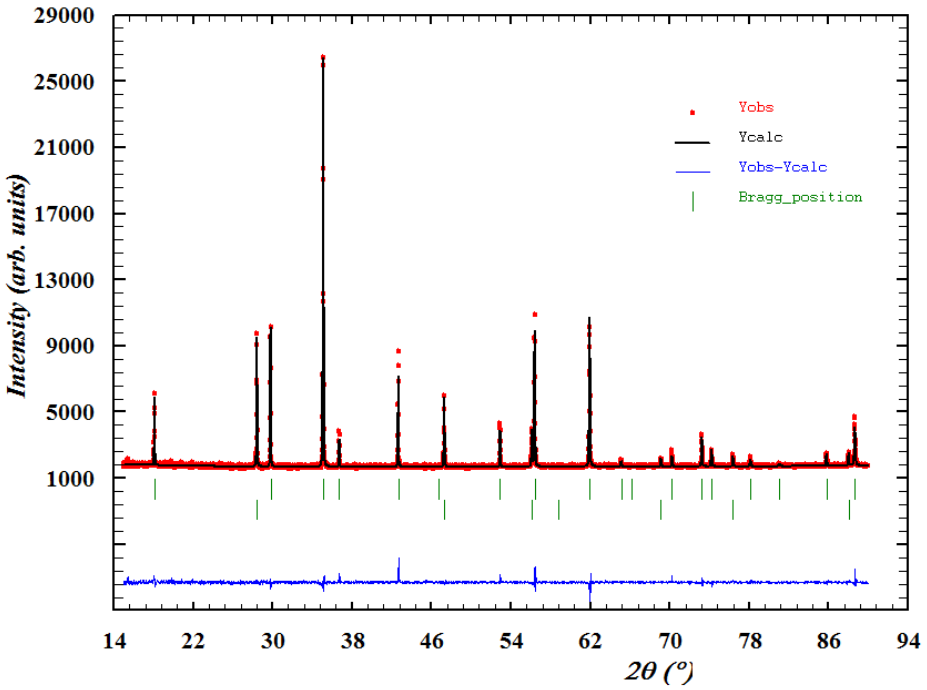

Figure 3-4 Rietveld refinement profiles of: a) $MnFe_{0.1}Cr_{1.9}O_4$ and b) $MnFeCrO_4$ with Si as internal standard. Observed data are represented with red dots, calculated profile with black line and difference profile with blue line.

Refinement parameter	$MnCr_2O_4$	$MnFe_{0.1}Cr_{1.9}O_4$	$MnFeCrO_4$
V (Å^3)	600.693(2)	601.661(2)	607.031(4)
B_iso_Mn_{td} (Å^2)	0.31(4)	0.57(6)	0.31(6)
B_iso_Cr (Å^2)	0.21(4)	0.47(5)	0.04(4)
B_iso_O (Å^2)	0.98(8)	1.70(1)	1.01(11)
B_iso_Fe_{oh} (Å^2)	-	0.47(5)	0.04(4)
R_p	2.46	2.73	2.11
R_{wp}	3.34	4.10	3.04
R_{exp}	2.96	2.98	2.34
χ^2	1.27	1.89	1.69

Table 3-1 Parameters resulted from refinement of $MnCr_2O_4$, $MnFe_{0.1}Cr_{1.9}O_4$ and $MnFeCrO_4$ XRD patterns and refinement reliability factors.

X-ray diffraction patterns of $MgM_xCr_{2-x}O_4$ spinel oxides were refined as described above, with cubic symmetry in the space group Fd-3m. Here are presented only results obtained for $MgCr_2O_4$ and $MgFeCrO_4$, with the results from full pattern

fitting of spinels are summarised in Table 3-3 and the refinement plots and other refined parameters are detailed in Appendix 2. For $MgCr_2O_4$ lattice parameter was determined a = 8.33508(5) Å, oxygen parameter u = 0.2613(1) Å and unit cell volume, V = 579.068(6) $Å^3$ and $MgFeCrO_4$ had a = 8.3670(2) Å, u = 0.2586(2) Å and V = 585.74(2) $Å^3$. Other refined parameters are listed in Table 3-2, except the inversion rate, which is summarised in Table 3-3 for $MnM_xCr_{2-x}O_4$ and $MgM_xCr_{2-x}O_4$ spinels.

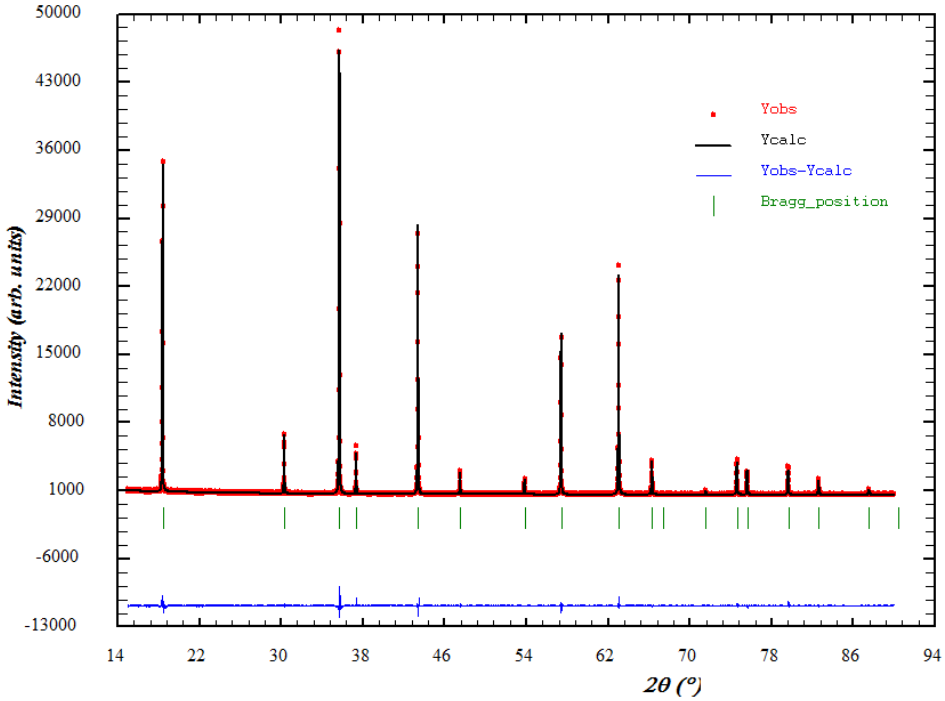

Figure 3-5 Rietveld refinement profiles of $MgCr_2O_4$ XRD pattern. Observed data are represented with red dots, calculated profile with black line and difference profile with blue line.

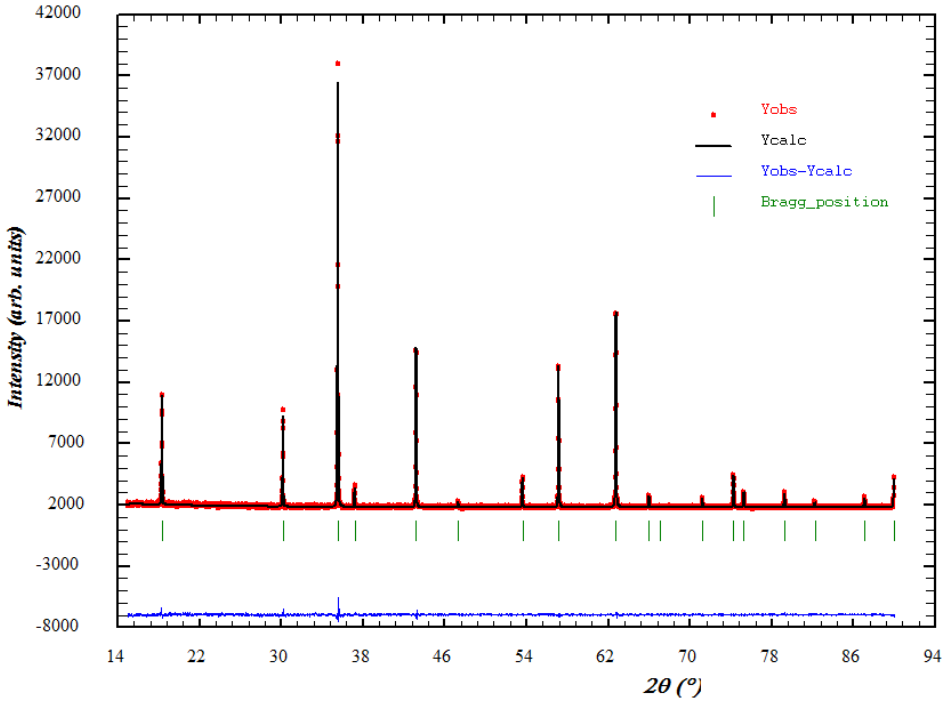

Figure 3-6 Rietveld refinement profiles of $MgFeCrO_4$ (random distribution). Observed data are represented with red dots, calculated profile with black line and difference profile with blue line.

Refinement parameter	$MgCr_2O_4$	$MgFeCrO_4$
V (Å^3)	579.068(6)	585.74(2)
B_iso_Mg_{td} (Å^2)	0.64(7)	0.31(7)
B_iso_Fe_{td} (Å^2)	-	0.31(7)
B_iso_Cr (Å^2)	0.43(4)	0.34(5)
B_iso_O (Å^2)	0.82(7)	0.91(8)
B_iso_Mg_{oh} (Å^2)	-	0.34(5)
B_iso_Fe_{oh} (Å^2)	-	0.34(5)
R_p	3.31	1.85
R_{wp}	4.46	2.46
R_{exp}	3.40	2.25
χ^2	1.72	1.19

Table 3-2 Parameters resulted from refinement of $MgCr_2O_4$ and $MgFeCrO_4$ XRD patterns and refinement reliability factors.

The cation distributions along with a and u values determined from Rietveld refinement are presented in Table 3-3 along with u parameter calculated with

equation 1.[17] The oxygen parameters determined from Rietveld refinement have close values to the ones calculated using Equation 3-1,[17] according to the refined cation distribution.

$$u = \frac{\bar{r}_A - \bar{r}_B}{\left[(1+\sqrt{3})a\right]} + 1.058/(1+\sqrt{3}) \qquad \text{Equation 3-1}$$

Where $\bar{r}_A$ is the average cation radius at tetrahedral site and $\bar{r}_B$ is the average cation radius at octahedral site. The calculated values for u parameters listed in Table 3-3 were calculated considering the average cation radius based upon the refined cation distributions.

Composition	Cation Distribution (td)	(oh)	$a_{Rietveld}$ (Å)	$u_{Rietveld}$ (Å)	u_{Calc}@ (Å)
$MnCr_2O_4$	(Mn)	(Cr_2)	8.43757(1)	0.2646(2)	0.2642
$Mn_{1.5}Cr_{1.5}O_4$	(Mn)	($Mn^{3+}_{0.5}Cr_{1.5}$)	8.46104(2)	0.2636(2)	0.2639
$MnFe_{0.1}Cr_{1.9}O_4$	(Mn)	($Fe_{0.1}Cr_{1.9}$)	8.44210(2)	0.2636(2)	0.2639
$MnFeCrO_4$	(Mn)	(FeCr)	8.46714(3)	0.2640(3)	0.2641
$MnLi_{0.1}Cr_{1.9}O_4$	($Mn^{2+}_{0.98}Li_{0.02}$)	($Mn^{3+}_{0.02}Li_{0.08}Cr_{1.9}$)	8.43203(2)	0.2657(3)	0.2636
$MgMnCrO_4$	($Mg_{0.8}Mn^{2+}_{0.2}$)	($Mg_{0.2}Mn^{3+}_{0.8}Cr$)	8.38080(8)	0.2620(2)	0.2596
$MgCr_2O_4$	(Mg)	(Cr_2)	8.33508(5)	0.2613(1)	0.2603
$MgGa_{0.1}Cr_{1.9}O_4$	($Mg_{0.93}Ga_{0.07}$)	($Ga_{0.03}Mg_{0.07}Cr_{1.9}$)	8.3330(1)	0.2604(2)	0.2603
$MgGa_{0.2}Cr_{1.8}O_4$	($Mg_{0.92}Ga_{0.08}$)	($Ga_{0.12}Mg_{0.08}Cr_{1.8}$)	8.3317(1)	0.2599(2)	0.2603
$MgFe_{0.1}Cr_{1.9}O_4$	($Mg_{0.98}Fe^{3+}_{0.02}$)	($Mg_{0.02}Fe^{3+}_{0.08}Cr_{1.9}$)	8.33814(5)	0.2604(2)	0.2603
$MgFe_{0.5}Cr_{1.5}O_4$	($Mg_{0.85}$ $Fe^{3+}_{0.15}$)	($Mg_{0.15}Fe^{3+}_{0.35}Cr_{1.5}$)	8.3566(1)	0.2605(2)	0.2602
$MgFeCrO_4$	($Mg_{0.6}Fe^{3+}_{0.4}$)	($Mg_{0.4}Fe^{3+}_{0.6}Cr$)	8.3670(2)	0.2586(2)	0.2603
$MgCu_{0.1}Cr_{1.9}O_4$	($Mg_{0.94}Cu_{0.06}$)	($Mg_{0.06}Cu_{0.04}Cr_{1.9}$)	8.33410(2)	0.2625(2)	0.2600
$MgLi_{0.1}Cr_{1.9}O_4$	(Mg)	($Li_{0.1}Cr_{1.9}$)	8.33448(2)	0.2617(2)	0.2600
$Mg_{1.5}Ti_{0.5}CrO_4$	(Mg)	($Ti_{0.5}Mg_{0.5}Cr$)	8.38704(5)	0.2606(1)	0.2593

Table 3-3 Cation distribution, a and u determined from the Rietveld refinement; (@) – u calculated with Equation 3-1.[17]

The unit cell parameter was plotted vs. the average ionic radii of B sites for $MnM_xCr_{2-x}O_4$ and $MgM_xCr_{2-x}O_4$ series and a linear trend was observed for both series (Figure 3-7). However, spinel $MnLi_{0.1}Cr_{1.9}O_4$ showed a deviation from the observed trend, while $MgM_xCr_{2-x}O_4$ series and $Mg_{1.5}Ti_{0.5}CrO_4$ had smaller deviations from linearity. The observed linearity indicated that cation distributions resulted from Rietveld refinement were reliable, although in the refinement it was not accounted for charge compensation effects, possible cation and anion vacancies forming. For a better evaluation of the considered cation distribution, Equation 3-1 was used to compare the value of refined u parameters with respect to their calculated value, as

illustrated in Figure 3-8. Considering the cation distributions resumed in Table 3-3, the $(\bar{r}_A - \bar{r}_B)/a$ values were calculated, thus the influence of both average ionic radii were accounted for, and the plot evidenced the samples for which other factors influence their u and a values. For $MgFe_xCr_{2-x}O_4$, the average ionic radii were calculated considering the existence of Fe^{3+} on A and B sites ($(Mg_{0.6}Fe^{3+}_{0.4})_{Td}(Mg_{0.4}Fe^{3+}_{0.6}Cr)_{Oh}O_4$ - Table 3-3) , or the existence of Fe^{2+} on A site and Fe^{3+} on B site ($(Mg_{0.6}Fe^{2+}_{0.4})_{Td}(Mg_{0.4}Fe^{3+}_{0.6}Cr)_{Oh}O_4$) (represented by empty squares in Figure 3-8). The existence of only Fe^{2+} on A site seemed to be a plausible approximation for $MgFe_{0.5}Cr_{1.5}O_4$ by improving the relative position between u refined and calculated. A similar effect was observed for $MgFeCrO_4$, for which the two considered possibilities demonstrate the existence of an intermediary Fe^{2+}/Fe^{3+} distribution, as the two extreme possibilities rely on the opposite sides of the calculated plot. $MnFeCrO_4$ was calculated as normal spinel and showed a smaller diffference between refined and calculated u values than $MgFeCrO_4$. However, the XRD cannot differentiate between Fe and Mn since they have very close scattering factors and for the determination of cation distribution in such case, other analysis techniques are required for a complete characterisation of the spinel. Samples $MgCu_{0.1}Cr_{1.9}O_4$, $MgLi_{0.1}Cr_{1.9}O_4$ and $Mg_{1.5}Ti_{0.5}CrO_4$ also showed deviation from the linear trend, probably due to charge compensation that takes places in the structure. Also $MgCr_2O_4$ showed a slight difference between refined and calculated u value that may be determined by nonstoichimetry of chromium as previously reported in ref[8–10].

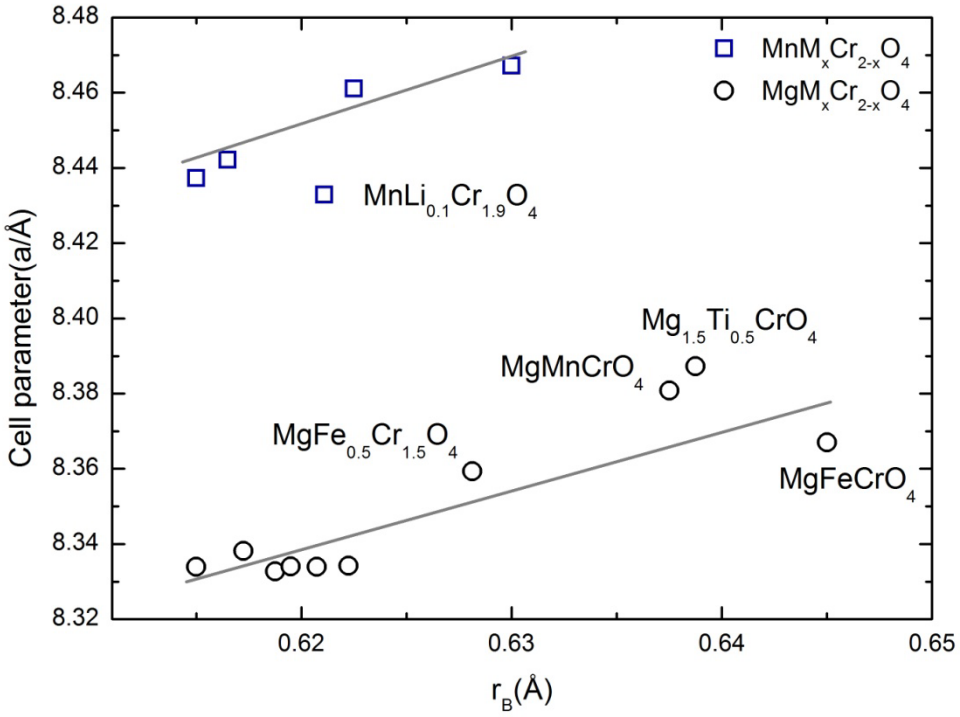

Figure 3-7 The evolution of the cell parameter with the average ionic radii for B sites; (empty squares) – r_B for $MnM_xCr_{2-x}O_4$; (empty circles) – r_B for $MgM_xCr_{2-x}O_4$; (grey line – guiding lines for linear trend)

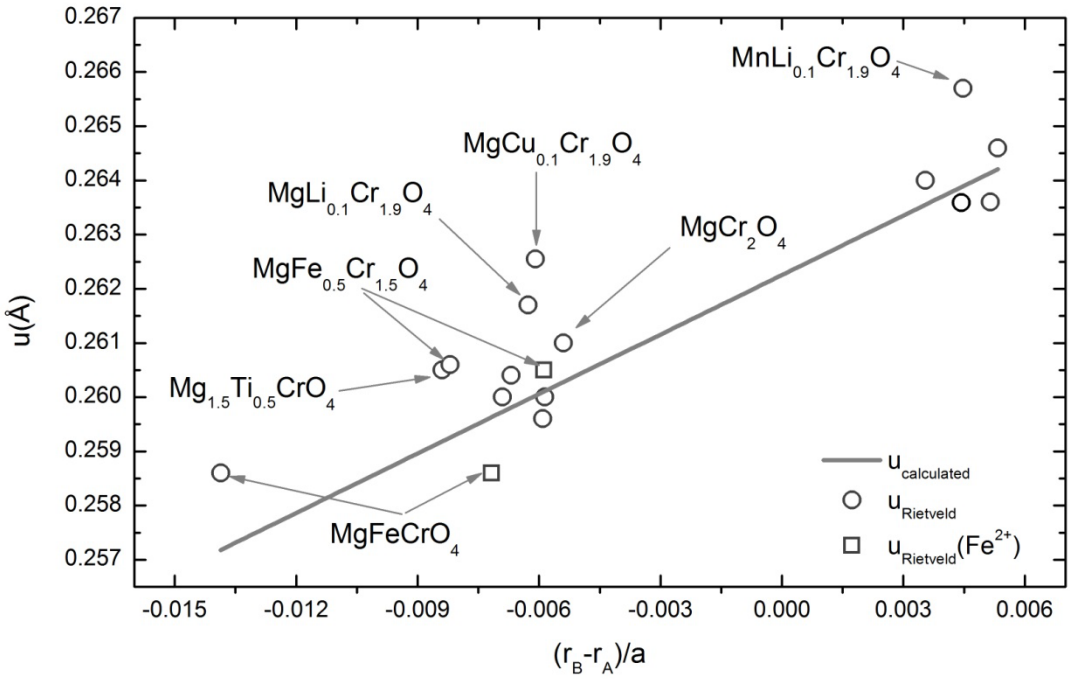

Figure 3-8 Variation of refined u parameter with $(r_A-r_B)/a$ based on Equation 3-1,[17] where r_A and r_B are average ionic radii resulted from the considered cation distribution; (empty squares) – refined u for $MnM_xCr_{2-x}O_4$; (empty circles) – refined u parameters for $MgM_xCr_{2-x}O_4$.

Microstructure studies showed the low sinterability of the spinels, confirmed by their low relative densities. Spinels microstructure could be characterised as highly porous, with particles described by definite crystalline faces and edges. Figure 3-9 illustrates the microstructures of $Mn_{1.5}Cr_{1.5}O_4$ and $MnFeCrO_4$ and $MgMnCrO_4$ spinels, which generally showed a bi-modal distribution of particles. The larger particles had dimensions of ~10-20 μm for $Mn_{1.5}Cr_{1.5}O_4$, 15-50 μm for $MnFeCrO_4$, 10-15 μm for $MgMnCrO_4$, while the small particles had dimensions of ~1-5 μm. $MnCr_2O_4$ had uni-modal particle distribution, with particle size ~1-7 μm. The magnification scale was chosen to be representative for different microstructures. Relative densities were higher for $MnFeCrO_4$ (90%), $Mn_{1.5}Cr_{1.5}O_4$ (71%) and $MgMnCrO_4$ (70%), while $MnCr_2O_4$, with 54% relative density had the lowest sinterability at 1400 °C.

Figure 3-10 illustrates microstructures for several $MgM_xCr_{2-x}O_4$ spinels. $MgM_xCr_{2-x}O_4$ spinel oxides had uni-modal particle distribution, with particle size ~1-3 μm observed for $MgCr_2O_4$, $MgFe_{0.1}Cr_{1.9}O_4$ and $MgGa_{0.1}Cr_{1.9}O_4$ (Figure 3-10 (a, b, c). $MgCu_{0.1}Cr_{1.9}O_4$ had particle size of 5-15 μm, while $MgLi_{0.1}Cr_{1.9}O_4$ and $Mg_{1.5}Ti_{0.5}CrO_4$ had particle size of ~1-10 μm (Figure 3-10 (d, e, f)). The relative densities showed very low sinterability for $MgCr_2O_4$ (54%) and $MgGa_xCr_{2-x}O_4$, for $x = 0.1$, 0.2 the relative density was ~55%. In the $MgFe_xCr_{2-x}O_4$ series, for $x = 0.1$ and 0.5 the relative density was ~55%, while for $x = 1$ it improved to 62%. Also $MgLi_{0.1}Cr_{1.9}O_4$ and $MgCu_{0.1}Cr_{1.9}O_4$ showed better sinterability with relative densities of 63% and 70%, respectively.

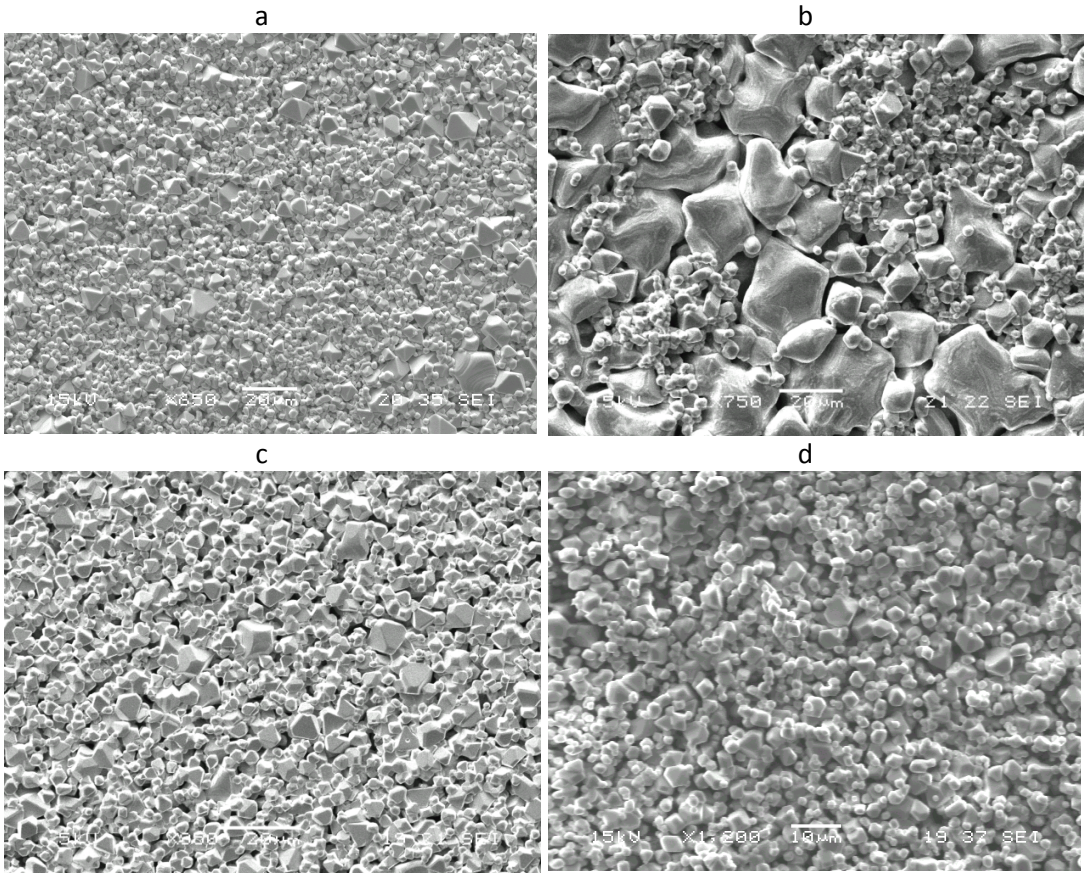

Figure 3-9 Micrographs of a) $Mn_{1.5}Cr_{1.5}O_4$; b) $MnFeCrO_4$; c) $MgMnCrO_4$ d) $MnCr_2O_4$ sintered at 1400 °C for 12 hours in air.

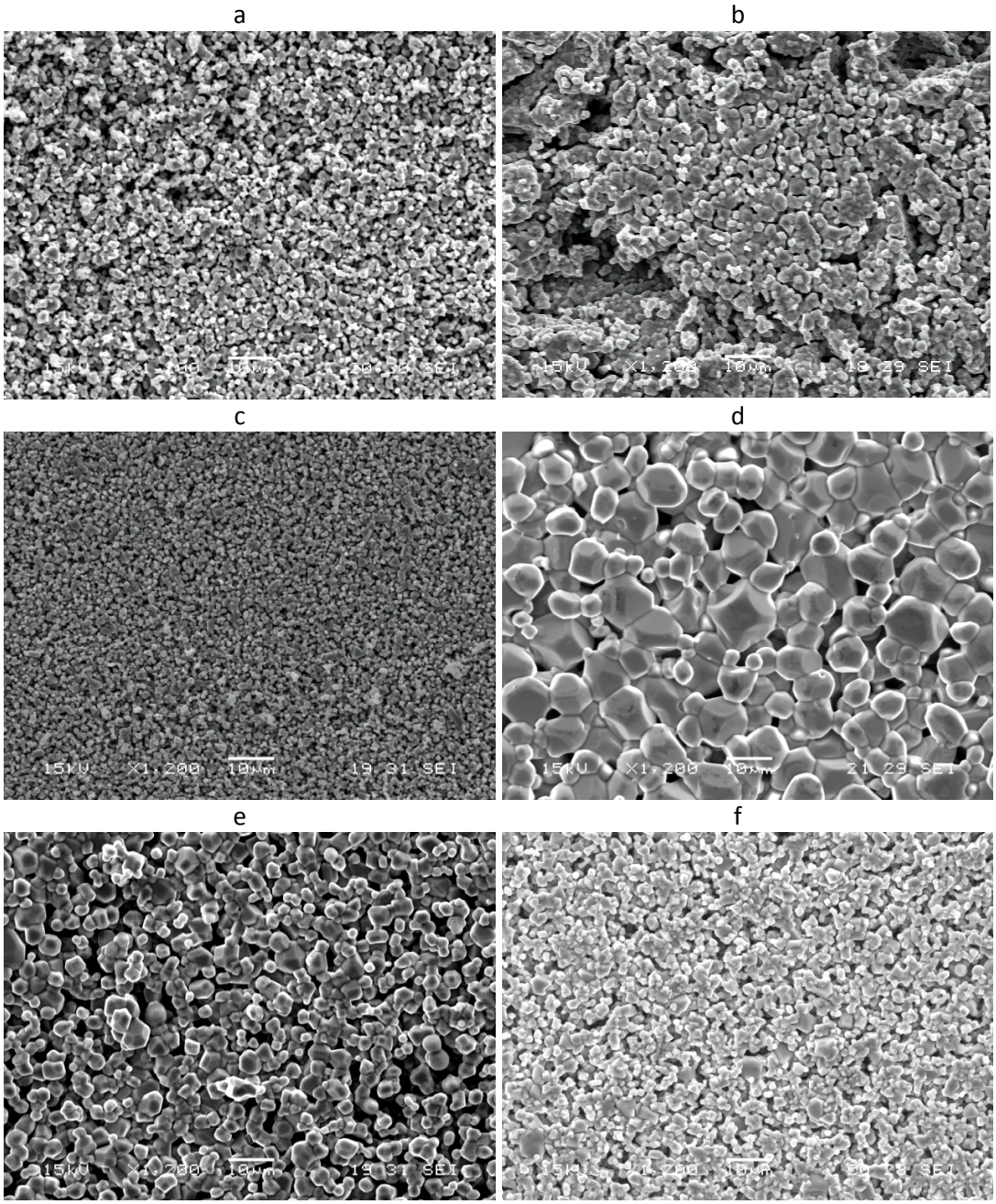

Figure 3-10 Micrographs of: a) $MgCr_2O_4$; b) $MgFe_{0.1}Cr_{1.9}O_4$ c) $MgGa_{0.1}Cr_{1.9}O_4$; d) $MgCu_{0.1}Cr_{1.9}O_4$; e) $MgLi_{0.1}Cr_{1.9}O_4$; f) $Mg_{1.5}Ti_{0.5}CrO_4$ sintered at 1400 °C for 12 hours in air.

3.3 Chemical stability in reducing conditions

Ceramic bodies sintered at 1400 °C were heated in a reducing atmosphere for 20 hours as described in chapter 2 - section 2.6 and the influence of the reduction was evaluated by X-ray diffraction analysis and Scanning Electron Microscopy. Phase analysis for reduced samples was performed on X-ray patterns collected on a Philips (PW 1710) X-ray Diffractometer in reflection mode. The morphology was studied on a JEOL JSM-5600 Scanning Electron Microscope (SEM) without gold coating for samples were conductive enough. The materials were reduced at 1000 °C for 20 hours and conditions were modified only when required. $MnM_xCr_{2-x}O_4$ (M = Mn, Fe) spinel series showed reduced stability in reducing conditions, resulting in segregation of secondary phases (Table 3-4)). Thus the reducing temperature was decreased to 950 °C, but the spinel decomposition with segregation of secondary phases was still observed. Reduction of $Mn_{1.5}Cr_{1.5}O_4$ in dry 5%H_2/Ar at 950 °C resulted in MnO depletion from the spinel. $MnFe_xCr_{2-x}O_4$ (x = 0.1, 1) when reduced in dry 5%H_2/Ar decomposed with formation of MnO and metallic Fe as secondary phases, while when reduced in humidified 5%H_2/Ar at 1000 °C, only MnO segregated as secondary phase (Figure 3-11).

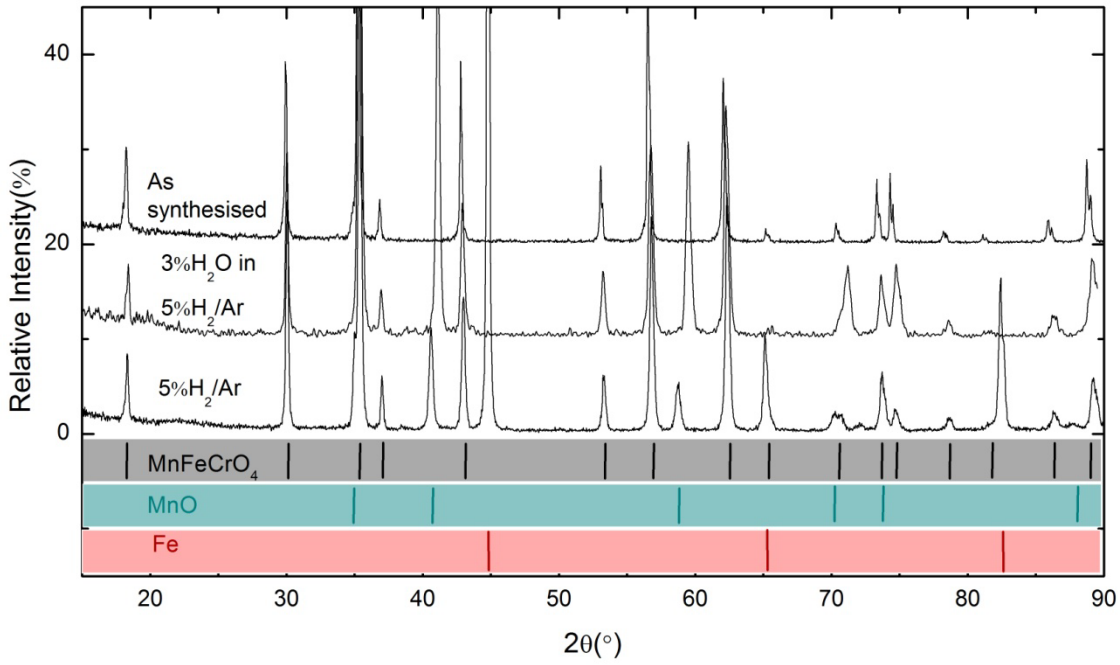

Figure 3-11 X-ray diffraction pattern of $MnFeCrO_4$ scaffold reduced in dry 5%H_2/Ar or humidified 5%H_2/Ar at 1000 °C for 20 hours.

However, $MnCr_2O_4$ showed good chemical stability when reduced in dry 5%H_2/Ar showing pure phase spinel even after being reduced for 50 hours at 1050 °C. The observed chemical stability may be well explained when considering the high preference of Cr^{3+} ($3d^3$, S = 3/2) cations for octahedral sites (the triply degenerate t_{2g} orbitals are occupied by three electrons) [18], thus Mn will form only Mn^{2+} ($3d^5$, S = 5/2) cations to occupy the tetrahedral sites. In reducing conditions the tendency of Cr^{3+} cations will be to maintain their stable electronic configuration ($3d^3$) and octahedral coordination, while Mn cations existing in the structure are already at the lower valence state, resulting in low tendency of decomposition for the spinel. Similar to $MnCr_2O_4$, $MgCr_2O_4$ also showed good chemical stability to reduction. A summary of reduction experiments is presented in Table 3-4 including the experimental conditions and formed secondary phases for considered compositions.

Composition	Temperature (°C)	Reduction time (h)	Atmosphere	Secondary phases
$MnCr_2O_4$	1050	20	Dry 5%H_2/Ar	-
	1050	50	Dry 5%H_2/Ar	-
$Mn_{1.5}Cr_{1.5}O_4$	950	20	Dry 5%H_2/Ar	MnO
$MnFe_{0.1}Cr_{1.9}O_4$	1050	50	Dry 5%H_2/Ar	MnO, Fe
$MnFeCrO_4$	950	20	Dry 5%H_2/Ar	MnO, Fe
	1000	20	Humid. 5%H_2/Ar	MnO
$MgMnCrO_4$	950	20	Dry 5%H_2/Ar	MnO
$MgCr_2O_4$	1000	20	Dry 5%H_2/Ar	-
$MgGa_{0.1}Cr_{1.9}O_4$	1000	20	Dry 5%H_2/Ar	-
$MgGa_{0.2}Cr_{1.8}O_4$	1000	20	Dry 5%H_2/Ar	-
$MgFe_{0.1}Cr_{1.9}O_4$	1000	20	Dry 5%H_2/Ar	-
$MgFeCrO_4$	1000	20	Dry 5%H_2/Ar	$MgO_{0.91}FeO_{0.09}$, Fe
	1000	20	Humid. 5%H_2/Ar	-
$MgCu_{0.1}Cr_{1.9}O_4$	1000	20	Dry 5%H_2/Ar	-
$Mg_{1.5}Ti_{0.5}CrO_4$	1000	20	Dry 5%H_2/Ar	-

Table 3-4 Summary of reduction experiments in terms of experimental conditions and formed secondary phases.

Significant changes in sample morphology were observed for $Mn_{1.5}Cr_{1.5}O_4$ and $MnFeCrO_4$ that demonstrated lower chemical stability on reduction, thus the segregation of secondary phases could be observed in the micrographs of the

samples. In Figure 3-12 there are presented the micrographs for $Mn_{1.5}Cr_{1.5}O_4$ as synthesized and after reduction. The morphology of the particles did not change significantly after reduction, with the same particle size and particles characterised by definite crystalline faces and edges, but separated areas could be observed on the surface of the pellet (Figure 3-12) (b, c)). These separated areas could be observed also on the pellet without any magnification as green spots (Figure 3-12 (d)). Micrographs of $MnFeCrO_4$ as synthesized and reduced in dry 5%H_2/Ar demonstrated a change in the morphology of the reduced sample. Small particles of segregated phases formed on the spinel particles surface, as presented in Figure 3-13.

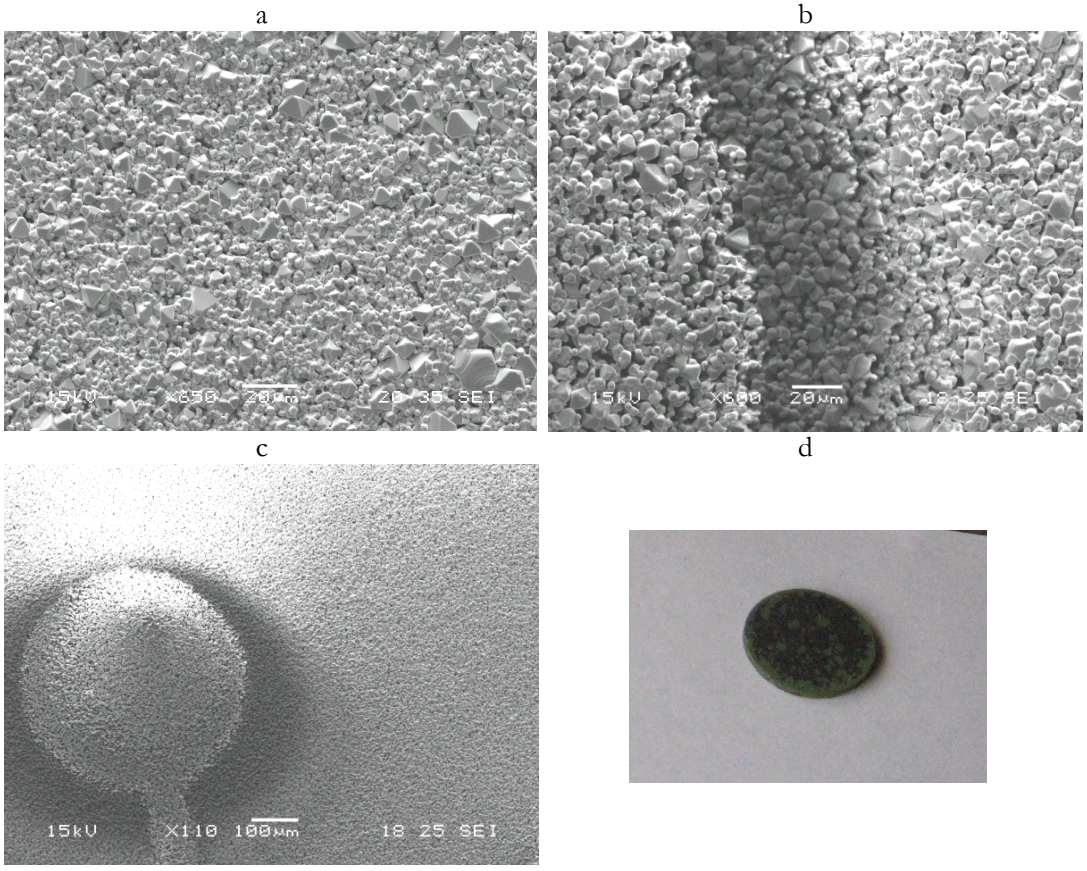

Figure 3-12 Micrographs and picture of $Mn_{1.5}Cr_{1.5}O_4$: a) as synthesized; b), c) - reduced for 20 hours at 950 °C; d) picture of $Mn_{1.5}Cr_{1.5}O_4$ after reduction.

a b

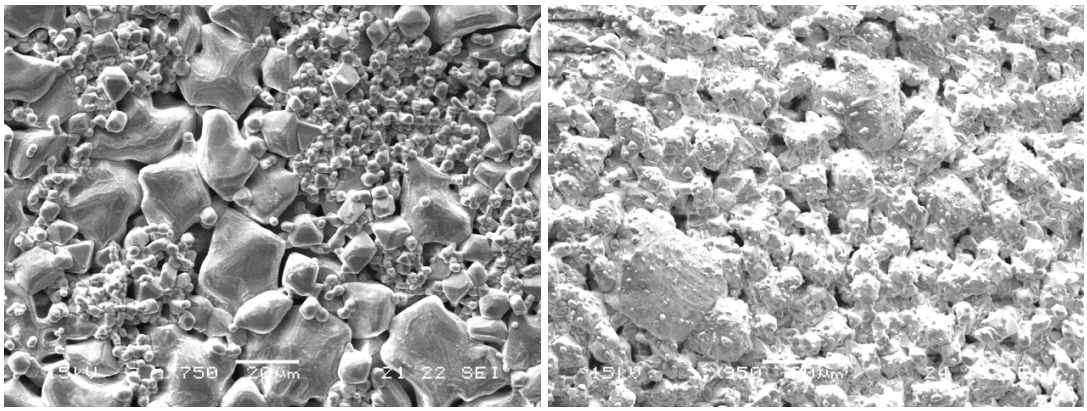

Figure 3-13 Micrographs of $MnFeCrO_4$: a) - as synthesized; b) - reduced for 20 hours at 950 °C; the magnification scale was chosen to be representative for different microstructures.

For the $MgM_xCr_{2-x}O_4$ (M = Mg, Ti, Fe, Cu, Ga) series, samples with M = Ga (x = 0.1, 0.2), Ti (x = 0.1) and Cu (x = 0.1) showed good stability upon reduction (Table 3-4), while samples with M = Fe (x = 0.1, 0.5, 1) decomposed with the formation of metallic Fe and $(MgO)_{0.91}(FeO)_{0.09}$. Figure 3-14 includes the XRD patterns of MgFeCrO4 as synthesized, reduced at 1000 °C for 20 hours in humidified 5%H_2/Ar and reduced at 1000 °C for 20 hours in dry 5%H_2/Ar. The corresponding partial pressure of the oxygen (p_{O_2}) for dry 5%H_2/Ar at 1000 °C was ~10^{-20}-10^{-21}. In case of reducing the material in humidified 5%H_2/Ar, the p_{O_2} was higher, about ~10^{-17} at 1000 °C and the decomposition of $MgFeCrO_4$ did not occur, as observed on the XRD pattern.

$MnCr_2O_4$ and $MgCr_2O_4$ showed good chemical stability in more extreme reducing conditions than the fuel cell testing conditions. Even so, other properties, such as the electrical conductivity did not show positive evolution in reducing conditions. The chemical stability to reduction of $MnFeCrO_4$ and $MgFeCrO_4$ was studied in milder conditions of reduction, such as humidified 5%H_2/Ar, because the spinels were of particular interest for the purpose of this study. Both, $MnFeCrO_4$ and $MgFeCrO_4$ showed an increase in electrical conductivity in reducing atmosphere and positive effects were observed for the stability to reduction, when humidified 5%H_2/Ar was used. Water would be present in fuel cell testing conditions, thus the considered

reduction conditions were appropriate. The next section describes the evolution of electrical conductivity for $MnM_xCr_{2-x}O_4$ and $MgM_xCr_{2-x}O_4$ spinels.

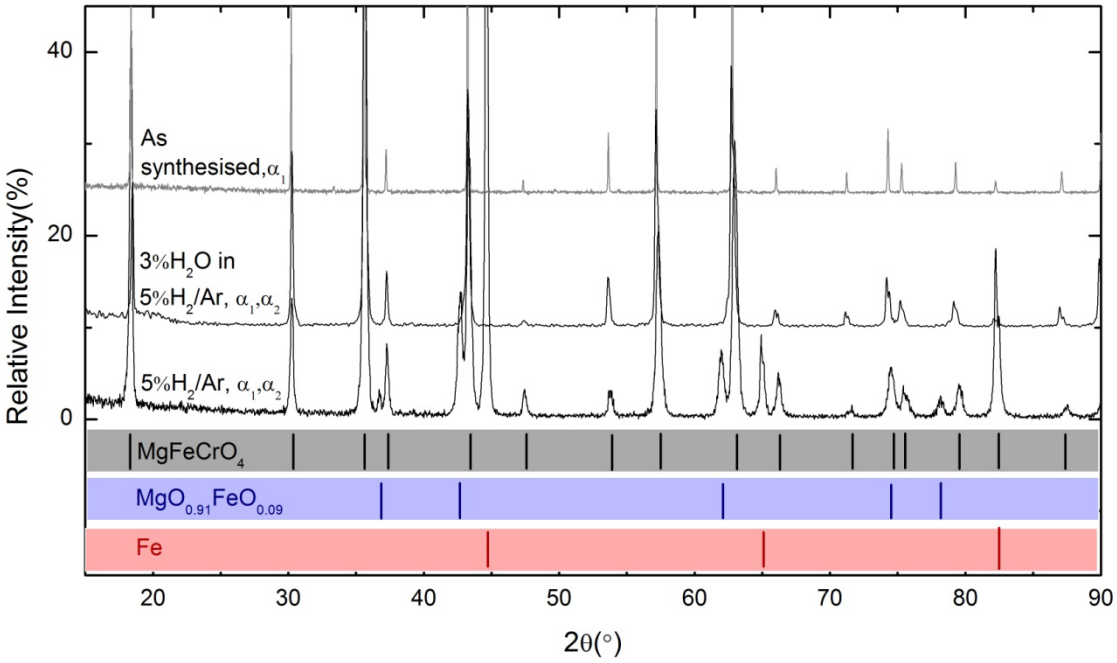

Figure 3-14 X-ray Diffraction Pattern of $MgFeCrO_4$ reduced at 1000 °C for 20 hours: (a) in humidified (3% H_2O) 5%H_2/Ar and (b) dry 5%H_2/Ar; Lines Cu Kα_1 and Kα_2 are specified in comparison with the: As synthesised scan that only contains Cu Kα_1 line.

3.4 Electrical properties

Electrical conductivity measurements were conducted on porous ceramic bodies formed by uni-axial pressing of the calcined spinel powders and sintering in air at 1400 °C (chapter 2 - section 2.1). Electrical conductivity of $MnM_xCr_{2-x}O_4$ series measured in air showed increase in conductivity for most of substitutions at B site, but for $MnFe_{0.1}Cr_{1.9}O_4$, whose conductivity was lower than for $MnCr_2O_4$. As most of the $MnM_xCr_{2-x}O_4$ spinels proved to be unstable to reduction, their conductivity was determined in air (Figure 3-15 (a)). $MnCr_2O_4$ showed chemical stability to reduction, as described in the previous subsection and the electrical conductivity was determined as a function of reduction time and also partial pressure of oxygen (p_{O_2}). The $MgM_xCr_{2-x}O_4$ series showed higher conductivities in air than $MnCr_2O_4$, but comparable with the conductivity of other $MnM_xCr_{2-x}O_4$ spinels. The conductivity of $MgM_{0.1}Cr_{1.9}O_4$ series (M = Ga, Li, Cu, Fe) showed an increase in conductivity for Li

and Cu both in air and reducing conditions, as observed in Figure 3-15 (b). The conductivity decreased in reducing conditions for all substituted cations, but the trend was similar with an increase in conductivity for Li and Cu doped samples. This observation is consistent with considering a formal increase of Cr cation charge induced by the aliovalent substitution (section 1.5).

The conductivity measured in air for $MgFe_xCr_{2-x}O_4$ (x = 0, 0.1, 0.5, 1) series decreased with the increase of the iron content. The composition with x = 0.5 had a minimum value of $2x10^{-3}$ $S{\cdot}cm^{-1}$ and for x = 1 conductivity increased again to 0.14 $S{\cdot}cm^{-1}$. In reducing conditions, the conductivity increased with the iron content, as shown in Figure 3-15 (c), where the maximum value corresponded to x = 1 with 0.4 $S{\cdot}cm^{-1}$.

The other cations considered for x = 0.1 series were studied as well for a higher extent of substitution on B site and the results indicated forming of secondary phases for Li and Cu. A higher amount of Ga (x = 0.2) has been included on B site with formation of pure phase spinel. The influence of Ga on the electrical conductivity was negative in air and reducing atmosphere with decreasing the conductivity from $MgCr_2O_4$, as presented in Figure 3-15 (d). The plotted points represent conductivity values after the apparent equilibration of the samples in air or reducing conditions (see Figure 5-1 and Figure 5-14).

a

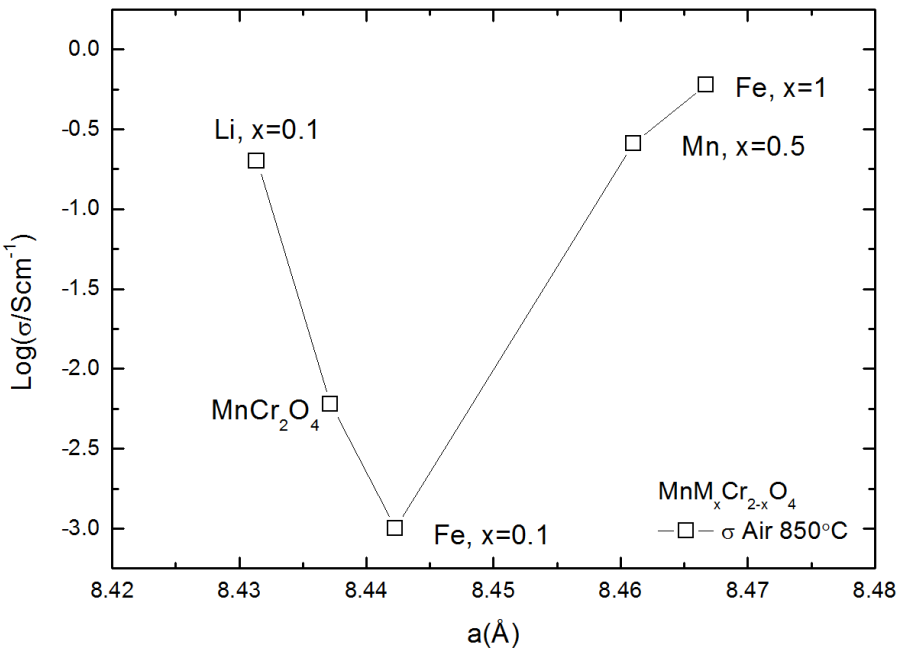

b

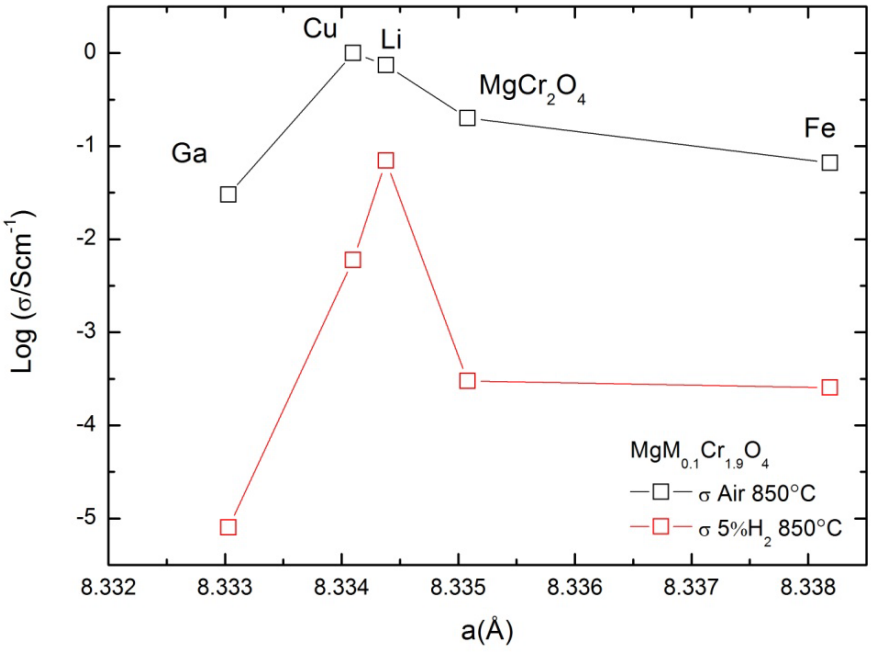
Cu
Li
MgCr2O4
Fe
Ga
Log (σ/Scm-1)
a(Å)
MgM0.1Cr1.9O4
σ Air 850°C
σ 5%H2 850°C

c

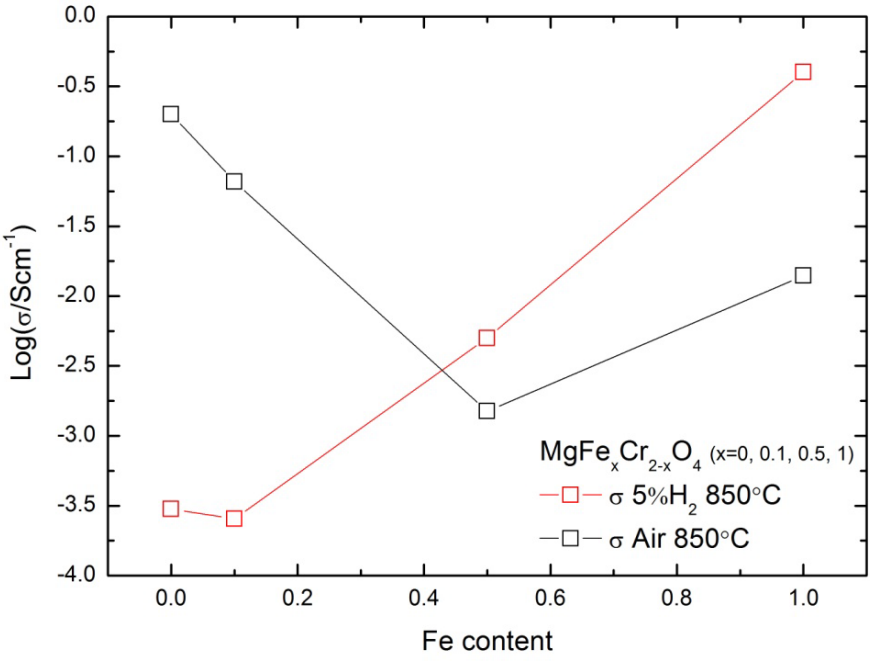
Log(σ/Scm-1)
Fe content
MgFexCr2-xO4 (x=0, 0.1, 0.5, 1)
σ 5%H2 850°C
σ Air 850°C

d

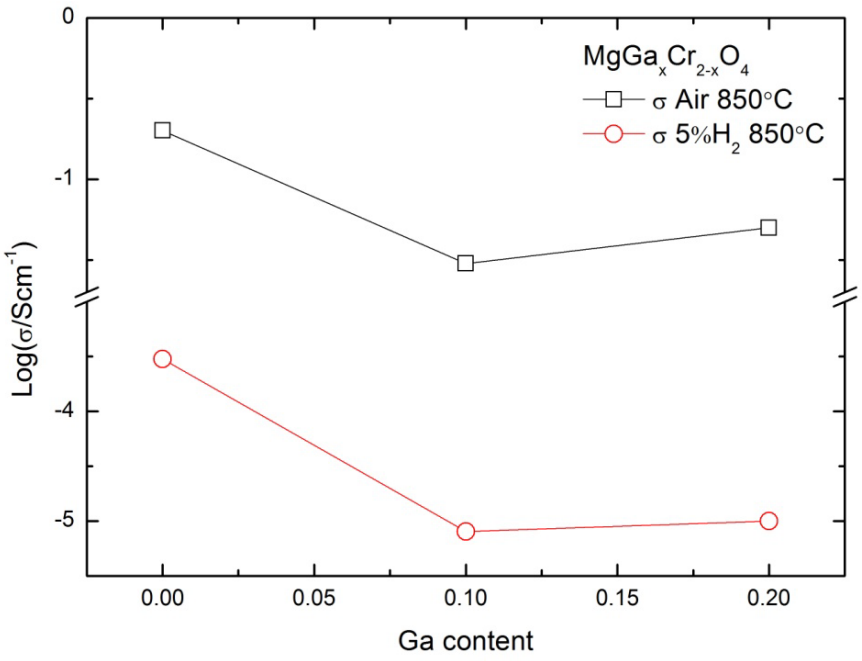

Figure 3-15 Log(σ) vs. a) cell parameter of $MnM_xCr_{2-x}O_4$; b) cell parameter of $MgM_{0.1}Cr_{1.9}O_4$; c) the Fe content of $MgFe_xCr_{2-x}O_4$; d) the Ga content of $MgGa_xCr_{2-x}O_4$ in air and reducing conditions at 850 °C.

Electrical conductivity measurements showed p-type conductivity, with a decrease of the conductivity in reducing conditions. Each considered substitution had the same p-type electronic conductivity as for $MnCr_2O_4$ and $MgCr_2O_4$, while $MnFeCrO_4$, $MgFeCrO_4$ and $Mg_{1.5}Ti_{0.5}CrO_4$ developed n-type conductivity in reducing conditions. Titanium containing samples showed n-type conductivity for low p_{O_2} and long reducing times, while Fe containing samples showed n-type conductivity for a higher amount of Fe content (x = 1) and the n-type response was almost instantaneous with switching the atmosphere from static air to 5%H_2/Ar. The apparently equilibrated data as a function of p_{O_2} is presented in Figure 3-16 for $MnCr_2O_4$, $Mg_{1.5}Ti_{0.5}CrO_4$ and $MgFeCrO_4$ (as discussed in section 1.5).

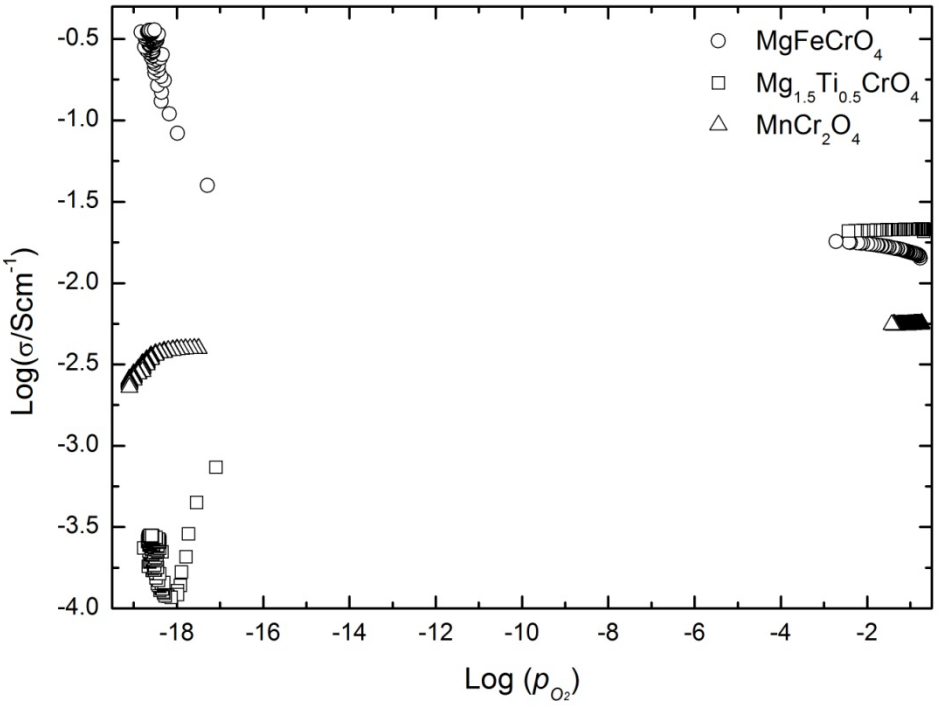

Figure 3-16 Evolution of electrical conductivity of $Mg_{1.5}Ti_{0.5}CrO_4$ and $MgFeCrO_4$ and $MnCr_2O_4$ in reducing conditions at 850 °C, with p-type conductivity of $MnCr_2O_4$ and n-type conductivity of $Mg_{1.5}Ti_{0.5}CrO_4$ and $MgFeCrO_4$.

The conductivity is influenced directly by the cation distribution in spinels. The conduction mechanism proposed for Cr^{3+} cations at B site (chapter 1 - section 1.5.3) anticipated that the reduction of these materials results in a decrease of the materials conductivity and this was confirmed by the experimental conductivity measurements. Substitution with Ga^{3+} on the B site facilitated the reduction of the spinel, with a more pronounced decrease of the electrical conductivity in fuel testing conditions, while substitutions with Cu^{2+} or Li^{+} would induce a higher charge for Cr cations with positive effects for the conductivity. The two spinel series $MgM_xCr_{2-x}O_4$, $MnM_xCr_{2-x}O_4$ had their electrical properties influenced positively by Fe substitution at the B site, increasing the conductivity when reduced. The phenomena was assumed to happen because of the formation of a conduction couple Fe^{2+}/Fe^{3+} resulting from the partial reduction of Fe^{3+} cations to Fe^{2+}, increasing the total number of charge carriers.

The variation of activation energy (E_a) values with temperature has been considered for two temperature domains resulting two E_a values for each spinel (see Figure 1-11), for low temperature range (100 to 450 °C) and for high temperature range

(450 to 850 °C). These E_a values were plotted vs. the cell parameter for $MgM_xCr_{2-x}O_4$ and $MnM_xCr_{2-x}O_4$. The plot illustrates that E_a decreased with increasing temperature for $MgM_xCr_{2-x}O_4$, while E_a increased with temperature for $MnM_xCr_{2-x}O_4$ and E_a generally increased with the unit cell. There are some exceptions from the linear trend for each spinel series and both are connected to the substitution of Cr with Fe on the B site. The samples and the corresponding activation energies represented in Figure 3-17 correspond to the unit cell parameters listed in Table 3-3.

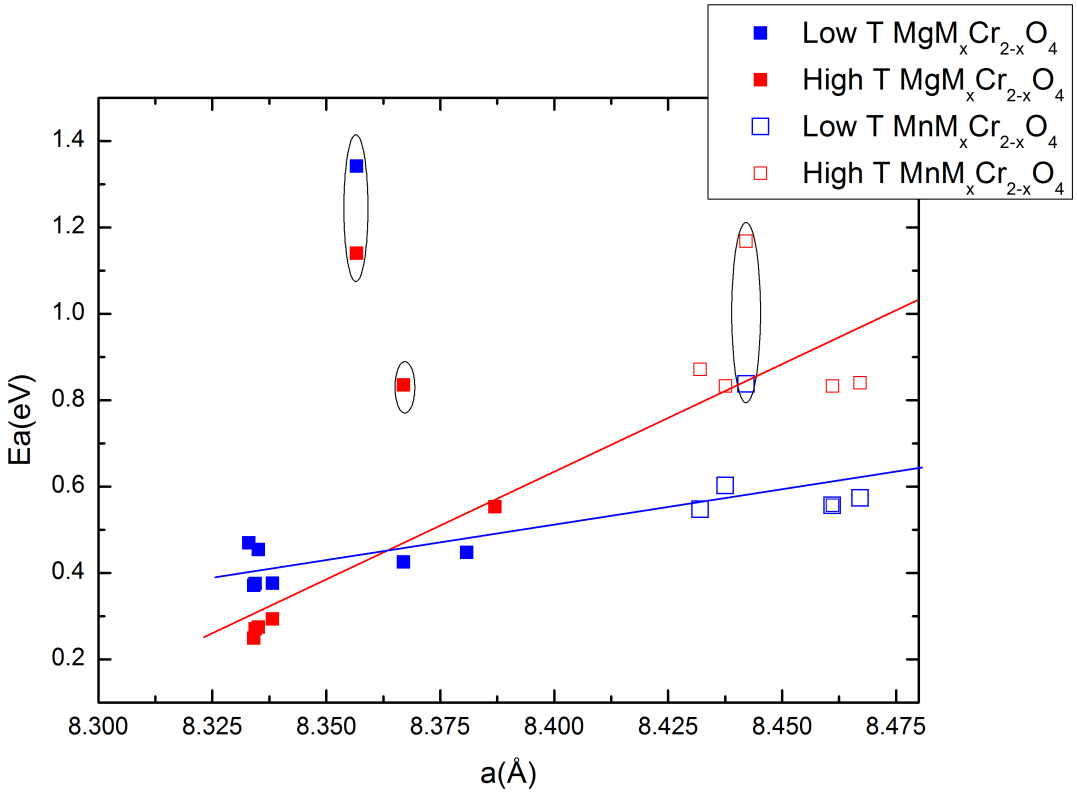

Figure 3-17 Activation energy dependence upon unit cell parameter and temperature in air of listed materials; the two marked positions correspond to $MgFe_{0.5}Cr_{1.5}O_4$ (full squares), $MgFeCrO_4$ (full square red) and $MnFe_{0.1}Cr_{1.9}O_4$ (empty squares).

3.5 Compatibility with yttrium stabilized zirconia

The mechanical and chemical compatibility of YSZ with spinels are limiting factors that would interfere with the application of a new material in SOFC tests. The mechanical and chemical compatibility of some spinels with YSZ were evaluated in terms of thermal expansion coefficient (TEC/K^{-1}), the sintering step and possible chemical reactions. The TEC was determined for several spinels and compared with

the YSZ thermal expansion coefficient ($10.5 \cdot 10^{-6}$ K^{-1}).[19] The determined values are listed in Table 3-5. TEC values were measured in air mostly for $MnM_xCr_{2-x}O_4$ spinels and for $MgCr_2O_4$, while in 5%H_2/Ar only the TEC values for $MnCr_2O_4$ and $MgCr_2O_4$ were measured.

Material	TEC(10^{-6} K^{-1})	
	Air	5%H_2/Ar
$MnCr_2O_4$	7.47	7.06
$MgMnCrO_4$	9.61	-
$MgCr_2O_4$	6.08	8.42
$MnFeCrO_4$	9.93	-
$MnFe_{0.1}Cr_{1.9}O_4$	9.57	-
$MgFeCrO_4$	7.43	-

Table 3-5.Thermal expansion coefficients between 100 and 900 °C.

The sintering step was determined on green ceramic bodies by measuring the shrinkage in one direction, dL/L_0 (%), for $MgCr_2O_4$, $MgCr_2O_4$/YSZ composite and for YSZ in the temperature range 30 to 1350 °C at a heating rate of 3 °C/min. The sintering of YSZ started at ~1060 °C, the main shrinkage step occurred at ~1300 °C and it was ~12.8% dL/L_0 (for a sample pre-sintered at 1000 °C/1h). For $MgCr_2O_4$ and $MgCr_2O_4$/YSZ composite the observed shrinkage was very small (1-2%) and the main sintering step occurred at ~1305 °C and 1280 °C, respectively (Figure 3-18).

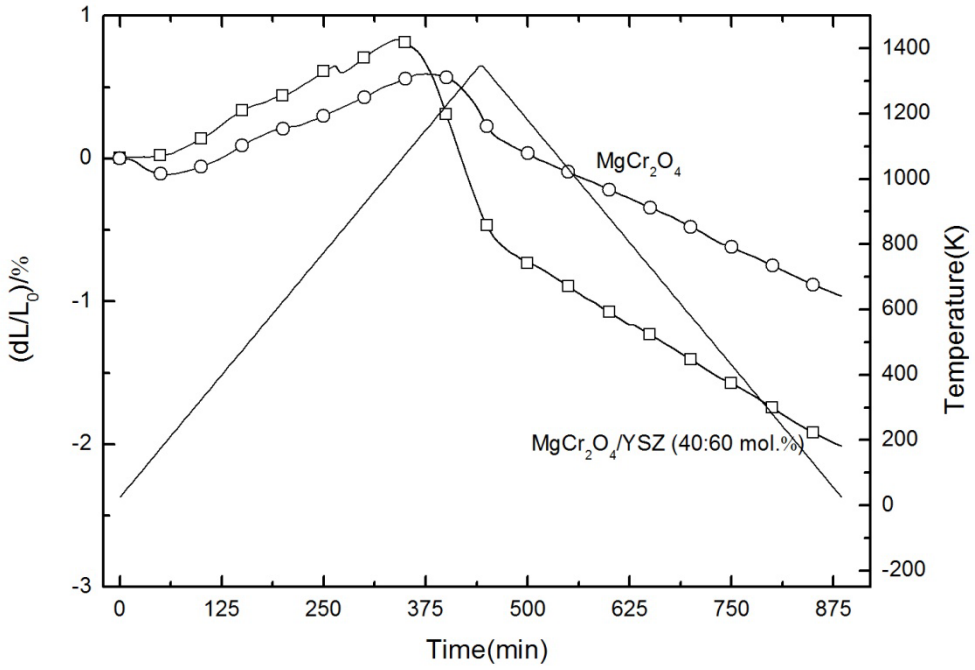

Figure 3-18 Sintering step determined for $MgCr_2O_4$, $MgCr_2O_4$/YSZ (40 : 60 mol.%) and YSZ at 1350 °C with dwell 15 minutes.

The sintering of YSZ started at again at ~1060 °C, the main shrinkage step occurred at ~1300 °C and it was ~17.8% .The sintering step for $MgFeCrO_4$ and $MnFeCrO_4$ was determined in the temperature range 30 to 1400 °C and the dwell time 1 hour, thus the results obtained for this set of compositions were more conclusive concerning the sintering behaviour: both spinels started their sintering step at about 1060 °C, similar with YSZ, but their sintering did not finish at 1400 °C. The materials continued to sinter during dwell time (~40 minutes) with final dL/L_0 variations of 6.3% for $MgFeCrO_4$ and ~7.5% for $MnFeCrO_4$, thus the sintering temperature of these spinels may be higher than 1400 °C (Figure 3-19). In conclusion, the final sintering temperature for spinels is higher than 1350 – 1400 °C and was not reached in present study. For sintering spinels at 1350-1400 °C, longer dwells are required.

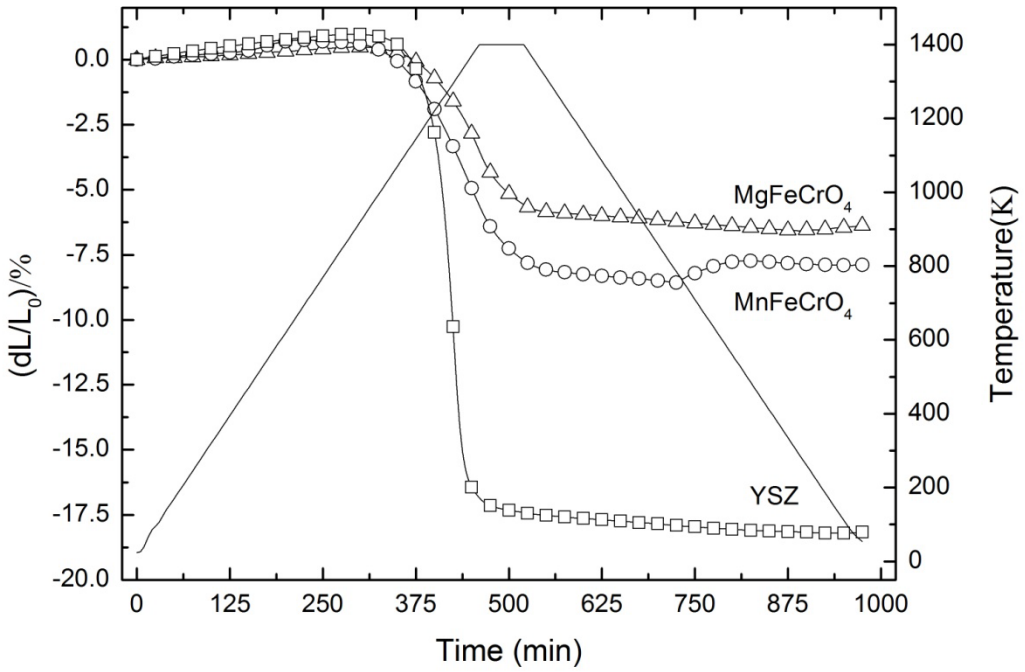

Figure 3-19 Sintering step for $MnFeCrO_4$, $MgFeCrO_4$ and YSZ at 1400 °C with 1 hour dwell.

The chemical compatibility of $MgMnCrO_4$, $MnFeCrO_4$ and $MgCr_2O_4$ with YSZ was tested by forming mixtures of spinel and YSZ (8 mol %) with ratio 1 : 1 (wt.), in an agate mortar. The mixtures of $MgMnCrO_4$, $MnFeCrO_4$ with YSZ were further homogenised by ball milling for 1.5 hours with acetone as milling solvent. The resultant powders were pressed into pellets and sintered at 1400 °C for 10 hours. Figure 3-20 and Figure 3-21 present the X-ray diffraction patterns for $MgCr_2O_4$/YSZ and $MnFeCrO_4$/YSZ sintered for 10 hours at 1400 °C, in comparison with the spinel XRD patterns. The comparison of the two patterns demonstrated that no solid state reaction occurred between YSZ and spinel, thus the two materials were found to be chemically stable. Micrographs of the samples confirmed the XRD results and also the mixing method, as the ball milled samples had a more uniform distribution of the two phases and they could also be distinguished as different phases. $MgCr_2O_4$/YSZ mixture was obtained in an agate mortar and further sintered as previously described, thus the spinel and YSZ are even more distinguishable in the micrograph (Figure 3-22 (b)). The micrographs of $MnFeCrO_4$/YSZ mixture illustrated the presence of two phases at lower magnification, for which more charging regions, associated with YSZ, and other non-charging regions were observed (Figure 3-22 (c, d)).

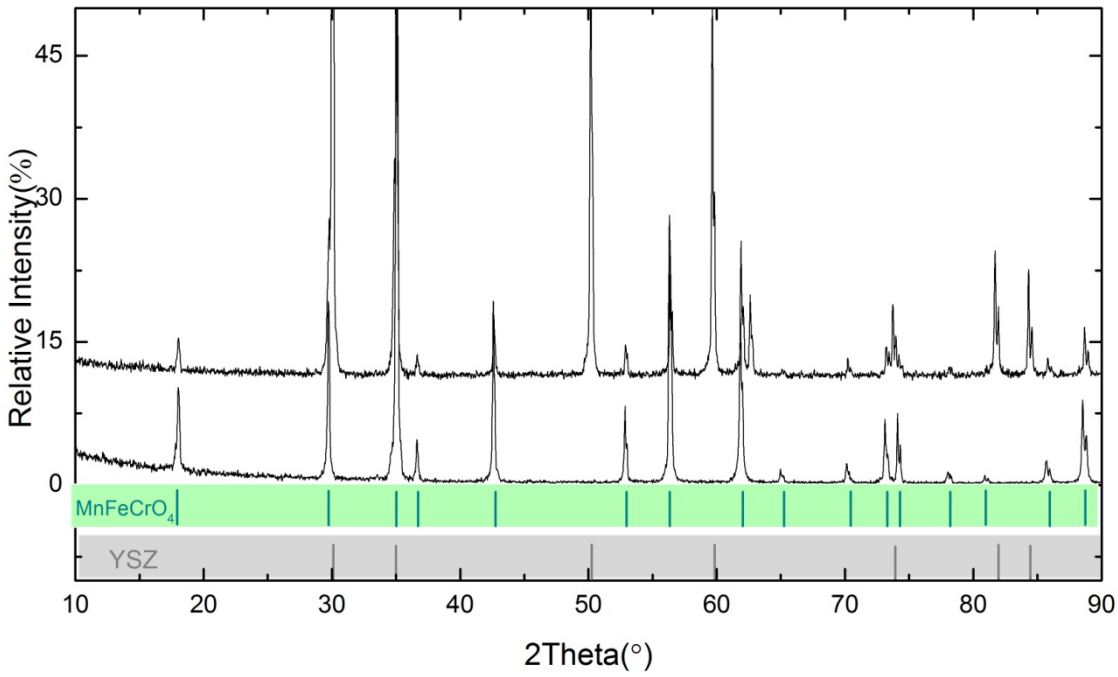

Figure 3-20 X-ray diffraction pattern of $MnFeCrO_4$ as synthesized and $MnFeCrO_4$/YSZ (1:1 wt.%) sintered at 1400 °C for 10 hours.

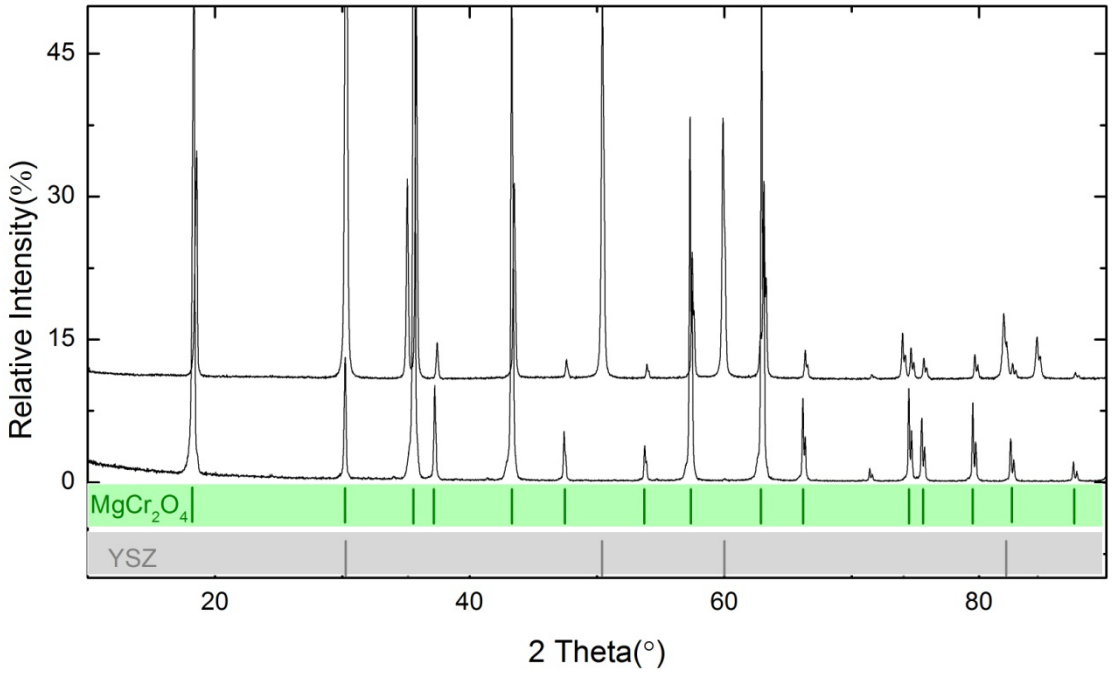

Figure 3-21 X-ray diffraction pattern of $MgCr_2O_4$ as synthesized and $MgCr_2O_4$/YSZ (1:1 wt.%) sintered at 1400 °C for 10 hours.

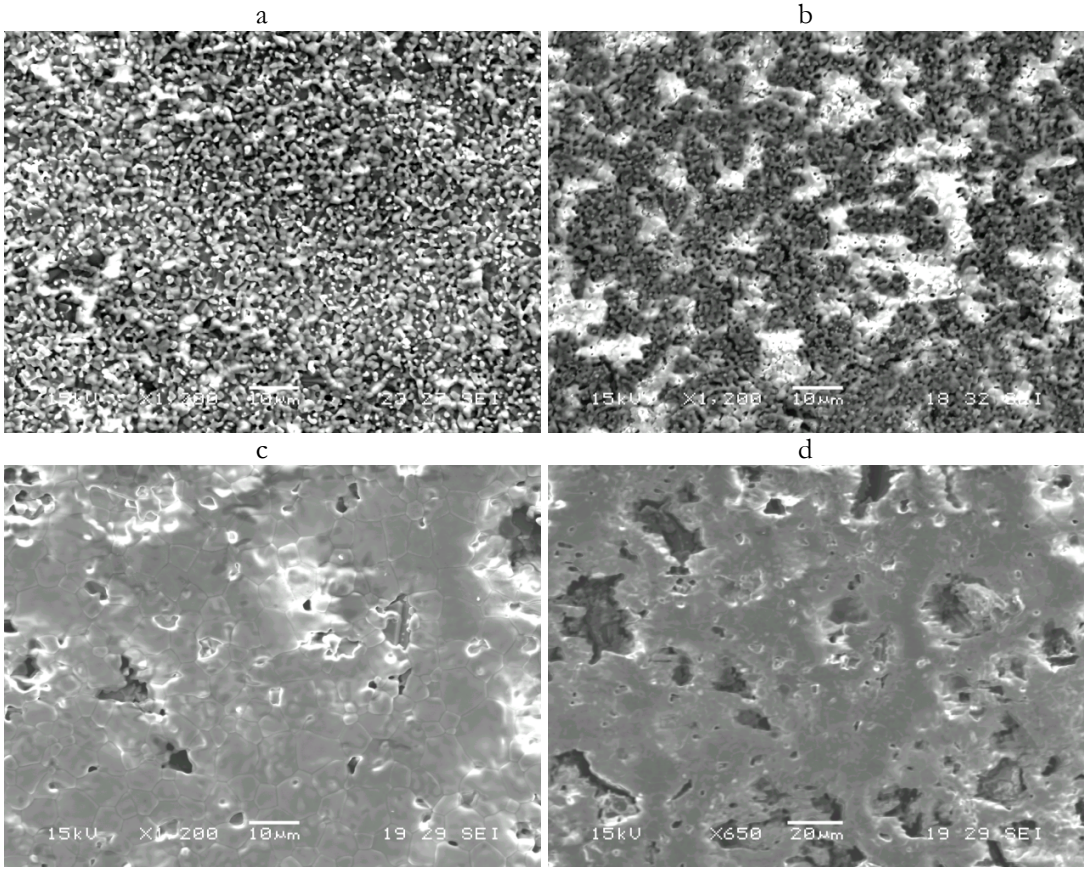

Figure 3-22 Micrographs of: a) $MgMnCrO_4$/YSZ; b) $MgCr_2O_4$/YSZ; c), d) $MnFeCrO_4$/YSZ mixtures after sintering at 1400 °C for 10 hours.

3.6 Conclusions

A large range of cation substitutions were successfully performed on $MnM_xCr_{2-x}O_4$ and $MgM_xCr_{2-x}O_4$ spinel oxides. $MnM_xCr_{2-x}O_4$ spinels showed low stability in reducing conditions, resulting in segregation of secondary phases. Among these oxides only $MnCr_2O_4$ showed good stability in reducing conditions (dry 5%H_2/Ar). However better results were obtained for milder reducing conditions (humidified 5%H_2/Ar and 1000 °C) in the case of $MnFeCrO_4$, which was of particular interest for proposed application. $MgM_xCr_{2-x}O_4$ series showed good stability upon reduction and only the samples with M = Fe (x = 0.1, 0.5, 1) decomposed when reduced in dry 5%H_2/Ar. Again their stability was improved for milder reducing conditions (humidified 5%H_2/Ar), particularly studied for $MgFeCrO_4$, as it was of interest. The interest for $MnFeCrO_4$ and $MgFeCrO_4$ was associated with the n-type conductivity

observed for these spinels in mild reducing conditions and the high content of Fe and Cr associated with ferritic steels composition.

The cation inversion determined from Rietveld refinement for $MgFe_xCr_{2-x}O_4$ was confirmed by their properties, as the conductivity in air decreased with the increase of Fe content and also the activation energy determined for these samples was high, as Mg^{2+} on B site does not participate in conduction.

Aliovalent and isovalent substitution determined changes into the conduction mechanism of chromium-rich spinels with positive effects for the conductivity in reducing conditions of $MgFeCrO_4$, which had n-type conductivity in reducing conditions due to partial reduction of Fe^{3+} cations to Fe^{2+} at B sites. Also $Mg_{1.5}Ti_{0.5}CrO_4$ had n-type conductivity in reducing conditions.

The charge compensation corresponding to the substitutions at B site with Li^+ and Cu^{2+} implied an increase of charge on Cr^{3+} cations, with the increase of the conductivity for $MgCu_{0.1}Cr_{1.9}O_4$, $MgLi_{0.1}Cr_{1.9}O_4$ and $MnLi_{0.1}Cr_{1.9}O_4$ both in air and reducing conditions. However their conductivity remained p-type.

Activation energies showed opposite tendencies for $MgM_xCr_{2-x}O_4$ and $MnM_xCr_{2-x}O_4$ series, with the unusual increase of the E_a values with temperature for $MnM_xCr_{2-x}O_4$.

The chemical compatibility tests between several spinels and YSZ demonstrated that no solid state reaction occurred, thus they could be processed into devices with adjacent layers spinel/YSZ.

3.7 References

1. Z. Lu, J. Zhu, E. Andrew Payzant, and M. P. Paranthaman, *J. Am. Cer. Soc.*, 2005, **88**, 1050–1053.
2. Sakai, T. Horita, Y. P. Xiong, K. Yamaji, H. Kishimoto, M. E. Brito, H. Yokokawa, and T. Maruyama, *Solid State Ionics*, 2005, **176**, 681–686.
3. A. Petric and H. Ling, *J. Am. Cer. Soc.*, 2007, **90**, 1515–1520.
4. X. Chen, P. Y. Hou, C. P. Jacobson, S. J. Visco, D. Jonghe, and L. C, 2004.
5. F. F. Fava, I. Baraille, A. Lichanot, C. Larrieu, and R. Dovesi, *J. Phys. Condens. Mat.*, 1997, **9**, 10715.
6. S. Wang, X. Liu, Y. Fei, Q. He, and H. Wang, *Phys. Chem. Miner.*, 2012, **39**, 189–198.
7. G. C. Allen and M. Paul, *Appl. Spectrosc.*, 1995, **49**, 451–458.
8. H. Moriwake, I. Tanaka, F. Oba, and H. Adachi, *Jpn. J. Appl. Phys.*, 2000, **39**, 513–516.
9. H. Moriwake, I. Tanaka, F. Oba, Y. Koyama, and H. Adachi, *Int. J. Quantum Chem.*, 2003, **91**, 208–210.
10. H. Moriwake, S. Watanabe, and K. Ogasawara, *Jpn. J. Appl. Phys.*, 2007, **46**, 4175–4178.
11. L. Morozova and V. Popov, *Glass Phys. Chem+*, 2010, **36**, 86–91.
12. R. J. Hilleard, *J. Phys. C Solid State*, 1975, **8**, L193.
13. L. Ortega-San-Martin, *J. Phys. Condens. Mat.*, 2008, **20**, 104238.
14. D. Lenaz, H. Skogby, F. Princivalle, and U. Hålenius, *Phys. Chem. Miner.*, 2004, **31**, 633–642.
15. V. S. Stubican and C. Greskovich, *J. Am. Cer. Soc.*, 1966, **49**, 518–518.
16. A. M. Alper, R. N. McNally, R. C. Doman, and F. G. Keihn, *J. Am. Cer. Soc.*, 1964, **47**, 30–33.
17. T. Yokoyama and T. Meguro, *Jpn. J. Appl. Phys.*, 2005, **44**, 6201–6203.
18. T. Suzuki, K. Adachi, and T. Katsufuji, *J. Magn. Magn. Mater.*, 2007, **310**, 780–781.
19. H. Yakabe, Y. Baba, T. Sakurai, and Y. Yoshitaka, *J. Power Sources*, 2004, **135**, 9 – 16.

Chapter 4

Contents

4 Studies on $LiTiCrO_4$ and related oxide spinels 105
4.1 Introduction 105
4.2 Spinel - ramsdellite phase transition temperature 105
4.2.1 Characterization of quenched materials 106
4.3 Structural characterization of non-quenched materials 114
4.4 Chemical stability in reducing conditions 119
4.5 Electrical properties 120
4.6 Conclusions 122
4.7 References 123

4 Studies on $LiTiCrO_4$ and related oxide spinels

4.1 Introduction

Lithium titanates, known in spinel and ramsdellite form, are generally studied as anode materials for lithium batteries.[1–3] $LiTiCrO_4$ has spinel structure stable up to 950 °C, in which Li is located at the tetrahedral 8a sites and transition metal ions, Cr^{3+} and Ti^{4+} are located at the octahedral 16d sites in a cubic close-packed oxygen array, space group Fd-3m.[4,5] The phase transformation spinel – ramsdellite for $LiTiCrO_4$ starts above 950 °C, is complete at 1250 °C[4] and is influenced by the presence of other cations at the B site, *e.g.* Cr. When Cr is replaced by other cation M, the phase transition temperature changes because the M metal determines the degree of inversion in the spinel and this is a key factor of controlling the transformation.

Khun *et al.*[6] estimated the transformation temperature ~ 900 °C for $LiTiCrO_4$ (normal spinel) from enthalpy calculations. When other cations than Cr were substituted at B site, for a higher degree of inversion in the spinel structure, they estimated much higher temperature for the transformation, confirmed by their experimental results. In this chapter are discussed the results concerning the structural analysis of $LiTiCrO_4$ in spinel form and the approached strategy to increase the temperature of phase transformation spinel – ramsdellite, with the purpose of new materials development (chapter 1 − section 1.7).

4.2 Spinel - ramsdellite phase transition temperature

The phase transition temperature was increased by simultaneous substitutions on the A and B sites, as follows: new compositions were formulated, formally considered as spinel solid solutions in the systems $MgCr_2O_4$ – $LiCrTiO_4$, Mg_2TiO_4 – $LiCrTiO_4$ and Mg_2TiO_4 – $LiCrTiO_4$ – $MgFeCrO_4$. $LiCrTiO_4$, $Li_{0.9}Mg_{0.1}Cr_{1.1}Ti_{0.9}O_4$, $Li_{0.9}Mg_{0.2}Cr_{0.9}TiO_4$, $Li_{0.85}Mg_{0.3}Cr_{0.85}TiO_4$, $Li_{0.8}Mg_{0.3}Cr_{0.9}Ti_{0.9}Fe_{0.1}O_4$ and $Li_{0.7}Mg_{0.4}Cr_{0.9}Ti_{0.8}Fe_{0.2}O_4$ were synthesized by solid state reaction and found to form single phase spinels up to temperatures of 900 – 1300 °C, as illustrated in Figure 4-1.

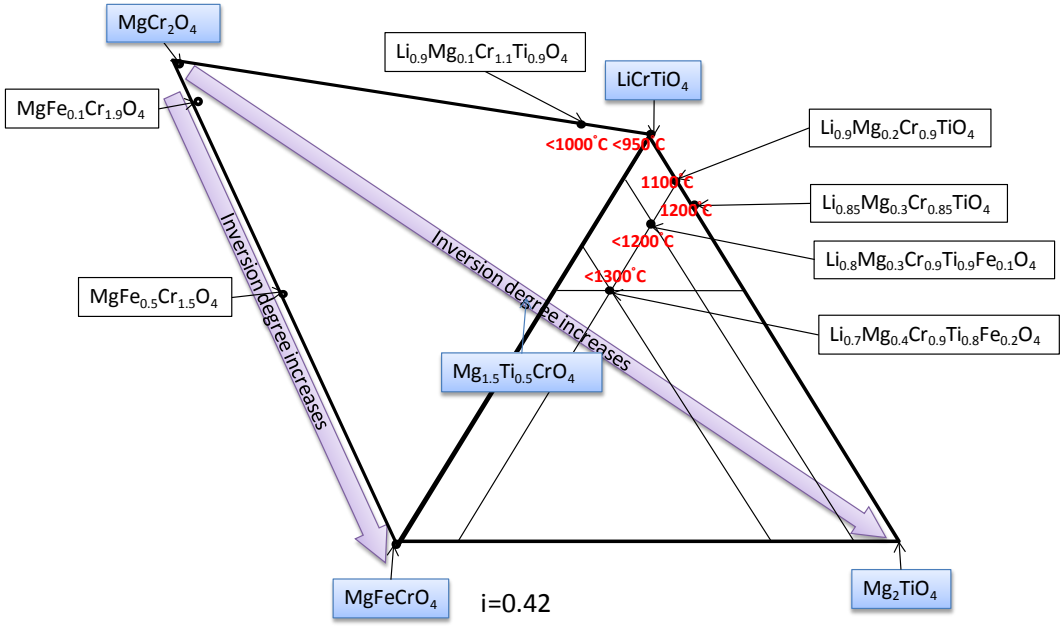

Figure 4-1 Schematic representation of studied oxides spinels with determined temperatures of phase transition spinel – ramsdellite. i = 0.42 represents the inversion degree determined of $MgFeCrO_4$ (chapter 3)

The incipient stage of phase transition for synthesized materials was determined from X-ray diffraction patterns for samples sintered at different temperatures (900 – 1300 °C) and quenched by removing the samples from the furnace at high temperatures.

4.2.1 Characterization of quenched materials

The characterization of the materials summarizes mostly, the structure analysis and the approximate temperature of phase transition initiation, as the purpose of this study was to increase the stability of spinel phase at elevated temperatures. The structural analysis, described by cell parameter values, a (Å), oxygen parameter, u (Å), and distribution of the cations amongst tetrahedral and octahedral sites were determined based on the Rietveld refinement of the XRD diffraction patterns.

Full pattern fitting of spinel oxides was refined using the Fullprof software, as described in Appendix 1. The space group considered was Fd-3m (Z = 8) with origin at -3m and positions 8a (¼, ¼, ¼), 16d (½, ½, ½) and 32e (u, u, u) for the cations on A, B sites and for oxygen anions, respectively. The refined parameters were scale factor, background polynomial parameters, peaks profile parameters u, v, w and η

(Lorentzian/Gaussian distribution), unit cell parameters, atomic positions, site occupancies and isotropic displacement factors (B factor). Because of low scattering factor of lithium ion, the B factor for A sites was fixed to B = 0.5, while the B factor for 16d cations and oxygen were refined (as reported in ref [7]).

Refinement plots for quenched samples are illustrated below with observed intensities represented with red dots, calculated intensities with black line and the difference between calculated and observed intensities is given as blue line.

In the refined pattern for $LiTiCrO_4$, quenched from 950 °C to room temperature (Figure 4-2), only reflections for spinel were identified. $LiTiCrO_4$ had lattice parameter a = 8.3141(1) Å, oxygen parameter u = 0.2624(2) Å and unit cell volume V = 574.70(1) $Å^3$. Values of other refined parameters are listed in Table 3-1. When higher temperature than 950 °C was used (*e.g.* 1000 °C), peaks corresponding to ramsdellite phase demonstrated the initiation of the spinel - ramsdellite phase transformation. These reflections were present in the XRD patterns even for samples cooled slowly to room temperature.

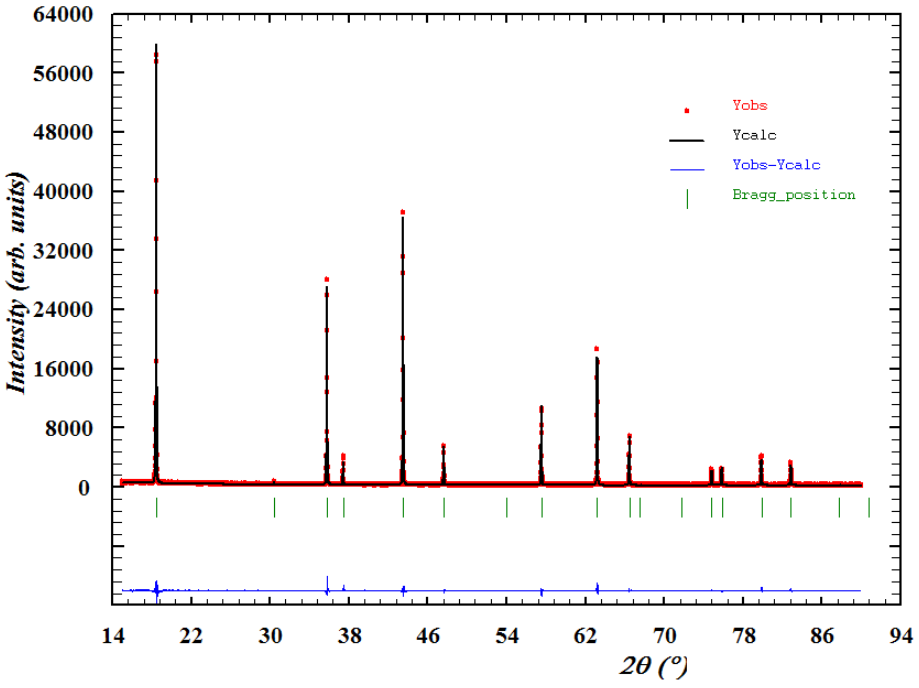

Figure 4-2 Rietveld refinement profiles of $LiTiCrO_4$ quenched from 950 °C to room temperature; Observed data are represented with red dots, calculated profile with black line and difference profile with blue line.

XRD patterns of $Li_{0.8}Mg_{0.3}Cr_{0.9}Ti_{0.9}Fe_{0.1}O_4$ quenched from 1200 °C and $Li_{0.7}Mg_{0.4}Cr_{0.9}Ti_{0.8}Fe_{0.2}O_4$ quenched from 1300 °C to room temperature, showed pure phase spinels, which demonstrates that substitution towards higher degree of inversion increased the stability of the spinel at higher temperatures.

Rietveld refinement shows that $Li_{0.8}Mg_{0.3}Cr_{0.9}Ti_{0.9}Fe_{0.1}O_4$ had lattice parameter a = 8.34072(5) Å, oxygen parameter u = 0.2630(2) Å and unit cell volume V = 580.244(6) $Å^3$. $Li_{0.7}Mg_{0.4}Cr_{0.9}Ti_{0.8}Fe_{0.2}O_4$ had lattice parameter a = 8.3494(1) Å, oxygen parameter u = 0.2607(2) Å and unit cell volume V = 582.06(2) $Å^3$. The refinement plots are illustrated in Figure 4-3 and Figure 4-4 and the values of refined parameters are listed in Table 4-1. The reliability factors demonstrate the good quality of the refinements. Inversion between A and B sites was considered and refined between Li^+ and Fe^{3+} and the cation distributions considered are included in Table 4-3.

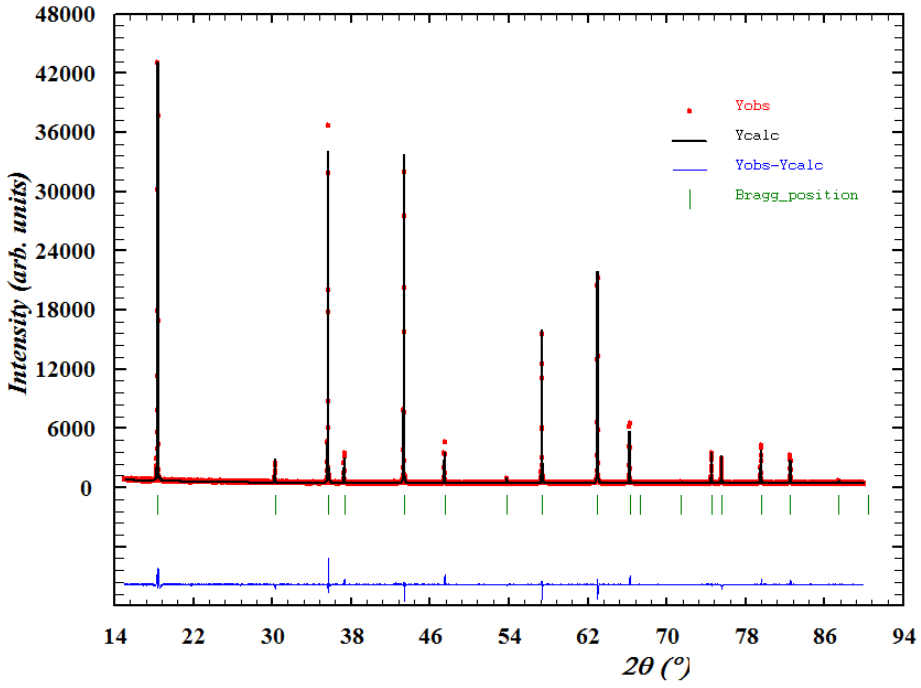

Figure 4-3 Rietveld refinement profiles of $Li_{0.8}Mg_{0.3}Cr_{0.9}Ti_{0.9}Fe_{0.1}O_4$ quenched from 1200 °C to room temperature. Observed data are represented with red dots, calculated profile with black line and difference profile with blue line.

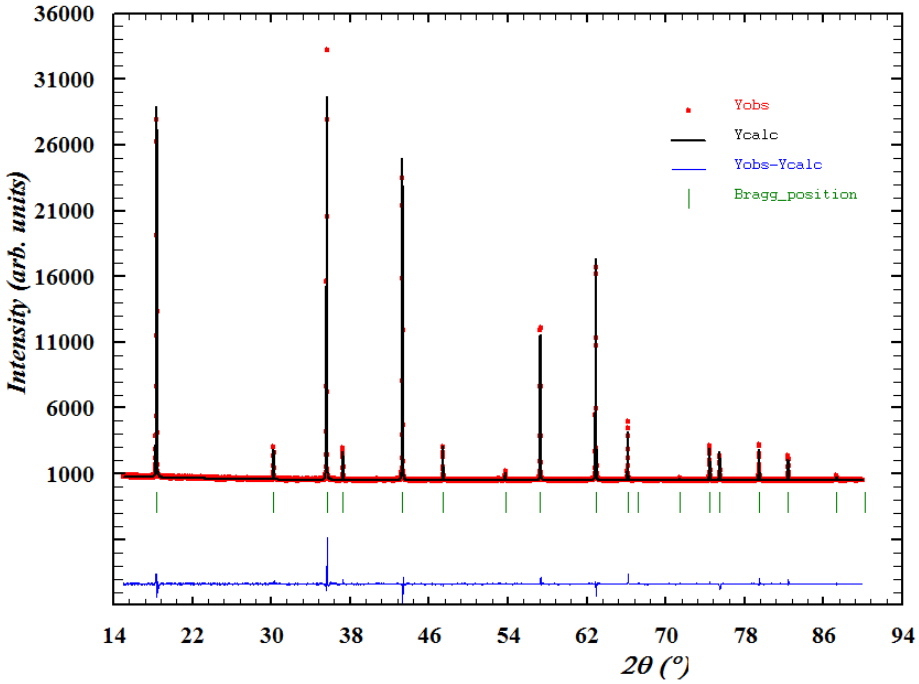

Figure 4-4 Rietveld refinement profiles of $Li_{0.7}Mg_{0.4}Cr_{0.9}Ti_{0.8}Fe_{0.2}O_4$ quenched from 1300 °C to room temperature. Observed data are represented with red dots, calculated profile with black line and difference profile with blue line.

Refinement parameter	$LiTiCrO_4$	$Li_{0.8}Mg_{0.3}Cr_{0.9}Ti_{0.9}Fe_{0.1}O_4$	$Li_{0.7}Mg_{0.4}Cr_{0.9}Ti_{0.8}Fe_{0.2}O_4$
a (Å)	8.3141(1)	8.34072(5)	8.3494(1)
u (Å)	0.2624(2)	0.2630(2)	0.2601(2)
V (Å^3)	574.70(1)	580.244(6)	582.06(2)
R_p	4.94	4.52	4.08
R_{wp}	6.96	6.29	5.40
R_{exp}	4.49	4.03	3.90
χ^2	2.41	2.44	1.92

Table 4-1 Parameters resulted from refinement of $LiTiCrO_4$, $Li_{0.8}Mg_{0.3}Cr_{0.9}Ti_{0.9}Fe_{0.1}O_4$ and $Li_{0.7}Mg_{0.4}Cr_{0.9}Ti_{0.8}Fe_{0.2}O_4$ XRD patterns and refinement reliability factors.

XRD patterns of $Li_{0.9}Mg_{0.2}Cr_{0.9}TiO_4$ quenched from 1100 °C to room temperature and $Li_{0.85}Mg_{0.3}Cr_{0.85}TiO_4$ quenched from 1200 °C demonstrated the co-existence of ramsdellite and spinel, with 1.5 wt.% and 2 wt.% of ramsdellite evaluated from Rietveld refinement. These results indicated the approximate temperature of phase transition initial stage.

The orthorhombic ramsdellite phase was refined in the space group Pbnm (Z = 2). The structure consists of edge-sharing [MO_6] octahedra, further linked by sharing corners and edges in an open 3D-structure with Li atoms occupying the channel space.[4] In Figure 4-5 is represented the ramsdellite structure for $LiTiCrO_4$ as described above. The cation occupancy considered was similar to the one reported for $LiTiCrO_4$ in ref [4].

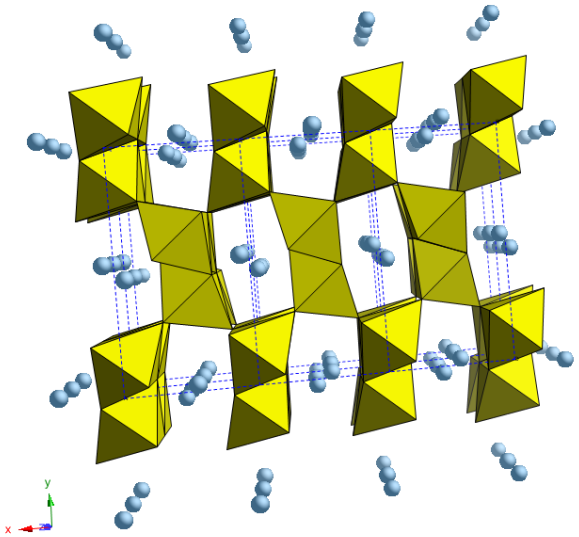

Figure 4-5 Ramsdellite structure of $LiTiCrO_4$ represented with polyhedral model; with yellow are represented the Cr/Ti octahedra and with blue, the Li cations located in the channels.

$Li_{0.9}Mg_{0.2}Cr_{0.9}TiO_4$ spinel (Figure 4-6) had lattice parameter a = 8.33118(3) Å, oxygen parameter u = 0.2638(1) Å and unit cell volume V = 578.257(4) $Å^3$, while the ramsdellite had lattice parameters a = 4.9933(3) Å, b = 9.537(1) Å, c = 2.9370(1) Å and unit cell volume V = 139.86(3) $Å^3$.

$Li_{0.85}Mg_{0.3}Cr_{0.85}TiO_4$ spinel (had lattice parameter a = 8.34034(3) Å, oxygen parameter u = 0.2632(1) Å and unit cell volume V = 580.165(4) $Å^3$, while the ramsdellite had lattice parameters a = 4.9937(3) Å, b = 9.5447(6) Å, c = 2.9383(2) Å and unit cell volume V = 140.05(2) $Å^3$. The values of refined parameters are shown in Table 4-2.

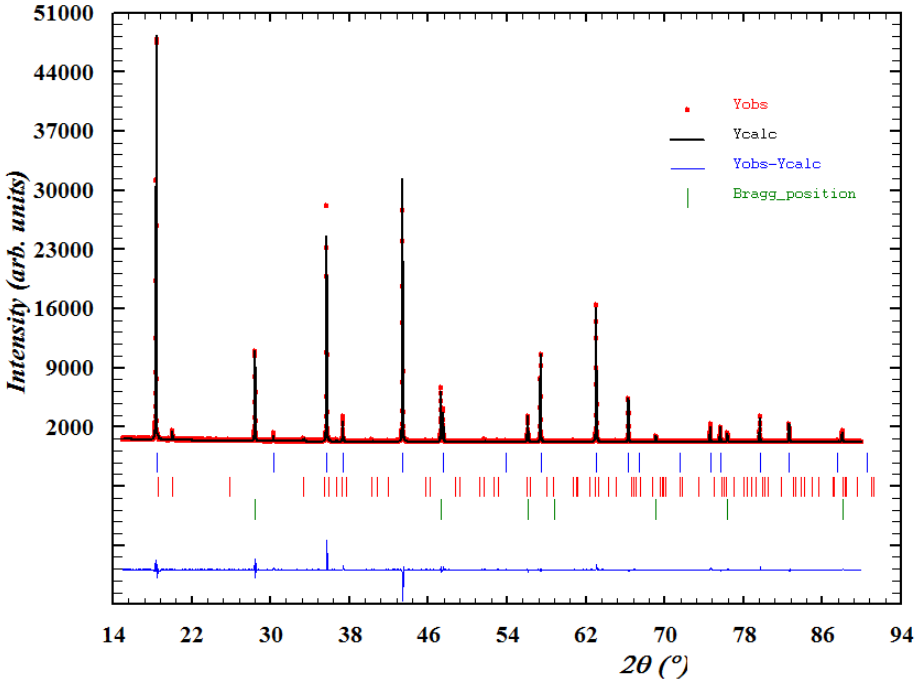

Figure 4-6 Rietveld refinement profiles of $Li_{0.9}Mg_{0.2}Cr_{0.9}TiO_4$ quenched from 1100 °C to room temperature. The pattern contains reflections corresponding to spinel (Bragg positions marked with blue) and ramsdellite (Bragg positions marked with red) forms of the material. The third phase is internal standard Si (green Bragg positions). Observed data are represented with red dots, calculated profile with black line and difference profile with blue line.

Refinement parameter	$Li_{0.9}Mg_{0.2}Cr_{0.9}TiO_4$	$Li_{0.9}Mg_{0.1}Cr_{1.1}Ti_{0.9}O_4$*	$Li_{0.85}Mg_{0.3}Cr_{0.85}TiO_4$
Spinel			
a (Å)	8.33118(3)	8.31810(7)	8.34034(3)
u (Å)	0.263891)	0.2615(3)	0.2632(1)
V (Å^3)	578.257(4)	575.53	580.165(4)
Ramsdellite			
a (Å)	4.9933(3)	4.9908(6)	4.9937(3)
b (Å)	9.537(1)	9.529(3)	9.5447(6)
c (Å)	2.9370(1)	2.9335(5)	2.9383(2)
V (Å^3)	139.86(3)	139.51(3)	140.05(2)
R_p	6.00	10.6	6.30
R_{wp}	8.13	15.3	8.55
R_{exp}	4.65	9.47	4.99
χ^2	3.05	2.62	2.93

Table 4-2 Parameters resulted from refinement of XRD data for $Li_{0.9}Mg_{0.2}Cr_{0.9}TiO_4$ quenched from 1100°C, $Li_{0.9}Mg_{0.1}Cr_{1.1}Ti_{0.9}O_4$ quenched from 1100°C and $Li_{0.85}Mg_{0.3}Cr_{0.85}TiO_4$ quenched from 1200 °C and refinement reliability factors; (*) - dataset collected on Philips diffractometer.

When quenched from 1100 °C to room temperature, the XRD pattern of $Li_{0.9}Mg_{0.1}Cr_{1.1}Ti_{0.9}O_4$ demonstrated the presence of spinel ~ 94.5 wt.% and ramsdellite

~5.5 wt.%. $Li_{0.9}Mg_{0.1}Cr_{1.1}Ti_{0.9}O_4$ spinel had lattice parameter a = 8.31810(7) Å, oxygen parameter u = 0.2615(3) Å and unit cell volume V = 575.534(8) $Å^3$, while the ramsdellite had lattice parameters a = 4.9908(6) Å, b = 9.529(3) Å, c = 2.9335(5) Å and unit cell volume V = 139.51(3) $Å^3$. The cation distribution resulted from Rietveld refinement is summarised in Table 4-3.

Composition	Cation Distribution	
	(td)	(oh)
$LiTiCrO_4$	(Li)	(TiCr)
$Li_{0.7}Mg_{0.4}Cr_{0.9}Ti_{0.8}Fe_{0.2}O_4$	$(Li_{0.6}Mg_{0.3}Fe_{0.1})$	$(Li_{0.1}Mg_{0.1}Cr_{0.9}Ti_{0.8}Fe_{0.1})$
$Li_{0.8}Mg_{0.3}Cr_{0.9}Ti_{0.9}Fe_{0.1}O_4$	$(Li_{0.7}Mg_{0.2}Fe_{0.1})$	$(Li_{0.1}Mg_{0.1}Cr_{0.9}Ti_{0.9})$

Table 4-3 Cation distribution determined from the Rietveld refinement for quenched oxides, as described above. Only the samples found to be pure spinels are listed.

The micrographs of the quenched samples, presented in Figure 4-7, demonstrated the presence of ramsdellite secondary phase for $Li_{0.9}Mg_{0.1}Cr_{1.1}Ti_{0.9}O_4$ and $Li_{0.85}Mg_{0.3}Cr_{0.85}TiO_4$ with change in particles shape when ramsdellite formed, from particles described by definite crystalline faces and edges to rod type particles. The micrograph of $Li_{0.85}Mg_{0.3}Cr_{0.85}TiO_4$ quenched from 1200 °C also shows very important densification of the sample. For $Li_{0.9}Mg_{0.2}Cr_{0.9}TiO_4$, the particle size increased and two types of particles are distinguishable, without forming rod type particles. The magnification scale was chosen to be representative for different microstructures.

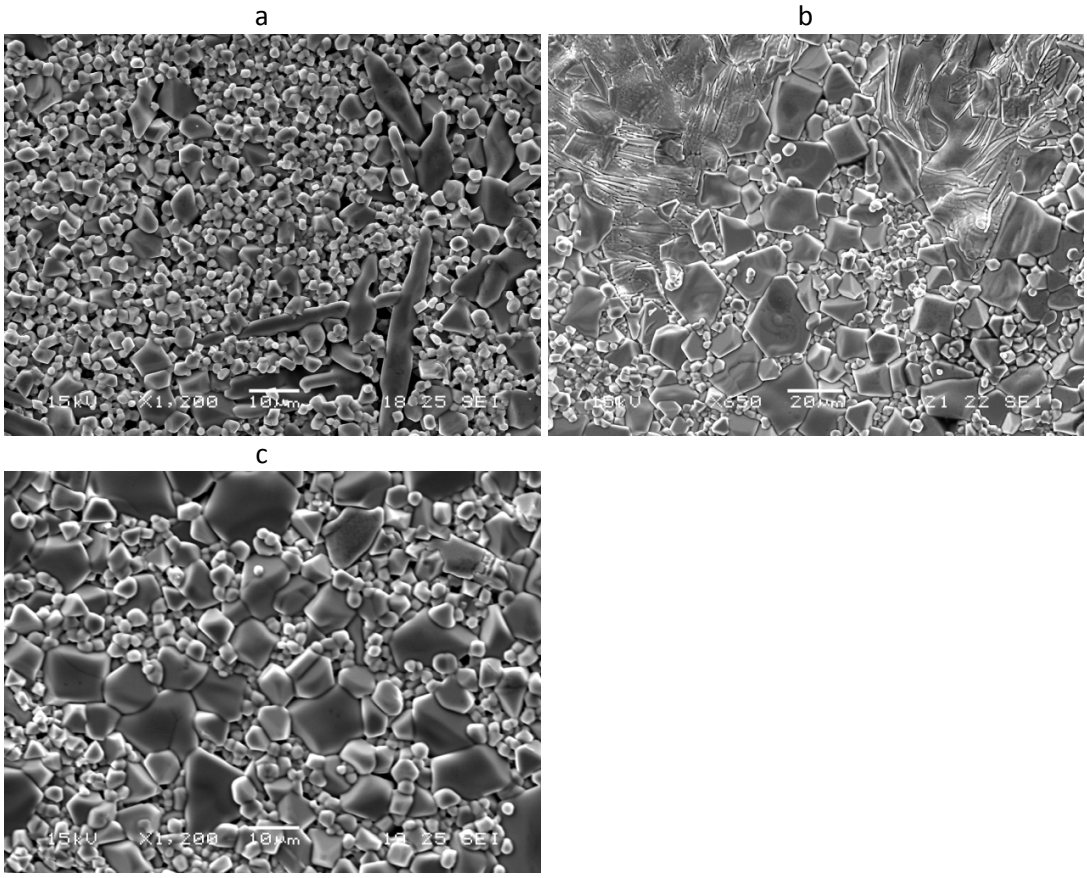

Figure 4-7 Micrographs of : a) $Li_{0.9}Mg_{0.1}Cr_{1.1}Ti_{0.9}O_4$ quenched from 1100 °C; b) $Li_{0.85}Mg_{0.3}Cr_{0.85}TiO_4$ quenched from 1200 °C; c) $Li_{0.9}Mg_{0.2}Cr_{0.9}TiO_4$ quenched from 1100 °C to room temperature.

Results from structure and phase analysis of quenched spinels proved that the approached strategy for increasing the stability of spinel phase at higher temperatures was successful. As the possibility of inversion between A and B sites in the spinel increased, also the temperature at which spinel structure was stable also increased. $Li_{0.9}Mg_{0.1}Cr_{1.1}Ti_{0.9}O_4$ was formally considered as a solid solution of $LiCrTiO_4 : MgCr_2O_4$ (9 : 1), both normal spinels and resulted in a transition temperature above 1000 °C (Figure 4-1). When spinel solid solutions were considered for spinels with higher degree of inversion (e.g. Mg_2TiO_4), the phase transition temperature, thus the stability of the spinel structure increased. $Li_{0.9}Mg_{0.2}Cr_{0.9}TiO_4$ considered as solid solution of $LiCrTiO_4 : Mg_2TiO_4$ (9 : 1) and $Li_{0.85}Mg_{0.3}Cr_{0.85}TiO_4$, as solid solution of $LiCrTiO_4 : Mg_2TiO_4$ (8.5 : 1.5), only developed ~1.5 wt.% and ~2 wt.% of ramsdellite when quenched from 1100 °C and 1200 °C, respectively.

The ramsdellite phases formed and characterised after quenching $Li_{0.9}Mg_{0.1}Cr_{1.1}Ti_{0.9}O_4$, $Li_{0.9}Mg_{0.2}Cr_{0.9}TiO_4$ and $Li_{0.85}Mg_{0.3}Cr_{0.85}TiO_4$ were different, as the determined cell parameters were different, mostly on b axis (Table 4-2), thus it was considered that each ramsdellite composition was identical with the initial spinel. Also the cell parameters of the spinel phases sintered at different temperatures and for the quenched (Q) samples did not show important differences that would indicate a different composition of the spinel at high temperature (Figure 4-8). In the next sub-section is discussed the structural analysis of spinel oxides sintered below the phase transition temperatures.

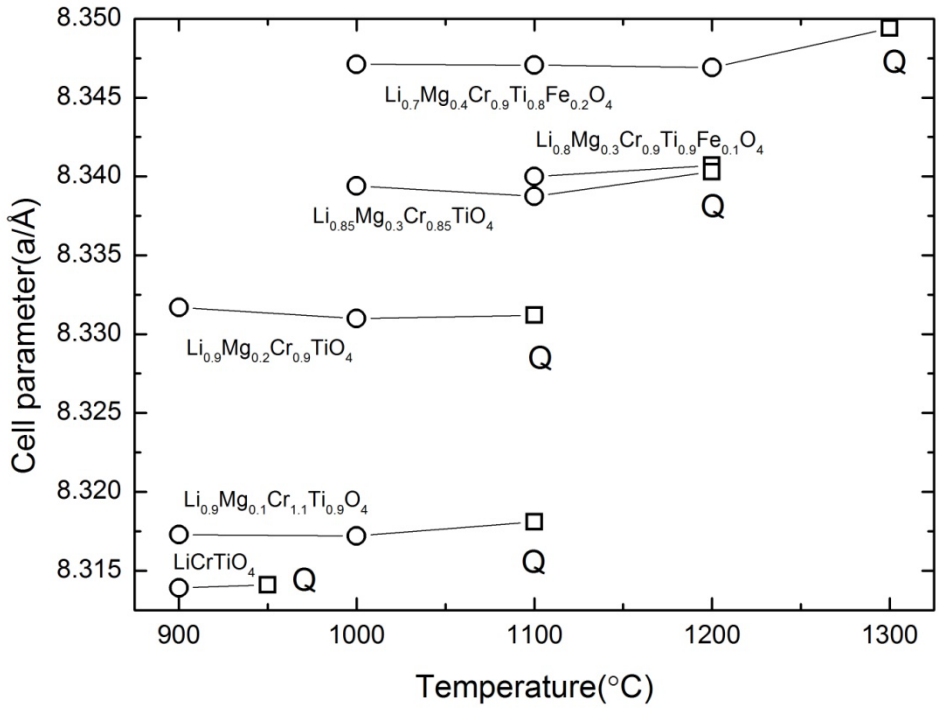

Figure 4-8 Cell parameter vs. sintering temperature for 5 °C/min heating-cooling rate (represented as open circle) and quenched samples (represented as open square).

4.3 Structural characterization of non-quenched materials

The spinel oxides with stable spinel structure were sintered at different temperatures below the phase transformation (1000 °C, 1100 °C, 1200 °C), cooled at 5 °C/min to room temperature and their structure analysed. Although the Li cations are not distinguished by X-ray diffraction, the remaining cation distribution could be obtained from Rietveld refinement structure model. The cation distribution

determined from the model is summarised in Table 4-4, along with a and u refined values. The unit cell parameter was plotted vs. the average ionic radii of B sites and a linear trend was observed (Figure 4-9), which indicated that cation distributions resulted from Rietveld refinement were well approximated, although in the refinement it was not accounted for charge compensation effects or possible cation and anion vacancies forming. For a better evaluation of the defect chemistry present in the analysed spinels, Equation 3-1 was used to compare the position of refined u parameters with respect to their calculated position, as illustrated in Figure 4-10. Observed differences between refined and calculated u values may denote migration of lithium cations from tetrahedral (8a) site to octahedral (16c) site[1,7] resulting in a miscalculation of the average ionic radii. The possibility of forming Li vacancies at A sites resulted after Li volatilisation could also be accounted for, but this phenomena is not much mentioned in literature, when similar sintering conditions are reported (temperature and sintering atmosphere).[4,6]

Composition	Temp (°C)	Cation Distribution		a (Å)	u (Å)
		(td)	(oh)		
$LiTiCrO_4$	900	(Li)	(TiCr)	8.31390(6)	0.2617(1)
$Li_{0.9}Mg_{0.1}Cr_{1.1}Ti_{0.9}O_4$	900	$(Li_{0.9}Mg_{0.1})$	$(Cr_{1.1}Ti_{0.9})$	8.3173(1)	0.2625(1)
	1000	$(Li_{0.9}Mg_{0.1})$	$(Cr_{1.1}Ti_{0.9})$	8.31718(4)	0.2617(3)
$Li_{0.9}Mg_{0.2}Cr_{0.9}TiO_4$	900	$(Li_{0.9}Mg_{0.1})$	$(Mg_{0.1}Cr_{0.9}Ti)$	8.33173(4)	0.2606(2)
	1000	$(Li_{0.9}Mg_{0.1})$	$(Mg_{0.1}Cr_{0.9}Ti)$	8.3310(1)	0.2612(2)
$Li_{0.85}Mg_{0.3}Cr_{0.85}TiO_4$	1000	$(Li_{0.75}Mg_{0.25})$	$(Li_{0.1}Mg_{0.05}Cr_{0.85}Ti)$	8.33934(3)	0.2617(2)
	1100	$(Li_{0.75}Mg_{0.25})$	$(Li_{0.1}Mg_{0.05}Cr_{0.85}Ti)$	8.33875(4)	0.2643(2)
$Li_{0.7}Mg_{0.4}Cr_{0.9}Ti_{0.8}Fe_{0.2}O_4$	1000	$(Li_{0.633}Mg_{0.3}Fe_{0.067})$	$(Li_{0.067}Mg_{0.1}Fe_{0.133}Cr_{0.9}Ti_{0.8})$	8.34711(3)	0.2606(2)
	1100	$(Li_{0.626}Mg_{0.3}Fe_{0.074})$	$(Li_{0.074}Mg_{0.1}Fe_{0.126}Cr_{0.9}Ti_{0.8})$	8.34706(4)	0.2633(2)
	1200	$(Li_{0.61}Mg_{0.3}Fe_{0.09})$	$(Li_{0.09}Mg_{0.1}Fe_{0.11}Cr_{0.9}Ti_{0.8})$	8.34690(2)	0.2624(2)
$Li_{0.8}Mg_{0.3}Cr_{0.9}Ti_{0.9}Fe_{0.1}O_4$	1100	$(Li_{0.76}Mg_{0.2}Fe_{0.04})$	$(Li_{0.04}Mg_{0.1}Fe_{0.06}Cr_{0.9}Ti_{0.9})$	8.33996(3)	0.2616(2)

Table 4-4 Cation distribution, a and u determined from the Rietveld refinement for stable spinel oxides cooled slowly to room temperature.

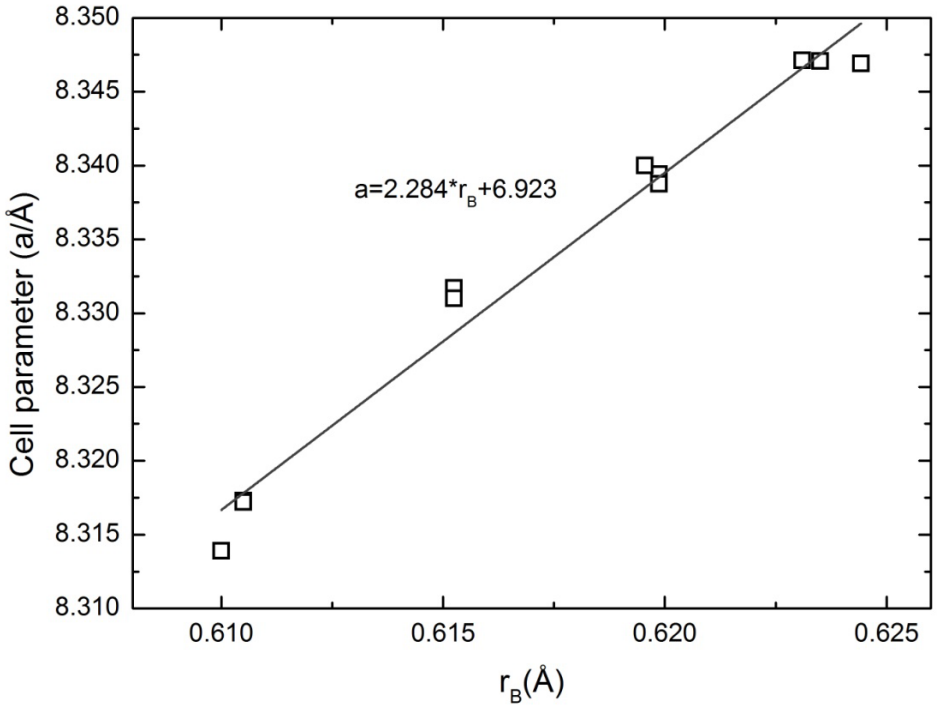

Figure 4-9 The evolution of the cell parameter with the average ionic radii for B sites; (grey line – guiding lines for linear trend)

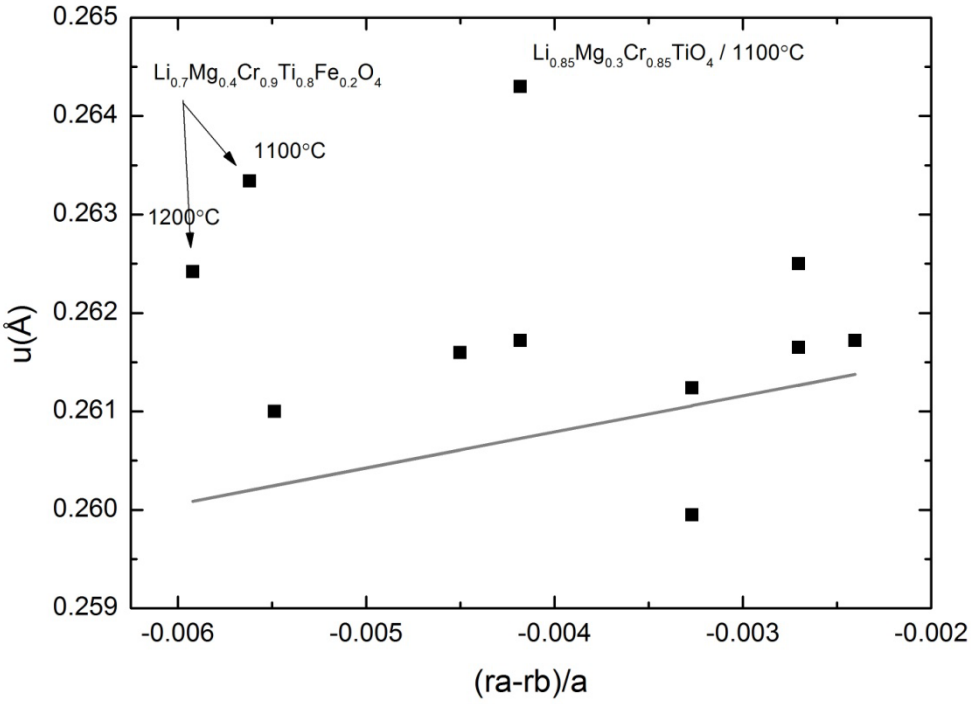

Figure 4-10 Variation of refined u parameter with (r_A-r_B)/a based on Equation 3-1,[8] where r_A and r_B are average ionic radii resulted from the considered cation distribution.

The spinel microstructure could be characterised as highly porous when samples were sintered at 900 °C and 1000 °C, with particles described by definite crystalline faces and edges. Figure 4-11 (a, b, c) illustrates the microstructures of $Li_{0.9}Mg_{0.2}Cr_{0.9}TiO_4$, $Li_{0.9}Mg_{0.1}Cr_{1.1}Ti_{0.9}O_4$, and $Li_{0.85}Mg_{0.3}Cr_{0.85}TiO_4$ sintered at 1000 °C for 12 hours, that generally showed a uni-modal distribution of particles, with particle size of 1-7 μm. For higher sintering temperatures, the increase of particle size was significant e.g. for $Li_{0.85}Mg_{0.3}Cr_{0.85}TiO_4$ when sintered at 1100 °C in comparison with the sample sintered at 1000 °C (Figure 4-11 (c, d)).

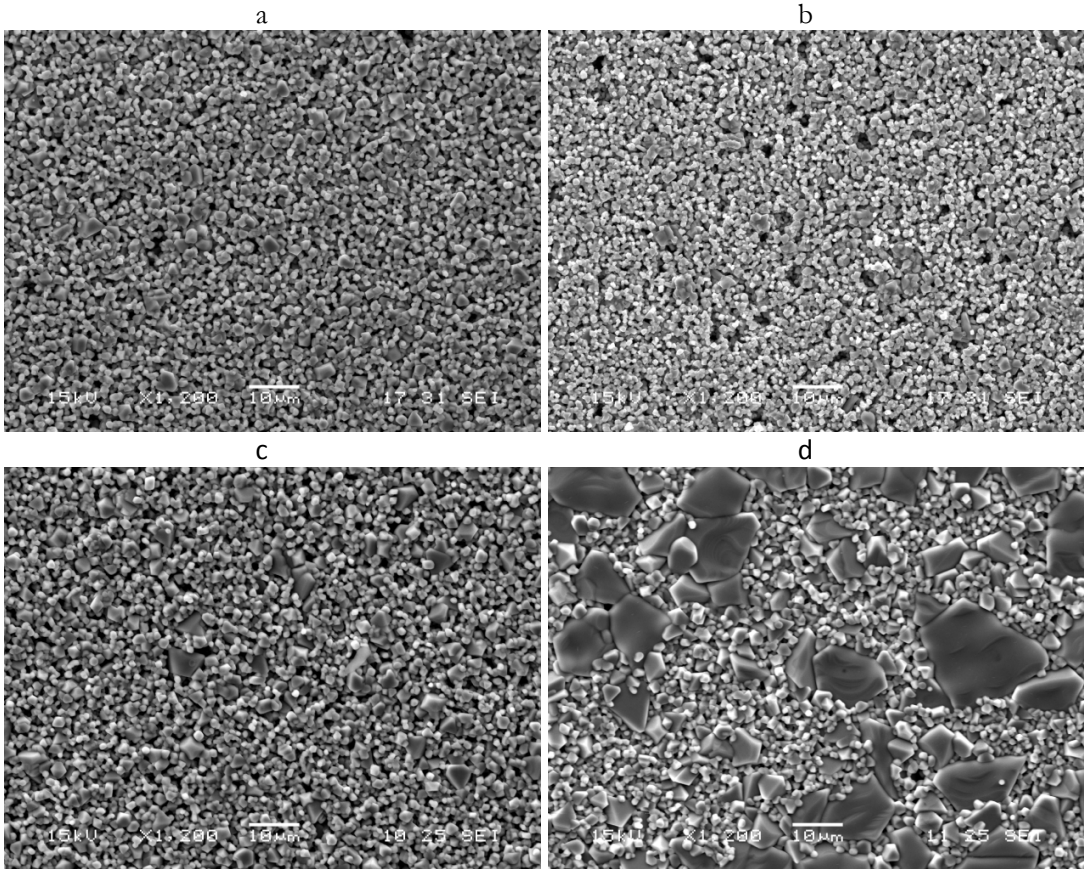

Figure 4-11 Micrographs of a) $Li_{0.9}Mg_{0.2}Cr_{0.9}TiO_4$; b) $Li_{0.9}Mg_{0.1}Cr_{1.1}Ti_{0.9}O_4$; c) $Li_{0.85}Mg_{0.3}Cr_{0.85}TiO_4$ sintered at 1000 °C for 12 hours and d) $Li_{0.85}Mg_{0.3}Cr_{0.85}TiO_4$ sintered at 1100 °C for 12 hours in air.

As described for $Li_{0.85}Mg_{0.3}Cr_{0.85}TiO_4$, similar observations are valid for $Li_{0.7}Mg_{0.4}Cr_{0.9}Ti_{0.8}Fe_{0.2}O_4$ microstructures at different temperatures. Figure 4-12 (a, b, c) illustrates the micrographs of the samples sintered at 1000 °C, 1100 °C and 1200 °C. When sintered at 1000 °C the spinel was porous and characterised by uni-modal particle distribution with particle size of 1-7 μm. At 1100 °C a better

densification of the sample was observed and the particles increased up to 20 μm, showing a wider range of particle size between 1-20 μm. When sintered at 1200 °C, $Li_{0.7}Mg_{0.4}Cr_{0.9}Ti_{0.8}Fe_{0.2}O_4$ was highly dense with particles described by definite crystalline faces and edges, specific for spinels with particle size between 5-20 μm. The micrograph of $Li_{0.8}Mg_{0.3}Cr_{0.9}Ti_{0.9}Fe_{0.1}O_4$ sintered at 1100 °C was similar with the micrograph of $Li_{0.7}Mg_{0.4}Cr_{0.9}Ti_{0.8}Fe_{0.2}O_4$ at 1100 °C, only with slightly smaller particle size of 1-15 μm.

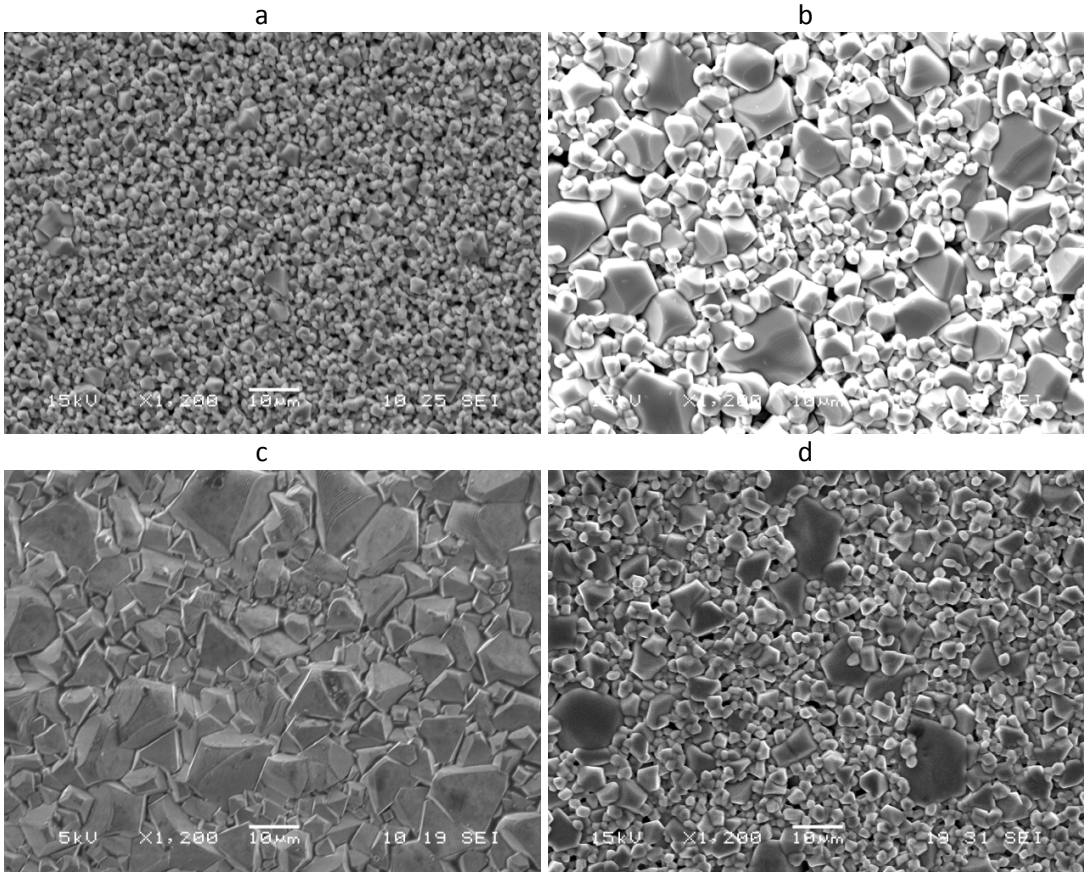

Figure 4-12 Micrographs of: a) $Li_{0.7}Mg_{0.4}Cr_{0.9}Ti_{0.8}Fe_{0.2}O_4$ sintered at 1000 °C; b) $Li_{0.7}Mg_{0.4}Cr_{0.9}Ti_{0.8}Fe_{0.2}O_4$ sintered at 1100 °C; c) $Li_{0.7}Mg_{0.4}Cr_{0.9}Ti_{0.8}Fe_{0.2}O_4$ sintered at 1200 °C; d) $Li_{0.8}Mg_{0.3}Cr_{0.9}Ti_{0.9}Fe_{0.1}O_4$ sintered at 1100 °C for 12 hours in air.

4.4 Chemical stability in reducing conditions

Ceramic bodies sintered at 900-1300 °C were reduced for 20 hours as described in chapter 2 - section 2.6 and the influence of the reduction was evaluated by X-ray diffraction analysis and Scanning Electron Microscopy. The reduction tests were made at 1000 °C for 20 hours in 5%H_2/Ar.

X-ray diffraction analysis on reduced samples demonstrated good stability in reducing conditions (dry 5%H_2/Ar) for $LiTiCrO_4$, $Li_{0.9}Mg_{0.1}Cr_{1.1}Ti_{0.9}O_4$, $Li_{0.9}Mg_{0.2}Cr_{0.9}TiO_4$ and $Li_{0.85}Mg_{0.3}Cr_{0.85}TiO_4$ without formation of secondary phases, as the component cations are mostly at their lowest valence state and stable in the spinel structure.

The samples containing Fe, $Li_{0.7}Mg_{0.4}Cr_{0.9}Ti_{0.8}Fe_{0.2}O_4$ and $Li_{0.8}Mg_{0.3}Cr_{0.9}Ti_{0.9}Fe_{0.1}O_4$ decomposed in reducing environment with the formation of metallic Fe as secondary phase.

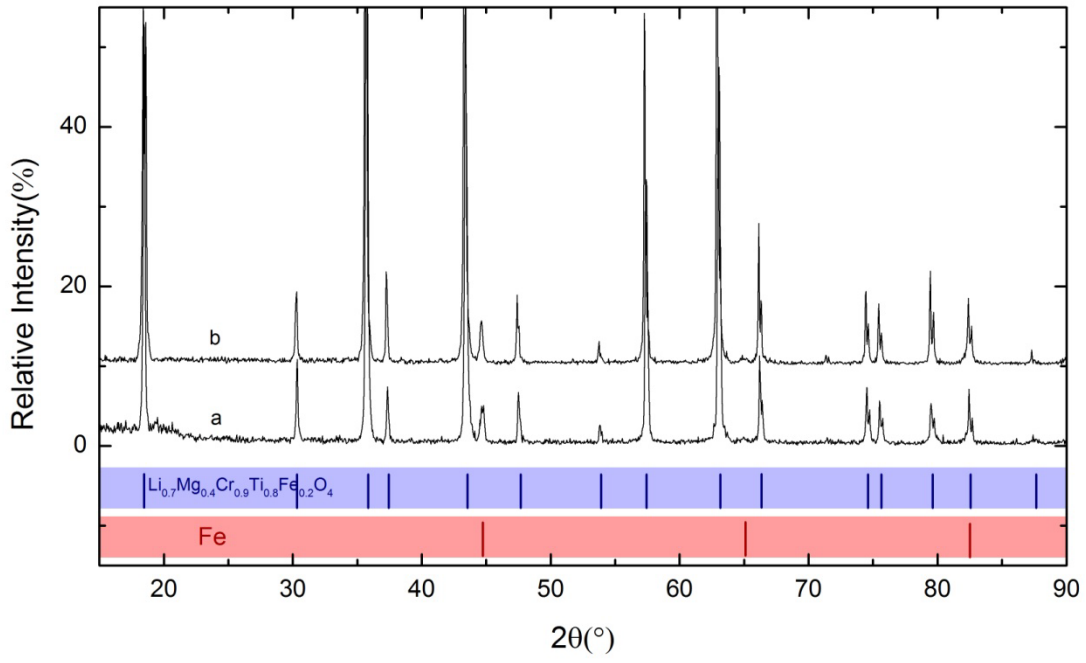

Figure 4-13 X-ray diffraction pattern of $Li_{0.7}Mg_{0.4}Cr_{0.9}Ti_{0.8}Fe_{0.2}O_4$ sintered at: a) 1100 °C and b) 1200 °C and reduced in dry 5%H_2/Ar at 1000 °C for 20 hours.

Figure 4-13 illustrates the XRD patterns of $Li_{0.7}Mg_{0.4}Cr_{0.9}Ti_{0.8}Fe_{0.2}O_4$ sintered at 1100 °C and 1200 °C and reduced with marked peak positions for spinel and metallic

Fe. As previously found for $MgFeCrO_4$ and $MnFeCrO_4$, it is expected that metallic Fe would not segregate in milder reducing conditions than dry 5%H_2/Ar.

4.5 Electrical properties

Electrical conductivity measurements were conducted on porous ceramic bodies. The total electrical (ionic/electronic) conductivity was measured in air, in temperature range 150 – 800 °C, by the four point method for $Li_{0.9}Mg_{0.2}Cr_{0.9}TiO_4$ sintered at 1000 °C, $Li_{0.85}Mg_{0.3}Cr_{0.85}TiO_4$ sintered at 1100 °C and 1200 °C, and $Li_{0.7}Mg_{0.4}Cr_{0.9}Ti_{0.8}Fe_{0.2}O_4$ sintered at 1100 °C. Electrical conductivity was also determined in 5%H_2/Ar at constant temperature, as a function of p_{O_2} and as a function of temperature (150-800 °C) for $Li_{0.85}Mg_{0.3}Cr_{0.85}TiO_4$ sintered at 1100 °C and 1200 °C and for $Li_{0.7}Mg_{0.4}Cr_{0.9}Ti_{0.8}Fe_{0.2}O_4$ sintered at 1100 °C. The materials had semiconducting type behaviour, as the conductivity increased with temperature.

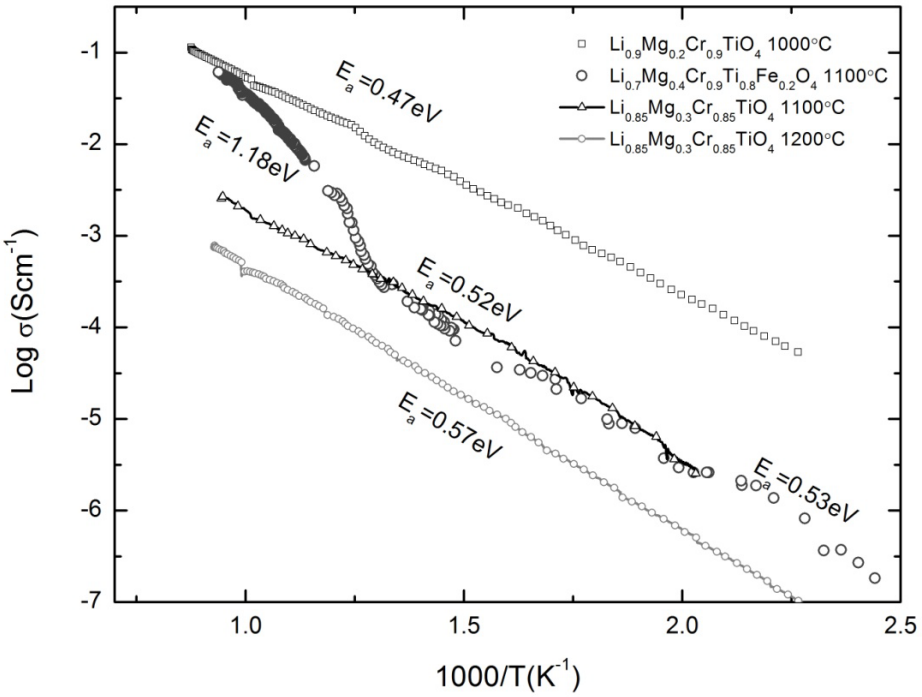

Figure 4-14 Arrhenius plots measured in air of $Li_{0.9}Mg_{0.2}Cr_{0.9}TiO_4$/1000 °C, $Li_{0.85}Mg_{0.3}Cr_{0.85}TiO_4$/1100 °C, $Li_{0.85}Mg_{0.3}Cr_{0.85}TiO_4$/1200 °C and $Li_{0.7}Mg_{0.4}Cr_{0.9}Ti_{0.8}Fe_{0.2}O_4$/1100 °C in temperature range 150 – 800 °C.

Figure 4-14 illustrates the Arrhenius plots for the samples measured in air and corresponding E_a values. $Li_{0.7}Mg_{0.4}Cr_{0.9}Ti_{0.8}Fe_{0.2}O_4$ showed a slope change at 450 °C

that resulted in increasing the E_a from 0.53 eV to 1.18 eV, that may have been caused by a change in charge carrier concentration. E_a values of $Li_{0.9}Mg_{0.2}Cr_{0.9}TiO_4$ and $Li_{0.85}Mg_{0.3}Cr_{0.85}TiO_4$ were in range 0.47-0.57 eV, without any slope change in temperature range 150-800 °C. When reduced, the materials showed much lower E_a values and again, slope change for $Li_{0.7}Mg_{0.4}Cr_{0.9}Ti_{0.8}Fe_{0.2}O_4$ at ~ 485 °C from 0.47 eV to 0.64 eV (Figure 4-15).

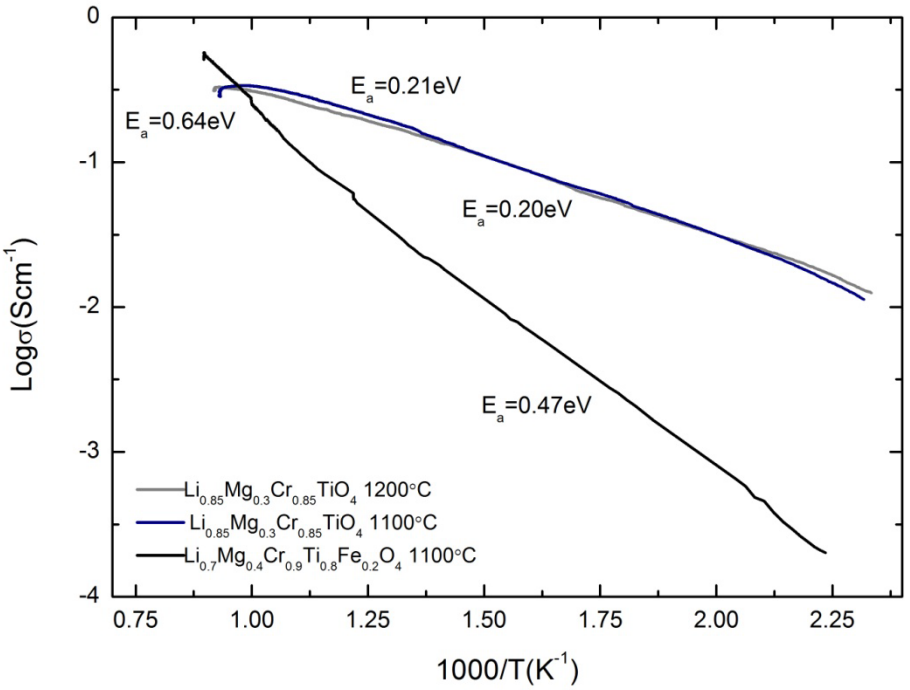

Figure 4-15 Arrhenius plots measured in 5%H_2/Ar of $Li_{0.85}Mg_{0.3}Cr_{0.85}TiO_4$/1100 °C, $Li_{0.85}Mg_{0.3}Cr_{0.85}TiO_4$/1200 °C and $Li_{0.7}Mg_{0.4}Cr_{0.9}Ti_{0.8}Fe_{0.2}O_4$/1100 °C in temperature range 180 – 800 °C.

Nakayama *et al.*[7] reported mixed ionic-electronic conduction for spinel solid solutions (1-x) $Li_{4/3}Ti_{5/3}O_4$ – x $LiCrTiO_4$, for x > 0.6 with an increase in conductivity towards $LiCrTiO_4$. Spinel oxides investigated in this work had the starting point in $LiCrTiO_4$, which was found to be mixed ionic electronic conductor,[7] and new compositions were developed as solid solutions with other electronic conducting spinels, thus is was considered that the conduction mechanism was dominated by electronic conductivity for these materials. The total conductivity was studied in reducing conditions at constant temperature for $LiCrTiO_4$ sintered at 900 °C, $Li_{0.9}Mg_{0.2}Cr_{0.9}TiO_4$ sintered at 1000 °C and $Li_{0.7}Mg_{0.4}Cr_{0.9}Ti_{0.8}Fe_{0.2}O_4$ sintered at

1100 °C. Figure 4-16 illustrates the apparently equilibrated data of conductivity vs. the p_{O_2} and p-type conductivity was observed specific for Cr^{3+} cations at the B site, while for lower p_{O_2}, n-type conductivity became predominant as Ti^{4+} reduced to Ti^{3+}. The conductivity of $LiCrTiO_4$ at 800 °C in air was 0.3 $S{\cdot}cm^{-1}$, it decreased to $5.5{\cdot}10^{-5}$ $S{\cdot}cm^{-1}$ for log (p_{O_2}) ~ -16 and increased to 2.8 $S{\cdot}cm^{-1}$ for log (p_{O_2}) ~ -18. $Li_{0.9}Mg_{0.2}Cr_{0.9}TiO_4$ had a similar evolution of the conductivity with 0.1 $S{\cdot}cm^{-1}$ at 800 °C in air, decreasing to $7.6{\cdot}10^{-4}$ $S{\cdot}cm^{-1}$ for log (p_{O_2}) ~ -16 and increased back to 3.8 $S{\cdot}cm^{-1}$ for log (p_{O_2}) ~ -18. $Li_{0.7}Mg_{0.4}Cr_{0.9}Ti_{0.8}Fe_{0.2}O_4$ showed only n-type conductivity when reduced, with 0.06 $S{\cdot}cm^{-1}$ in air and 0.6 $S{\cdot}cm^{-1}$ for log (p_{O_2}) ~ -18.

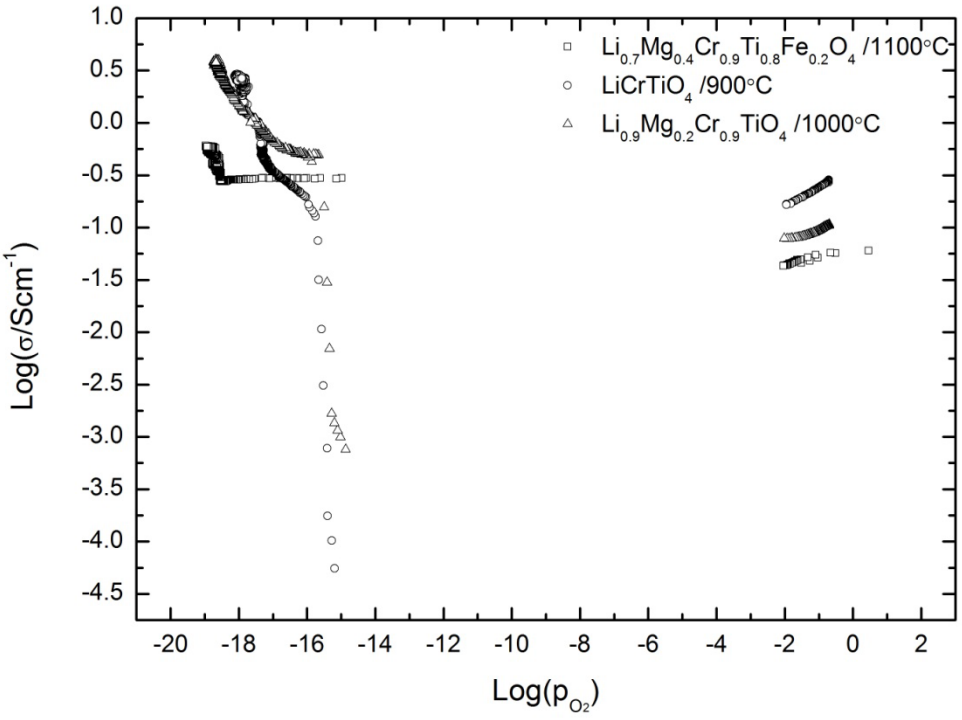

Figure 4-16 Evolution of electrical conductivity for LiCrTiO4, $Li_{0.9}Mg_{0.2}Cr_{0.9}TiO_4$ and $Li_{0.7}Mg_{0.4}Cr_{0.9}Ti_{0.8}Fe_{0.2}O_4$ in reducing conditions at 800 °C, with p-type conductivity for LiCrTiO4 and $Li_{0.9}Mg_{0.2}Cr_{0.9}TiO_4$ initially, and n-type conductivity for longer reducing time and lower pO_2.

4.6 Conclusions

Characterisation of quenched samples demonstrated that spinels with higher degree of inversion were stable at higher temperatures, thus the approached strategy for increasing the stability of spinel phase was successful.

$LiCrTiO_4$, $Li_{0.9}Mg_{0.1}Cr_{1.1}Ti_{0.9}O_4$ $Li_{0.9}Mg_{0.2}Cr_{0.9}TiO_4$ and $Li_{0.85}Mg_{0.3}Cr_{0.85}TiO_4$ demonstrated good stability in reducing conditions, while for $Li_{0.8}Mg_{0.3}Cr_{0.9}Ti_{0.9}Fe_{0.1}O_4$ and $Li_{0.7}Mg_{0.4}Cr_{0.9}Ti_{0.8}Fe_{0.2}O_4$ metallic Fe formation was observed after reduction.

Conductivity measurements showed electrical conductivity higher than 0.1 $S \cdot cm^{-1}$ for these materials in air and reducing conditions. The evolution of conductivity with p_{O_2} demonstrated the existence of electronic conductivity, thus it was concluded that the conductivity was dominated by electronic behaviour.

Even though positive results were obtained in improving the properties (Li, Cr, Ti) based spinels for their possible application as electrode support materials, it was considered that the new developed materials are still not the best option for electrode supports.

4.7 References

1. R. K. . Gover, J. T. . Irvine, and A. . Finch, *J. Solid State Chem.*, 1997, **132**, pp. 382–388(7).
2. A. Kuhn, C. Baehtz, and F. García-Alvarado, *J. Power Sources*, 2007, **174**, 421 – 427.
3. T. Ohzuku, K. Tatsumi, N. Matoba, and K. Sawai, *J. Electrochem. Soc.*, 2000, **147**, 3592.
4. A. Kuhn, M. Martín, and F. García-Alvarado, *Z. Anorg. Allg. Chem.*, 2008, **634**, 880–886.
5. C. V. Rao and B. Rambabu, *Solid State Ionics*, **VOL 181**, pages 839–843.
6. A. Kuhn, P. Díaz-Carrasco, M. E. Arroyo y de Dompablo, and F. García-Alvarado, *Eur. J. Inorg. Chem.*, 2007, **2007**, 3375–3384.
7. M. Nakayama, Y. Ishida, H. Ikuta, and M. Wakihara, *Solid State Ionics*, 1999, **117**, 265 – 271.
8. T. Yokoyama and T. Meguro, *Jpn. J. Appl. Phys.*, 2005, **44**, 6201–6203.

Chapter 5

Contents

5.1 Introduction 125

5.2 $MnFeCrO_4$ based electrodes tests 125

5.2.1 Phase analysis, conductivity and microstructure of the scaffold 126

5.2.2 Phase analysis and microstructure of impregnated scaffolds 128

5.2.3 Performance of impregnated scaffolds 132

5.2.4 Influence of reduction upon electro-chemical performance 141

5.3 MgFeCrO4 based electrodes tests 146

5.3.1 Electrical conductivity and microstructure of the scaffold 147

5.3.2 Phase analysis and microstructure of impregnated scaffolds 148

5.4 Performance of impregnated scaffolds 151

5.5 Influence of reduction upon electro-chemical performance 156

5.6 Conclusions 161

5.7 References 163

5 Development and performance of $MnFeCrO_4$ and $MgFeCrO_4$ - based electrodes for SOFC

5.1 Introduction

In this chapter is reported the performance of chromium rich spinels ($MnFeCrO_4$ and $MgFeCrO_4$) as electrode support materials, when used alone or impregnated with $(La_{0.75}Sr_{0.25})_{0.97}Cr_{0.5}Mn_{0.5}O_3$, $La_{0.8}Sr_{0.2}FeO_3$, $Ce_{0.9}Gd_{0.1}O_2$, CeO_2 or Pd.

In Chapter 3, the chemical stability analysis and electrical conductivity measurements indicated sufficient chemical stability and electrical conductivity in reducing and oxidizing conditions, leading us to investigate $MnFeCrO_4$ and $MgFeCrO_4$ as support materials for both anodes and cathodes. In addition, $MnFeCrO_4$ and $MgFeCrO_4$ contain elements that are also present in ferritic stainless steels, while similar spinels were observed to form in the oxide scales on interconnect surfaces following oxidation.

5.2 $MnFeCrO_4$ based electrodes tests

Previous experimental studies[1–3] have reported porous yttria-stabilised zirconia (YSZ) scaffolds impregnated with electrode materials, however none have considered $MnFeCrO_4$ as an alternative scaffold.

Therefore, here are described results for $MnFeCrO_4$ scaffolds in terms of thermo – mechanical stability to a multi-step impregnation process and chemical stability to impregnated electrode materials, and the evaluation of electrochemical performance of symmetrical cells based on such scaffolds impregnated with the electrode materials $(La_{0.75}Sr_{0.25})_{0.97}Cr_{0.5}Mn_{0.5}O_3$ (LSCM), $La_{0.8}Sr_{0.2}FeO_3$ (LSF), $Ce_{0.9}Gd_{0.1}O_2$ (CGO), CeO_2 and Pd. LSCM enhances the electronic conductivity in composite electrodes and has been shown to be redox stable.[4–7] CGO and CeO_2 provide ionic conductivity[8] since these materials are well known ionic conductors in air and under reducing conditions, respectively. CeO_2 and Pd have been added as catalysts in order to enhance electrochemical reactions.[9] LSF has been studied as a cathode material[1,10] and demonstrated to show mixed ionic/electronic conductivity (MIEC) according to ionic conductivity measurements.[11] In Table 5-1 are listed the materials impregnated into $MnFeCrO_4$ scaffold, the corresponding wt.% and the labels of the samples used throughout the discussion of the results.

No	Composition (wt.%)	Label
1	$MnFeCrO_4$	$MnFeCrO_4$
2	$MnFeCrO_4$ – LSF (20%)	$MnFeCrO_4$/LSF
3	$MnFeCrO_4$ – LSCM (27%)	$MnFeCrO_4$/LSCM
4	$MnFeCrO_4$ – LSCM (22%) – CGO (12%)	$MnFeCrO_4$/LSCM/CGO
5	$MnFeCrO_4$ – LSCM (22%) – CeO_2 (6%)	$MnFeCrO_4$/LSCM/CeO_2
6	$MnFeCrO_4$ – LSCM (22%) – CGO (12%) – Pd (1%)	$MnFeCrO_4$/LSCM/CGO/Pd
7	$MnFeCrO_4$ – LSCM (22%) – CeO_2 (6%) – Pd (1%)	$MnFeCrO_4$/LSCM/CeO_2/Pd

Table 5-1 Materials impregnated into $MnFeCrO_4$ porous substrates in wt.% and labels used throughout this chapter.

5.2.1 Phase analysis, conductivity and microstructure of the scaffold

Chemical and microstructural stability under reducing and oxidizing conditions are requirements for the application of $MnFeCrO_4$ as electrode supports on the fuel and air sides of SOFCs.

Previously we assessed the chemical stability of $MnFeCrO_4$ in dry 5%H_2/Ar at 950 °C, with the observation that MnO and metallic Fe secondary phases form. When reduced in humidified (3% H_2O) 5%H_2/Ar at the slightly higher temperature of 1000 °C, it was observed that, in contrast with previous results for dry 5%H_2/Ar, only MnO was formed as secondary phase (chapter 3 - section 3.3). This was due to the higher p_{O_2} of humidified 5%H_2/Ar compared to dry 5%H_2/Ar, meaning that the conditions were not reducing enough for the formation of metallic Fe.

Figure 5-1 shows changes in the DC conductivity at 850 °C of an 80% dense pellet of $MnFeCrO_4$ upon switching from static air to humidified 5%H_2/Ar ($\log p_{O_2} \sim -18$). The conductivity increased from ~ 0.2 S·cm^{-1} to ~ 0.4 S·cm^{-1} with the switch in atmosphere, indicating n-type behaviour for the material. After ~ 15 hours of reduction, no further significant improvement in conductivity was observed. This suggests that when reducing $MnFeCrO_4$ porous scaffolds is ought to be enough to dwell for 11 hours to ensure complete reduction of the thin electrode layer (~ 180 μm).

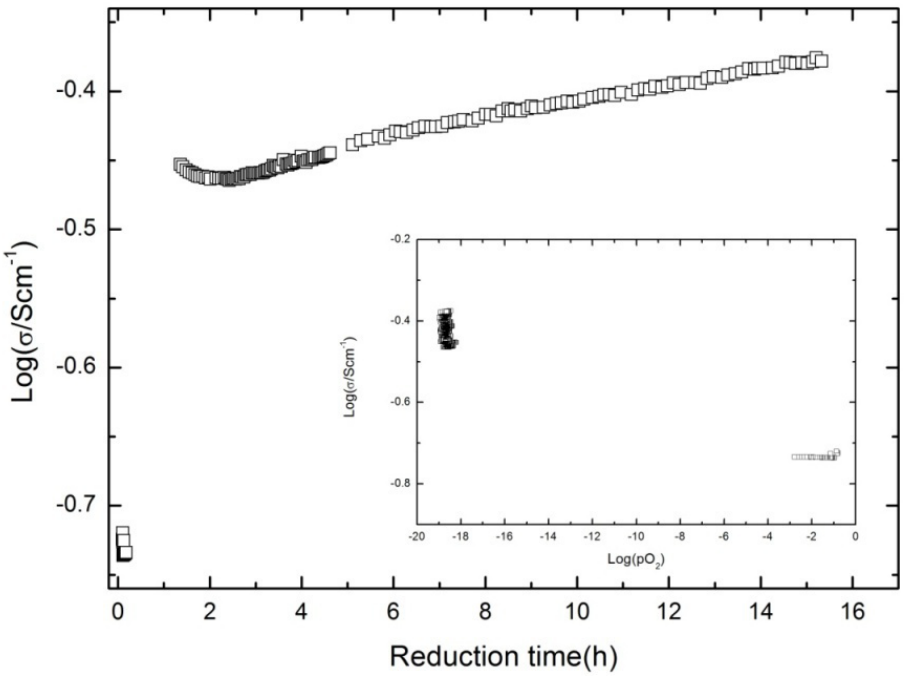

Figure 5-1 DC electrical conductivity of a dense $MnFeCrO_4$ pellet as a function of time after switching from static air to humidified 5%H_2/Ar. The inset shows the same data as a function of p_{O_2}.

Figure 5-2 shows cross-sectional SEM images of the $MnFeCrO_4$ scaffold, with a general overview of the three layered wafer and more detailed images of electrode microstructure after measurement in air or humidified 5%H_2/Ar. The interface between scaffold and electrolyte demonstrated good interlayer contact (Figure 5-2 (a)), while the microstructure of the porous layer was suitable for application as electrode support. The spinel particles were observed to change morphology from smooth in air (Figure 5-2 (b)) to roughened under reducing conditions (Figure 5-2 (c, d)). The roughening of the spinel under reducing conditions corresponded with the incipient stages of segregation of the MnO secondary phase (chapter 3 – section 3.3).

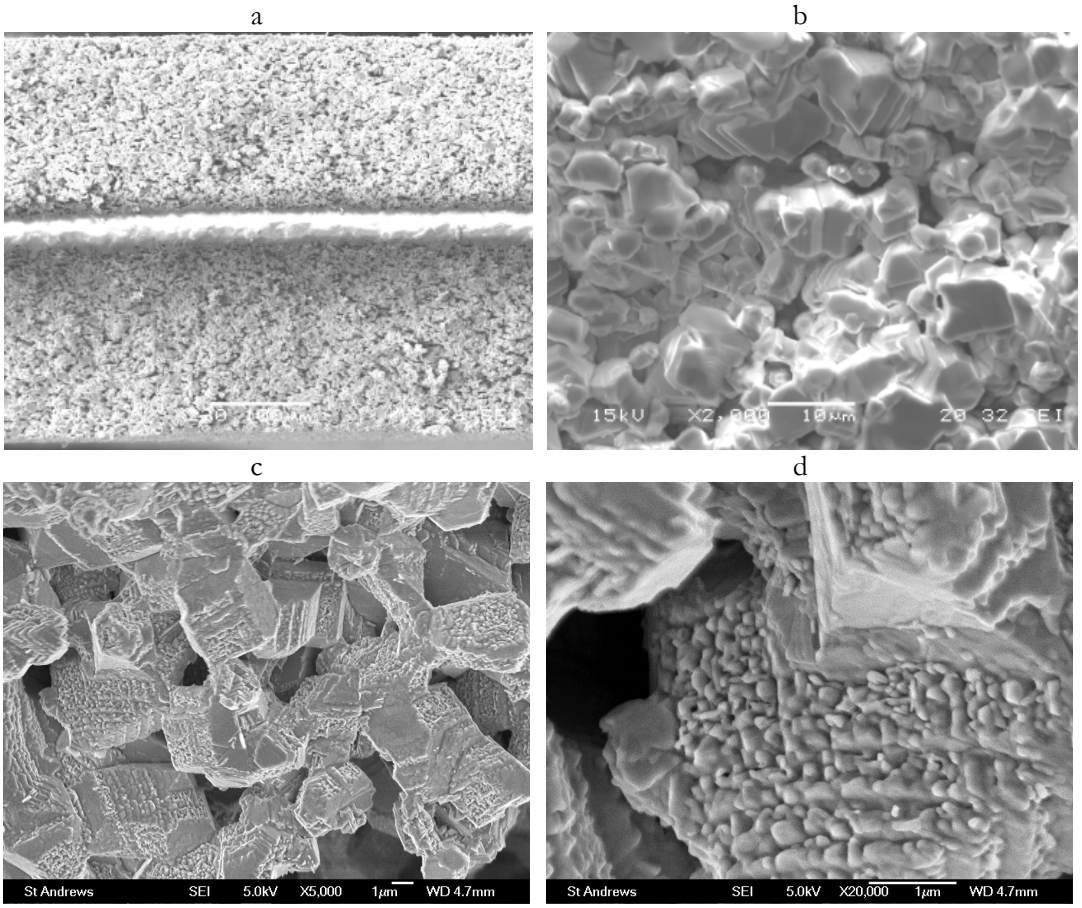

Figure 5-2 SEM images of $MnFeCrO_4$ scaffold: a) – three layer wafer consisting of dense YSZ electrolyte with porous $MnFeCrO_4$ on either side; b) – microstructure of spinel layer after testing in air; c) – microstructure of spinel layer after testing in humidified 5%H_2/Ar at 850 °C for 11 hours; d) – detail of the sample tested.

5.2.2 Phase analysis and microstructure of impregnated scaffolds

After final sintering step of impregnated $MnFeCrO_4$ scaffolds, the formation of peroskite phases was confirmed by X-ray diffraction (XRD). Small amounts of secondary phases were identified as (La,Sr,Cr,Mn) intermediary reacted oxides for $MnFeCrO_4$/LSCM and $MnFeCrO_4$/LSCM/CGO samples (Figure 5-3), while for $MnFeCrO_4$/LSF a secondary phase of Fe_2O_3 (hematite) was identified (Figure 5-4) . XRD patterns corresponding to these samples are presented in Figure 5-3 and Figure 5-4. The identified secondary phases were not expected to have a negative impact on symmetrical cell electrochemical performance. For example, Fe/FeO has been used as a catalyst in SOFCs.[12]

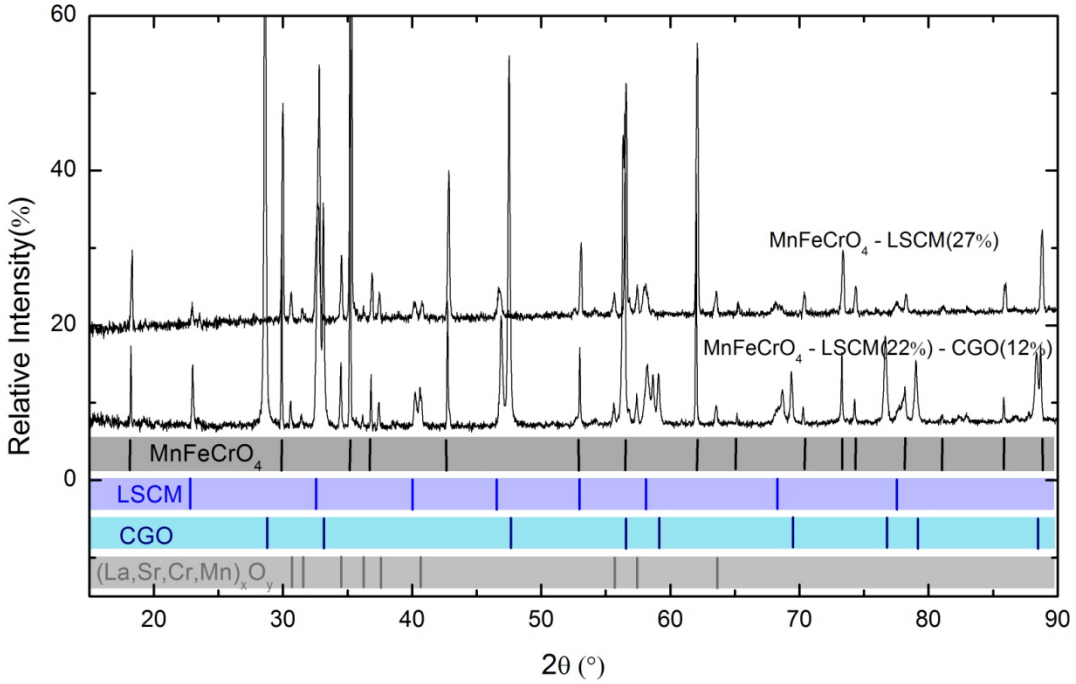

Figure 5-3 X-ray diffraction pattern of $MnFeCrO_4$ – LSCM(27%) and $MnFeCrO_4$ – LSCM(22%) – CGO(12%) with LSCM sintered at 1200 °C for 4 hours and CGO sintered at 1000 °C for 4 hours.

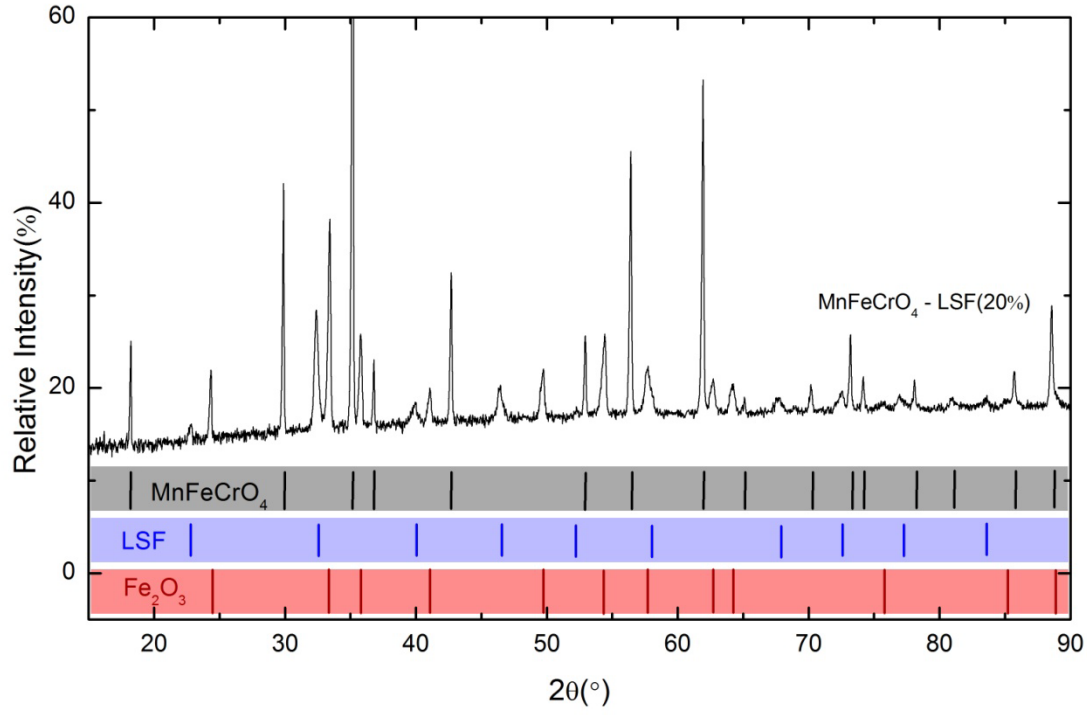

Figure 5-4 X-ray diffraction pattern of $MnFeCrO_4$ – LSF(20%) sintered at 900 °C for 4 hours; Fe_2O_3 (hematite) marked peaks are observed on this pattern.

Figure 5-5 presents cross-sectional SEM images of different symmetrical cells tested in air ($MnFeCrO_4$/LSF) or in air followed by humidified 5%H_2/Ar ($MnFeCrO_4$/LSCM). For $MnFeCrO_4$/LSCM (Figure 5-5 (a)) spinel particles coated with seemingly well-adhered LSCM particles (~1 μm) were observed. A similar morphology of LSF particles for the $MnFeCrO_4$/LSF sample was also observed (Figure 5-5 (b)).

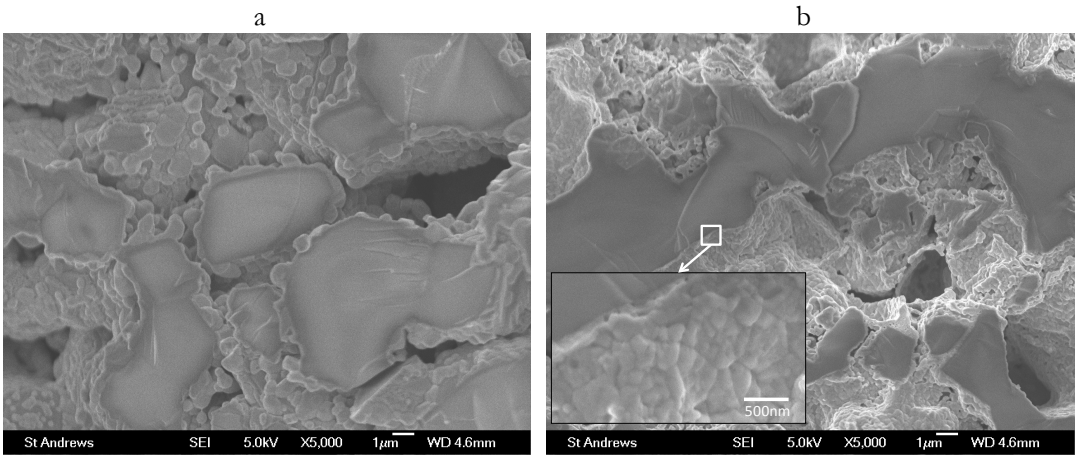

Figure 5-5 SEM images of: a) $MnFeCrO_4$ - LSCM(27%) tested in air and humidified 5%H_2/Ar; b) $MnFeCrO_4$ - LSF(20%) tested in air.

The microstructures of $MnFeCrO_4$/LSCM/CeO_2 and $MnFeCrO_4$/LSCM/CGO samples without Pd are presented in Figure 5-6. Additional thermal treatments following impregnation of CGO and CeO_2 led to densification of the LSCM layer compared to Figure 5-5 (a) leading to almost continuous coating on the spinel scaffold, while CGO particles of size 0.2-0.5 μm were apparently very well connected to the LSCM layer (Figure 5-6 (b)). The sample containing CeO_2 was only calcined at 450 °C and the presence of CeO_2 particles approaching nano-dimensions on LSCM was observed (Figure 5-6 (a)). Some of these particles increased their dimensions after testing.

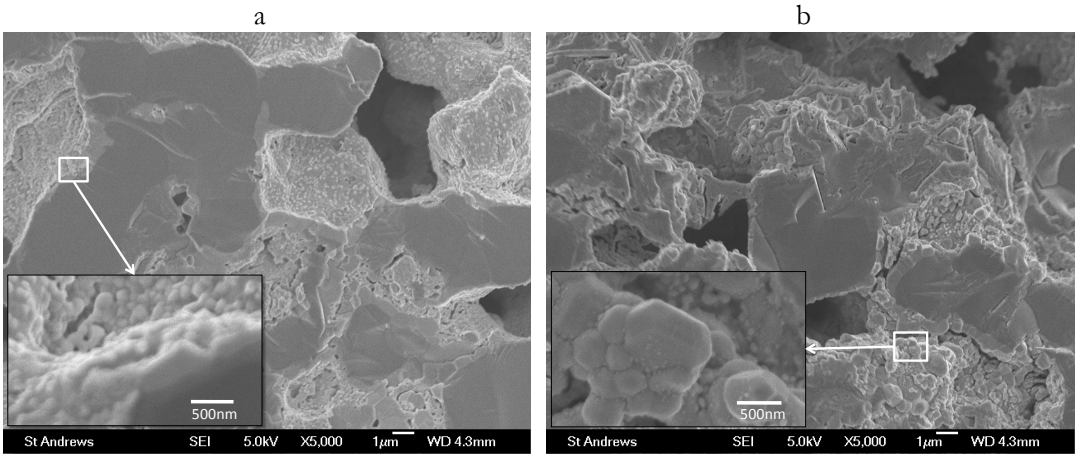

Figure 5-6 SEM images of: a) $MnFeCrO_4$ – LSCM(22%) – CGO(12%) after tests in air and humidified 5%H_2/Ar; b) $MnFeCrO_4$ – LSCM(22%) – CeO_2(6%) tested in humidified – 5%H_2/Ar.

SEM images for $MnFeCrO_4$/LSCM/CGO/Pd and $MnFeCrO_4$/LSCM/CeO_2/Pd (Figure 5-7) suggest the presence of Pd nanoparticles with size ~10-20 nm on top of larger particles of CGO or CeO_2. Such nanoparticles of Pd would be expected to behave as electrocatalytic sites during symmetrical cell electrochemical testing.

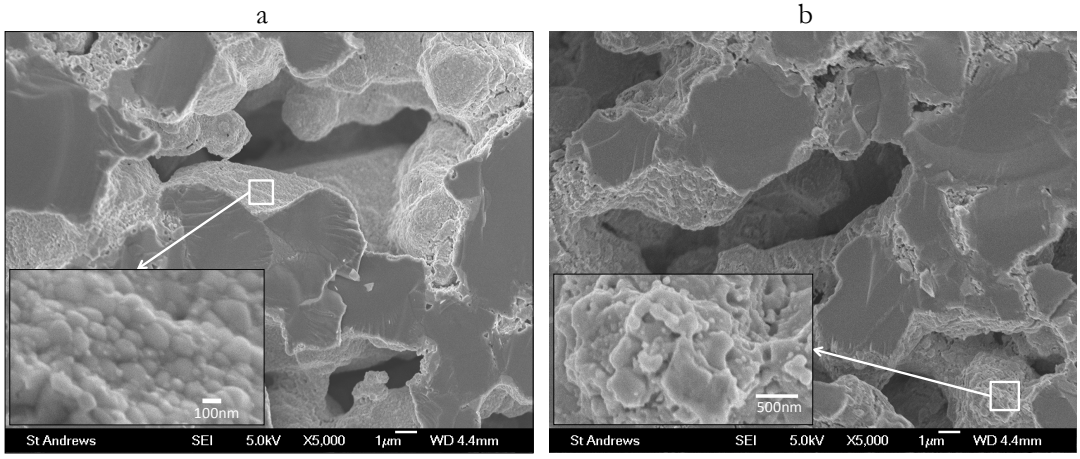

Figure 5-7 SEM images of: a) $MnFeCrO_4$ –LSCM(22%) – CGO(12%) –Pd(1%) tested in humidified 5%H_2/Ar; b) $MnFeCrO_4$ – LSCM(22%) – CeO_2(6%) – Pd(1%) tested in humidified 5%H_2/Ar.

5.2.3 Performance of impregnated scaffolds

5.2.3.1 Tests of symmetrical cells in air

Figure 5-8 (a, b) presents the Electrochemical Impedance Spectroscopy (EIS) results in the form of Nyquist and Bode plots for symmetrical cells based on MnFeCrO4, $MnFeCrO_4$/LSCM, $MnFeCrO_4$/LSCM/CGO and $MnFeCrO_4$/LSF tested at 870 °C, in air. The temperature dependence of R_s and polarisation resistance (R_p) values are provided in Figure 5-8 (c, d), where values were determined by fitting the equivalent circuit illustrated in Figure 5-9. A detailed description of the equivalent circuit fitting procedure is included in Appendix 3.(see also chapter 2 – section 2.8)

The EIS data in Figure 5-8 (a, b) indicated two processes, one at higher frequency and one at lower frequency, which was more significant for the unimpregnated scaffold. For composite electrodes, the arcs generated by the two processes in the Nyquist plots overlapped, forming a broader depressed arc.

a

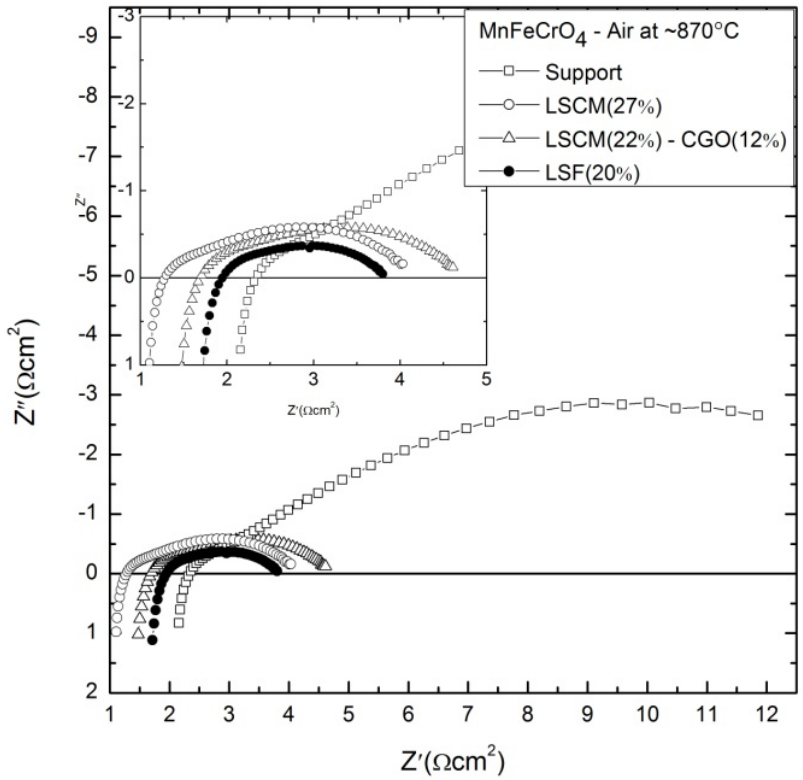

b

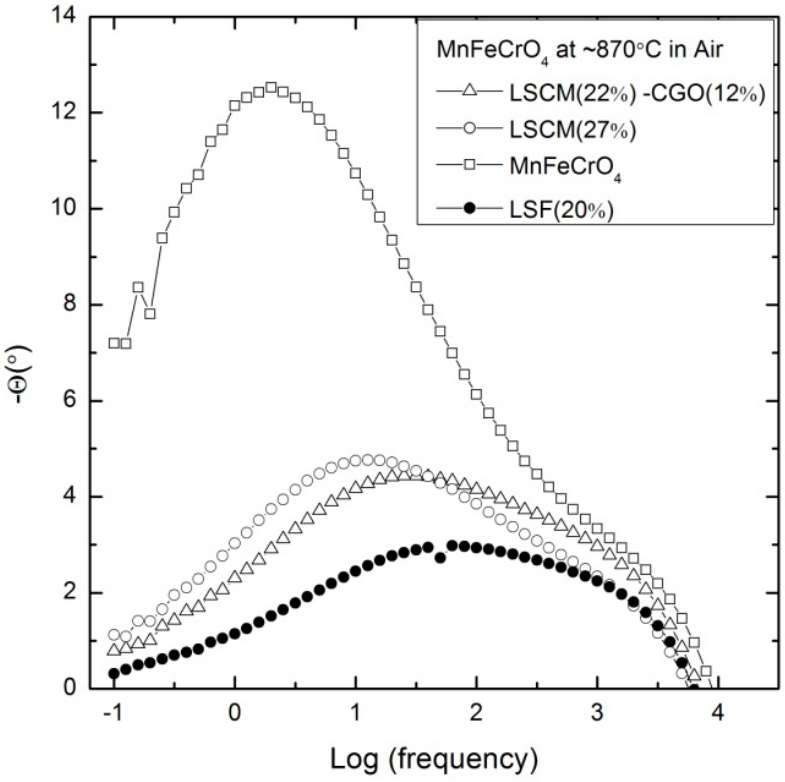
MnFeCrO4 at ~870°C in Air
LSCM(22%) -CGO(12%)
LSCM(27%)
MnFeCrO4
LSF(20%)
-Θ(°)
Log (frequency)

c

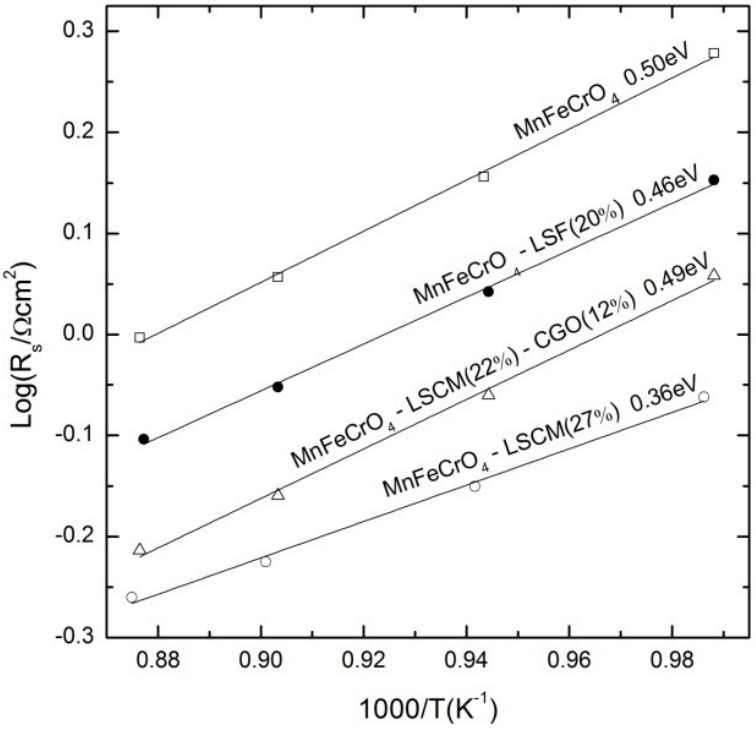
MnFeCrO4 0.50eV
MnFeCrO4 - LSF(20%) 0.46eV
MnFeCrO4 - LSCM(22%) - CGO(12%) 0.49eV
MnFeCrO4 - LSCM(27%) 0.36eV
Log(Rs/Ωcm2)
1000/T(K-1)

d

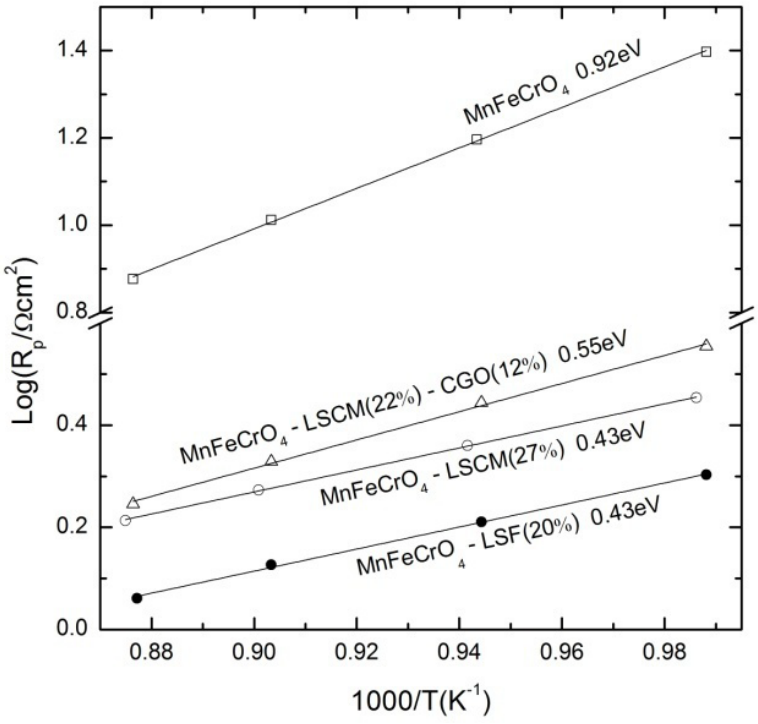

Figure 5-8 Symmetrical cells measured in stagnant air at 870 °C: a) – Nyquist plot containing data for the whole cell (2 equal electrodes); b) – Bode plot of phase angle vs frequency; c), d) – Arrhenius plots for R_s and R_p obtained from equivalent circuits fitting of experimental data; plotted R_s and R_p values are for one electrode.

Electrode	R_s [Ω·cm²]	R_p [Ω·cm²]	f_{max1} [Hz]	Process 1	f_{max2} [Hz]	Process 2	R_{p1} [Ω·cm²]	R_{p2} [Ω·cm²]
$MnFeCrO_4$	1	7.53	1200	Charge transfer	0.7	Gas diffusion	0.40	7.13
$MnFeCrO_4$/LSCM	0.46	1.63	630	Charge transfer	7	Gas diffusion	0.44	1.19
$MnFeCrO_4$/LSCM/ CGO	0.61	1.76	1000	Charge transfer	13	Gas diffusion	0.58	1.18
$MnFeCrO_4$/ LSF	0.79	1.15	1200	Charge transfer	39	O_2 dissociative adsorption	0.29	0.86

Table 5-2 Relaxation frequencies and polarisation resistances for symmetrical cells tested in air at ~ 870 °C; R_{p1} and R_{p2} are determined from equivalent circuits fitting and listed values are for one electrode, where $R_{p1}+ R_{p2} = R_p$.

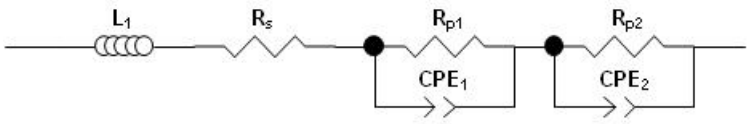

Figure 5-9 Equivalent circuit used to fit experimental data, where L = inductor; R_s = series resistance; R_p = polarisation resistance and CPE = constant phase element.

R_s and R_p values decreased significantly for the composite cathodes (Figure 5-8 (a)), since the impregnated materials formed a new conducting path at the surface of the scaffold with better conducting and catalytic properties compared to the $MnFeCrO_4$ scaffold (Table 5-2). R_p values were lowered from 7.53 $\Omega \cdot cm^2$ at 870 °C for $MnFeCrO_4$ to 1.76 Ωcm^2 for $MnFeCrO_4$/LSCM/CGO and 1.63 $\Omega \cdot cm^2$ for $MnFeCrO_4$/LSCM. $MnFeCrO_4$/LSF demonstrated the lowest R_p value (1.15 $\Omega \cdot cm^2$) amongst the cathodes tested in this study. As reported in the literature,[13–17] the attribution of limiting processes is based on relaxation frequencies. The high frequency process (R_{p1} - Table 5-2) was similar for all electrodes, with relaxation frequency (peak in –Z" vs. f plots) values of ~1-1.5·10^3 Hz. The low frequency arc described the predominant limiting process (R_{p2} - Table 5-2) and it was influenced by the electrode material impregnated, as observed in the Bode plots in Figure 5-8 (b). That is, relaxation frequency values for the lower frequency process shifted towards higher frequencies for impregnated electrodes (Table 5-2).

The high and low frequency processes observed in Figure 5-8 (a, b) could be attributed to charge transfer and electrode surface gas kinetics, respectively. Gas kinetics likely included dissociative adsorption of active species and surface diffusion. Regarding the $MnFeCrO_4$ scaffold, the high frequency process most likely reflected electronic transfer, while the lower frequency process, with relaxation frequency of 0.7 Hz, probably corresponded to gas diffusion.[13] Considering impregnated electrode materials, LSCM is known to possess low ionic conductivity and therefore the charge transfer remains mainly electronic. The low frequency process seemed to have better gas kinetics, with relaxation frequency value of 7 Hz for $MnFeCrO_4$/LSCM compared to 0.7 Hz for the scaffold. Relaxation frequency values for the low frequency process were raised further still for the composite electrodes $MnFeCrO_4$/LSCM/CGO (13 Hz) and $MnFeCrO_4$/LSF (39 Hz), due to their mixed ionic/electronic conduction achieved via the electronic conductivity of the scaffold and LSCM, and ionic conductivity of CGO and LSF.[11] Furthermore, the low frequency process relaxation frequency for $MnFeCrO_4$/LSF of 39 Hz was more specific to dissociative adsorption of O_2 followed by electrochemical reduction and transfer of oxygen species at the triple phase boundary (TPB).[14]

Activation energy (E_a) values for R_s and R_p are included in Figure 5-8 (c, d), where E_a for R_s is related to the conduction activation and E_a for R_p is related to the electrochemical processes described by the impedance spectra in Figure 5-8 (a, b). The determined E_a with regard to R_s (0.36 eV) for $MnFeCrO_4$/LSCM was not surprisingly between the E_a values known for LSCM in air (0.24 eV)[4,18] and determined here for the scaffold (0.50 eV). The E_a value for LSCM measured in air is not significantly high, thus the thermal activation was more significant for the contribution of the scaffold material $MnFeCrO_4$ (see chapter 3 section 3.4) in the E_a values for MnFeCrO4/LSCM sample. $MnFeCrO_4$/LSCM/CGO showed a similar E_a value of 0.49 eV. E_a values with regard to R_p showed a significant improvement from the scaffold (0.92 eV) to the composite $MnFeCrO_4$/LSCM/CGO (0.55 eV) and $MnFeCrO_4$/LSCM (0.43 eV) electrodes. This corresponded to a decrease in the E_a of the limiting surface gas kinetics, as confirmed by f_{max2} relaxation frequency values (Table 5-2). $MnFeCrO_4$/LSF showed similar E_a values to $MnFeCrO_4$/LSCM/CGO and $MnFeCrO_4$/LSCM, namely 0.46 eV for R_s and 0.43 eV for R_p.

LSCM and LSCM/YSZ composite have been previously studied as SOFC cathode materials, mostly as a thin layer on the electrolyte [5,6,19] with performance reported for symmetrical cells and half-cell measurements. Bastidas *et al.*[5] reported the performance of LSCM in dry oxygen at 900 °C with R_p of 0.35 Ω·cm^2, while Ruiz-Morales *et al.*[6] reported R_p in oxygen and air of 0.11 Ω·cm^2 and 0.16 Ω·cm^2, respectively, for a 1 : 1 LSCM-YSZ composite cathode at 900 °C. In a similar approach, Jiang *et al.*[19] characterised cathodes based on LSCM/YSZ composites in air at 900 °C, with R_p values of 0.52 Ω·cm^2 and 1.4 Ω·cm^2 for LSCM synthesised via gel-casting and solid state reaction, respectively. The R_p values obtained in this study for LSCM-containing composite electrodes (1.63 Ω·cm^2 and 1.76 Ω·cm^2) were modest compared to the above, although several dissimilarities, such as the infiltration here of LSCM into a porous scaffold, the lack of ionic conductivity of the $MnFeCrO_4$ scaffold, the amount of LSCM, LSCM/CGO or LSF impregnated and the testing temperature, might have contributed.

LSF has been studied as a cathode material impregnated into porous YSZ substrates[1,11,20,21] and its performance typically measured at 700 °C. It was concluded that its performance is dependent on calcination temperature, with relatively high

temperatures (*e.g.* 1100 °C) leading to diminished performance, while relatively low temperatures (*e.g.* 700 °C) were not sufficient to obtain maximum electronic conductivity. Wang *et al.*[20] investigated composite cathodes within symmetric cells with 40 wt.% LSF impregnated into a porous YSZ substrate, measured at 700 °C and calcined at 850 °C or 1100 °C, giving R_p values of 0.13 $\Omega \cdot cm^2$ and 2.5 $\Omega \cdot cm^2$, respectively. According to Küngas *et al.*[21], the R_p of 40 wt.% LSF/YSZ calcined at 850 °C and measured at 700 °C within a symmetrical cell at open circuit voltage (OCV) was 0.14 $\Omega \cdot cm^2$. In the same study the R_p measured under the same conditions was 0.91 $\Omega \cdot cm^2$ for calcination performed at 1100 °C. The authors also concluded that the ionic conductivity of the electrolyte (and by extension, the ionic conductivity of the scaffold) influenced R_p. In this study the $MnFeCrO_4$/LSF composite showed an R_p of 1.15 $\Omega \cdot cm^2$ at 870 °C, which was lacking compared the literature values cited above. This was likely due to the lack of ionic conductivity of the scaffold, although future optimisation of LSF loading and calcination temperature might improve performance.

5.2.3.2 Tests of symmetrical cells in 3%H_2O – 5%H_2/Ar

The performance and temperature dependence in humidified 5%H_2/Ar at 850 °C of $MnFeCrO_4$, $MnFeCrO_4$/LSCM and the influence of the catalysts CGO, CeO_2 and Pd are shown in Figure 5-10, while Table 5-3 summarises electrochemical data obtained via the fitting of experimental data to the equivalent circuit illustrated in Figure 5-9. The CGO-containing composites $MnFeCrO_4$/LSCM/CGO and $MnFeCrO_4$/LSCM/CGO/Pd each showed a kind of tail at low frequencies in the Nyquist plots in Figure 5-10 (a) likely due to gas diffusion. Due to generally insufficient data at low frequencies, a desire not to compromise the quality of data fitting, and considering that gas diffusion is a manifestation of electrode microstructure and not reflective of electrode chemistry,[15] data obtained for AC perturbation frequencies < 1 Hz were excluded from the data fitting. The extra resistance at low frequencies may correspond to a concentration effect caused by electrode microstructure.[13] The slow diffusion process of active species towards the grain boundaries or active sites may be hindered by a low concentration of active species or electrode's surface blocked by adsorbed species *e.g.* water molecules, thus the extra resistance.

a

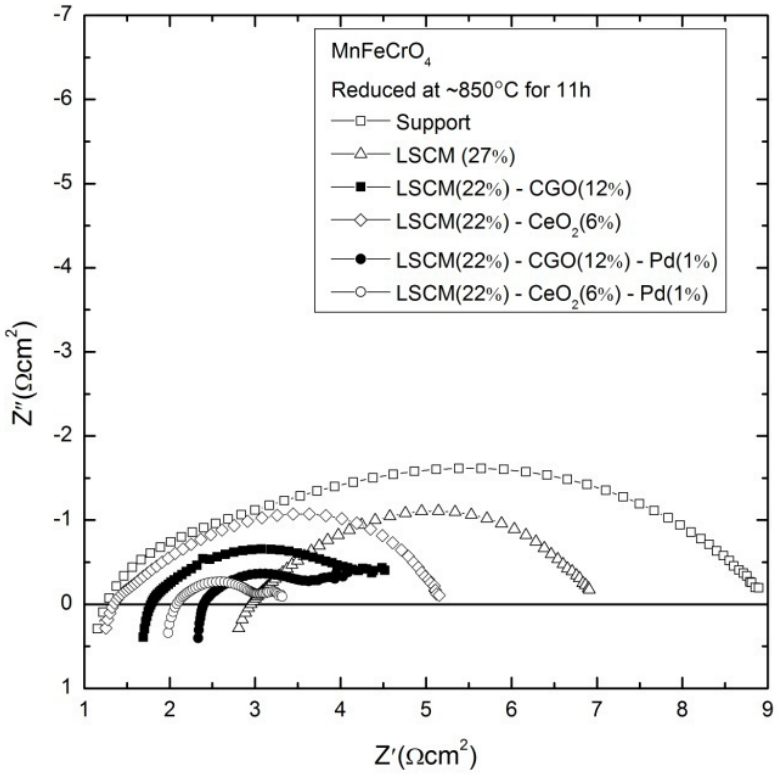
MnFeCrO4
Reduced at ~850°C for 11h
Support
LSCM (27%)
LSCM(22%) - CGO(12%)
LSCM(22%) - CeO2(6%)
LSCM(22%) - CGO(12%) - Pd(1%)
LSCM(22%) - CeO2(6%) - Pd(1%)
Z''(Ωcm2)
Z'(Ωcm2)

b

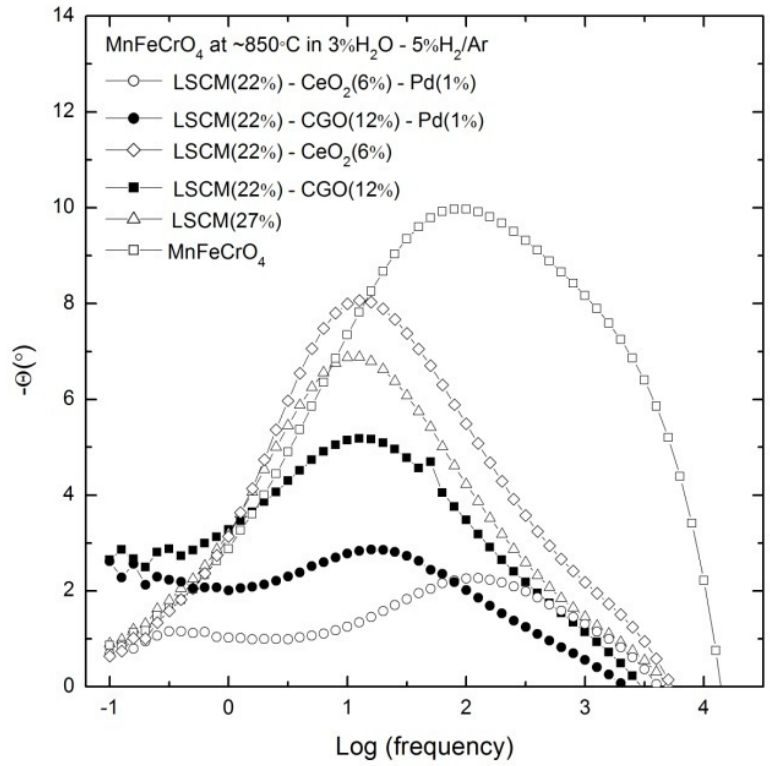
MnFeCrO4 at ~850°C in 3%H2O - 5%H2/Ar
LSCM(22%) - CeO2(6%) - Pd(1%)
LSCM(22%) - CGO(12%) - Pd(1%)
LSCM(22%) - CeO2(6%)
LSCM(22%) - CGO(12%)
LSCM(27%)
MnFeCrO4
-Θ(°)
Log (frequency)

c

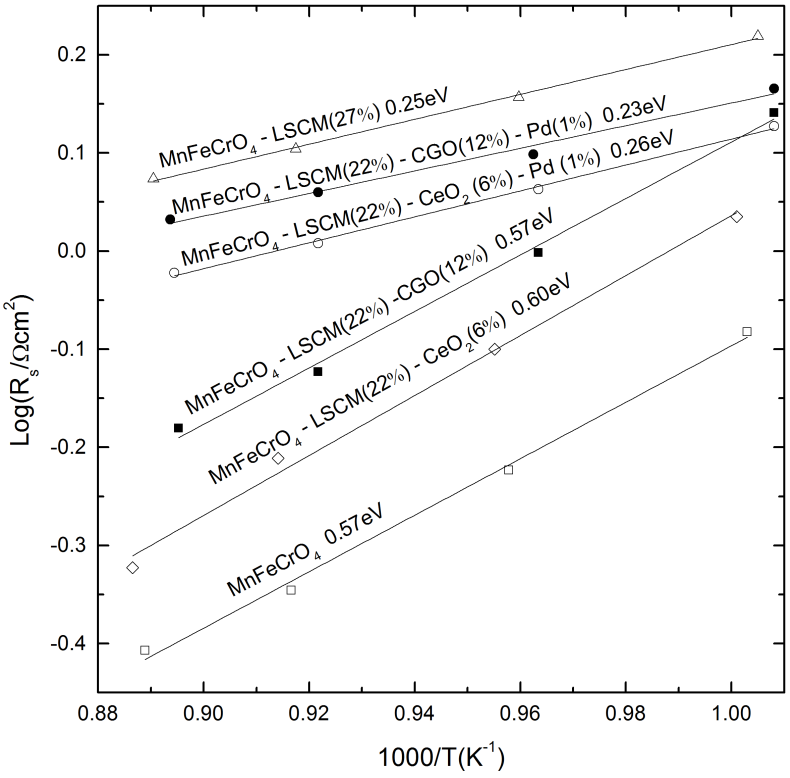

d

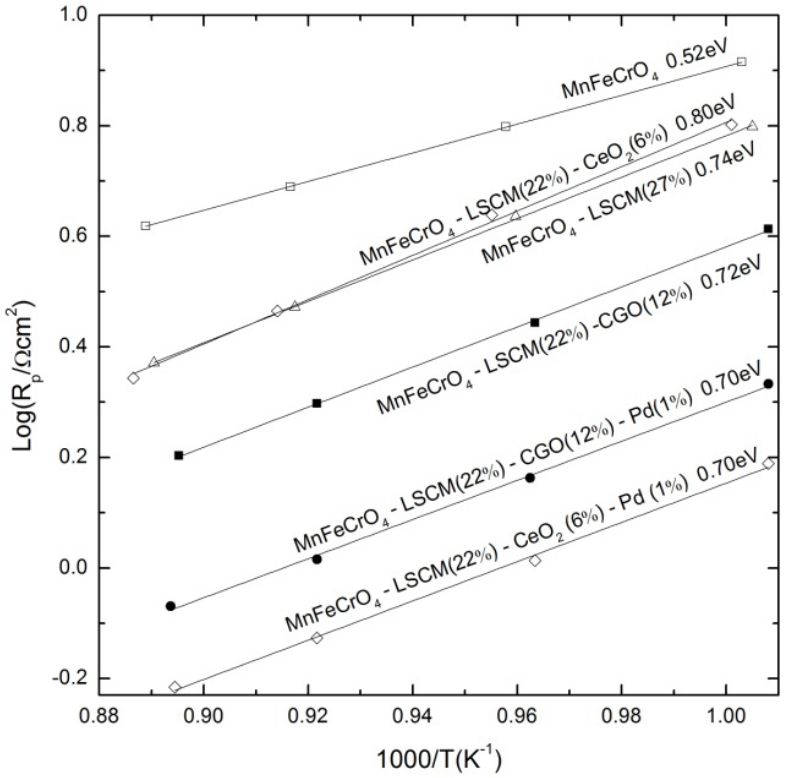

Figure 5-10 Symmetrical cells measured in humidified 5%H_2/Ar at 850 °C: a) – Nyquist plot containing data for the whole cell (2 equal electrodes); b) – Bode plot of phase angle vs frequency; c), d) – Arrhenius plots for R_s and R_p obtained from equivalent circuits fitting of experimental data; plotted R_s and R_p values are for one electrode.

Electrode	R_s [Ω·cm²]	R_p [Ω·cm²]	f_{max1} [Hz]	Process 1	f_{max2} [Hz]	Process 2	R_{p1} [Ω·cm²]	R_{p2} [Ω·cm²]
$MnFeCrO_4$	0.39	4.15	2000	Charge transfer	32	Dissociative gas adsorption	0.70	3.45
$MnFeCrO_4$/LSCM	1.18	2.35	700	Charge transfer	8	Gas diffusion	0.37	1.98
$MnFeCrO_4$/LSCM/CGO	0.66	1.60	190	Charge transfer	8	Gas diffusion	0.25	1.35
$MnFeCrO_4$/LSCM/CeO2	0.48	2.21	700	Charge transfer	10	Gas diffusion	0.54	1.67
$MnFeCrO_4$/LSCM/CGO /Pd	1.08	0.85	400	Charge transfer	14	Gas diffusion	0.15	0.70
$MnFeCrO_4$/LSCM/CeO2 /Pd	0.95	0.61	700	Charge transfer	91	Dissociative gas adsorption	0.15	0.46

Table 5-3 Relaxation frequencies and polarisation resistances for symmetrical cells tested in humidified – 5%H_2/Ar at ~850 °C; R_s and R_p (R_{p1}, R_{p2})are determined from equivalent circuits fitting and listed values are for one electrode.

Rs and Rp values for $MnFeCrO_4$ were lower under reducing atmosphere compared with the performance obtained in air due to the n-type character of this material (Figure 5-1). In contrast, when reduced, $MnFeCrO_4$/LSCM and $MnFeCrO_4$/LSCM/CGO showed increased R_s and R_p in comparison with their performance in air. The increase in resistance of composite electrodes containing LSCM under reducing conditions compared to air was likely due to a decrease in electronic conductivity[3,4] of this p-type material.

$MnFeCrO_4$/LSCM/CeO_2 showed performance similar to $MnFeCrO_4$/LSCM with regard to R_p, while R_s was improved with the addition of CeO_2. Addition of 1% Pd catalyst resulted in good performance with major decreases in R_p values down to 0.61 Ω·cm^2 for $MnFeCrO_4$/LSCM/CeO_2/Pd. Relaxation frequencies determined for composite electrodes in humidified 5%H_2/Ar (Table 5-3) were similar to those measured in air (Table 5-2). This suggested that similar limiting processes (*e.g.* adsorption/ desorption, dissociation/association) were at work in both reducing and oxidizing atmospheres. Regarding further the Bode plots in Figure 5-10 (b), $MnFeCrO_4$ showed f_{max2} of 32 Hz, which may be attributed to gas adsorption/desorption and dissociation/association processes. In comparison, $MnFeCrO_4$/LSCM/CeO_2/Pd showed f_{max2} of 91 Hz, suggesting similar limiting

processes to the scaffold however where such processes had more rapid kinetics due to the presence of the perovskite LSCM and CeO_2 and Pd catalysts.

The good electrochemical performance of $MnFeCrO_4$/LSCM/CeO_2/Pd in particular was comparable to results reported for LSCM used as an SOFC anode material. In humidified 5%H_2/Ar at 850 °C, R_p of 0.59 Ω·cm^2 has been observed,[4,6] while at 900 °C R_p values of 0.51 Ω·cm^2 and 0.43 Ω·cm^2, according to ref [4,6], respectively, have been measured. In humidified H_2 at 900 °C Bastidas *et al.*[5] reported an R_p of 0.3 Ω·cm^2, while Jiang *et al.*[19] reported R_p values for a 1 : 1 LSCM/YSZ composite, with LSCM obtained via gel-casting or solid state reaction, of 1.1 Ω·cm^2 or 1.9 Ω·cm^2, respectively. The comparable results obtained here relative to results reported in the literature are particularly encouraging since the $MnFeCrO_4$ scaffold is not ionically conducting and since the amount of loaded perovskite was limited. Furthermore, E_a values for R_p included in Figure 5-10 (c, d) were in good agreement with the E_a values of between 0.70 – 0.90 eV reported by Jiang *et al.*[19] for LSCM/YSZ composite anodes.

5.2.4 Influence of reduction upon electro-chemical performance

The reduction process was analysed on symmetrical cells at ~ 850 °C in humidified 5%H_2/Ar, by impedance measurements taken periodically, for 11 hours. Impedance spectra measured after 1 hour and 11 hours of reduction are presented in Figure 5-11, Figure 5-12 and Figure 5-13 as Nyquist plots, in order to quantify the influence of reduction time upon tested cells with different catalysts inserted. A positive effect was observed on reduction, with a decrease in R_s and R_p values for $MnFeCrO_4$ and $MnFeCrO_4$/LSCM, while for $MnFeCrO_4$/LSCM/CGO and $MnFeCrO_4$/LSCM/CGO/Pd the effect of reduction was negative and determined a small increase in R_s and R_p values. Samples $MnFeCrO_4$/LSCM/CeO_2 and $MnFeCrO_4$/LSCM/CeO_2/Pd show a more important deactivation after reduction, with an increase in R_s and R_p values. The observation may be related to an increase of ceria particles as a consequence of exposure to higher temperature (~ 850 °C) for 11 hours. Gross *et al.*[1] also observed deterioration in performance for cells containing different loading ceria into YSZ porous substrates and tested as CeO_2/YSZ anodes. They related this behaviour to either sintering of ceria, a decreased connectivity in

the ceria layer or a lower surface conductivity of high-temperature ceria. Another noticeable aspect was an increase of R_s. $MnFeCrO_4$/LSCM showed an important increase in R_s that could be correlated to the reduction of LSCM layer, as explained in section 3.3.2. R_s and R_p values were observed to increase with reduction time for $MnFeCrO_4$/LSCM/CGO/Pd and $MnFeCrO_4$/LSCM/CeO_2/Pd, observation that may be related to passivation of Pd while Pt paste was sintered at 800 °C as electrical contacts.

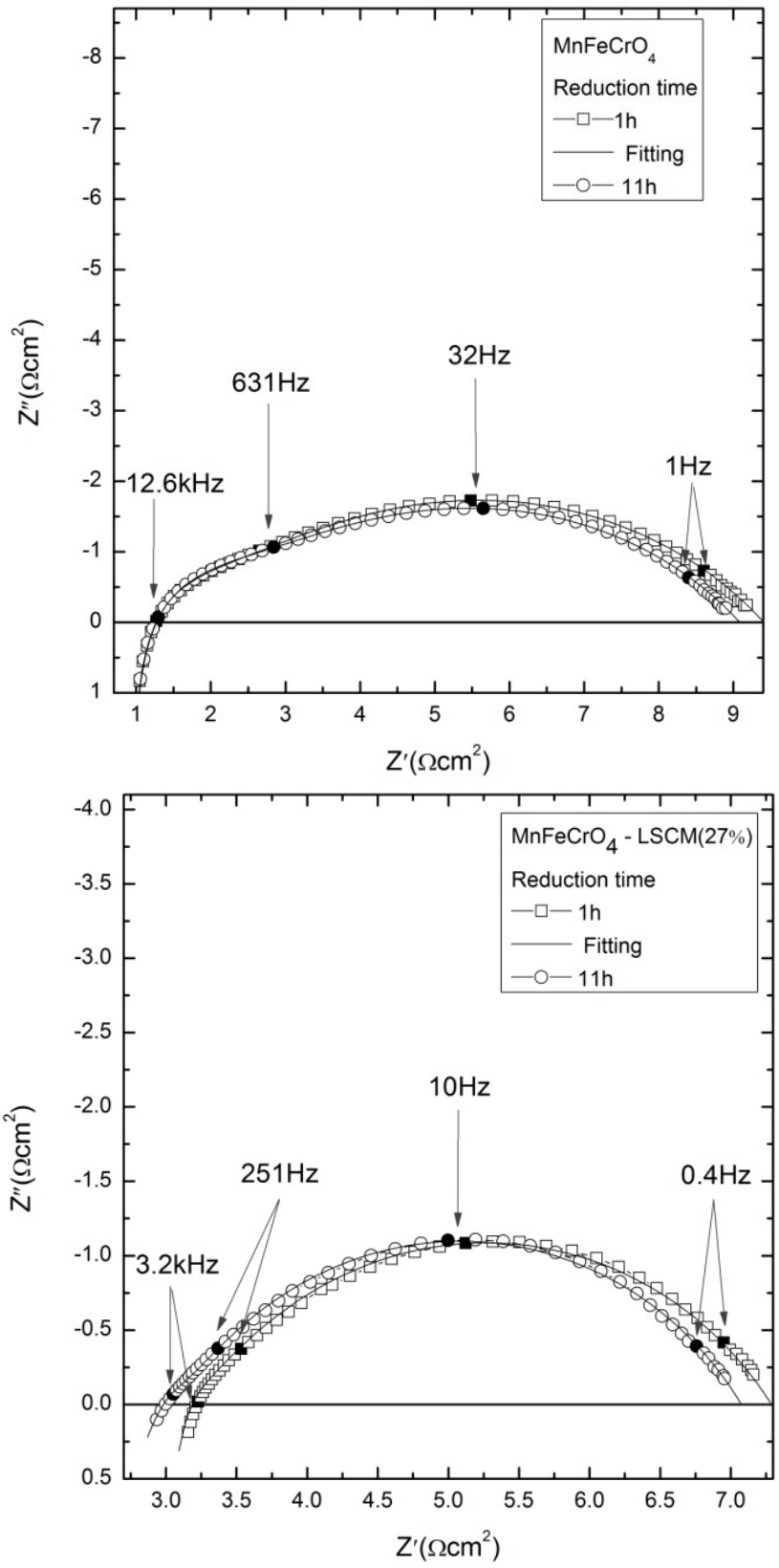

Figure 5-11 Nyquist plots of $MnFeCrO_4$ scaffold and $MnFeCrO_4$/LSCM reduced at 850 °C for 1 hour/ 11 hours and corresponding equivalent circuits fit; spectra contain data for two identical electrodes.

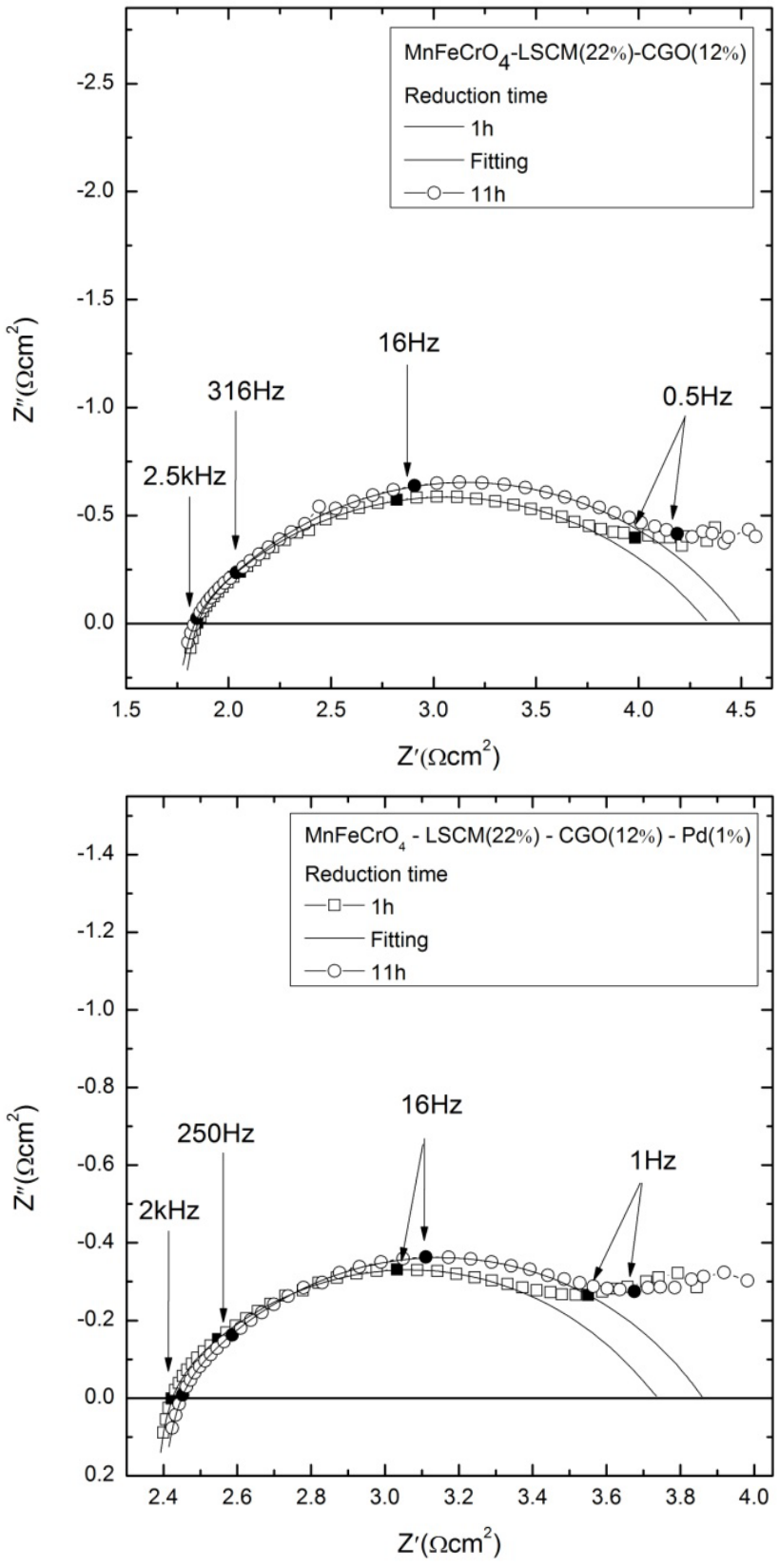

Figure 5-12 Nyquist plots of $MnFeCrO_4$/LSCM/CeO_2 and $MnFeCrO_4$/LSCM/CeO_2/Pd reduced at 850 °C for 1 hour/ 11 hours and corresponding equivalent circuits fit; spectra contain data for two identical electrodes.

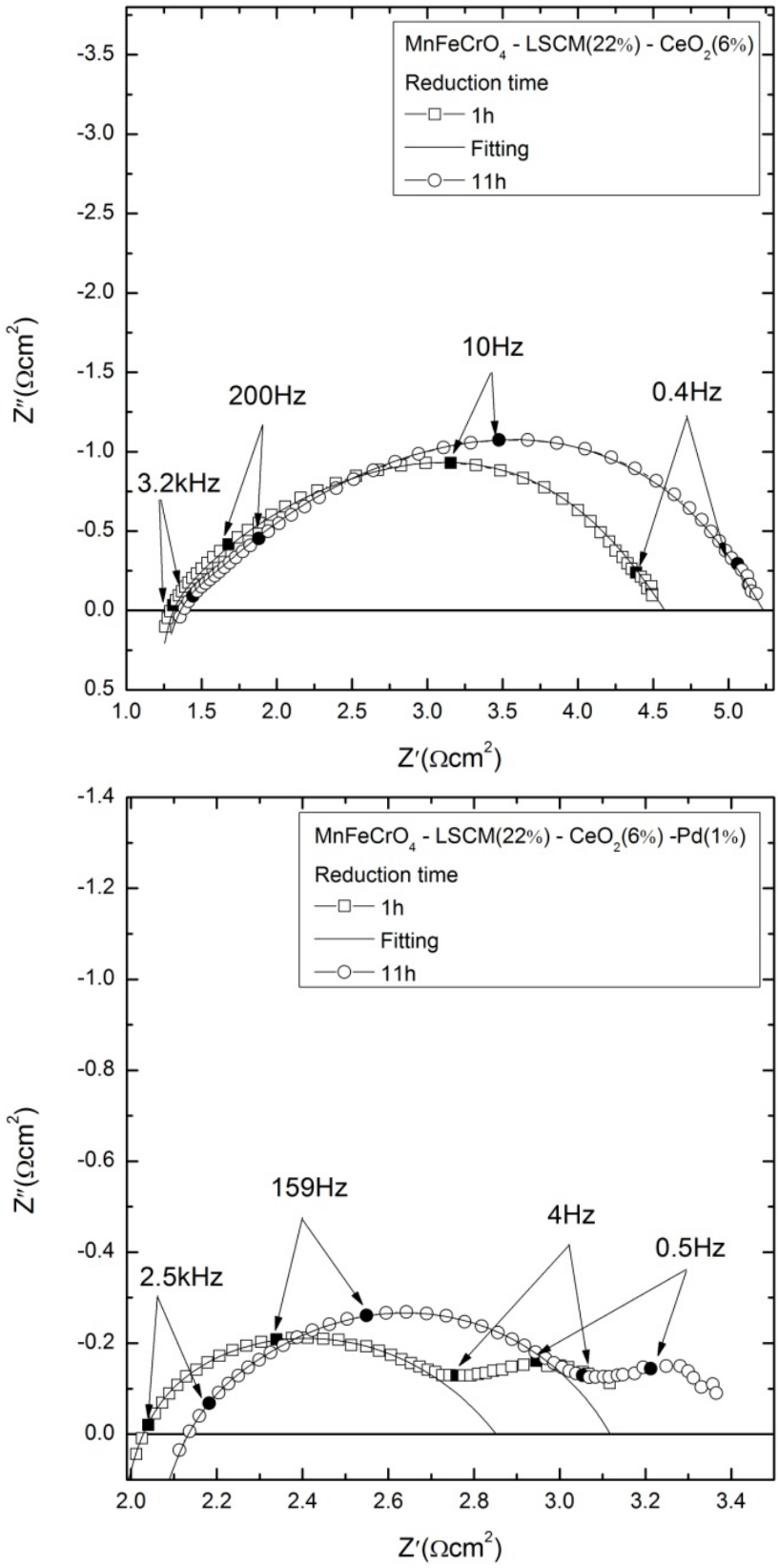

Figure 5-13 Nyquist plots of $MnFeCrO_4$/LSCM/CGO and $MnFeCrO_4$/LSCM/CGO/Pd reduced at 850 °C for 1 hour/ 11 hours and corresponding equivalent circuits fit; spectra contain data for two identical electrodes.

After impregnation of electrode materials into scaffolds, the effect of reduction is more important for the impregnated layer. It was a core-shell effect that led to a better stability for spinel, avoiding decomposition of the material. Effects of prolonged reduction periods did not improve the cells performance, only the negative effect of ceria sintering contributed to a decrease in R_s and R_p values. It was found that the dominant contribution to R_p consists of surface kinetics, including diffusion process and dissociative adsorption of active species on electrodes surface (see Figure 5-6 (a, b) and Figure 5-7 (a, b) micrographs of the tested samples to observe the increase in size particle of CeO_2 after the reduction prolonged thermal treatment at 850 °C and the good appearance (integrity) of the scaffold, the impregnated layer and their interface.)

5.3 $MgFeCrO_4$ based electrodes tests

In this section is discussed the performance of $MgFeCrO_4$ as an electrode support material when used alone or impregnated with $(La_{0.75}Sr_{0.25})_{0.97}Cr_{0.5}Mn_{0.5}O_4$, $Ce_{0.9}Gg_{0.1}O_2$, CeO_2 or Pd. As previously described for $MnFeCrO_4$, composite anodes for solid oxide fuel cells (SOFC) were prepared by aqueous infiltration of nitrate salts to produce $(La_{0.75}Sr_{0.25})_{0.97}Cr_{0.5}Mn_{0.5}O_4$ into a 45% porous $MgFeCrO_4$ scaffold and studied by electrochemical impedance spectroscopy in symmetrical cell configuration. The performance of the composite anodes was evaluated in humidified 5%H_2/Ar in order to understand their stability and performance at 850 °C or lower temperature with respect to the $MgFeCrO_4$ porous substrate. Corresponding loadings, in wt.% and labels of the samples used throughout this section are listed in Table 5-4.

No	Composition (wt.%)	Label
1	$MgFeCrO_4$	$MgFeCrO_4$
2	$MgFeCrO_4$ – LSCM (31%)	$MgFeCrO_4$/LSCM
3	$MgFeCrO_4$ – LSCM (27%) – CGO (15%)	$MgFeCrO_4$/LSCM/CGO
4	$MgFeCrO_4$ – LSCM (27%) – CeO_2 (6%)	$MgFeCrO_4$/LSCM/CeO_2
5	$MgFeCrO_4$ – LSCM (27%) – CGO (15%) – Pd (1%)	$MgFeCrO_4$/LSCM/CGO/Pd
6	$MgFeCrO_4$ – LSCM (27%) – CeO_2 (6%) – Pd (1%)	$MgFeCrO_4$/LSCM/CeO_2/Pd

Table 5-4 Materials impregnated into $MgFeCrO_4$ porous substrates in wt.% and labels used throughout this section.

5.3.1 Electrical conductivity and microstructure of the scaffold

The requirements for the application of $MgFeCrO_4$ as electrode support on the fuel side of SOFCs comprise chemical and microstructural stability of the spinel under reducing conditions. Previously we assessed the chemical stability of $MgFeCrO_4$ in dry and humidified 5%H_2/Ar at 1000 °C for 20 hours. When reduced in dry 5%H_2/Ar, $MgFeCrO_4$ decomposed with segregation of metallic Fe and $(MgO)_{0.91}(FeO)_{0.09}$. The material reduced in humidified (3% H_2O) 5%H_2/Ar did not decompose, as the p_{O_2} was above a certain stability limit for which secondary phases did not segregate from spinel (chapter 3 - section 3.3).

DC conductivity was measured at 850 °C on 63% dense pellet upon switching from static air to humidified 5%H_2/Ar (log p_{O_2}~ -18). The conductivity increased significantly from 0.014 S·cm^{-1} to 0.36 S·cm^{-1} with the switch in atmosphere, indicating the n-type behaviour for the material, as illustrated in Figure 5-14.

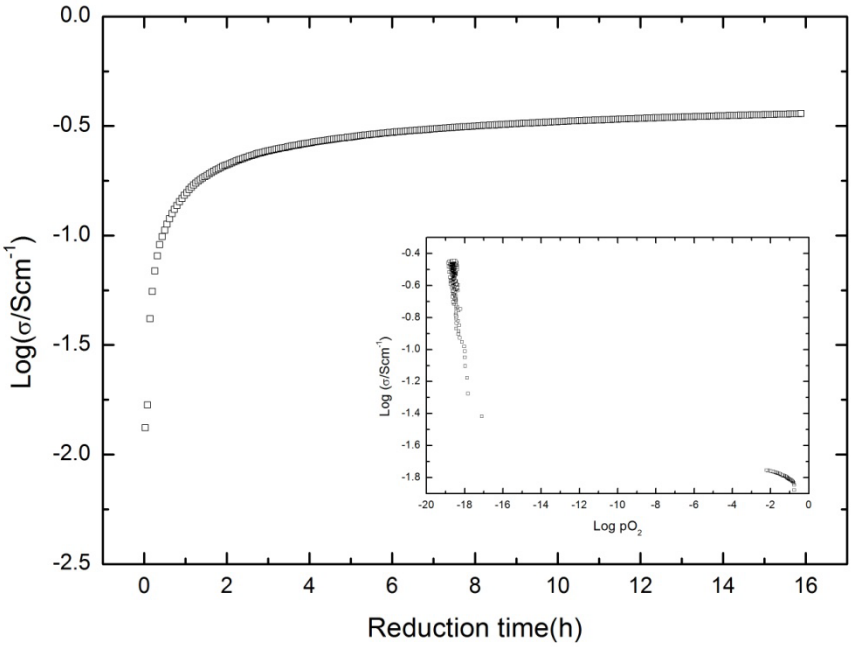

Figure 5-14 Electrical conductivity plotted as a function of time in reducing conditions at 850 °C; the inner plot shows the same data as a function of the partial pressure of the oxygen;

Figure 5-15 presents SEM images in cross-section of $MgFeCrO_4$ scaffold, with a general overview of the symmetrical architecture, the thickness of the YSZ electrolyte and the interface formed between YSZ and spinel. Sintered ceramic

bodies were not cracked or curved after sintering, thus it can be concluded that when co-sintering of YSZ and the spinel, the difference in thermal expansion coefficient did not imply a significant mechanical stress. The spinel had particle size 1-5 μm and optimum porosity for loading other materials by impregnation.

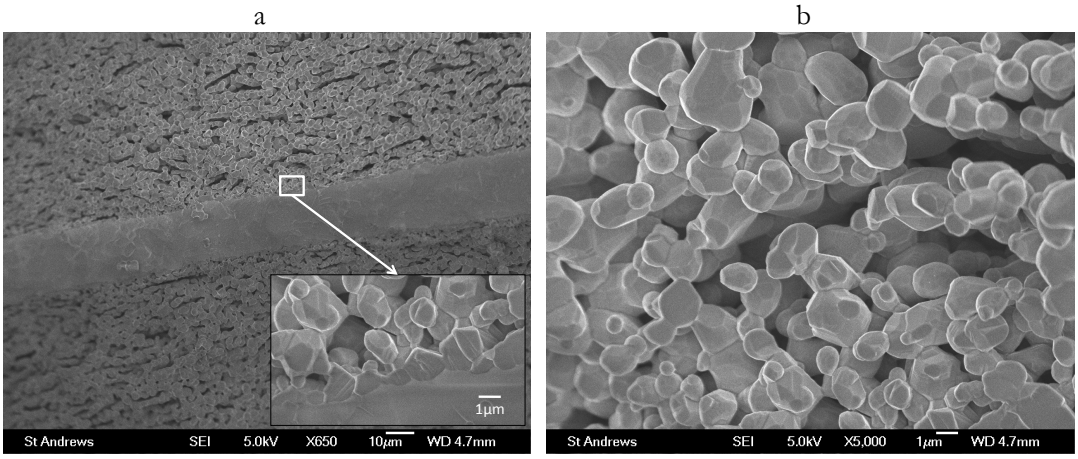

Figure 5-15 SEM images of $MgFeCrO_4$|YSZ|$MgFeCrO_4$ three layer wafer with details presented for the spinel - YSZ interface and the microstructure of the spinel porous layer.

5.3.2 Phase analysis and microstructure of impregnated scaffolds

The formation of perovskite phase within the scaffolds was confirmed by X-ray diffraction (Figure 5-16 and Figure 5-17). All the peaks observed in the XRD pattern correspond to phases present in the sample: spinel and perovskite or spinel, perovskite and CGO, respectively CeO_2. The XRD pattern for $MgFeCrO_4$/LSCM/CeO_2 (Figure 5-17) showed wide peaks corresponding to CeO_2 which was a good indication of the Ce nitrate decomposition with formation of CeO_2 with very small particle size.

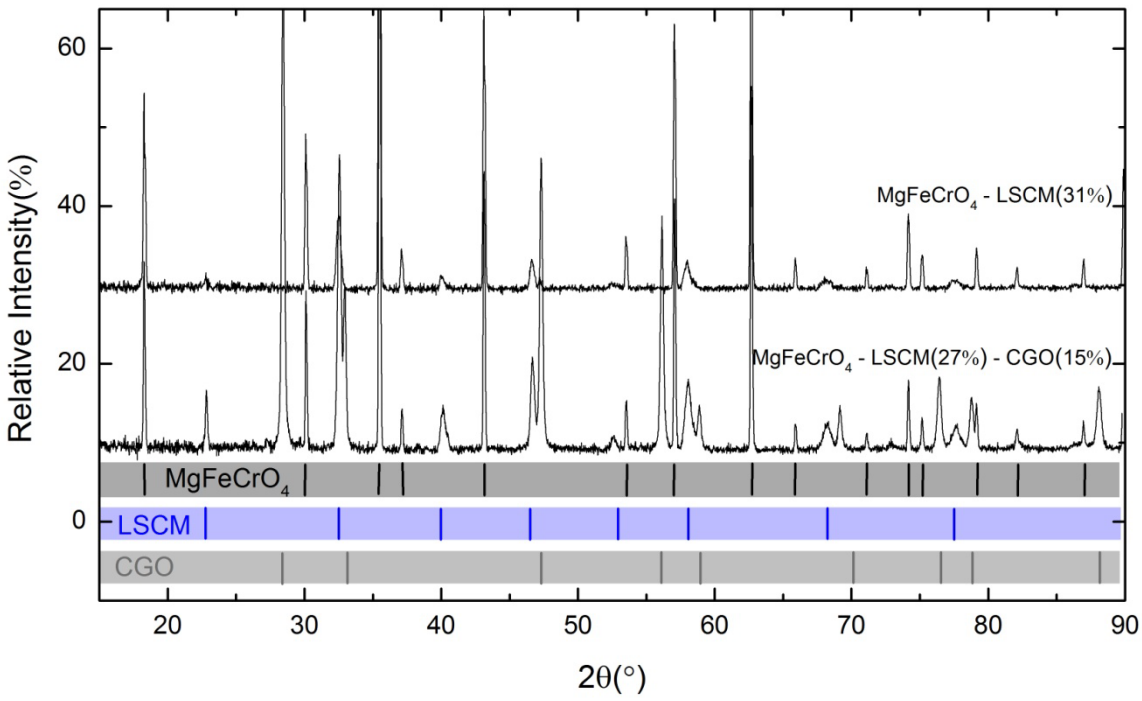

Figure 5-16 XRD pattern of $MgFeCrO_4$/LSCM and $MgFeCrO_4$/LSCM/CGO with LSCM sintered at 1200 °C (4 hours) and CGO at 1000 °C (4 hours); Oxide phases: spinel, perovskite and CGO.

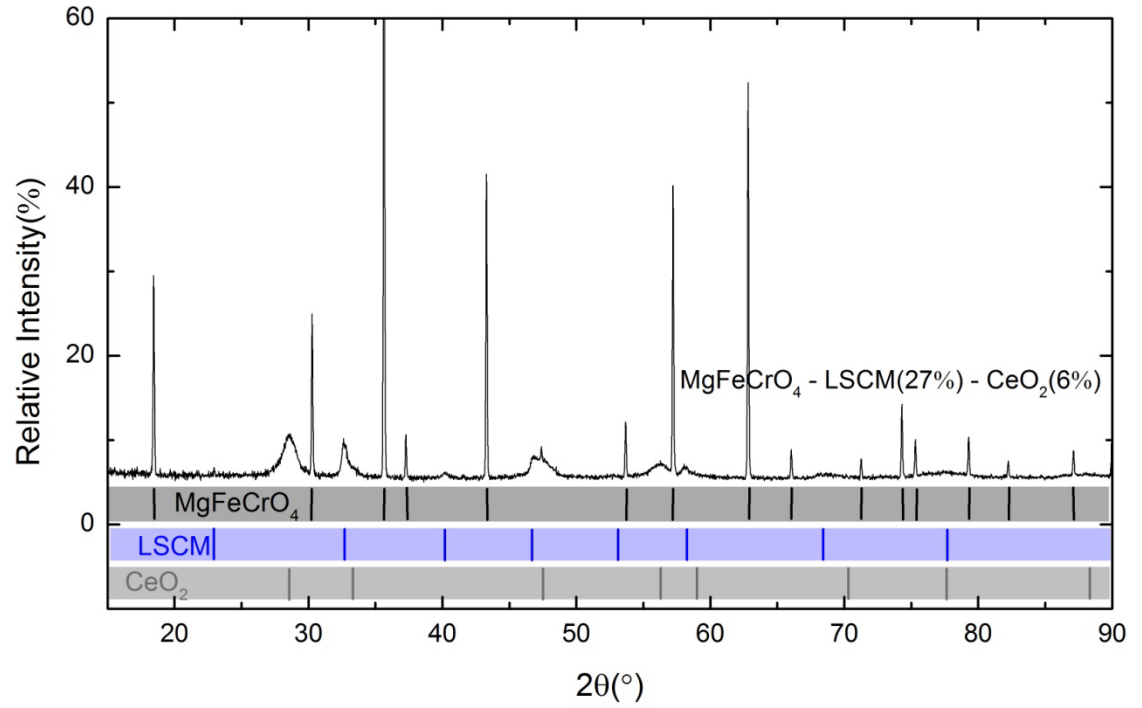

Figure 5-17 XRD pattern of MgFeCrO4/LSCM/CeO_2 with LSCM sintered at 1200 °C for 4 hours and CeO_2 at 450 °C (4 hours); Oxide phases: spinel, perovskite and CeO_2.

Figure 5-18 presents cross-sectional SEM images for samples tested in humidified 5%H_2/Ar. Cross-sectional SEM images confirm that impregnated phases have good adherence to the scaffold, while images from the surface show mostly the microstructure of the impregnated phases. In Figure 5-18 (a) the micrograph for $MgFeCrO_4$/LSCM showed LSCM particles (500 nm – 1 μm) that adhere well to the spinel particles. $MgFeCrO_4$/LSCM/CeO_2 (Figure 5-18 (b)) had a microstructure similar to $MgFeCrO_4$/LSCM samples and ceria nano-particles could be observed. The micrograph of $MgFeCrO_4$/LSCM/CGO (Figure 5-18 (c)) confirmed that additional thermal treatments at 1000 °C following the infiltration of CGO, led to densification of LSCM layer, while CGO particles of size 0.1-0.5 μm were apparently very well connected to the LSCM layer. For $MgFeCrO_4$/LSCM/CeO_2/Pd, CeO_2 and Pd nano-particles could be observed on the LSCM layer. Figure 5-18 (e, f) illustrates the microstructure of $MgFeCrO_4$/LSCM/CGO/Pd in cross section (e) and surface micrograph (f) suggesting the presence of Pd nanoparticles with size ~10-20 nm on top of larger particles of CGO. Pd nanoparticles are expected to behave as electrocatalytic sites during symmetrical cell electrochemical testing.

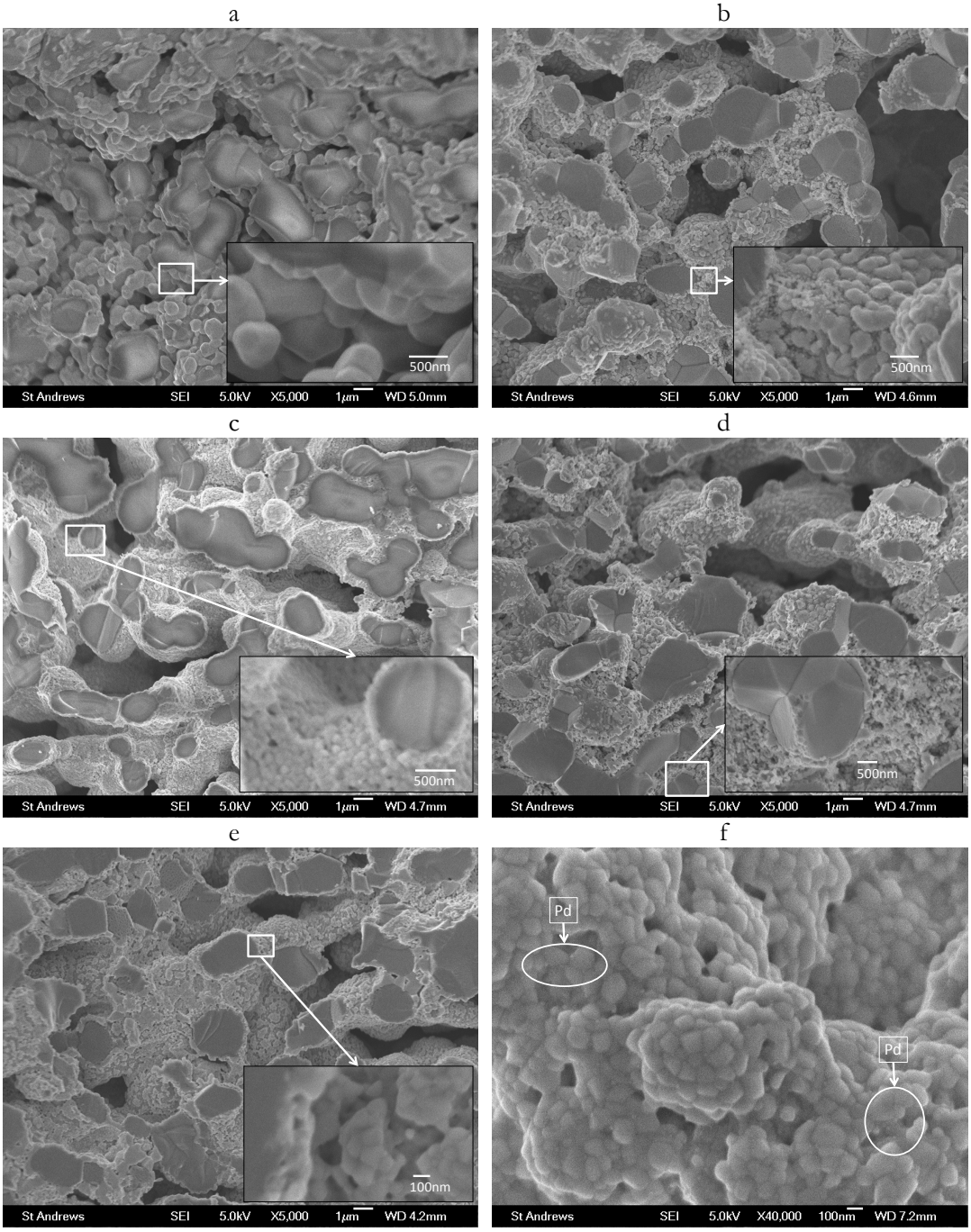

Figure 5-18 SEM images in cross section of: a) MgFeCrO4/LSCM; b) MgFeCrO4/LSCM/CeO_2; c) $MgFeCrO_4$/LSCM/CGO; d) $MgFeCrO_4$/LSCM/CeO_2/Pd; e) $MgFeCrO_4$/LSCM/CGO/Pd and f) surface micrograph for $MgFeCrO_4$/LSCM/CGO/Pd – Pd particles are present; the micrographs were made after the samples were tested in humidified – 5%H_2/Ar.

5.4 Performance of impregnated scaffolds

Figure 5-19 (a,b) presents impedance spectra as Nyquist and Bode plots for the symmetrical cells at 850 °C in humidified 5%H_2/Ar displayed in a comparative manner, for a better overview of the contribution of different catalysts. Table 5-5

summarises electrochemical data obtained by fitting of experimental data to the equivalent circuit illustrated in Figure 5-20. Temperature dependence of series resistances (R_s) and polarisation resistances (R_p) values are shown in Figure 5-19 (c, d) as Arrhenius plots. A significant difference observed between $MgFeCrO_4$ and $MgFeCrO_4$/LSCM consisted in R_s value of $MgFeCrO_4$/LSCM that remained very high even after reducing the sample. This may have been caused by two different contributions: first, LSCM impregnated into the scaffolds had a good adherence to spinel particles leading to a decrease in efficiency of reducing the scaffold. The resultant effect was the partial obstruction in enhancing the spinels electrical conductivity. Secondly, LSCM has p-type conductivity and in reducing atmosphere, its electronic conductivity decreases.[4,3] However, the infiltration of LSCM into the scaffold had a positive effect for the Rp value, as its electrochemical properties are superior to the spinel. The addition of CeO_2 or CGO further improved the cells performances, with both R_s and R_p decreasing. R_s values for $MgFeCrO_4$/LSCM/CGO and $MgFeCrO_4$/LSCM/CeO_2 were about the same, while R_p values were apparently proportional with the quantity of ionic conducting material into the sample. $MgFeCrO_4$/LSCM/CGO/Pd and $MgFeCrO_4$/LSCM/CeO_2/Pd showed even better performance in R_s and R_p, as presented in Figure 5-19 (a). Thus, the addition of catalysts contributed positively to the electrochemical tests, by facilitating the reduction of the scaffold at surface that resulted in formation of a layer with increased conductivity at scaffolds surface.

a

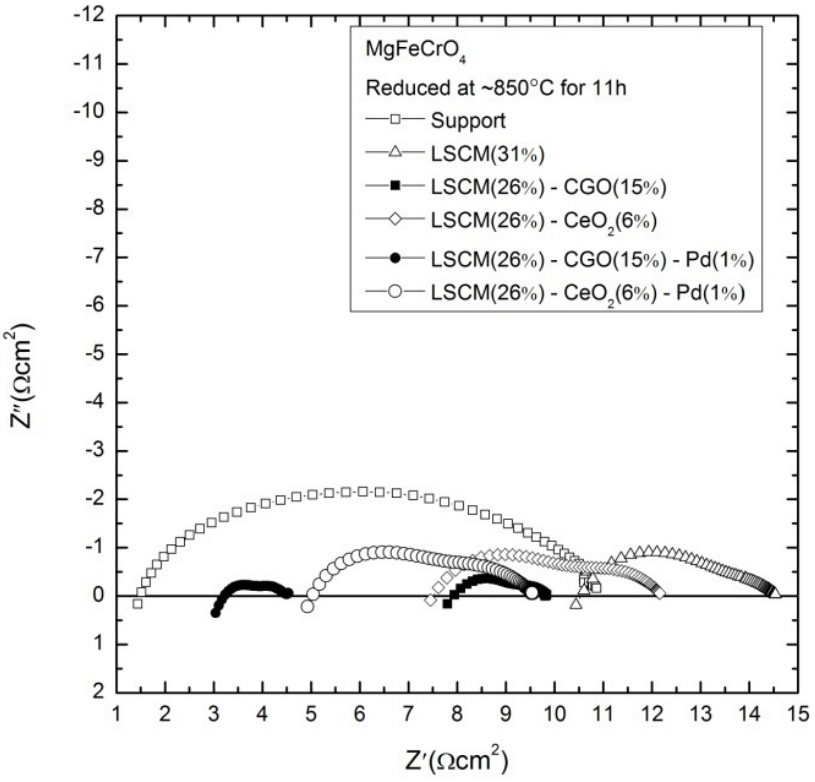
MgFeCrO4
Reduced at ~850°C for 11h
Support
LSCM(31%)
LSCM(26%) - CGO(15%)
LSCM(26%) - CeO2(6%)
LSCM(26%) - CGO(15%) - Pd(1%)
LSCM(26%) - CeO2(6%) - Pd(1%)
Z''(Ωcm2)
Z'(Ωcm2)

b

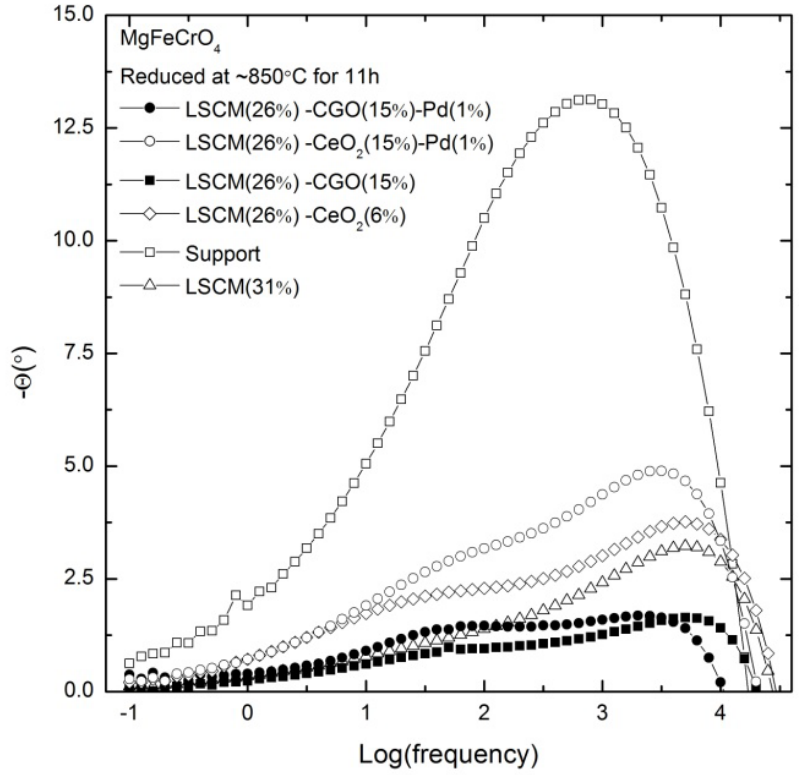
MgFeCrO4
Reduced at ~850°C for 11h
LSCM(26%) -CGO(15%)-Pd(1%)
LSCM(26%) -CeO2(15%)-Pd(1%)
LSCM(26%) -CGO(15%)
LSCM(26%) -CeO2(6%)
Support
LSCM(31%)
-Θ(°)
Log(frequency)

c

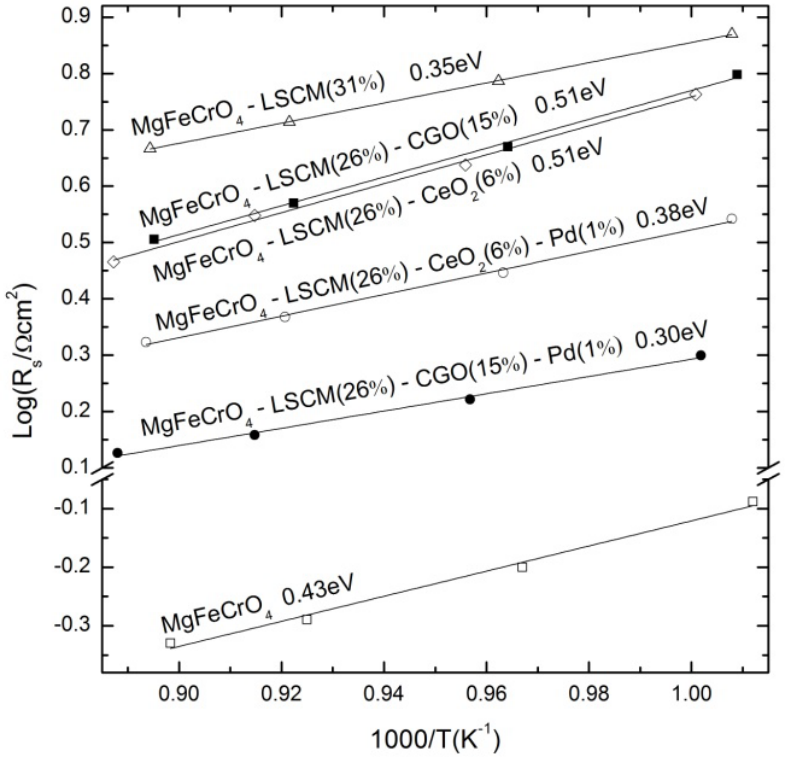

d

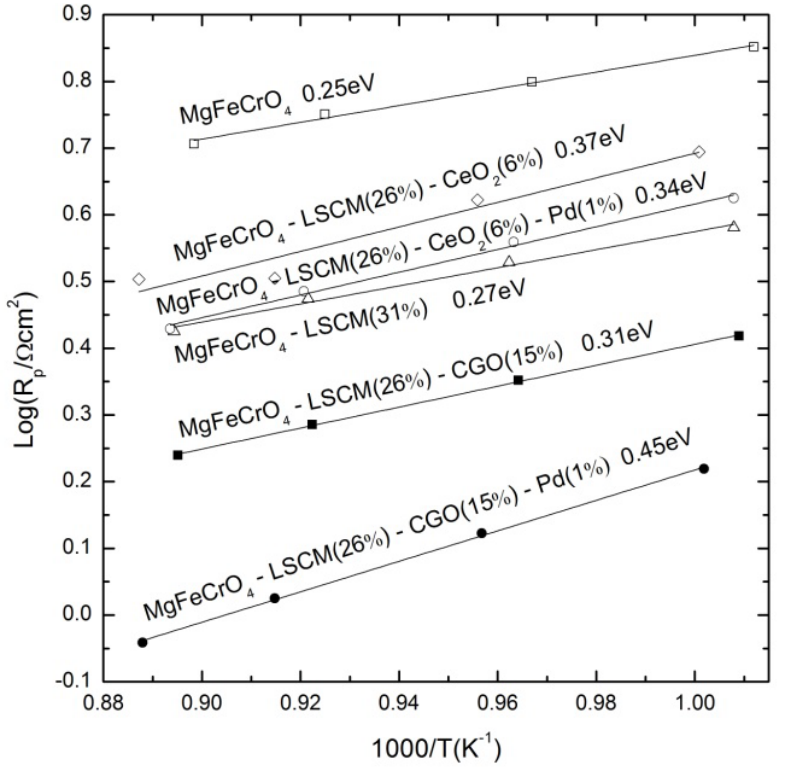

Figure 5-19 Symmetrical cells measured in humidified 5%H_2/Ar at 850 °C: a) Nyquist plot containing data for the whole cell (2 equal electrodes); b) – Bode plot of phase angle vs frequency; c), d) – Arrhenius plots for R_s and R_p obtained from equivalent circuits fitting of experimental data; plotted R_s and R_p values are for one electrode.

Electrode	R_s [Ω·cm²]	R_p [Ω·cm²]	f_{max1} [Hz]	Process 1	f_{max2} [Hz]	Process 2	R_{p1} [Ω·cm²]	R_{p2} [Ω·cm²]
$MgFeCrO_4$	0.47	5.09	1200	Charge transfer	132	Dissociative gas adsorption	0.80	4.29
$MgFeCrO_4$/LSCM	4.65	2.66	5250	Charge transfer	190	Dissociative gas adsorption	1.68	0.98
$MgFeCrO_4$/LSCM/CGO	3.20	1.74	6310	Charge transfer	76	Dissociative gas adsorption	1.25	0.48
$MgFeCrO_4$/LSCM/CeO_2	2.92	3.19	5250	Charge transfer	30	Dissociative gas adsorption	2.23	0.96
$MgFeCrO_4$/LSCM/CGO/Pd	1.33	0.91	3020	Charge transfer	63	Dissociative gas adsorption	0.56	0.35
$MgFeCrO_4$/LSCM/CeO_2/Pd	2.10	2.68	3630	Charge transfer	63	Dissociative gas adsorption	1.60	1.10

Table 5-5 Relaxation frequencies and polarisation resistances for symmetrical cells tested in humidified 5%H_2/Ar at ~ 850 °C; R_s and R_p (R_{p1}, R_{p2}) determined from equivalent circuits fitting and listed values are for one electrode.

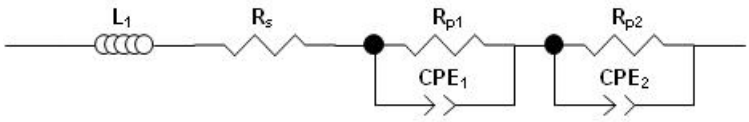

Figure 5-20 Equivalent circuit used to fit experimental data, where L = inductor; R_s = series resistance; R_p = polarisation resistance and CPE = constant phase element.

Impedance spectra showed two arcs, one process specific to high frequency and one process at low frequency. The presence of two semicircles was distinguishable for the impregnated samples, while the scaffold showed a bigger and depressed arc. The high frequency arc represented the predominant process and both processes were changing for different catalysts impregnated into scaffolds. The attribution of processes is based on relaxation frequencies [13,17,14], which in this study, were determined from equivalent circuits fitted to Bode plots (-Z"vs.f, Appendix 3) in order to attribute observed processes. The high frequency process corresponded to charge transfer and the low frequency process could be attributed to gas adsorption/desorption or association/dissociation. $MgFeCrO_4$ is not an ionic conductor, thus the high frequency process with f_{max1} = 1200 Hz corresponded to electronic transfer, while the low frequency process with f_{max2} = 132 Hz, was gas adsorption/desorption. Relaxation frequencies determined for $MgFeCrO_4$/LSCM had similar magnitudes to the scaffold ones, 5250 Hz for high frequency process and

190 Hz at low frequency, so probably they were determined by the same processes as previously described. In Table 5-5 are summarized relaxation frequencies, the associated processes at high and low frequency and R_{p1} and R_{p2} values corresponding to each process. Samples impregnated with different materials showed the same trend, the resistance was higher for charge transfer than for gas adsorption/desorption and association/dissociation, while the scaffold showed higher resistance for gas kinetics processes than for charge transfer. Activation energies, E_a for R_s and R_p are included in Figure 5-19 (c, d), where E_a for R_s is related to the conduction activation and E_a for R_p is related to the electrochemical processes described by the impedance spectra in Figure 5-19 (a). Determined E_a with regard to R_s (0.35 eV) for $MgFeCrO_4$/LSCM was lower than E_a value of 0.56 eV measured for LSCM in 5%H_2/Ar,[4] and the E_a value 0.43 eV determined for the scaffold. Ea values for R_s generally remained below 0.51 eV, maximum value corresponding to $MgFeCrO_4$/LSCM/CGO and $MgFeCrO_4$/LSCM/CeO_2. The E_a values for R_p showed an increase from the scaffold (0.25 eV) to the composite electrodes, with a maximum value of 0.45 eV observed for $MgFeCrO_4$/LSCM/CGO/Pd.

The good electrochemical performance of $MgFeCrO_4$/LSCM/CGO/Pd (0.91 $\Omega \cdot cm^2$) in particular, was comparable to results reported for LSCM used as an SOFC anode material. In humidified 5%H_2/Ar at 850 °C, R_p of 0.59 $\Omega \cdot cm^2$ has been observed [4,6], while at 900 °C R_p values of 0.51 $\Omega \cdot cm^2$ and 0.43 $\Omega \cdot cm^2$ have been measured, as reported in ref [4,6], respectively. In humidified H_2 at 900 °C Bastidas *et al.*[5] reported an R_p of 0.3 $\Omega \cdot cm^2$, while Jiang *et al.*[19] reported R_p values for a 1 : 1 composite LSCM-YSZ, with LSCM obtained by gel-casting or solid state reaction of 1.1 $\Omega \cdot cm^2$ and 1.9 $\Omega \cdot cm^2$, respectively. The comparable results obtained here relative to results reported in the literature are encouraging since the $MgFeCrO_4$ scaffold is not an ionic conducting material and since the amount of loaded perovskite was limited. Furthermore, E_a values for R_p included in Figure 5-19 (c, d) were lower than Ea values of between 0.70-0.90 eV reported by Jiang *et al.*[19] for LSCM/YSZ composite anodes.

5.5 Influence of reduction upon electro-chemical performance

The reduction process was studied on symmetrical cells at ~850 °C in humidified 5%H_2/Ar, with impedance measurements taken periodically for 11 hours. In this

study are discussed impedance spectra measured after 1 hour and 11 hours in order to quantify the influence of reduction time upon tested cells. In Figure 5-21, Figure 5-22 and Figure 5-23 are presented Nyquist plots for measurements at 1 hour and 11 hours and the corresponding equivalent circuits fit. Measured results are in a good agreement with the modelled data points indicating a good fit of the equivalent circuit with the electrochemical processes. The performance of the cells improved with reducing time consistently: for $MgFeCrO_4$ the reduction had a significant effect on the R_p value (3.26 $\Omega \cdot cm^2$), decrease corresponding to the low frequency process, possibly due to improvements in the gas surface exchange kinetics after reduction. MgFeCrO4/LSCM showed a decrease in R_s and an increase in R_p corresponding to an increase in resistance of both high and low frequency processes: 0.12 $\Omega \cdot cm^2$ for R_{p1}, and 0.21 $\Omega \cdot cm^2$ for R_{p2}. $MgFeCrO_4$/LSCM/CeO_2 had a small decrease of R_p and an important decrease of R_s with ~0.55 $\Omega \cdot cm^2$ after 11hour of reduction. Reduction of $MgFeCrO_4$/LSCM/CGO showed a significant improvement in R_s (~ 1 $\Omega \cdot cm^2$ decrease) and R_p (~ 0.22 $\Omega \cdot cm^2$ decrease in R_{p1} and ~0.08 $\Omega \cdot cm^2$ decrease in R_{p2}). $MgFeCrO_4$/LSCM/CeO_2/Pd and $MgFeCrO_4$/LSCM/CGO/Pd had similar improvement in the cells performance after reduction with a decrease of R_s values (~ 0.3 $\Omega \cdot cm^2$), while R_p did not change. The values reported above are for one electrode. The reduction process had positive effects for cell performance and this contribution was more important than the negative effect corresponding to sintering of ceria nano-particles,[10] a process that cannot be noticed here.

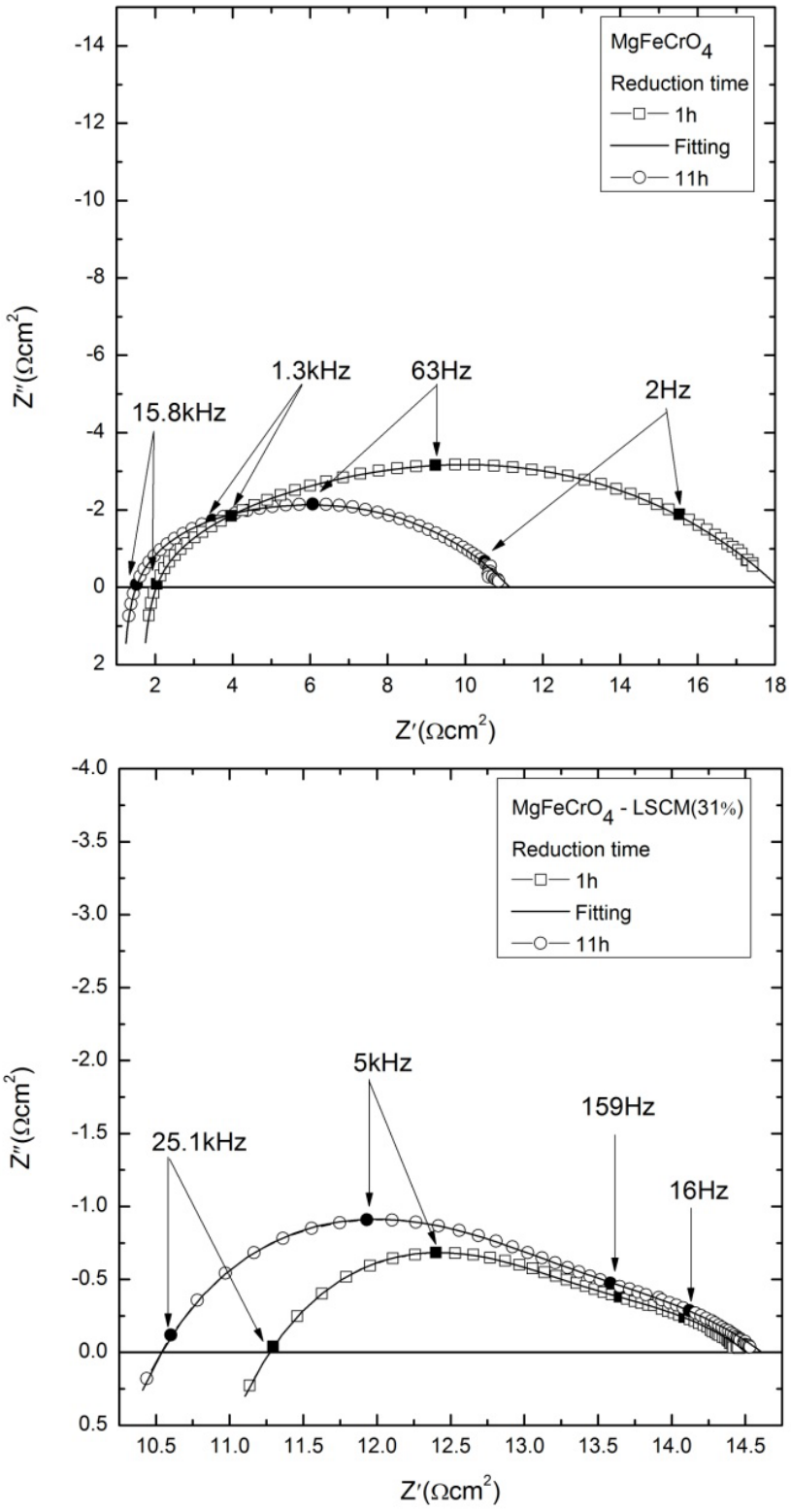

Figure 5-21 Nyquist plots of $MgFeCrO_4$ and $MgFeCrO_4$/LSCM reduced at 850 °C for 1 hour/ 11 hours and corresponding equivalent circuits fit; spectra contain data for two identical electrodes.

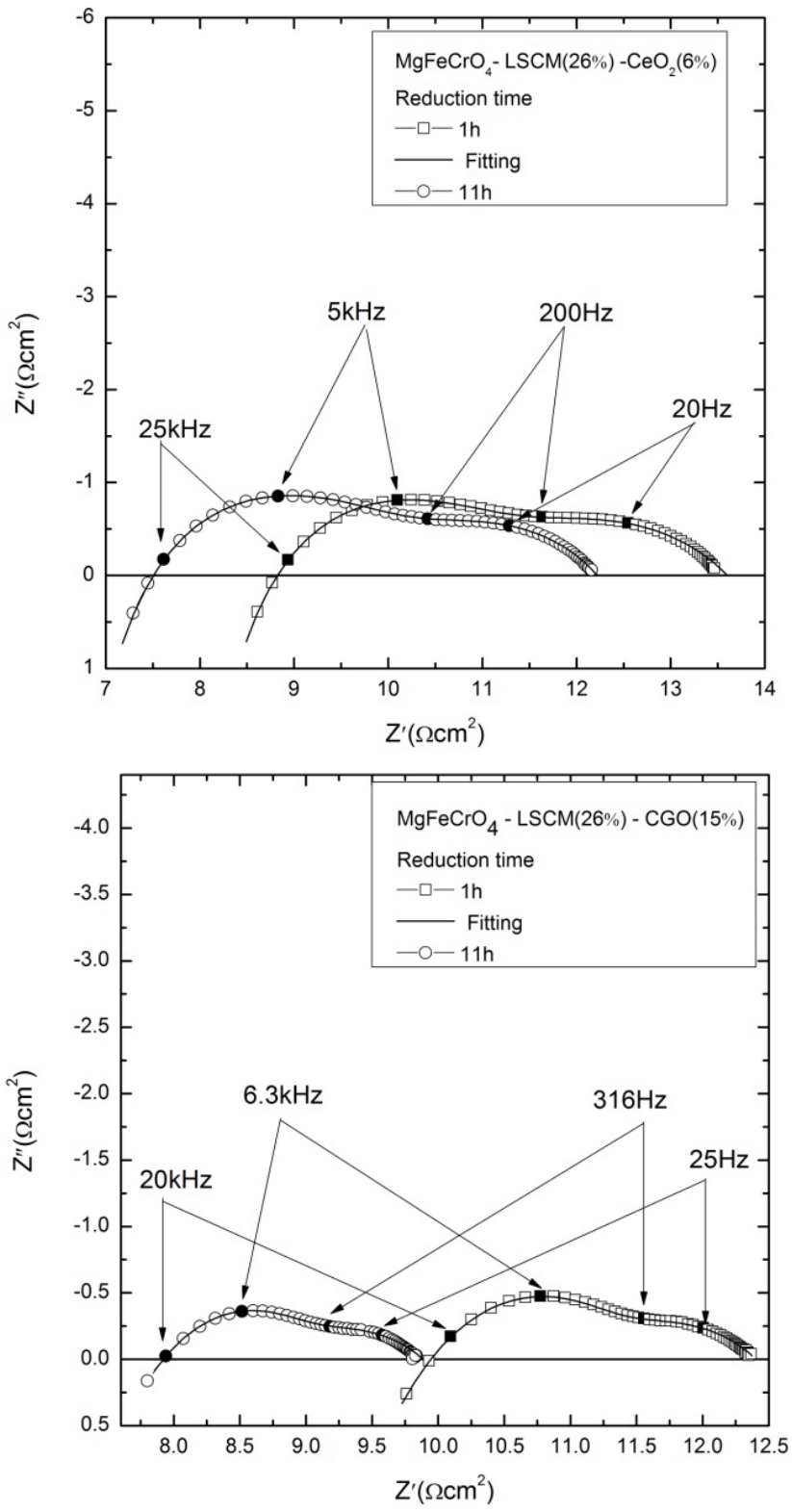

Figure 5-22 Nyquist plots of $MgFeCrO_4$/LSCM/CeO_2 and $MgFeCrO_4$/LSCM/CGO reduced at 850 °C for 1 hour/ 11 hours and corresponding equivalent circuits fit; spectra contain data for two identical electrodes.

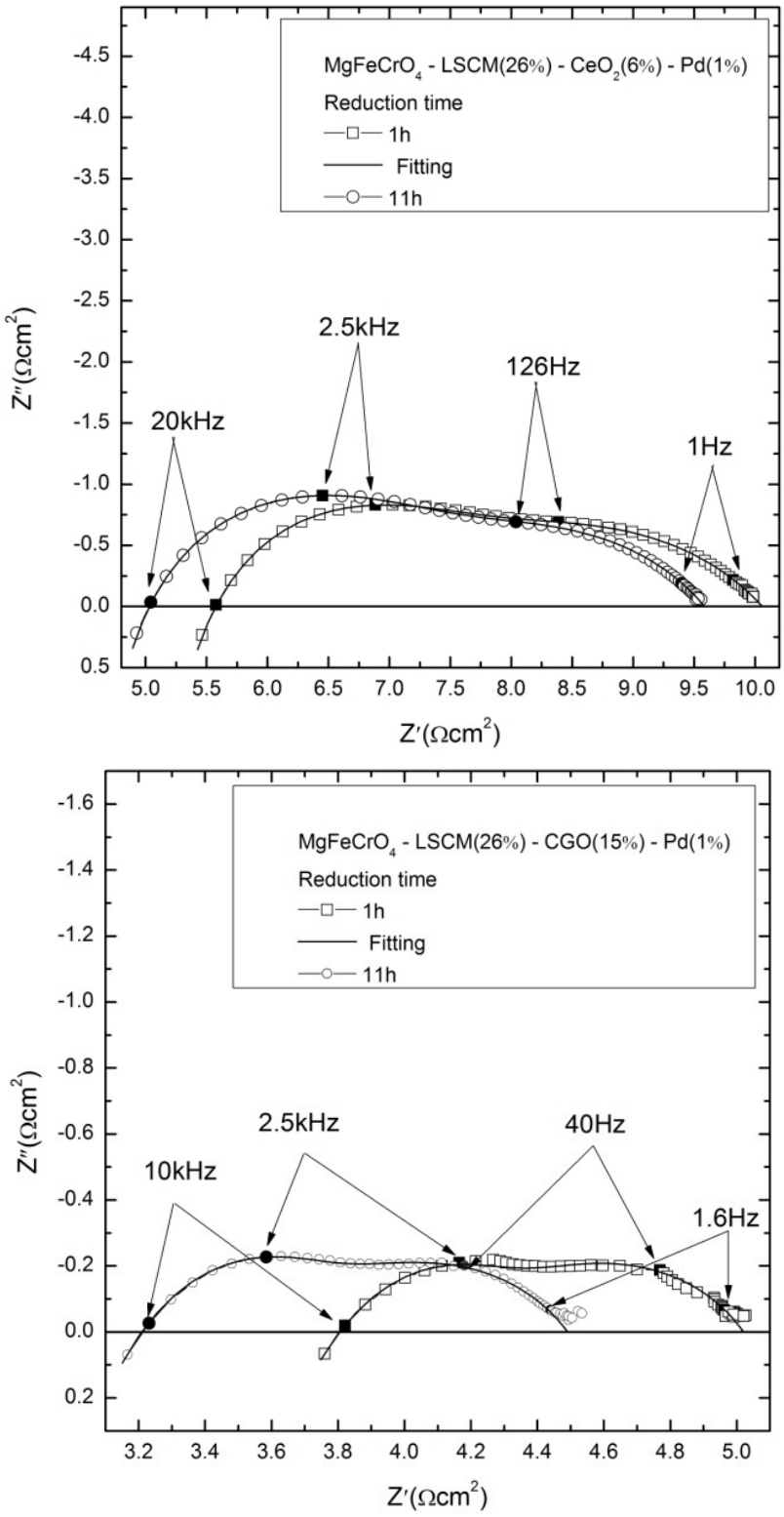

Figure 5-23 Nyquist plots of $MgFeCrO_4$/LSCM/CeO_2/Pd and $MgFeCrO_4$/LSCM/CGO/Pd reduced at 850 °C for 1 hour/ 11 hours and corresponding equivalent circuits fit; spectra contain data for two identical electrodes.

The reduction process had a positive influence for the symmetrical cells performance even if hindered by impregnated electrode materials. The formed coating diminished the scaffolds reduction, thus leading to an increase in R_s for tested samples. However, the insertion of electrode materials into the scaffolds decreased polarisation resistances of the cells, as it formed a new conducting path and their electrochemical activity was superior to the spinel. Further catalysts insertion enhanced the performance of symmetrical cells, by facilitating the reduction of the scaffold at surface and new electrocatalytic active sites were formed.

Overall, both reduction process and increase of electrocatalytic activity determined improvements in the electrochemical performance of tested cells. Important changes were not expected for these samples after reduction, as the micrographs illustrated in Figure 5-18 showed a good integrity of the scaffold, of the impregnated layers and their interface. A change in microstructure consisted in the densification of the impregnated CeO_2 layer after prolonged thermal treatment (850 °C) at a temperature higher than the calcining temperature (450 °C) - see Figure 5-18 (b, d).

5.6 Conclusions

$MnFeCrO_4$ and $MgFeCrO_4$ were successfully processed into porous substrates for electrode materials and the impedance spectra for symmetrical cells with composite electrodes were studied in air and humidified 5%H_2/Ar with Pt paste as current collector.

$MnFeCrO_4$ porous scaffold showed good performance as cathode electrode support and promising results as anode electrode support since infiltrated electrode materials had good adherence to spinel particles, thus greatly improving the stability of $MnFeCrO_4$in reducing conditions. Cathodes tests demonstrated substantial and coherent improvement in R_s and R_p of measured symmetrical cells.

Anode tests are concluded with very good improvement, decreasing R_p values, although they showed a certain inconsistency in the R_s values. The best notable results corresponded to the samples containing catalysts as CGO, CeO_2, CGO-Pd and CeO_2-Pd.

After impregnation of electrode materials into scaffolds, the effects of reduction are more important for the impregnated layer. It was a core-shell effect that led to a

better stability for spinel, avoiding decomposition of the material. Prolonged reduction periods did not improve the cell performances, only the negative effect of ceria sintering contributed to a decrease in R_s and R_p values. It was found that the dominant contribution to R_p consists of surface kinetics, including diffusion process and dissociative adsorption of active species on electrodes surface.

$MgFeCrO_4$ had good performance as anode an electrode support and the infiltrated materials also had a good adherence to the spinel particles. The formed coating diminished the scaffold's reduction, thus leading to an increase in R_s for tested samples. However, the insertion of electrode materials into the scaffolds decreased polarisation resistances of the cells, as it formed a new conducting path and their electrochemical activity was superior to the spinel. Further catalysts insertion enhanced the performance of symmetrical cell as new electrocatalytic sites were active during electrochemical tests.

The reduction process had a positive influence for the symmetrical cells performance even if hindered by infiltrated electrode materials. Overall, both reduction process and increase of electrocatalytic activity determined improvements in the electrochemical performance of tested cells.

5.7 References

1. Y. Huang, J. M. Vohs, and R. J. Gorte, *J. Electrochem. Soc.*, 2004, **151**, A646.
2. Corre, G. Kim, M. Cassidy, J. M. Vohs, R. J. Gorte, and J. T. S. Irvine, *Chem. Mater.*, 2009, **21**, 1077–1084.
3. G. Kim, G. Corre, J. T. S. Irvine, J. M. Vohs, and R. J. Gorte, *Electrochem. Solid St.*, **11**.
4. S. Tao and J. T. S. Irvine, *Nat. Mater.*, 2003, **2**, 320–323.
5. D. M. Bastidas, S. Tao, and J. T. S. Irvine, *J. Mater. Chem.*, 2006, **16**, 1603–1605.
6. J. C. Ruiz-Morales, J. Canales-Vázquez, J. Peña-Martínez, D. Marrero-López, and P. Núñez, *Electrochim. Acta*, **52**, 278–284.
7. X. Yang and J. T. S. Irvine, *J Mater Chem*, 2008, **18**, 2349–2354.
8. M. Mogensen, N. M. Sammes, and G. A. Tompsett, *Solid State Ionics*, 2000, **129**, 63 – 94.
9. J. H. Kim, D. Miller, H. Schlegl, D. McGrouther, and J. T. S. Irvine, *Chem. Mater.*, 2011, **23**, 3841–3847.
10. M. Gross, J. Vohs, and R. Gorte, *J. Electrochem. Soc.*, 2007, **154**, B694–B699.
11. F. Bidrawn, S. Lee, J. M. Vohs, and R. J. Gorte, *J. Electrochem. Soc.*, 2008, **155**, B660–B665.
12. J. Rossmeisl and W. G. Bessler, *Solid State Ionics*, 2008, **178**, 1694 – 1700.
13. M. J. Jørgensen and M. Mogensen, *J. Electrochem. Soc.*, **148**, A433–A442.
14. I. M. Torres da Silva, J. Nielsen, J. Hjelm, and M. Mogensen, *ECS Transactions*, 2009, **25**, 489–498.
15. G. Tsekouras and J. T. S. Irvine, *J. Mater. Chem.*, 2011, **21**, 9367–9376.
16. A. Ghosh, A. Azad, and J. T. S. Ivine, *ECS Transactions*, 2011, **35**, 1337–1343.
17. T. Ramos, J. Hjelm, and M. Mogensen, *J. Electrochem. Soc.*, **158**.
18. S. Tao and J. T. S. Irvine, *J. Electrochem. Soc.*, 2004, **151**, A252–A259.
19. S. P. Jiang, L. Zhang, and Y. Zhang, *J. Mater. Chem.*, 2007, **17**, 2627–2635.
20. W. Wang, M. Gross, J. Vohs, and R. Gorte, *J. Electrochem. Soc.*, 2007, **154**, 8439–8445.
21. R. Küngas, J. Vohs, and R. Gorte, *J. Electrochem. Soc.*, 2011, **158**, B743–B748.

6 Conclusions

The work summarised in this thesis focused on the development and characterisation of new chromium-rich spinels and their integration and testing as electrode supports for SOFC. Initially, the structure, stability in reducing conditions and conductivity of the newly prepared materials was assessed and then the most suitable candidates were brought forward for device testing.

It was found that $MnM_xCr_{2-x}O_4$ (M = Fe, Mn, Mg or Li) spinels generally have low stability when reduced. Segregation of secondary phases, such as MnO and metallic Fe occurred when materials were reduced in dry 5%H_2/Ar. Better stability was observed when samples were reduced in humidified 5%H_2/Ar that corresponded to milder reducing conditions, and which is in fact closer to real SOFC operating conditions. $MnCr_2O_4$ showed very good stability on reduction, however, it exhibits low conductivity which further decreases upon reduction due to its p-type behaviour. Among this series only $MnFeCrO_4$ showed n-type conductivity.

$MgM_xCr_{2-x}O_4$ (M = Cr, Li, Mg, Ti, Fe, Cu, Ga) spinels demonstrated good stability in reducing conditions and only the samples containing Fe showed segregation of metallic Fe after reduction. The electrical conductivity determined was mainly p-type semiconductor behaviour. $MgFeCrO_4$ demonstrated n-type conductivity and its stability to reduction was improved when determined in humidified 5%H_2/Ar.

The spinel stability on reduction may be influenced by a combination factors including the reducibility of constituting cations, the cation size and coordination number in lower oxidation states in the spinel structure and the inability of the spinel structure to accommodate significant oxygen deficiency.

Cation inversion was determined by performing Rietveld refinement on XRD data, based on the initial assumptions that Cr^{3+} cations are located only at B sites, the A and B sites are fully occupied. The as-determined inversion degree was confirmed to some extent indirectly by the way conductivity correlated with the determined cation occupancy. For example, $MgFe_xCr_{2-x}O_4$ showed that Mg inversion on the B-site increased with Fe doping while conductivity was found to decrease with Fe doping. Since conductivity occurs on the B-site in the spinel lattice, and Mg does not

contribute to conduction, it follows that the determined cation inversion explains well the conductivity data.

Similar correlations between determined cation inversion and conductivity was found for $MgM_xCr_{2-x}O_4$ upon substituting x = 0.1 Cr with Cu, Ga, Li, Fe. The materials maintained the p-type conductivity, with lower conductivities for Fe and Ga substitutions and higher conductivities for Cu and Li substitutions than the parent composition, $MgCr_2O_4$. The higher conductivity for Cu and Li substitutions may have been caused by the charge compensation which induced formation of electron holes in the spinel at the B site, with formation of Cr^{4+} cations.

In the case of cations with similar atomic numbers, the refinement of the inversion degree (*e.g.* Mn, Fe, Cr) was not considered, as their scattering factors are very similar in XRD, thus the spinels $MnM_xCr_{2-x}O_4$ were refined mostly as normal spinels. Also, in some cases, the cation inversion did not correlate well to other data, perhaps due to similar scattering factors between cations and the fact that oxygen is not a strong scatterer of X-rays which overall may induce errors in the refinement and hence in the cation site occupancy and oxygen atomic position.

Lithium titanates were stable as spinels for temperatures up to 1300 °C, enough to be processed into SOFC devices if considered. The spinels demonstrated good stability in reducing conditions and had good conductivity in air and reducing atmosphere. However, because of their high Li content, these materials were not considered as a good option for electrode support materials.

$MnFeCrO_4$ and $MgFeCrO_4$ were processed as porous scaffolds for electrode materials via tape casting and screen printed with YSZ electrolyte. Symmetrical cells were produced by co-laminating the screen printed tape with another spinel tape. The obtained cells showed good thermo-mechanical stability to a multi-step impregnation process with the phases: LSF, LSCM, LSCM/CGO, LSCM/CGO/Pd, LSCM/CeO_2 and LSCM/CeO_2/Pd. $MnFeCrO_4$ based cells were tested in air, as cathodes and in humidified 5%H_2/Ar, as anodes, while $MgFeCrO_4$ based cells were tested only in 5%H_2/Ar, as anodes.

The infiltrated electrode materials had good adherence to the $MnFeCrO_4$ spinel particles, which determined substantial and coherent improvement in series and

polarisation resistances with impregnation. It also greatly improved the stability of $MnFeCrO_4$ in reducing conditions. The reduction process at constant temperature of the symmetrical cells with different catalysts did not initiate notable improvements, but the performance remained mostly constant during reduction.

A good adherence of the infiltrated phases to the spinel particles was observed also for $MgFeCrO_4$. The electrochemical performance of $MgFeCrO_4$/LSCM as anode was characterised by an increase in the ohmic resistance, simultaneous with decreasing the polarisation resistance. The formed LSCM coating diminished the reduction of $MgFeCrO_4$ support. The insertion of catalysts may have catalysed the reduction of the scaffold to some extent, since the ohmic resistance decreased when CeO_2, CGO, Pd were present along with LSCM in the composite electrodes. Furthermore, the insertion of electrode materials into the scaffolds decreased polarisation resistances of the cells, as it formed a new conducting path and the electrochemical activity was superior to the spinel. Further catalyst insertion enhanced the performance of symmetrical cell as new electrocatalytic sites were active during electrochemical tests. The best results were obtained when CeO_2/Pd or CGO/Pd were employed for both types of tested scaffolds. The ASR values for $MnFeCrO_4$/LSCM/CGO/Pd and for $MnFeCrO_4$/LSCM/CeO_2/Pd were 0.85 Ωcm^2 and 0.61 Ωcm^2, respectively. While for $MgFeCrO_4$ scaffold, the lowest ASR values were obtained for the cells $MgFeCrO_4$/LSCM/CGO and $MgFeCrO_4$/LSCM/CGO/Pd, with 1.74 Ωcm^2 and 0.91 Ωcm^2, respectively.

7 Appendix 1 – Rietveld refinement – general procedure and detailed steps exemplified on a selected composition

The Rietveld refinement procedure employed in this thesis is described in detail here. The main purpose of the refinement is to assess the suitability of the considered structural model and derive other crystal structure parameters such as the unit cell parameter, the oxygen atomic parameter and cation site distribution.

7.1 Structural models reported in literature

In literature, spinels are described as stoichiometric materials. The charge distribution on the A and B cations is allocated by balancing the positive and negative charge between cations and oxygen anions, or by inversion in the case of $MgAl_2O_4$ (subsection 1.4.2).[1–7]

The Rietveld refinement applied on spinels is generally performed using stoichiometric structural models, for which cation site occupancy is constrained to its stoichiometric value and the oxygen content is stoichiometric as well.[8–12] A comparison to other possible structural models described in literature may offer a better portrait of the limitations and accuracy of the method applied.

Gaudon et al.[8] used different models when refining X-ray diffraction patterns (PANalytical X'PERT PRO diffractometer, and 2θ step = 0.017°, with a counting time over 200 s per step, 10-120° 2θ range) for $MgFe_2O_4$ and $ZnFe_2O_4$, complemented by Mössbauer studies to evaluate Fe^{3+} local environments and magnetic ordering. They considered in their refinement structural model cationic and anionic vacancies and/or interstitial atoms instead of partial inversion rate. As a starting refinement model they used the fully inverted spinel, without any cationic/anionic vacancies. The considered model was not satisfying since the isotropic displacement factors for 16d site cations were negative (the electronic density too low with this structural hypothesis). When they considered partially inverted spinel, they observed a very important improvement of the refinement (Mg atoms z = 12 contain less than half as many electrons as Fe : z = 26, for which their scattering factors could be differentiated by XRD). Two criteria were considered that led to again modify the structural models applied. One included the isotropic displacement factors for the A site cations being slightly larger than for the B site

cations. The second criterion was based on the comparison of the M-O bond lengths deduced from the refinement with theoretical values. Thus, the structural model considered for Rietveld refinement was fully inverted $MgFe_2O_4$ with cation/anion vacancies considered: $Fe_{1-3x}[Mg_{1-x}Fe_{1+x}]O_{4-4x}$. A similar approach was used for $ZnFe_2O_4$, with the final model considered as $Zn_{1-3x}[Zn_{2x}Fe_{2-2x}]O_{4-4x}$ and refined as only cation/anion vacancies and refined also with interstitial oxygen. Based on the refined models, they generated Fourier maps and observed important improvement for the partially inverted model and great improvement of the electronic residues when cation/ anion vacancies and/or interstitial atoms model was used.

A similar approach to Gaudon *et al.*[8] for the diffraction patterns refined here would rather be over-refining the experimental data. In this thesis, the XRD data were refined considering as starting refinement model the normal spinel and at later stages of the refinement, the partially inverted spinel was considered.

7.2 The intermediary stages of the refinement

The stages of the full pattern fitting used in this work are described and intermediary stages are presented for the refinement of $MgFeCrO_4$. The refinement strategy was adopted based on the refinement strategies described in ref [13]. Starting with a reasonably good structural model is recommended: known chemical formulae (composition), space group, atomic positions and initial values for peak profile parameters of the used diffraction machine.[13,14]

7.2.1 Initial premises of the structural model

The model implemented initially in FullProf for $MgFeCrO_4$, considered the space group Fd-3m (Z=8) with origin at -3m and positions 8a (¼, ¼, ¼), 16d (½, ½, ½) and 32e (u, u, u) for the cations on A, B sites and for oxygen anions, respectively, as described in chapter 3.

The occupancy of the cations on the A and B sites was considered $(Mg_{0.99}Fe^{3+}_{0.01})_{Td}(Mg_{0.01}Fe^{3+}_{0.99}Cr)_{Oh}O_4$, with a formal 1% of inversion between A and B sites and considering that inversion occurs only between Mg^{2+} and Fe^{3+} cations. Cr was considered to be situated only at the B sites since its strong preference for octahedral coordination is well known, as a consequence of the crystal field

stabilisation.[2,4,5,15–18] Only Fe^{3+} was considered to be present on both A and B sites. The initial value considered for the cell parameter was a = 8.3673 Å (determined from peak indexing with WinXPOW software), u = 0.260 Å and a general thermal factor, B_iso = 0.2 $Å^2$.

7.2.2 Rietveld refinement steps

Briefly, the refinement was conducted according to the steps:

Stage 1: background;

Stage 2: background + scale factor;

Stage 3: background, scale factor, cell parameter and oxygen parameter;

Stage 4: peak profile parameters;

Stage 5: background, scale factor, cell parameter and oxygen parameter; add peak profile parameters;

Stage 6: thermal factor;

Stage 7: cation distribution on the A and B sites; (two intermediary stages with alternating the refinement of the cation inversion and cell parameter + oxygen parameter + scale factor led to significant improvement of the profile fitting)

Stage 8: atomic isotropic displacement factors;

Stage 9: background, scale factor, cell parameter and oxygen parameter; the peak profile parameters and cation distribution on the A and B sites were added; next, the cation distribution was fixed and the atomic isotropic displacement factors refined.

Thus, initially, the global parameters were refined: the background as a polynomial function, and the scale factor. The zero shift value was calibrated for, using internal or external Si standard. Subsequently were refined the unit cell parameter and the oxygen parameter, considering a fixed general thermal factor.

The next stage consisted of refinement of the peak profile parameters, while the other parameters were fixed. A further improvement was obtained by re-starting the refinement of the background, scale factor, unit cell parameter, oxygen parameter with the peak profile parameters fixed, followed by their release and refinement along with the other parameters. After this stage, the general thermal factor was refined as well. In Figure 7-1 is presented the Rietveld refinement profiles (observed, calculated and difference) and Table 7-1 summarizes several refined parameters along with the reliability factors of the refinement at this stage. The peak profile is well

refined, while the difference profile between observed and calculated intensities shows important difference between calculated and observed intensity, which is an indication of a certain inversion degree in the spinel structure.

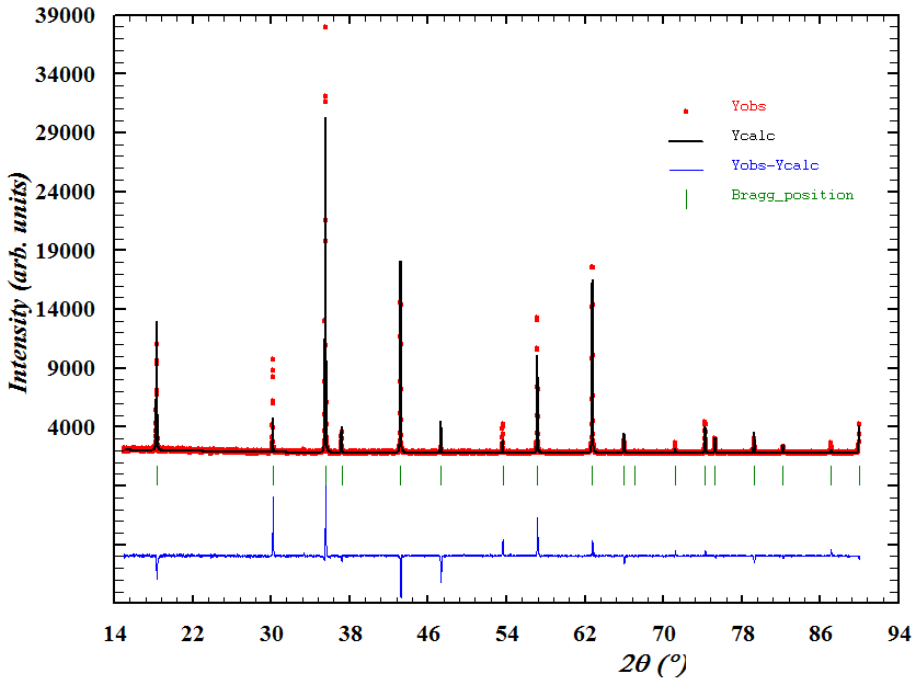

Figure 7-1 Rietveld refinement profiles of MgFeCrO4 after initial stages of refinement and before refining the degree of inversion in the spinel and the atomic isotropic displacement factors, which corresponds to stages 1-6 described in the refinement strategy.

Refined parameter	$MgFeCrO_4$
a (Å)	8.36715(8)
u (Å)	0.2507(4)
V (Å^3)	585.776(9)
Cation distribution	$(Mg_{0.99}Fe^{3+}_{0.01})_{Td}(Mg_{0.01}Fe^{3+}_{0.99}Cr)_{Oh}$
B_iso (Å^2)	0.13632
R_p	3.32
R_{wp}	6.93
R_{exp}	2.25
χ^2	9.45

Table 7-1 Parameters resulted from refinement of $MgFeCrO_4$ XRD pattern and refinement reliability factors at corresponding the stage of the refinement illustrated in Figure 7-1.

7.2.3 The refinement of the inversion degree:

Occupancies of Mg^{2+} and Fe^{3+} were refined from a starting value of 1% inversion in the structure and the occupancies were constrained as: the amount of Mg^{2+} situated at the B site is replaced by Fe^{3+} at the A site to an occupancy equal to 1 on each site. Possible formation of cation vacancies in the structure was not implemented into the structural model used for refinement. In Figure 7-2 is illustrated the implementation of constraints, as explained above and the refined profile at this stage of the refinement. Table 7-2 summarises several parameter values for which the cation inversion was refined, the inversion degree resulted after this stage, and the reliability factors.

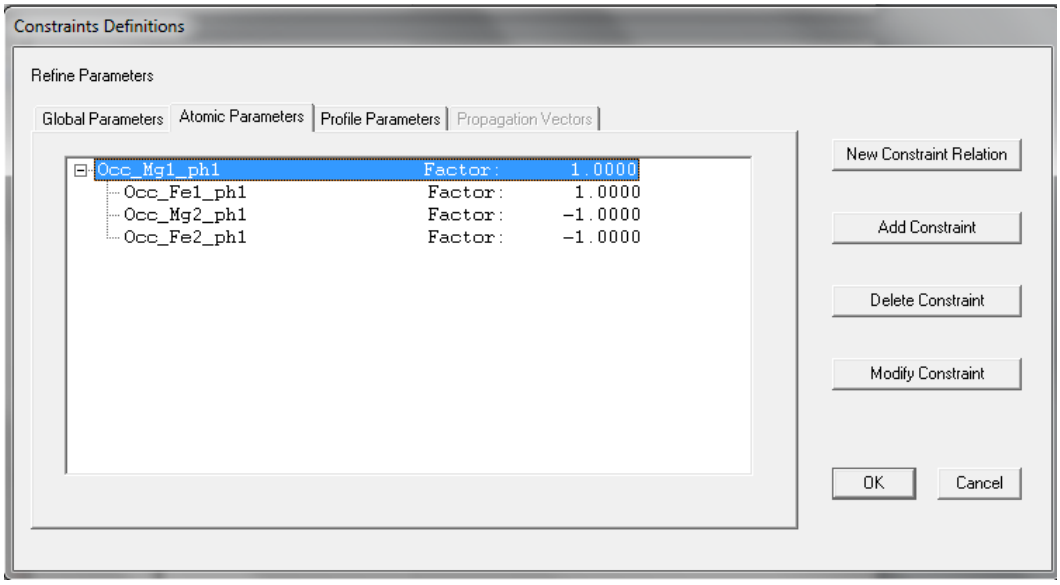

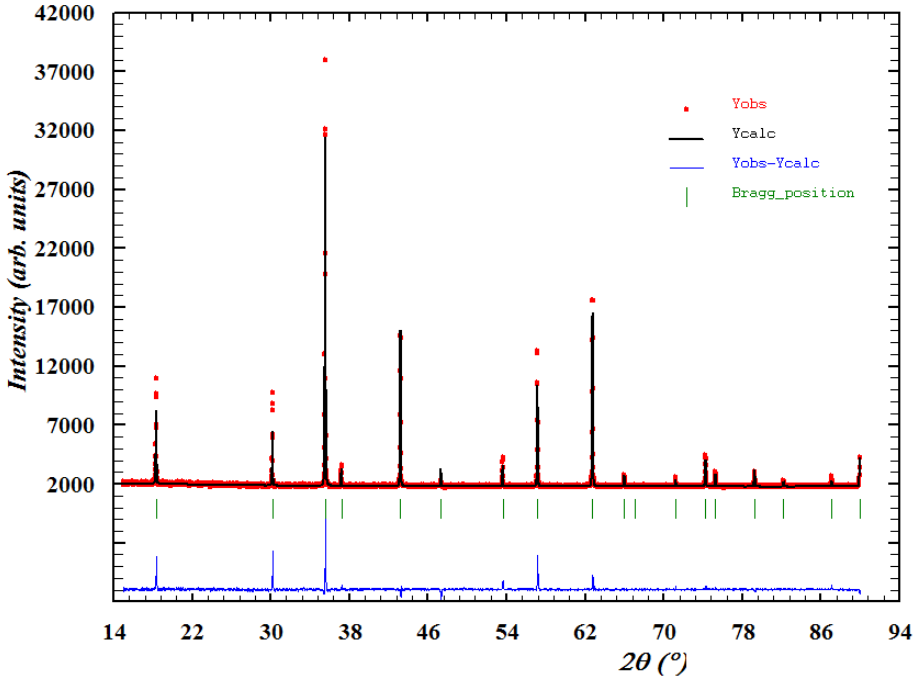

Figure 7-2 Rietveld refinement profiles of $MgFeCrO_4$ after refining the degree of inversion in the spinel.

Refined parameter	$MgFeCrO_4$
a (Å)	8.36715(8)
u (Å)	0.2507(4)
V (Å^3)	585.776(9)
Cation distribution	$(Mg_{0.73}Fe_{0.27})_{Td}(Mg_{0.27}Fe_{0.73}Cr)_{Oh}$
B_iso (Å^2)	0.13632
R_p	2.71
R_{wp}	4.81
R_{exp}	2.26
χ^2	4.55

Table 7-2 Parameters resulted from refinement of $MgFeCrO_4$ diffraction pattern and the reliability factors at corresponding the stage of the refinement illustrated in Figure 7-2.

After the inversion of the Mg^{2+} and Fe^{3+} cations at the A and B sites was refined, further refinement of the scale factor, cell parameter, oxygen parameter and peak profile parameters determined improvement of the profile fitting. At this stage it can be noted from Figure 7-3 and Table 7-3 the positive effects of refining the cation

distribution, with decreasing the difference between observed and calculated peak intensities.

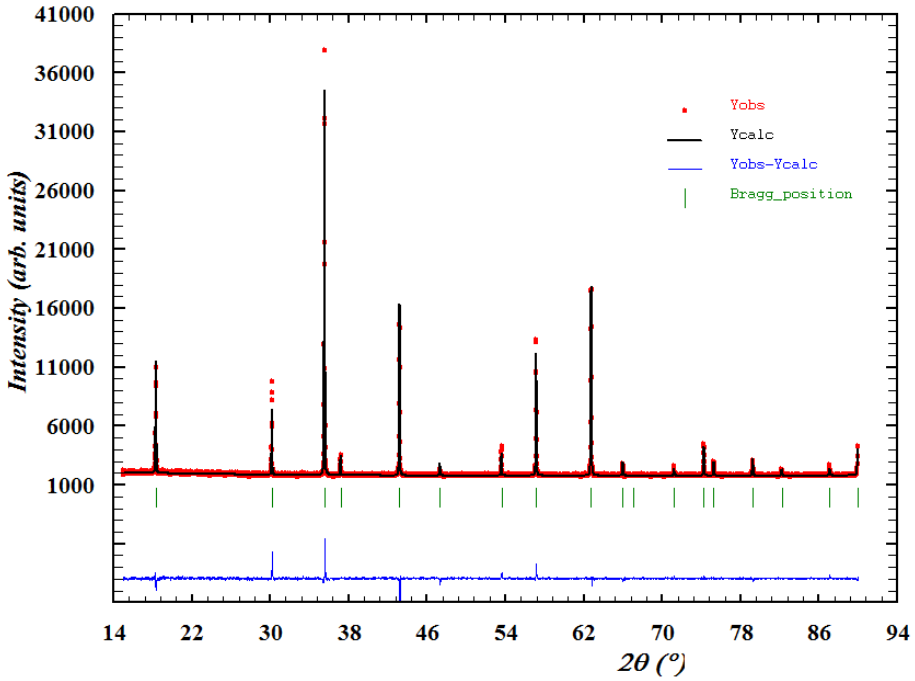

Figure 7-3 Rietveld refinement profiles of $MgFeCrO_4$ after refining the degree of inversion in the spinel and scale factor, cell parameter, oxygen parameter and peak profile parameters.

Refined parameter	$MgFeCrO_4$
a (Å)	8.36710(3)
u (Å)	0.2556(3)
V (Å^3)	585.770(4)
Cation distribution	$(Mg_{0.73}Fe_{0.27})_{Td}(Mg_{0.27}Fe_{0.73}Cr)_{Oh}$
B_iso (Å^2)	0.13632
R_p	2.26
R_{wp}	3.40
R_{exp}	2.25
χ^2	2.28

Table 7-3 Parameters resulted from refinement of $MgFeCrO_4$ diffraction pattern and the reliability factors at corresponding the stage of the refinement illustrated in Figure 7-3.

The next stage consisted of the refinement of the general thermal factor, with B_iso=0.17026 (Å^2) and it did not determine a significant improvement of the

refinement. The refinement of the cation inversion and cell parameter + oxygen parameter + scale factor was again performed alternatively and led to significant improvement of the profile fitting prior to Stage 8 (refining the atomic isotropic displacement factors). In Figure 7-4 is illustrated the refinement plot and the values of the refined parameters are listed in Table 7-4.

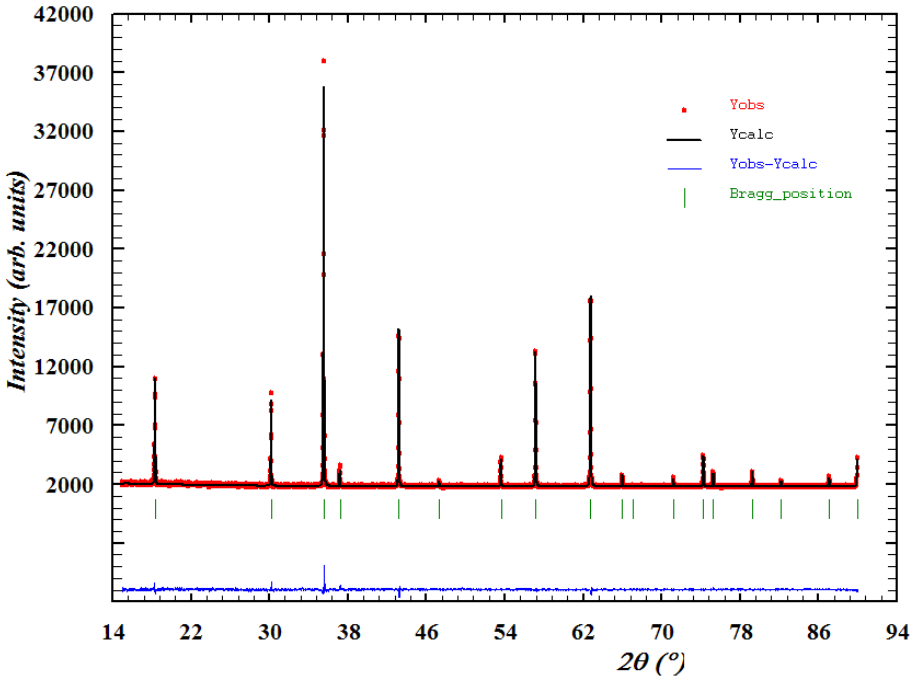

Figure 7-4 Rietveld refinement profiles of $MgFeCrO_4$ after refining the degree of inversion in the spinel and scale factor, cell parameter, oxygen parameter and peak profile parameters repeated several times.

Refined parameter	$MgFeCrO_4$
a (Å)	8.36712(2)
u (Å)	0.2587(2)
V (Å^3)	585.771(3)
Cation distribution	$(Mg_{0.613}Fe_{0.387})_{Td}(Mg_{0.387}Fe_{0.613}Cr)_{Oh}$
B_iso (Å^2)	0.17026
R_p	1.91
R_{wp}	2.55
R_{exp}	2.26
χ^2	1.28

Table 7-4 Parameters resulted from refinement of $MgFeCrO_4$ diffraction pattern and the reliability factors at corresponding the stage of the refinement illustrated in Figure 7-4.

The refinement of the atomic isotropic displacement factors was carried out with the initial value of the thermal factor (B_iso) and all other refinable parameters were fixed. Next, the atomic isotropic displacement factors were fixed and the other parameter refined, excluding the cation inversion. The last step of the Stage 8 described in the **refinement strategy**, consists of refining in the same time: the atomic isotropic displacement factors, scale factor, unit cell parameter, oxygen parameter and peak profile parameters, in order to conclude if the structural model is stable at this stage (Figure 7-5, Table 7-5).

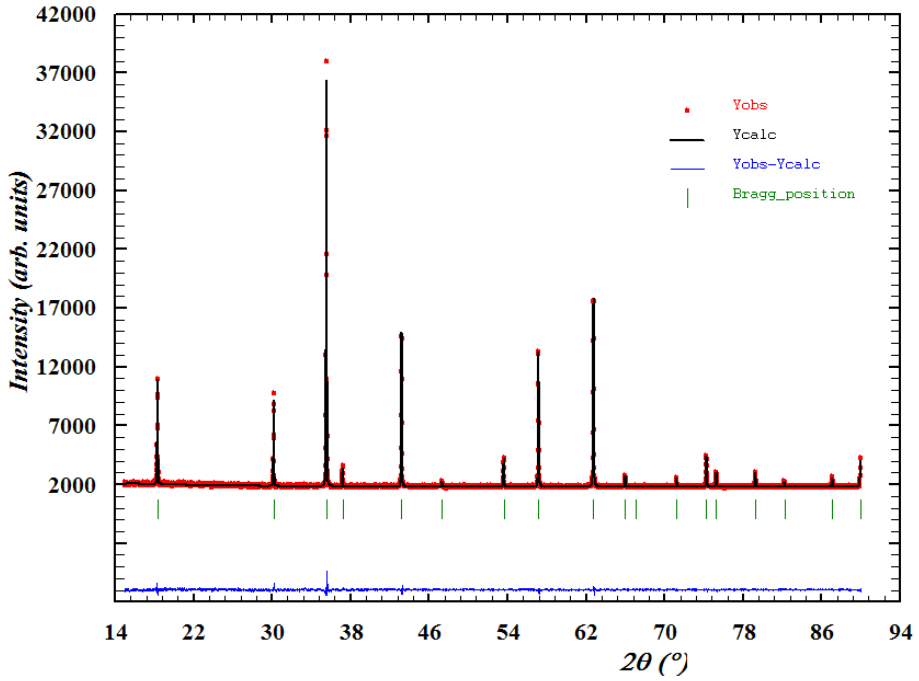

Figure 7-5 Rietveld refinement profiles of $MgFeCrO_4$ after refining the atomic isotropic displacement factors, scale factor, cell parameter, oxygen parameter and peak profile parameters.

Refined parameter	$MgFeCrO_4$
a (Å)	8.36706(2)
u (Å)	0.2585(2)
V (Å^3)	585.758(3)
Cation distribution	$(Mg_{0.613}Fe_{0.387})_{Td}(Mg_{0.387}Fe_{0.613}Cr)_{Oh}$
B_iso_A (Å^2)	0.27(7)
B_iso_B (Å^2)	0.36(5)
B_iso_O (Å^2)	0.92(8)
R_p	1.87
R_{wp}	2.49
R_{exp}	2.25
χ^2	1.22

Table 7-5 Parameters resulted from refinement of $MgFeCrO_4$ diffraction pattern and the reliability factors at corresponding the stage of the refinement illustrated in Figure 7-5.

The final step of the refinement consists in replacing the refinement of the atomic isotropic displacement factors with the refinement of the degree of cation inversion: the atomic displacement factors were fixed and the cation inversion was released for refinement along with the other parameters, in order to conclude if the refinement is stable with respect to the cation inversion, after the refinement of the atomic displacement factors. In Figure 7-6 is shown the refined plot, with experimental, calculated and difference profile and Table 7-6 summarises final values of several refined parameters and the final reliability factors.

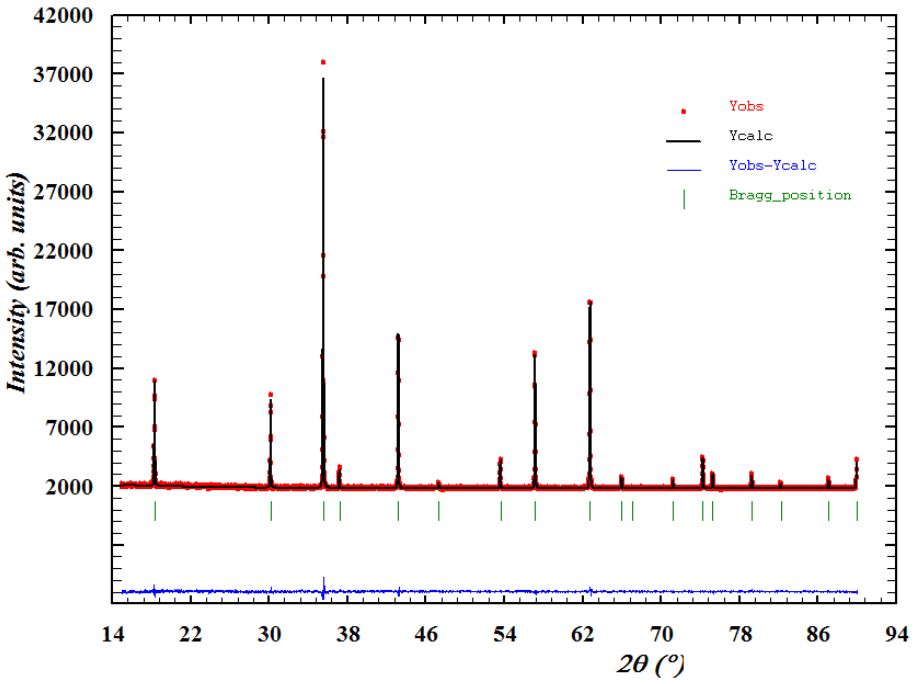

Figure 7-6 Final stage of the Rietveld refinement of $MgFeCrO_4$, after refining the atomic isotropic displacement factors, and cation inversion alternatively, along with the other refinable parameters: scale factor, cell parameter, oxygen parameter and peak profile parameters.

Refined parameter	$MgFeCrO_4$
a (Å)	8.36704(2)
u (Å)	0.2585(2)
V (Å^3)	585.755(3)
Cation distribution	$(Mg_{0.613}Fe_{0.387})_{Td}(Mg_{0.387}Fe_{0.613}Cr)_{Oh}$
B_iso_A (Å^2)	0.32(7)
B_iso_B (Å^2)	0.34(5)
B_iso_O (Å^2)	0.91(8)
R_p	1.87
R_{wp}	2.48
R_{exp}	2.25
χ^2	1.21

Table 7-6 Final parameters resulted from refinement of $MgFeCrO_4$ diffraction pattern and the reliability factors of the refinement illustrated in Figure 7-5.

The cation occupancies and the oxygen content were constrained to the stoichiometric values and the cation inversion degree and the atomic isotropic displacement factors were refined, as described above. The scattering power of the atoms in X-ray is influenced by the temperature factor (B factor), which is a diminishing factor. The temperature factor is also 2θ angle-dependent similar to the scattering power of the atoms, thus affects the high angle reflections considerably.[13] Thus, refining the cation inversion degree and atomic isotropic displacement factors, at the same time would not be the best option. Also in the case of cations with similar atomic numbers, the refinement of occupancies or inversion degree (*e.g.* Mn, Fe, Cr) would be irrelevant for the real structure, as their scattering factors are very similar in XRD.

In the case of oxygen content, XRD full profile fitting may give a good insight on the oxygen deficiency or excess, when combined with other techniques, such as thermo-gravimetry. However, it should be noted that oxygen is not a strong scatterer of X-rays, and thus the overall oxygen occupancy and atomic position determined from XRD are not very reliable. Oxygen scatters neutrons much stronger and such, more precise oxygen occupancies and atomic positions could be obtained by using neutron powder diffraction (NPD).

In comparison with the scattering power of the atoms in X-ray, the diffraction of neutrons is not angle-dependent. The neutrons are scattered by nuclei, thus neutron scattering factors are independent of diffraction angle and atomic number. Thus, the technique is recommended for detecting light atoms like H, Li, O, but also to differentiate between cation species with similar number of electrons, as Mn, Fe, Cr.[13,19] Nonetheless, the majority of crystal structure determinations are carried out using XRD and the role of NPD in structure determination is the validation and completion of structures determined using XRD.[14]

As described above, there are certain limitations of the structural model considered for the full profile pattern fitting of spinels when only XRD data are available. However, the model applied was appropriate for the limitations of the technique and stable during refinement. The refinement strategy described above was suitable in all cases and only when cations as Mn, Fe, Cr were implied, the inversion degree of the cations was not refined and the structural model corresponded to normal distribution. The pattern fitting resulted in a good approximation of the cation

distribution when cations with sufficiently different scattering factors were implied (refined).

7.3 References

1. H. S. C. O'Neill and A. Navrotsky, *Am. Mineral.*, 1983, **68**, 181–194.
2. A. Petric and H. Ling, *J. Am. Cer. Soc.*, 2007, **90**, 1515–1520.
3. X. Chen, P. Y. Hou, C. P. Jacobson, S. J. Visco, D. Jonghe, and L. C, 2004.
4. Z. Lu, J. Zhu, E. Andrew Payzant, and M. P. Paranthaman, *J. Am. Cer. Soc.*, 2005, **88**, 1050–1053.
5. Sakai, T. Horita, Y. P. Xiong, K. Yamaji, H. Kishimoto, M. E. Brito, H. Yokokawa, and T. Maruyama, *Solid State Ionics*, 2005, **176**, 681–686.
6. S. Wang, X. Liu, Y. Fei, Q. He, and H. Wang, *Phys. Chem. Miner.*, 2012, **39**, 189–198.
7. E. Rios, P. Lara, D. Serafini, A. Restovic, and J. L. Gautier, *J. Chil. Chem. Soc.*, 2010, **55**, 261–265.
8. M. Gaudon, N. Pailhé, A. Wattiaux, and A. Demourgues, *Mater. Res. Bull.*, 2009, **44**, 479–484.
9. I. S. Ahmed Farag, M. A. Ahmed, S. M. Hammad, and A. M. Moustafa, *Cryst. Res. Technol.*, 2001, **36**, 85–92.
10. K. S. Lohar and S. M. Patange, *International Journal of Advances in Engineering & Technology*, 2012, **3**, 354–361.
11. A. A. Birajdar, S. E. Shirsath, R. H. Kadam, S. M. Patange, D. R. Mane, and A. R. Shitre, *International Scholarly Research Network ISRN Ceramics*, **2012**, 5.
12. S. M. Patange, S. E. Shirsath, G. S. Jangam, K. S. Lohar, S. S. Jadhav, and K. M. Jadhav, *J. Appl. Phys.*, Mar, **109**, 053909–053909–9.
13. V. Pecharsky and P. Zavalij, *Fundamentals of Powder Diffraction and Structural Characterization of Materials*, 2nd Edition., 2009.
14. W. I. F. David, K. Shankland, L. B. McCusker, and C. Baerlocher, *Structure Determination from Powder Diffraction Data*, Oxford University Press, 2002.
15. T. Suzuki, K. Adachi, and T. Katsufuji, *J. Magn. Magn. Mater.*, 2007, **310**, 780–781.
16. P. Kovtunenko, *Glass Ceram+*, 1997, **54**, 143–148.
17. E. W. Gorter, *Saturation Magnetisation and Crystal Chemistry of Ferrimagnetic Oxides*, Phillips, 1954.
18. L. Morozova and V. Popov, *Glass Phys. Chem+*, 2010, **36**, 86–91.
19. A. R. West, *Basic Solid State Chemistry*, Wiley-Blackwell, 2nd Edition., 1999.

8 Appendix 2 - Rietveld refinement result for spinel oxides

The refinement data included in chapters 3 and 4 is further completed here with more results from Rietveld refinement for various spinel compounds studied.

Refinement plots are illustrated below with observed intensities plotted with red dots, calculated intensities with black line and the difference between calculated and observed intensities is given as blue line. $MnLi_{0.1}Cr_{1.9}O_4$ (Figure 8-1) had lattice parameter a = 8.43203(2) Å, oxygen parameter u = 0.2657(2) Å and unit cell volume V = 599,511(2) $Å^3$. Values of other refined parameters are listed in Table 8-1.

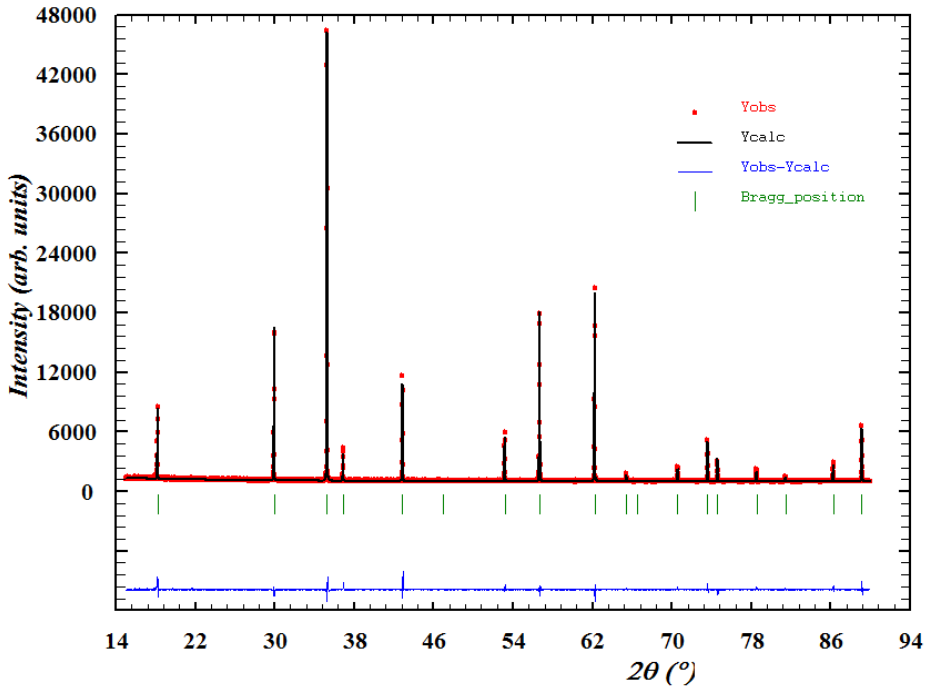

Figure 8-1 Rietveld refinement profiles for $MnLi_{0.1}Cr_{1.9}O_4$ with Si as internal standard; Observed data is represented with red dots, calculated profile with black line and difference profile with blue line.

Figure 8-2 presents the refined XRD pattern of $Mn_{1.5}Cr_{1.5}O_4$, with cell parameter a = 8.46104(2) Å, oxygen parameter u = 0.2636(2) Å and unit cell volume V = 605,720(3) $Å^3$. $Mn_{1.5}Cr_{1.5}O_4$ was refined as normal spinel with substituted Mn cations on B site. $MgMnCrO_4$ was refined (Figure 8-3) considering the possible inversion between Mg and Mn cations on A and B sites and had the cell parameter

a = 8.38080(8) Å, oxygen parameter u = 0.2620(2) Å and unit cell volume V = 588,646(9) Å^3.

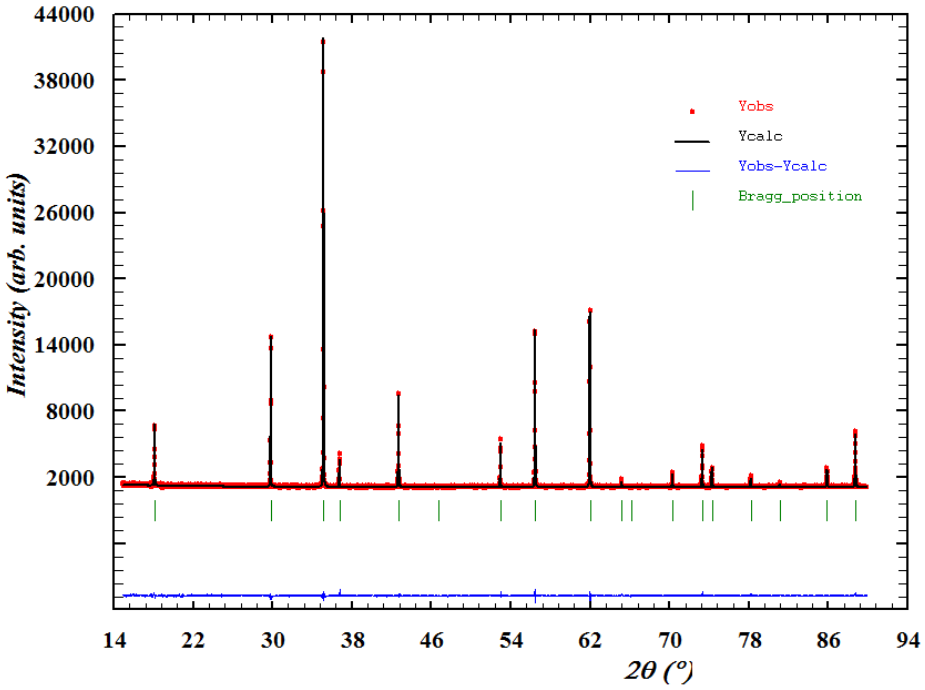

Figure 8-2 Rietveld refinement profiles for $Mn_{1.5}Cr_{1.5}O_4$. Experimental data is represented with red dots, calculated profile with black line and difference profile with blue line.

Refinement parameter	$MnLi_{0.1}Cr_{1.9}O_4$	$Mn_{1.5}Cr_{1.5}O_4$	$MgMnCrO_4$
V (Å^3)	599.511(3)	605.720(3)	588.646(9)
B_iso_A (Å^2)	0.80(7)	0.41(5)	0.53(6)
B_iso_B (Å^2)	0.34(6)	0.50(4)	0.44(2)
B_iso_O (Å^2)	1.43(1)	1.34(1)	1.45(7)
R_p	2.58	2.29	2.63
R_{wp}	3.91	3.11	3.65
R_{exp}	2.89	2.28	2.85
χ^2	1.83	1.21	1.64

Table 8-1 Parameters resulted from refinement of $MnLi_{0.1}Cr_{1.9}O_4$, $Mn_{1.5}Cr_{1.5}O_4$ and $MgMnCrO_4$ XRD patterns and refinement reliability factors; B_iso_A, B_iso_B and B_iso_O are isotropic thermal factors for cations at A and B sites and oxygen anions.

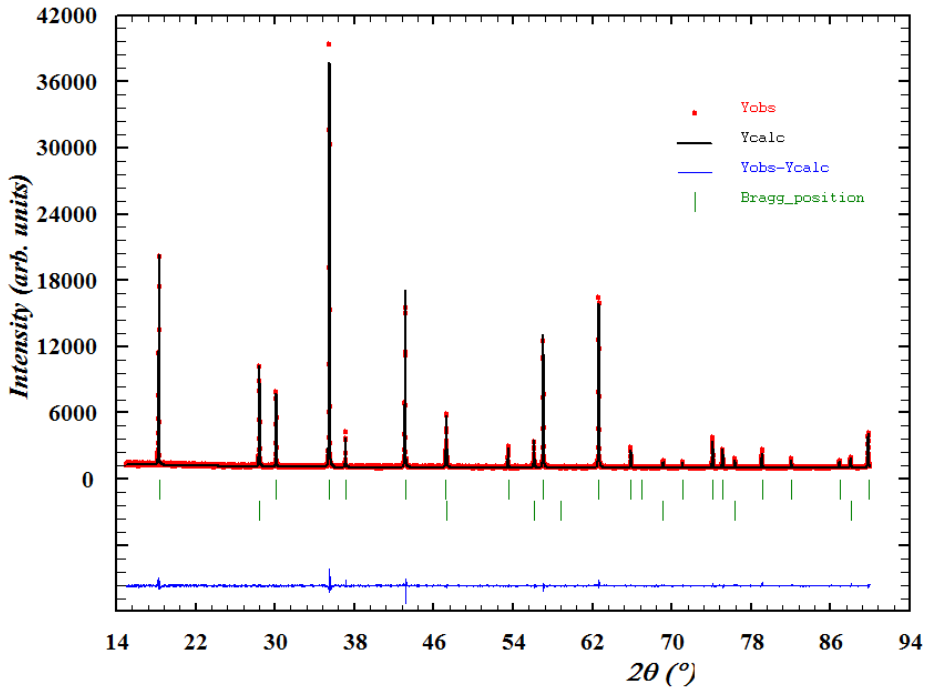

Figure 8-3 Rietveld refinement profiles for $MgMnCrO_4$ with Si as internal standard.

X-ray diffraction patterns of $MgFe_{0.1}Cr_{1.9}O_4$ and $MgFe_{0.5}Cr_{1.5}O_4$ were refined (Figure 8-4) considering the possibility of inversion between Fe and Mg on A and B sites. $MgFe_{0.1}Cr_{1.9}O_4$ had lattice parameter a = 8.33819(2) Å, oxygen parameter u = 0.2604(2) Å and unit cell volume V = 579.705(6) $Å^3$. $MgFe_{0.5}Cr_{1.5}O_4$ had lattice parameter a = 8.3566(1) Å, oxygen parameter u = 0.2605(2) Å and unit cell volume V = 583.58(2) $Å^3$. $MgLi_{0.1}Cr_{1.9}O_4$ had lattice parameter a = 8.33438(2) Å, oxygen parameter u = 0.2617(2) Å and unit cell volume V = 578.922(2) $Å^3$. The values of refined parameters are listed in Table 8-2.

a

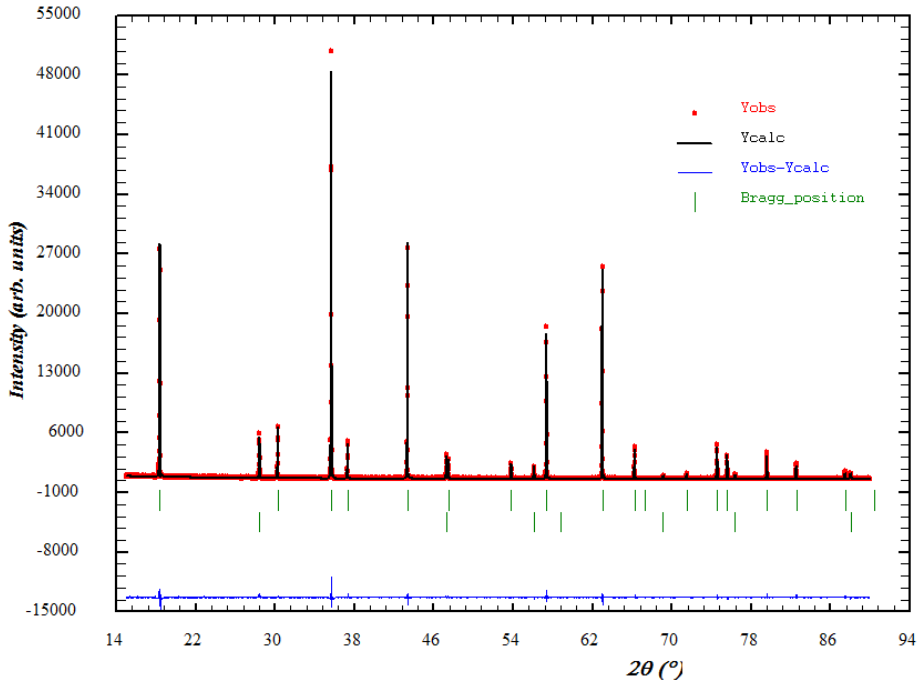

b

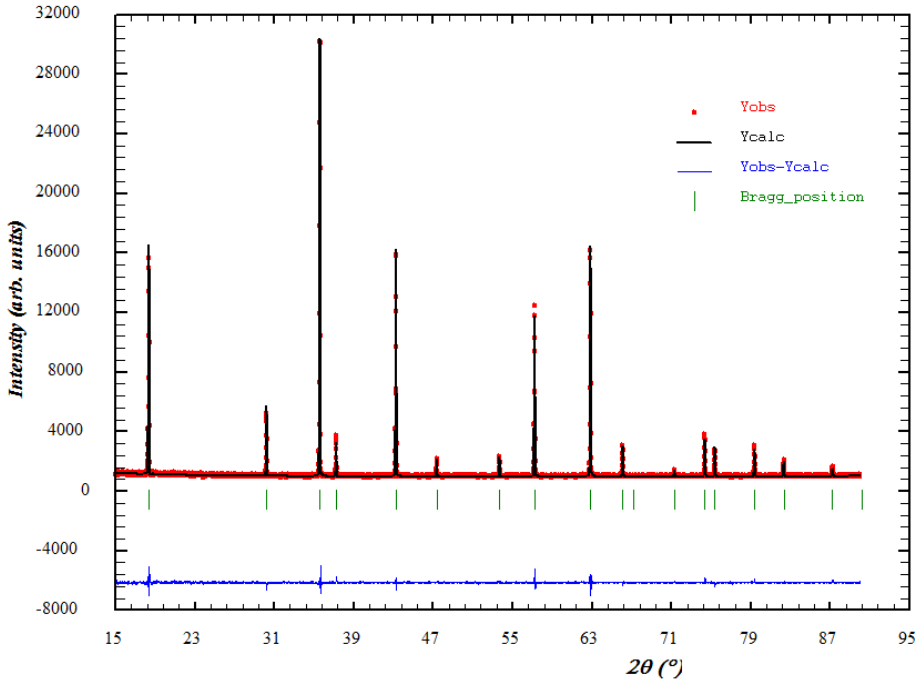

Figure 8-4 Rietveld refinement profiles for: a) $MgFe_{0.1}Cr_{1.9}O_4$ and b) $MgFe_{0.5}Cr_{1.5}O_4$. Experimental data is represented with red dots, calculated profile with black line and difference profile with blue line.

Refinement parameter	$MgFe_{0.1}Cr_{1.9}O_4$	$MgFe_{0.5}Cr_{1.5}O_4$	$MgLi_{0.1}Cr_{1.9}O_4$
V (Å^3)	579.705(6)	583.58	578.922(2)
B_iso_A (Å^2)	0.33(8)	1.04(7)	0.94(8)
B_iso_B (Å^2)	0.27(4)	0.05(4)	0.38(4)
B_iso_O (Å^2)	0.88(8)	0.92(8)	1.34(8)
R_p	3.53	2.56	3.55
R_{wp}	4.92	3.48	5.08
R_{exp}	3.52	2.94	3.63
χ^2	1.96	1.40	1.96

Table 8-2 Parameters resulted from refinement of $MgFe_{0.1}Cr_{1.9}O_4$, $MgFe_{0.5}Cr_{1.5}O_4$ and $MgLi_{0.1}Cr_{1.9}O_4$ XRD patterns and refinement reliability factors, with B_iso_A, B_iso_B and B_iso_O isotropic thermal factors.

Also $MgGa_{0.1}Cr_{1.9}O_4$, $MgGa_{0.2}Cr_{1.8}O_4$ and $MgCu_{0.1}Cr_{1.9}O_4$ were refined in cubic system, space group Fd-3m resulting in very good refinement plots and the refined parameters are resumed in Table 8-3.

Refinement parameter	$MgGa_{0.1}Cr_{1.9}O_4$	$MgGa_{0.2}Cr_{1.9}O_4$	$MgCu_{0.1}Cr_{1.9}O_4$
V (Å^3)	578.64(1)	578.37(2)	578.863(2)
B_iso_A (Å^2)	0.11(7)	0.22(5)	0.92(7)
B_iso_B (Å^2)	0.18(4)	0.22(2)	0.28(2)
B_iso_O (Å^2)	0.61(7)	0.68(6)	1.71(7)
R_p	3.30	3.40	4.13
R_{wp}	4.52	4.77	5.83
R_{exp}	3.26	3.28	376
χ^2	1.93	2.12	2.43

Table 8-3 Parameters resulted from refinement of $MgGa_{0.1}Cr_{1.9}O_4$, $MgGa_{0.2}Cr_{1.8}O_4$ and $MgCu_{0.1}Cr_{1.9}O_4$ XRD patterns and refinement reliability factors, with B_iso_A, B_iso_B and B_iso_O isotropic thermal factors.

$Mg_{1.5}Ti_{0.5}CrO_4$ (Figure 8-5) was considered with an inversion degree of 0.5 since this composition could be formally written as solid solution of 1 $MgCr_2O_4$: 1 Mg_2TiO_4. $Mg_{1.5}Ti_{0.5}CrO_4$ had lattice parameter a = 8.38704(5) Å, oxygen parameter

u = 0.2606(1) Å and unit cell volume V = 589.964(6) Å^3. The isotropic thermal factors for A, B and oxygen sites were B_iso_A = 0.37(6) Å^2, B_iso_B = 0.19(3) Å^2, and B_iso_O = 0.72(6) Å^2 and the refinement reliability factor were R_p = 4.49, R_{wp} = 6.29, R_{exp} = 4.14 and χ^2 = 2.31.

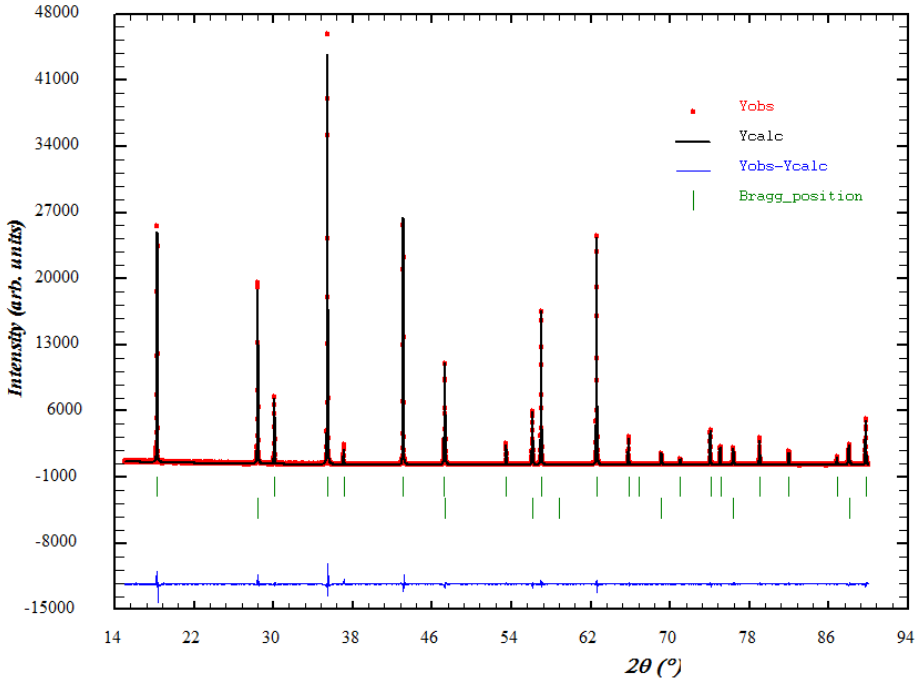

Figure 8-5 Rietveld refinement profiles for $Mg_{1.5}Ti_{0.5}CrO_4$. Experimental data is represented with red dots, calculated profile with black line and difference profile with blue line.

Rietveld refinements results for Li,Cr titanates with spinel structure sintered at different temperatures below the phase transformation, demonstrated good fitting results completed here by refinement plots and other refined parameters. Since every composition was sintered and refined for several temperatures only several refinement plots are presented. The cell parameters and oxygen parameters determined for these spinels are listed in chapter and the cell parameters were plotted against sintering temperatures to observe if important changes occur in composition with temperature. Other refined parameters for given plots and for the refinements corresponding to other temperatures are listed in Table 8-4, Table 8-5 and Table 8-6.

a

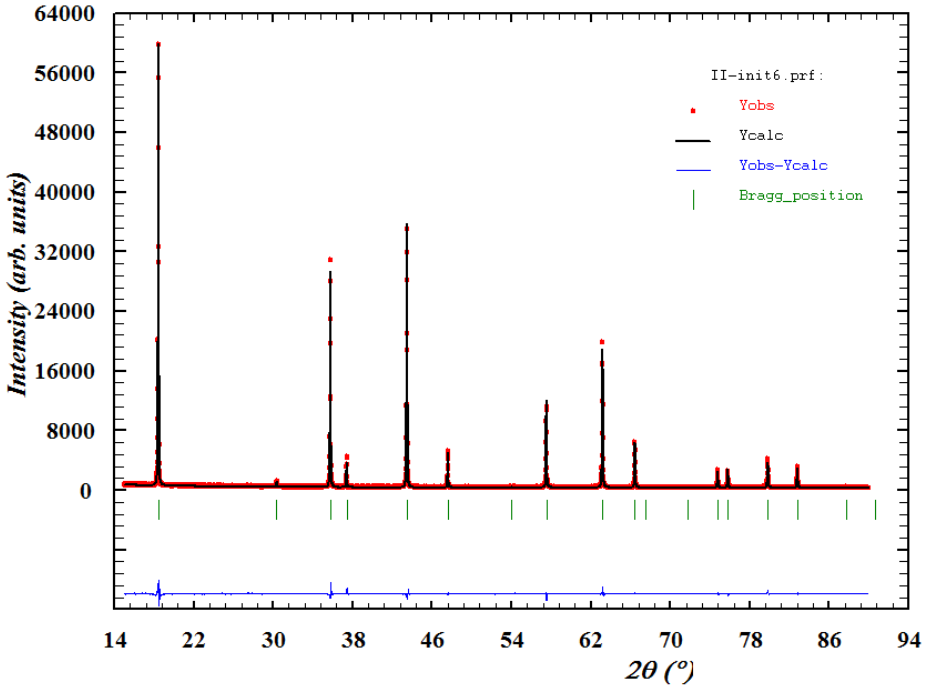
II-init6.prf:
Yobs
Ycalc
Yobs-Ycalc
Bragg_position
Intensity (arb. units)
64000
56000
48000
40000
32000
24000
16000
8000
0
14
22
30
38
46
54
62
70
78
86
94
2θ (°)

b

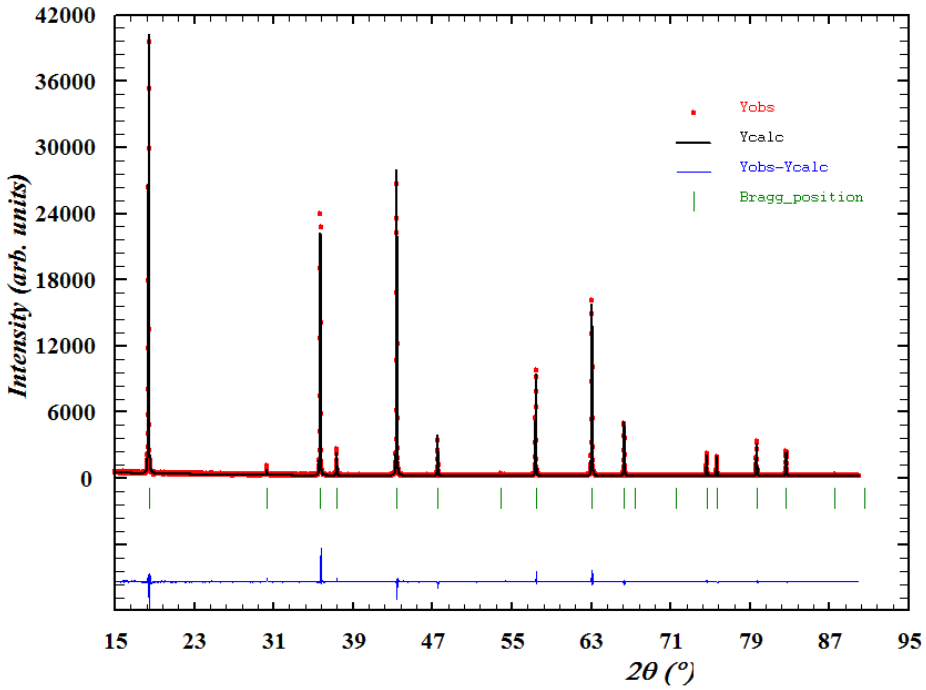
Yobs
Ycalc
Yobs-Ycalc
Bragg_position
Intensity (arb. units)
42000
36000
30000
24000
18000
12000
6000
0
15
23
31
39
47
55
63
71
79
87
95
2θ (°)

c

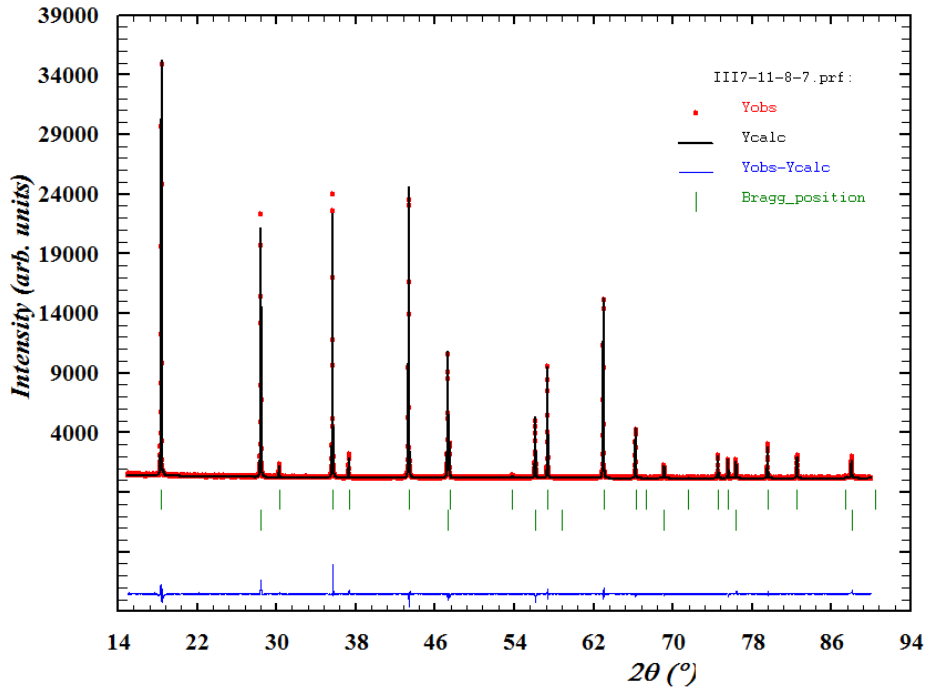

d

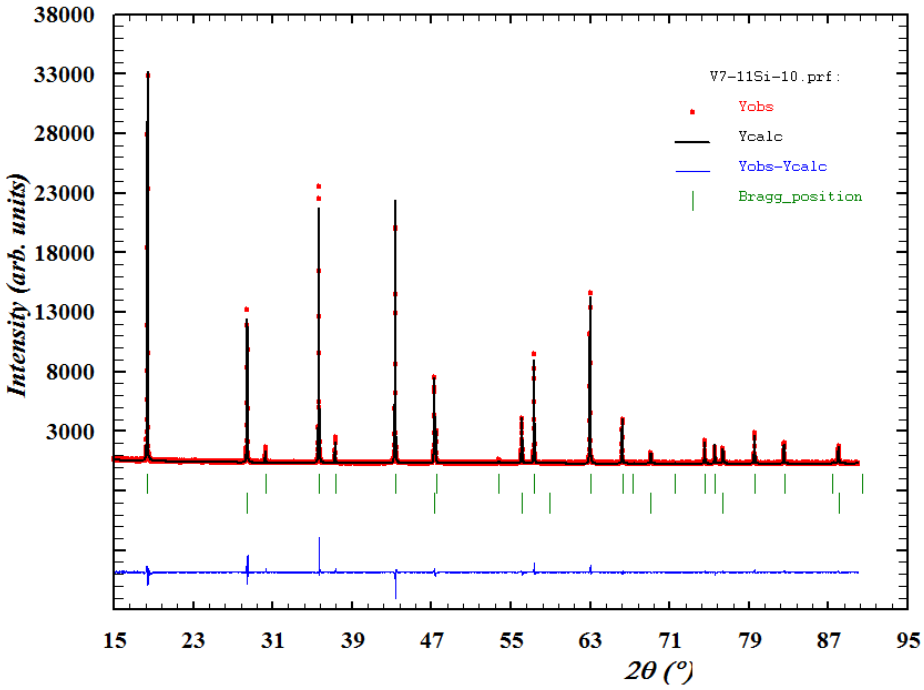

Figure 8-6 Rietveld refinement profiles for: a) $Li_{0.9}Mg_{0.1}Cr_{1.1}Ti_{0.9}O_4$ sintered at 900 °C, b) $Li_{0.9}Mg_{0.2}Cr_{0.9}TiO_4$ sintered at 1000 °C, c) $Li_{0.85}Mg_{0.3}Cr_{0.85}TiO_4$ sintered at 1000 °C and d) $Li_{0.8}Mg_{0.3}Cr_{0.9}Ti_{0.9}Fe_{0.1}O_4$ sintered at 1100 °C. Observed data is represented with red dots, calculated profile with black line and difference profile with blue line.

Refinement parameter	$Li_{0.9}Mg_{0.2}Cr_{0.9}TiO_4$ (900 °C)	$Li_{0.9}Mg_{0.2}Cr_{0.9}TiO_4$ (1000 °C)	$Li_{0.9}Mg_{0.1}Cr_{1.1}Ti_{0.9}O_4$ (900 °C)	$Li_{0.9}Mg_{0.1}Cr_{1.1}Ti_{0.9}O_4$ (1000 °C)
V (Å^3)	578.370(5)	578.22(2)	575.36	575.35
B_iso_A (Å^2)-fixed	0.5	0.5	0.5	0.5
B_iso_B (Å^2)	0.04(4)	0.31(4)	0.42(3)	0.13(4)
B_iso_O (Å^2)	0.37(4)	0.58(8)	0.77(7)	0.59(8)
R_p	5.96	5.43	4.20	5.45
R_{wp}	7.74	7.18	5.89	7.45
R_{exp}	4.90	4.88	3.99	4.70
χ^2	2.50	2.16	2.18	2.51

Table 8-4 Parameters resulted from refinement of $Li_{0.9}Mg_{0.2}Cr_{0.9}TiO_4$ sintered at 900 °C, $Li_{0.9}Mg_{0.2}Cr_{0.9}TiO_4$ sintered at 1000 °C, $Li_{0.9}Mg_{0.1}Cr_{1.1}Ti_{0.9}O_4$ sintered at 900 °C, $Li_{0.9}Mg_{0.1}Cr_{1.1}Ti_{0.9}O_4$ sintered at 1000 °C XRD patterns and refinement reliability factors, with B_iso_A, B_iso_B and B_iso_O isotropic thermal factors.

Refinement parameter	$Li_{0.85}Mg_{0.3}Cr_{0.85}TiO_4$ (1000 °C)	$Li_{0.85}Mg_{0.3}Cr_{0.85}TiO_4$ (1100 °C)	$Li_{0.8}Mg_{0.3}Cr_{0.9}Ti_{0.9}Fe_{0.1}O4$ (1100 °C)
V (Å^3)	579.957(4)	579.832(5)	580.087(3)
B_iso_A (Å^2)-fixed	0.5	0.5	0.5
B_iso_B (Å^2)	0.30(4)	0.32(5)	0.48(4)
B_iso_O (Å^2)	0.73(7)	1.01(9)	1.01(8)
R_p	5.58	6.64	4.98
R_{wp}	7.43	8.499	6.64
R_{exp}	5.00	5.37	4.48
χ^2	2.21	2.50	2.20

Table 8-5 Parameters resulted from refinement of $Li_{0.85}Mg_{0.3}Cr_{0.85}TiO_4$ sintered at 1000 °C, $Li_{0.85}Mg_{0.3}Cr_{0.85}TiO_4$ sintered at 1100 °C and $Li_{0.8}Mg_{0.3}Cr_{0.9}Ti_{0.9}Fe_{0.1}O_4$ sintered at 1100 °C XRD patterns and refinement reliability factors, with B_iso_A, B_iso_B and B_iso_O isotropic thermal factors.

Refinement parameter	$Li_{0.7}Mg_{0.4}Cr_{0.9}Ti_{0.8}Fe_{0.2}O_4$ (1000 °C)	$Li_{0.7}Mg_{0.4}Cr_{0.9}Ti_{0.8}Fe_{0.2}O_4$ (1100 °C)	$Li_{0.7}Mg_{0.4}Cr_{0.9}Ti_{0.8}Fe_{0.2}O_4$ (1100 °C)
V (Å^3)	581.579(3)	581.569(5)	581.535(2)
B_iso_A (Å^2)-fixed	0.5	0.5	0.5
B_iso_B (Å^2)	0.42(5)	0.50(5)	0.42(4)
B_iso_O (Å^2)	0.87(9)	1.29(1)	1.59(8)
R_p	4.51	4.99	3.99
R_{wp}	6.28	6.87	5.41
R_{exp}	4.05	4.34	4.01
χ^2	2.41	2.50	1.82

Table 8-6 Parameters resulted from refinement of $Li_{0.7}Mg_{0.4}Cr_{0.9}Ti_{0.8}Fe_{0.2}O_4$ sintered at 1000 °C, $Li_{0.7}Mg_{0.4}Cr_{0.9}Ti_{0.8}Fe_{0.2}O_4$ sintered at 1100 °C and $Li_{0.7}Mg_{0.4}Cr_{0.9}Ti_{0.8}Fe_{0.2}O_4$ sintered at 1200 °C XRD patterns and refinement reliability factors, with B_iso_A, B_iso_B and B_iso_O isotropic thermal factors.

9 Appendix 3 – Impedance spectra analysis by equivalent circuit method

As described by Jørgensen and Mogensen[1], the impedance spectra typically include a high frequency induction tail (originating from the measurement apparatus), an ohmic resistance (generally, electrolyte resistance) and two to four electrode processes. The equivalent circuit used to fit experimental data in chapter 5, also illustrated in Figure 9-1 is constructed according to the general considerations of Jørgensen and Mogensen mentioned above (see also section 2.8.2), and to other literature data on similar cell configurations and/or impedance spectra.[2–4] Presented here, is the equivalent circuit modelling method applied in this thesis on the electrochemical impedance data, in terms of fitting impedance spectra and assigning the electrode processes.

As example, the parameters resulted from fitting and the corresponding plots are shown for $MnFeCrO_4$/LSCM symmetrical cell measured at several temperatures in 5%H_2/Ar. The deconvolution of the impedance spectra was achieved in two steps: first was performed a fitting of the data for a selected range of points and secondly a simulation was made on a frequency range from 100.000 Hz – 0.001 Hz. The simulation step keeps constant the fitted parameter values achieved in the first stage and applies the fitting for a wider range of frequencies, usually selected by the user. The relaxation frequencies were determined as reported in ref [1], and for lower temperatures these were easily distinguishable, as the two time constants were well separated. At higher temperatures the two semicircles started to overlap and they were differentiated by equivalent circuit fitting of the data, which can be helpful to deconvolute overlapped components.

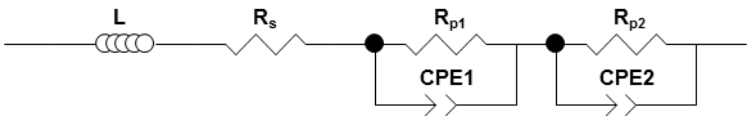

Figure 9-1 Equivalent circuit model for characterising the impedance spectra for $MnFeCrO_4$/LSCM symmetrical cell.

There is also the possibility that more arcs are present in the impedance spectra but it is not always easy to distinguish, as impedance arcs may overlap partially or completely.[1]

Figure 9-2 illustrates the electrochemical impedance spectra in the form of Nyquist and Bode plots for $MnFeCrO_4$/LSCM symmetrical cells measured in 5%H_2/Ar upon cooling, after reduction. The parameters resulted from equivalent circuit fitting are summarised in Table 9-1. The given values are for one electrode. The equivalent capacitance, C_{eq} was calculated using the Equation 2-14,[5,6] and the formula accounts for transforming the constant phase element (CPE) obtained values into a real capacitance value. In section 2.8.1 the concept of CPE was introduced, which is used in equivalent circuit modelling to compensate for non-homogeneity in the system (*e.g.* surface roughness at interfaces).[7,8]

$$C_{eq} = \frac{(RQ)^{\frac{1}{n}}}{R}$$ Equation 9-1

Where R is the resistance in the R-CPE parallel element, Q is "pseudo"-capacitance value that has to be corrected for the non-ideal character of the modelled capacitor with the n value (for n=1 the CPE is an ideal capacitor and n=0 CPE is an ideal resistor).

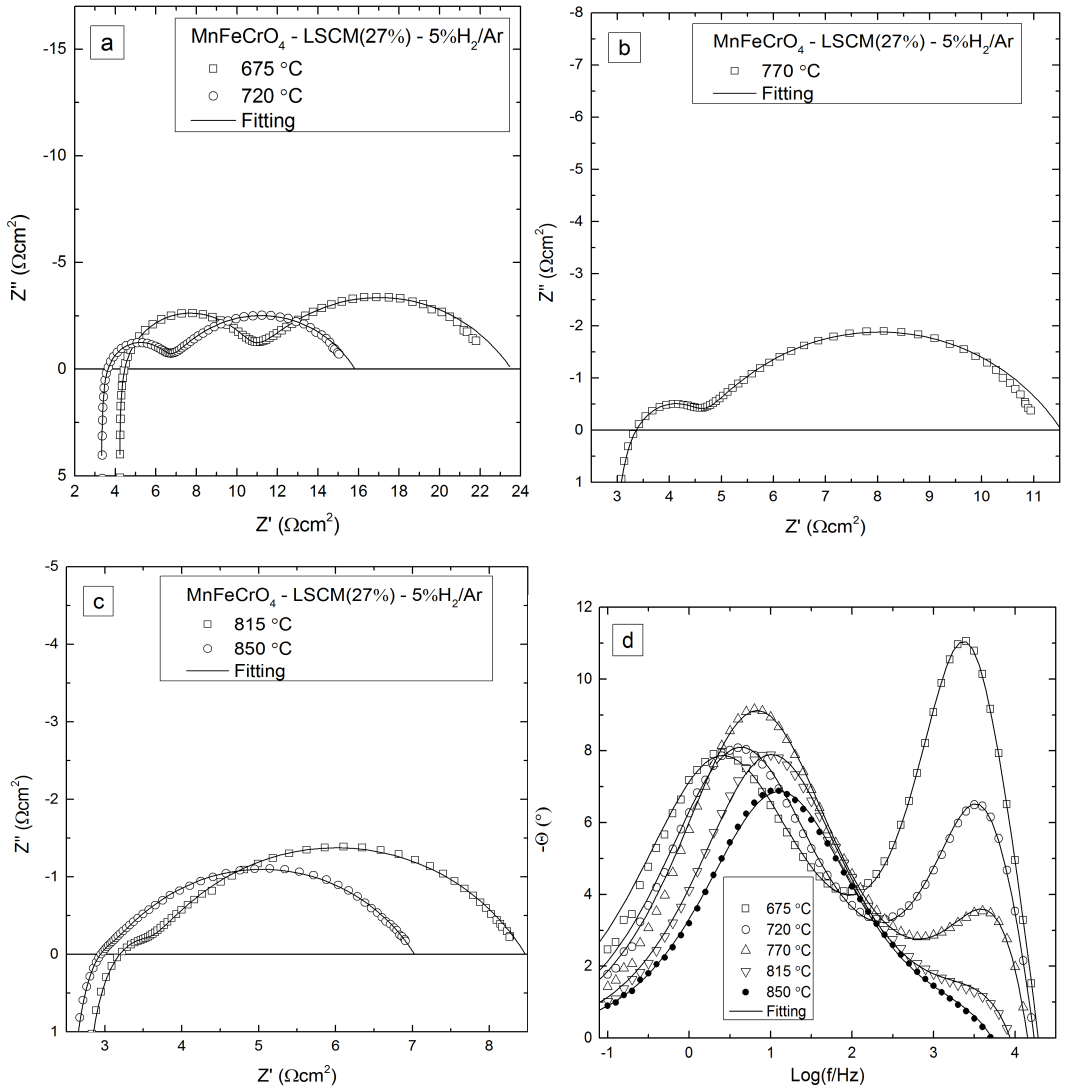

Figure 9-2 Electrochemical impedance spectroscopy of $MnFeCrO_4$/LSCM symmetrical cell measured in 5%H_2/Ar at several temperatures between 675 °C and 850 °C: a), b) and c) Nyquist plots containing data for the whole cell (2 equal electrodes); d) Bode plots.

Temperature (°C)	675	720	770	815	850
L (H)	5.5785E-6	5.6096E-6	5.5803E-6	5.6146E-6	5.6088E-6
R_s (Ω)	2.09	1.66	1.43	1.27	1.18
R_{p1} (Ωcm^2)	3.20	1.65	0.86	0.52	0.37
n_1	0.8579	0.8425	0.8382	0.741	0.6822
f_{max1} (Hz)	2000	3160	3980	2000	700
C_{eq1} (Fcm^{-2})	1.6E-4	2.54E-4	1.17E-5	3.55E-4	1.17E-3
Process 1	Charge transfer	Charge transfer	Charge transfer	Charge transfer	Charge transfer
R_{p2} (Ωcm^2)	6.5	4.63	3.46	2.45	1.98
n_2	0.60586	0.6325	0.623	0.651	0.6434
f_{max2} (Hz)	2	3	5	6	8
C_{eq2} (Fcm^{-2})	3.4E-2	3.5E-2	4.0E-2	4.1E-2	4.7E-2
Process 2	Gas diffusion	Gas diffusion	Gas diffusion	Gas diffusion	Gas diffusion
$R_p=R_{p1}+R_{p2}$	9.7	6.28	4.32	2.96	2.35

Table 9-1 Fitting results of $MnFeCrO_4$/LSCM symmetrical cell measured in 5%H_2/Ar at temperatures between 675-850 °C.

The impedance spectra (Figure 9-2) collected at lower temperatures show two time constants (components) and with increasing temperature, the two components start to overlap. The high frequency arc is shifted with temperature towards lower frequencies, while the low frequency arc shifts slightly to higher frequency values. The frequency shift could be noticed in the Nyquist and mostly, in the Bode plots of the impedance spectra. The quality of the fit has decreased slightly with increasing temperature, but still a good quality fit even for 850 °C dataset. In Figure 9-3 is presented the Nyquist and Bode plots of the impedance spectra collected at 850 °C, and the separation of the component arcs resulted from the equivalent circuit fitting.

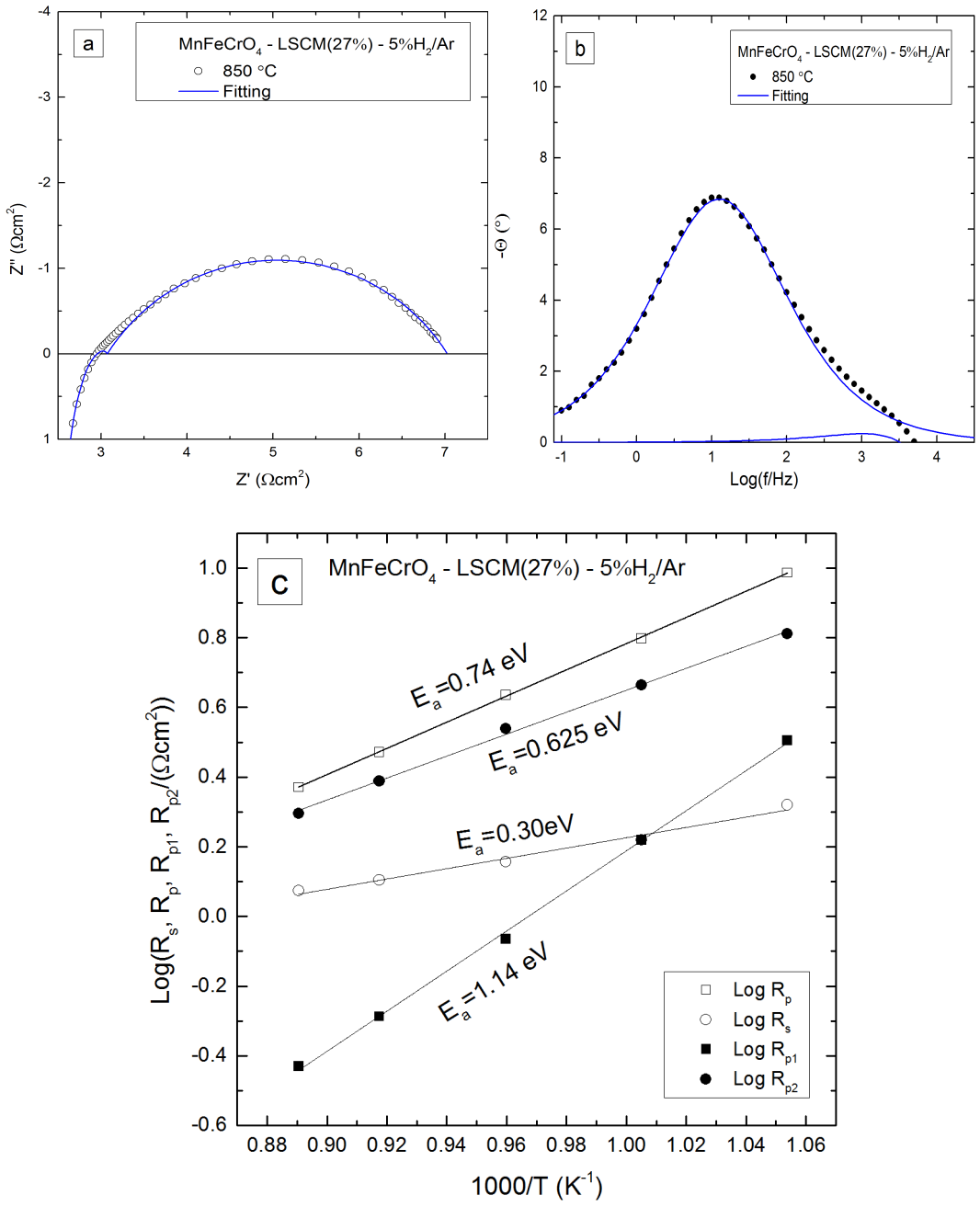

Figure 9-3 Fitting of the experimental data using the equivalent circuit presented above: a) Nyquist plot; b) Bode plot; c) Arrhenius plots for R_s, R_p, R_{p1} and R_{p2} resulted from the data fitting.

The activation energy, E_a for the ohmic resistances (R_s) showed a slight increase, from 0.25 to 0.30 eV, in comparison with the data plotted in Figure 5-10, chapter 5. The temperature range for data representation was 720-850 °C, while here the temperature range for data representation was 675-850 °C. However, the E_a for polarisation resistances (R_p) remained unchanged 0.74 eV, when the temperature

range was extended. In Figure 9-3 are also represented the Arrhenius plot for the two components, R_{p1} and R_{p2} of the polarisation resistance determined form equivalent circuit fitting. The E_a value for R_{p1}, which is related to charge transfer process is much higher than for R_{p2}, related to gas kinetics. This is a sensible observation, since charge transfer is generally activated with increasing temperature (described in section 1.5.3) and both $MnFeCrO_4$ and LSCM are semiconducting materials. In reducing conditions, LSCM retains its p-type semiconductor behaviour and the E_a reported in $5\%H_2/Ar$ was 0.56 eV[9]. The R_{p1} and R_{p2} values determined from equivalent circuit fitting were observed to slightly change when the fitting range was modified. For this reason the fitting frequency range for each temperature was modified as little as possible. The low frequency range may sometimes show scattering of the measured points or inconsistency with the semicircle. Thus the fitting range was considered between 100.000 - 1 Hz and the simulation frequency as described above.

The variation in composition of the symmetrical cells, as presented in chapter 5 – i.e. LSCM, LSCM/CGO, LSCM/CGO/Pd etc., did not have a strong influence for quality of the fit, since mostly two components were observed in the impedance spectra for the composite electrodes. Thus, no extra resistance was observed due to the presence of more interfaces. The two components observed in the impedance spectra were related to charge transfer and gas kinetics.

9.1 References

1. M. J. Jørgensen and M. Mogensen, *J. Electrochem. Soc.*, **148**, A433–A442.
2. G. Tsekouras and J. T. S. Irvine, *J Mater Chem*, 2011, **21**, 9367–9376.
3. S. R. Gamble and J. T. S. Irvine, *Solid State Ionics*, 2011, **192**, 394–397.
4. X. Yue and J. T. S. Irvine, *Ecs Trans.*, 2012, **41**, 87–95.
5. I. M. Torres da Silva, J. Nielsen, J. Hjelm, and M. Mogensen, *Ecs Trans.*, 2009, **25**, 489–498.
6. T. Ramos, J. Hjelm, and M. Mogensen, *J. Electrochem. Soc.*, **158**.
7. Q.-A. Huang, R. Hui, B. Wang, and J. Zhang, *Electrochim. Acta*, 2007, **52**, 8144 – 8164.
8. J. R. Macdonald, *J. Electrochem. Soc.*, 1988, **135**, 2274–2279.
9. S. Tao and J. T. S. Irvine, *J. Electrochem. Soc.*, 2004, **151**, A252–A259.